Study of III-V nanostructures on GaP for lasing emission on Si

Cédric Robert Robert

Résumé

Ce travail de thèse porte sur l'étude de nanostructures semi-conductrices III-V pour le développement d'émetteurs laser sur silicium dans une approche pseudomorphique. Une croissance en accord de maille d'alliages à base de GaP ou plus précisément de nitrures dilués GaPN doit garantir une faible densité de défauts cristallins. Le modèle des liaisons fortes à base étendue est tout d'abord présenté afin de simuler les propriétés électroniques et optiques de structures semi-conductrices sur substrats de GaP ou Si. Les propriétés des alliages massifs GaPN et GaAsPN sont étudiées par des expériences de photoluminescence continue en fonction de la température et de photoluminescence résolue en temps. Les potentialités des puits quantiques GaAsPN/GaP en tant que zone active sont étudiées théoriquement par le modèle des liaisons fortes et expérimentalement en spectroscopie de photoluminescence en température et résolue en temps. Les effets de désordre engendrés par l'incorporation d'azote sont notamment mis en évidence. L'alliage AlGaP est ensuite proposé pour les couches de confinement optique des structures laser. Un contraste d'indice optique entre AlGaP et GaP est mesuré par ellipsométrie spectroscopique. Ce contraste doit permettre un confinement efficace du mode optique. Le problème de l'alignement des bandes en présence d'aluminium est ensuite évoqué. L'utilisation de l'alliage quaternaire GaAsPN est proposée pour résoudre ce problème. Enfin, les boites quantiques InGaAs/GaP sont étudiées en tant qu'alternative aux puits quantiques GaAsPN/GaP dans la zone active. Une forte densité de boites quantiques et une émission de photoluminescence à température ambiante sont ainsi obtenues pour ce système. Les états électroniques des boîtes quantiques sont simulés par la technique des liaisons fortes et la méthode k.p. La photoluminescence résolue en temps couplée à des expériences de photoluminescence continue sous pression hydrostatique, permet de montrer que la transition fondamentale de ces boîtes implique majoritairement des états de conduction de type X.

Abstract

This PhD work focuses on the study of III-V semiconductor nanostructures for the development of laser on Si substrate in a pseudomorphic approach. GaP-based alloys and more specifically dilute nitride GaPN-based alloys are expected to guarantee a low density of crystalline defects through a perfect lattice-matched growth. An extended tight-binding model is first presented to deal with the theoretical challenges for the simulation of electronic and optical properties of semiconductor structures grown on GaP or Si substrate. The optical properties of bulk GaPN and GaAsPN alloys are then studied through temperature dependent continuous wave photoluminescence and time-resolved photoluminescence experiments. The potential of GaAsPN/GaP quantum wells as a laser active zone is discussed in the framework of both theoretical simulations (with the tight-binding model) and experimental studies (with temperature dependent and time-resolved photoluminescence). In particular, the N-induced disorder effects are highlighted. The AlGaP alloy is then proposed as a candidate for the cladding layers. A significant refractive index contrast between AlGaP and GaP is measured by spectroscopic ellipsometry which may lead to a good confinement of the optical mode in a laser structure. The issue of band alignment is highlighted. Solutions based on the quaternary GaAsPN alloy are proposed. Finally, the InGaAs/GaP quantum dots are studied as an alternative to GaAsPN/GaP quantum wells for the active zone. The growth of a high quantum dot density and room temperature photoluminescence are achieved. The electronic band structure is studied by time-resolved photoluminescence and pressure dependent photoluminescence as well as tight-binding and k.p simulations. It demonstrates that the ground optical transition involves mainly X-conduction states.

N° d'ordre : 13ISAR 19 / D13-19
Institut National des Sciences Appliquées de Rennes
20, Avenue des Buttes de Coësmes • CS 70839 • F-35708 Rennes Cedex 7
Tel : 02 23 23 82 00 - Fax : 02 23 23 83 96

Thèse

2013

Cédric ROBERT

THESE INSA Rennes
sous le sceau de l'Université européenne de Bretagne
pour obtenir le titre de
DOCTEUR DE L'INSA DE RENNES
Spécialité : Physique-Optoélectronique

présentée par
Cédric Robert

ECOLE DOCTORALE : *SDLM*
LABORATOIRE : *FOTON*

Study of III-V nanotructures on GaP for lasing emission on Si

Thèse soutenue le 27.08.2013
devant le jury composé de :

Olivier Durand
Professeur (FOTON, INSA Rennes) / Président du jury
Paul Voisin
Directeur de recherches CNRS (LPN) / Rapporteur
Yves Rouillard
Maître de conférences HDR (IES, Université Montpellier 2) / Rapporteur
Udo W. Pohl
Professor Doctor (Technische Universität Berlin) / Examinateur
Alejandro R. Goñi
Professor (CSIC-ICMAB Barcelona) / Examinateur
Marc-André Dupertuis
Maître d'enseignement et de recherche (EPFL Lausanne) / Examinateur
Jacky Even
Professeur (FOTON, INSA Rennes) / Directeur de thèse
Charles Cornet
Maître de conférences (FOTON, INSA Rennes) / Co-encadrant de thèse

Study of III-V nanostructures on GaP for lasing emission on Si

Cédric Robert

Remerciements

Si cette page se trouve être la première du manuscrit, elle est pourtant bien la dernière à avoir été écrite. Non pas qu'elle fut la plus dure à écrire, car j'ai longtemps rêvé ces derniers mois de n'avoir plus que cette page à insérer, mais bien parce qu'elle adresse les traditionnels remerciements finaux à toutes celles et ceux qui ont permis, lors de ces trois dernières années, à ce travail d'aboutir.

Ainsi, je remercie Alain Le Corre, directeur de l'équipe Foton-Ohm, pour m'avoir accueilli si chaleureusement dans son laboratoire.

Je remercie bien évidemment mes encadrants de thèse. Tout d'abord, mon directeur Jacky Even pour le temps et la confiance qu'il m'a accordés, et Charles Cornet pour son enthousiasme indéfectible. Sans eux, j'aurais surement sombré dans le pessimisme qui guette le doctorant sans laser. Je ne pouvais rêver meilleurs encadrants, et j'ai beaucoup appris auprès d'eux.

Je remercie Yves Rouillard, Paul Voisin, Alejandro Goñi, Marc-André Dupertuis et Udo Pohl de m'avoir fait l'honneur de composer mon jury de thèse. Je m'excuse de les avoir contraints à lire mon manuscrit au plein cœur de l'été. J'en profite également pour remercier Aurore Goin du service de la recherche qui a tout fait pour que je puisse soutenir au mois d'août.

Je tenais à remercier toutes les personnes extérieures à Foton avec qui j'ai pu collaborer, notamment Andrea Balocchi et Xavier Marie et leur équipe qui m'ont accueilli plusieurs semaines dans leur laboratoire à Toulouse pour la TRPL, Mikhail Nestoklon pour les nombreux échanges sur le code supercellule, Alejandro Goñi pour les expériences de PL en pression et l'équipe de Benoît Deveaud pour nous avoir accueillis à Lausanne malgré des résultats infructueux.

Mais surtout je voudrais remercier tous les membres de Foton-Ohm pour ces trois années passées auprès d'eux. Je n'oublierai pas ma première visite au laboratoire plusieurs mois avant le début de ma thèse, qui a énormément joué sur mon choix de Foton pour effectuer cette thèse. J'avais alors été marqué par les qualités humaines de tous les membres, et jamais durant ces trois ans je ne les ai remises en défaut ce qui m'a permis d'interagir avec la quasi-totalité des personnes.

Parmi eux, je voudrais remercier les instigateurs et/ou animateurs de la thématique photonique sur silicium : Olivier Durand et Slimane Loualiche entre autres sans qui je n'aurais sans doute pas eu un sujet de thèse aussi passionant. Je remercie le clan des opticiens barbus, Mathieu Perrin, Yoan Léger, Hervé Folliot (non barbu mais opticien quand même), pour le temps qu'ils ont passé à réfléchir avec moi sur ces satanés spectres de PL. Jean-Marc Jancu, mon maître liaisons fortes et Laurent Pedesseau pour le temps passé (et qu'il passe encore) à régler mes problèmes informatiques. Un grand merci, à Tony Rohel, alias le James Bond de l'épitaxie pour m'avoir fourni les échantillons. Merci, à Tra Nguyen Thanh dont le travail est indissociable de ma thèse et à Thomas Quinci d'avoir surveillé mon taux de sucre. Merci à l'équipe du midi, toujours à l'heure pour aller manger : Tonton, Marianne, Rozenn, Julie, Karine, Olivier, Jérôme, Thomas, Mickael, Julien pour ne citer que les plus fidèles. Enfin, bon courage à tous les doctorants même ceux qui se sont jeté comme des vautours sur mon bureau et mon ordinateur à peine après avoir quitté l'INSA.

Enfin merci à ma famille d'être venu assister à ma soutenance.

Abbreviation Glossary

APB	Anti-Phase Boundary
BAC	Band Anti-Crossing
CBM	Conduction Band Minimum
DFT	Density Functional Theory
DOS	Density Of States
EPM	Empirical Pseudo-potential Method
FWHM	Full Width at Half Maximum
GSMBE	Gas Source Molecular Beam Epitaxy
HE	High Energy
HH	Heavy Hole
HRXRD	High Resolution X-Ray Diffraction
IC	Integrated Circuit
LCE	Linear Continuum Elasticity
LCINS	Linear Combination of Isolated Nitrogen States
LE	Low Energy
LED	Light Emitting Diode
LH	Light Hole
MBE	Molecular Beam Epitaxy
ML	MonoLayer
MOSFET	Metal Oxyde Semiconductor Field Effect Transistor
MOCVD	MetalOrganic Chemical Vapour Deposition
OEIC	Opto-Electronic Integrated Circuit
PIC	Photonic Integrated Circuit
PL	PhotoLuminescence
PLE	PhotoLuminescence Excitation
QD	Quantum Dots
QW	Quantum Wells
RSM	Reciprocal Space Mapping
RTA	Rapid Thermal Annealing
SE	Spectroscopic Ellipsometry
SK	Stranski-Krastanov
SOI	Silicon On Insulator
SSMBE	Solid Source Molecular Beam Epitaxy
STM	Scanning Tunneling Microscopy
TB	Tight-Binding
TE	Transverse Electric
TEM	Transmission Electronc Microscopy
TM	Transverse Magnetic
TRPL	Time Resolved PhotoLuminescence

UHV-CVD	Ultra High Vacuum Chemical Vapour Deposition
VBM	Valence Band Maximum
VBO	Valence Band Offset
VFF	Valence Force Field
VLSI	Very Large Scale Integration
WDM	Wavelength Division Multiplexing
WL	Wetting Layer
XPS	X-ray Photoelectron Spectrometry
X-STM	Cross sectional Scanning Tunneling Microscopy

Introduction

The explosion of computing and communicating information technologies has been probably one of the most important vectors of development of our societies for the past 60 years. Everyone may admit that both risings of computing and communication are, at least from the application view, intimately linked: exchanging more and more data may have appeared unnecessary if one has been unable to handle such a massive number of data. Between 1986 and 2007, the world general-purpose computing capacity (including personal computers, servers, supercomputers, videogame consoles and mobile phones) has been increasing at an annual rate of 58% enabling humankind to carry out a total number of 6.4×10^{18} instructions per second[1]. In the same time, the world's technological capacity to telecommunicate information has been increasing at a rate of 28% per year to reach almost 2×10^{21} bytes in 2007[1]. This increase has even been accelerating for the past few years, mainly because of the explosion of the IP data traffic which is forecast to pass the zettabyte (10^{21} bytes) threshold by the end of 2016[2]. These spectacular evolutions are the consequences of some scientific breakthroughs.

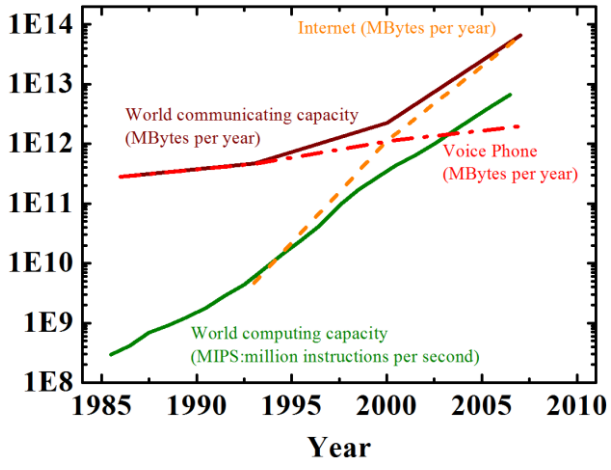

World's technological installed capacity to compute information on general-purpose computer and world's technological effective capacity to telecommunicate information. From Ref. 1.

The major date for computing is December 23, 1947 when J. Bardeen, W. H. Brattain and W. Shockley demonstrated their first transistor at AT&T's Bell Labs[3]. Hitherto, electronic computing was based on high power consuming and cumbersome vacuum tubes. The transistor became the fundamental building block of electronic logical gates. In 1958, the first transistor-based integrated circuit (IC) was demonstrated by J. Kilby. The invention of the IC revealed the potential for extending the cost and operating benefits of transistors to every mass-produced electronics circuit, including the microprocessors that control computer operations. Thereafter, the computer processors complexity has been growing up thanks to the increasing integration of the number of transistors in an IC. Since 1965, the integrated electronics industry has been governed by the so-called Moore's law which originally predicted that the number of transistors on ICs at minimum cost would double each year[4] (Moore actually corrected his law in 1975 and predicted a doubling density every eighteen months[5]). Following the scaling of the density of transistors, the clock rate of processors has been increasing following a similar law. Nevertheless, this evolution hit a first wall in 2005, when the clock speeds stopped increasing, although the miniaturization of transistors kept on increasing. The reason for this break is power dissipation through thermal heating of interconnects.

Indeed, the metallic interconnects linking transistors also follow the scaling of the density of transistors. The power dissipation in an interconnection is mainly given by:

$$P \approx C_l V_r^2 f$$

where C_l is the capacitance of the interconnection (which is proportional to the length of the interconnection and to the linear capacitance ~2 pF/cm), V_r is the signal voltage and f the clock rate. Increasing the total length of interconnects is unavoidable if one wants to keep on growing the density of transistors. Decreasing V_r is no more possible because of signal integrity. Thus, to keep the dissipated power density to reasonable values, processors manufacturers decided to overcome the clock rate increasing, by multiplying the number of cores running in parallel. Nevertheless, this solution only postpones the issue of metallic interconnects to a higher scale. Communication between cores or between processors has also to satisfy the growing demand on bandwidth. Unfortunately, the bit rate in an electrical wire is limited to:

$$B \propto \frac{A}{L^2}$$

where A and L are respectively the cross-sectional area and the length of the wire. This means that scaling the size of electrical interconnects does not increase the bandwidth limit[6].

To deal with this double issue of limited bandwidth/power consumption, the idea of replacing electrical interconnects by optical interconnects was first proposed by Goodman *et al.*[7], in order to reach a very large scale integration (VLSI). Indeed, optics avoids the resistive loss physics of wires that leads to the bandwidth density problems. Moreover, unlike electronics, optics does not have to charge the interconnect line to the logic voltage. Thus the energy dissipation in interconnects can be significantly reduced. Among other advantages provided by optical signals instead of electrical signals, we can mention signal integrity, absence of crosstalk between adjacent wires, increase of data transfer capacity by wavelength division multiplexing (WDM) or low-loss waveguides. Optics can be already found at the heart of today's long distance communications with optical fibers. The challenge now consists in adapting optical communications to shorter distance communications: between cards, between chips and even on chips.

For that purpose, we need to integrate optical functions in so-called photonic integrated circuits (PIC) or opto-electronic integrated circuits (OEIC). Moreover, this integration has to fulfill the requirements for low-cost and massive production, driven for years by the electronic integrated circuits industry based on silicon CMOS technology. Thus, photonics components have to be developed on silicon. During the last decade, many research teams in the world have spent a lot of efforts to develop photonics components on silicon and are now on the verge of supplying photodetectors[8], modulators[9], multiplexers[10] using low enough energy per bit (at least for inter-chip interconnects applications). Nevertheless, the basic light source, the silicon laser, still remains one of the main challenges.

In this dissertation, a study on the development of a laser on silicon is presented. The study is focused on the pseudomorphic approach, which consists of growing a lattice-matched III-V heterostructure on silicon to realize the laser structure.

In chapter 1, the reasons why silicon has been the material of microelectronics are briefly discussed. Then, we show why silicon seems to be unsuitable for photonics, especially for light emission. A state-of-the-art on silicon laser is given, highlighting the benefits and

limitations of the various approaches. Finally, the pseudomorphic approach is presented in details. The main issues that this approach raises, and that this thesis aims to address, are described.

In chapter 2, we present the theoretical challenges of the pseudomorphic approach. We show that the simulation of electronic and optical properties of semiconductors structures grown on Si requires dealing with indirect band gap semiconductors, accurately including strain effects and modeling the unusual properties of dilute nitride alloys. The tight-binding model is presented as a possible solution.

In chapter 3, the dilute nitride GaPN bulk alloy and GaAsPN quantum wells are studied experimentally and theoretically. The nature of the optical transitions (indirect, direct or emerging from localized centers) is discussed in the framework of temperature dependent photoluminescence measurements, time-resolved photoluminescence and tight-binding simulations. The choice of cladding layers based on AlGaP alloy is justified by spectroscopic ellipsometry measurements of the refractive index.

In chapter 4, we study the potential of InGaAs/GaP quantum dots as an alternative to GaAsPN quantum wells for the laser active zone. Temperature, pressure dependent photoluminescence as well as time-resolved photoluminescence measurements are presented and results are confronted to theoretical calculations based on **k**·**p** and tight-binding simulations. Finally, a brief study on dilute nitride InGaAsN/GaP quantum dots is presented.

References

[1] M. Hilbert and P. López, Science **332**, 60 (2011).
[2]Cisco (n.d.).
[3] J. Bardeen and W.H. Brattain, Phys. Rev. **74**, 230 (1948).
[4] G. Moore, Electronics **38**, 114 (1965).
[5] R.R. Schaller, Ieee Spectr. **34**, 52 (1997).
[6] D. Miller, Proc. Ieee **97**, 1166 (2009).
[7] J.W. Goodman, F.J. Leonberger, S.-Y. Kung, and R.A. Athale, Proc. Ieee **72**, 850 (1984).
[8] L. Vivien, J. Osmond, J.-M. Fédéli, D. Marris-Morini, P. Crozat, J.-F. Damlencourt, E. Cassan, Y. Lecunff, and S. Laval, Opt. Express **17**, 6252 (2009).
[9] G.T. Reed, G. Mashanovich, F.Y. Gardes, and D.J. Thomson, Nat. Photon. **4**, 518 (2010).
[10] W. Bogaerts, S.K. Selvaraja, P. Dumon, J. Brouckaert, K. De Vos, D. Van Thourhout, and R. Baets, Sel. Top. Quantum Electron. Ieee J. **16**, 33 (2010).

Chapter 1

Introduction to laser on Si

In this chapter, we first present a state-of-the-art of lasers on silicon highlighting the results and the limitations of the various approaches. Finally, we present the pseudomorphic approach: its advantages and the challenges which motivate this thesis.

1.1 Silicon for electronics and silicon for photonics

1.1.1 Silicon for electronics

In their original paper, J. Bardeen and W. H. Brattain demonstrated for the first time a transistor effect using a germanium crystal[1]. The reference to silicon was only present in a small note at the end of the paper: *"While the effect has been found with both silicon and germanium, we describe only the use of the latter."* At this time, they were probably not aware that this note was almost as important as the entire paper. Indeed, the spectacular rising of microelectronics industry is due, for a significant part, to the choice of silicon as the semiconductor material. Yet, silicon is not intrinsically the best semiconductor material for achieving high performance transistors (for instance the electron mobility is lower in silicon as compared to germanium by a factor of 2.7). But silicon has several great advantages: a high thermal conductivity, the ability to easily control the oxide formation and the doping levels, and the ability to synthetize very pure crystals at low cost. These characteristics have enabled silicon foundries to develop mature and mass-productive technologies. For years, microelectronic industry investments have consisted in scaling the CMOS (Complementary Metal Oxyde Semiconductor) technology. It is commonly agreed, as stressed by the International Technology Roadmap for Semiconductors, that implementation of breakthroughs (including silicon photonics) in the short-term and mid-term future will have to be CMOS-compatible and that development of processes that utilize existing infrastructure is of paramount importance[2].

1.1.2 Silicon for photonics

A basic photonic circuit is composed of individual blocks: a light emitter (preferably a laser), photodetectors, modulators, multiplexers, demultiplexers and waveguides.

Guiding the light with Si is not the hardest task. Indeed, light can be efficiently confined in Si waveguides using the high refractive index contrast between Si and SiO_2 (Δn=2). Thus, waveguides can be designed on silicon-on-insulator (SOI) substrates[3]. Nevertheless, the wavelengths have to be at least in the transparency window of Si (above 1.1 µm) and ideally in the frequently used telecommunication windows of SiO_2 (1.3 µm or 1.55µm). Many Si-photonics integration schemes are based on these guides (Intel, CEA). Nevertheless, shorter wavelengths (visible and NIR) can also be guided by using Si_3N_4/SiO_2 waveguides[4].

On the other hand, Si is not the ideal candidate for modulators and near infrared photodetectors. Indeed, Si is centrosymmetric, thus modulators based on electro-refractive Pockels effect are impossible. Kerr effect is also very weak. Moreover, Si is transparent for wavelengths above 1.1 µm. Thus, modulators based on electro-absorption and photodetectors in this range of wavelengths are scarce. Silicon-based carrier depletion modulators have been developed[5,6], but they suffer from high energy consumption. One solution to get electro-absorption modulators and photodetectors on Si substrate consists in growing Ge/SiGe quantum wells (QW)[7–10]. This solution benefits from the abrupt absorption threshold of Ge QW and from the ability to adjust the wavelength in the telecommunication window.

Light emission on silicon remains one of the biggest challenges. Indeed, Si being an indirect bandgap material, free electrons tend to relax in the X valleys of the conduction band whereas the free holes are located in the Γ valence band (see Fig. 1-1).

Thus, a radiative recombination between an electron and a hole can only occur if a third particule (a phonon) is involved in the mechanism to satisfy the momentum conservation. The poor light emission efficiency of Si is directly related to the low probability of such a three-particle event. At the same time, non-radiative processes are more likely to occur. Free-carrier absorption, wherein free electrons are promoted to higher conduction band levels by absorbing photons, is the main mechanism preventing lasing from bulk Si[12]. Another common non-radiative process is Auger recombination, wherein the energy released by the recombination of an electron

with a hole is gained by another electron (or a hole) which is promoted to a higher energy level. The internal quantum efficiency, which is defined by the ratio between the probability of a radiative recombination and the probability of any recombination, is thus very weak in bulk silicon (10^{-6}). We will now describe various approaches studied by many research teams in the world to achieve lasing on silicon.

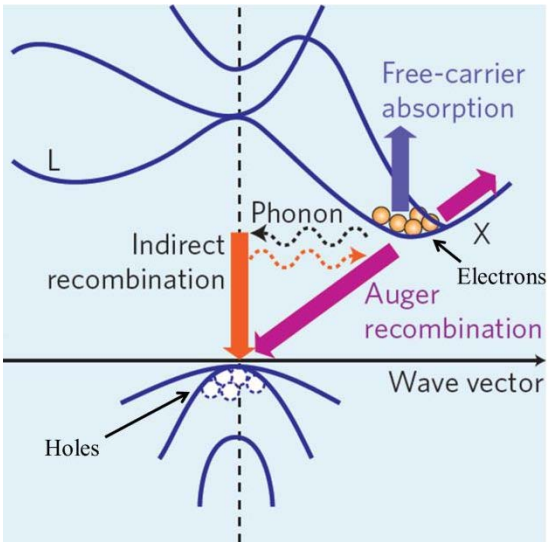

Fig. 1-1: Energy band structure of bulk Si and main carrier transition processes. From Ref. 11.

1.2 Laser emitters on silicon

1.2.1 Silicon-based sources

Using ultra-purity and optimized light extraction, Green *et al.* have demonstrated a light emitting diode based on bulk Si[13], but lasing in bulk Si has not been shown yet. To enhance the radiative recombination, many research teams have been studying Si nanostructures[14,15]. Indeed, if carriers are localized in a small region of real space, their wave functions are delocalized in the reciprocal space. Thus, the k-space selection rule responsible for the low efficiency in bulk Si, is partially broken. Optical gain in Si nanocrystals embedded in a SiO_2 matrix has been proved[16,17]. The emitted light is red but the 1.55 μm telecommunications window can be reached by the incorporation of Er ions[15,18]. The main issue of this approach is the electrical injection through the SiO_2 insulator. Although the electrical injection can be enhanced by tailoring the energy band structure of graded-size Si nanocrystals[19], only light emitting diodes have been demonstrated.

Another approach to achieve lasing emission in silicon aims at exploiting the stimulating Raman scattering effect[20]. Room temperature continuous-wave pumping has even been achieved by combining a ring cavity and a p-i-n structure to limit losses due to free carrier and two-photon absorption[21]. Unfortunately, this technique needs a pumping laser which prevents any industrial application.

1.2.2 Hybrid III-V/silicon lasers

If Si has been the material of microelectronics for sixty years, III-V compounds have undoubtedly been the materials of photonics. Indeed, since the first demonstrations of semiconductor laser diode in 1962 (by Hall *et al.* for infrared wavelength[22] and Holonyak *et al.* for the visible range[23]), III-V direct band gap GaAs, InP, GaSb or GaN related compounds are used in most of semiconductor laser diodes.

The heterogeneous integration of III-V materials on a silicon wafer is one of the most advanced approaches to provide an efficient laser for integrated silicon photonics. III-V heterostructures are first grown on their native substrates before being processed into individual dies which are afterwards individually bonded onto the Si platform (see Fig. 1-2).

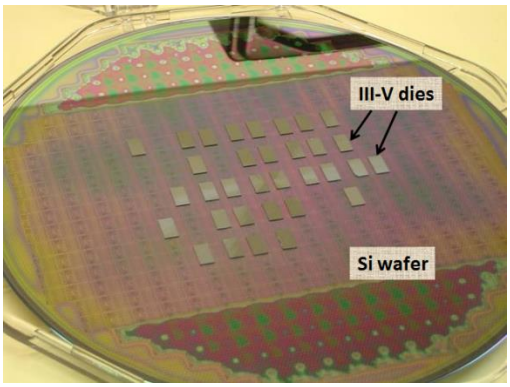

Fig. 1-2: III-V dies bonded on a Si wafer. (CEA)

Bonding a complete III-V laser structure on Si substrate was first demonstrated by Wada *et al.*[24]. Nevertheless, a special coupling scheme involving submicron precision alignment would be required to integrate it with a PIC imbedded in a layer of Si. To deal with this issue, the group of J. Bowers in Santa Barbara has developed a technique which combines the bonding of thin III-V films with an evanescent coupling to an SOI waveguide[25]. Several research teams have

been working on this approach to improve bonding techniques[26], to adjust the coupled optical mode between the III-V active zone and the Si waveguide[27] and to increase the compacity[28].

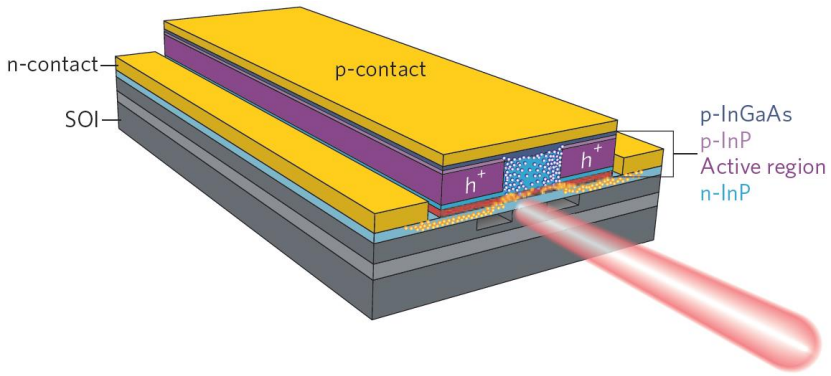

Fig. 1-3: Evanescent coupling between a III-V active zone and a SOI waveguide. From Ref. 11.

This approach is considered by Intel as a very potent short-term solution to address the medium volume applications of high-bandwidth data transmissions in servers and data centers[29]. However, the reliability, the performance, the uniformity and the costs of this approach, especially for high volume VLSI on-chip interconnects applications, are still unknown[11,30].

1.2.3 Monolithic epitaxial lasers

On a longer term, monolithic integration of laser sources on silicon is expected to match more surely with the very large scale integration requirements. The monolithic approach consists in growing a light-emissive crystalline semiconductor structure onto the Si substrate. The main challenge of this approach is to reach a high quality crystalline structure, compatible with reliable laser devices (with a very low dislocation density). This is mainly prevented by the lattice constant mismatch between the semiconductors of the grown layers and the Si substrate. Indeed, the epitaxial growth of a semiconductor onto another, with different lattice constants, results in strain/stress energy accumulation in the layer. In this situation, if the lattice mismatch or the thickness is too large, misfit dislocations appear during the growth to minimize the energy[31,32]. These defects act as non-radiative recombination centers in the device. They actually add electrical resistance during the current flow through it, or limit the quantum efficiency of optical devices by decreasing the number of electron-hole pairs recombined in photons. Fig. 1-4 represents the energy of the band gap as a function of the lattice constant for the usual group IV and group III-V semiconductor compounds. It shows that most of the semiconductors classically

used for the photonics applications (GaAs, InP and their related compounds) cannot be lattice matched to Si. For a monolithic laser on Si, the main challenge is thus the improvement of the crystalline quality through the limitation of threading misfit dislocations in the grown structure (based on group IV or group III-V semiconductors) on Si.

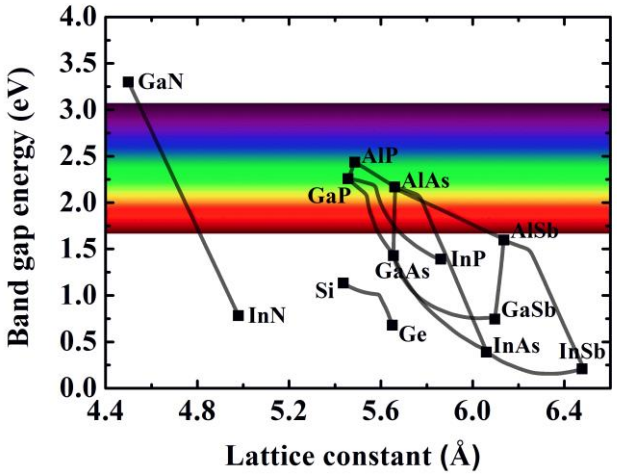

Fig. 1-4: Bandgap energy of semiconductors as a function of their lattice constant.

1.2.3.1 Monolithic integration of group IV semiconductors

Using group IV semiconductors for integrated photonics on silicon is expected to have several technological advantages as compared with the monolithic integration of group III-V semiconductors. Indeed, growths of III-V and group IV semiconductors require two distinct chambers because of the cross-contamination and face the difficulty to deal with the intrinsic difference between crystallographic structures. Moreover, the monolithic integration of modulators and photodetectors on Si has already been demonstrated using Ge based structures[7-10]. For laser sources, the use of Ge is more difficult because of its indirect band gap. Nevertheless, as shown in Fig. 1-5, the difference between the L and the Γ conduction bands can be reduced by engineering the strain in Ge. A very high-doping level is then used to provide a significant concentration of free electrons in the Γ conduction band[33]. Recently, the group of L. Kimerling in MIT has demonstrated a room temperature, pulsed electrically pumped laser based on bulk Ge on Si[34]. The 0.2% tensile strain has been achieved thanks to the difference in thermal expansion coefficients between Ge and Si. Nevertheless, the threshold current density remains extremely high: 280 kA.cm^{-2}.

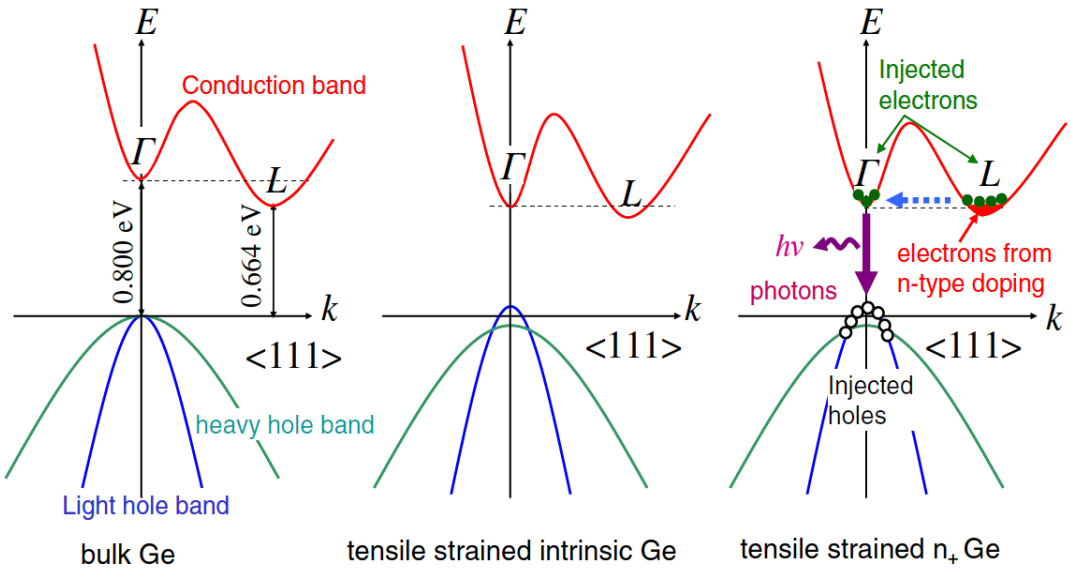

Fig. 1-5: Engineering of the band structure of Ge. From Ref. 33.

Another solution to engineer the band structure and get a direct band gap is the incorporation of Sn to SiGe alloys[35]. But the issue of the lattice mismatching with Si still remains. To try to limit the effects of the crystalline defects on the electrical and optical properties, the lattice constant can be progressively changed by growing composition graded SiGe(Sn) buffer layer[36]. But this generally requires very thick layers (which are incompatible with an evanescent coupling with a waveguide embedded in the silicon chip) and dislocations are not completely removed (which is incompatible with an electrical injection through the buffer layer).

1.2.3.2 Monolithic integration of III-V semiconductors on Si: the metamorphic approach

The idea of monolithically integrating III-V materials on silicon is of course not new and first investigations already started in the 80's with attempts in growing well-known GaAs or InP based structures. However, the direct growth of these materials is very difficult due to the polar/non-polar character of the III–V/Si interface, the mismatch of their respective lattice constants (4 % for GaAs/Si and 8 % for InP/Si) and thermal expansion coefficients ($2.6.10^{-6}$ K^{-1} for Si, $5.7.10^{-6}$ K^{-1} for GaAs, $4.6.10^{-6}$ K^{-1} for InP). Fig. 1-6 shows typical resulting dislocations in a GaAs layer grown on Si. Although laser structures based on GaAs/AlGaAs QW or InGaAsP/InP QW have already been grown on Si, the very high density of dislocations ($> 10^{7}$ cm^{-2}) results in a rapid deterioration of the devices[37–41].

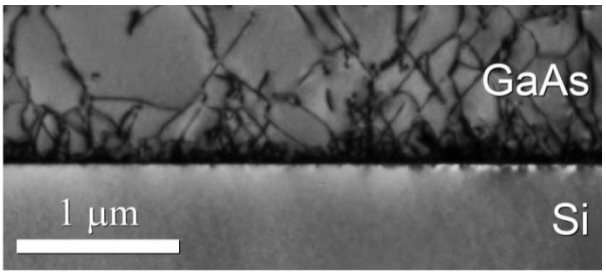

Fig. 1-6: Cross-sectional transmission electron microscope (TEM) image highlighting the dislocations in a GaAs layer grown on a Si substrate. From Ref. 42.

If crystalline defects cannot be totally prevented when growing lattice-mismatched layers, many research teams have developed strategies to try to confine the dislocations far away from the active zone. The use of strained short-period superlattices has been demonstrated to act as a filter for dislocations[42,43] (see Fig. 1-7(a)). On the same idea, the group of P. Bhattacharya has developed a dislocations filter buffer layer based on InAs/GaAs QD (see Fig. 1-7(b)). Using this technique, encouraging results have been demonstrated with lasing structures exhibiting a threshold current of 900 A.cm^{-2} under pulsed electrical pumping at room temperature[44].

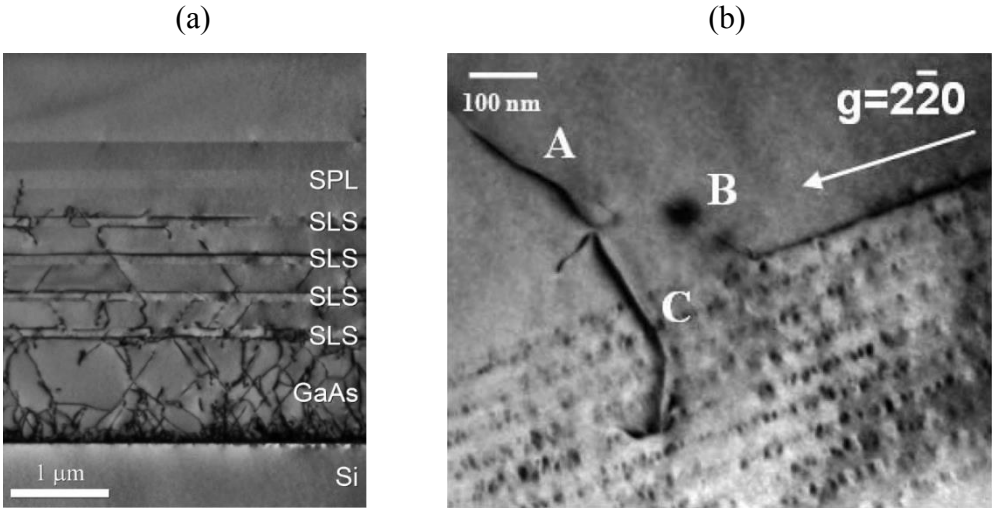

Fig. 1-7: Cross-sectional TEM image of: (a) a threading dislocations filter based on strained-layer superlattices (SLS) and short-period superlattices (From Ref. 42) and (b) a blocked dislocation by a QD buffer layer (From Ref. 44).

Another way to deal with the lattice-mismatch issue is the growth of the III-V structure on an oxide/Si layer such as SrTiO3/Si template. In principle, this technique should enable the III-V layer to immediately adopt its bulk lattice constant and thus prevent any threading dislocations, but only room temperature photoluminescence has been reported up to now[45].

Another interesting approach to confine dislocations is the use of antimonide-based materials. As shown in Fig. 1-4, the lattice-mismatch between Si and III-Sb compounds is very large (12 % for GaSb/Si). But contrary to most of other III-V material systems, this very large lattice-mismatch is an advantage in the case of III-Sb material, since it is believed to be the main driving force for the formation of two-dimensional arrays of efficient strain-relieving misfit dislocations. Fig. 1-8 shows the relaxation of an AlSb layer by the formation of dislocations confined at the AlSb/Si hetero-interface[46]. Using this AlSb nucleation layer and a GaSb fully relaxed buffer layer, a laser diode operating at room temperature and under continuous-wave electrical pumping has been demonstrated[47]. The wavelength is 2 µm and the threshold current density is high (1.4 kA.cm^{-2}). A structure emitting at 1.55 µm has also been achieved, but the threshold current density is higher (5 kA.cm^{-2}) and only pulsed regime has been demonstrated[48].

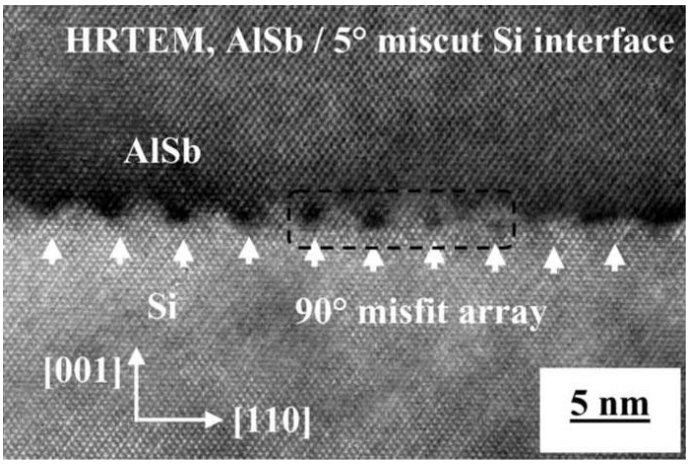

Fig. 1-8: Cross-sectional TEM image of a two-dimensional dislocation network confined at the AlSb/Si interface. From Ref. 46.

The lowest room-temperature threshold current density for a metamorphic laser on Si has been achieved by the group of A. Seeds and H. Liu in the University College of London. Their idea is to benefit from both low threshold InAs/GaAs QD laser structure and significant improvements in crystalline quality of Ge on Si. Indeed, as shown in Fig. 1-4, the lattice-mismatch between GaAs and Ge is small (0.08 %). Moreover, their thermal expansion coefficients are also very close (5.7.10^{-6} K^{-1} for GaAs and 5.9.10^{-6} K^{-1} for Ge). They have first demonstrated an InAs/GaAs QD laser on Ge substrate operating at room temperature with a low threshold current density of 55.2 A.cm^{-2} under continuous-wave electrical pumping[49], followed

by a similar structure on Ge-on-Si substrate with threshold current densities of 163 A.cm^{-2} (continuous-wave operation) and 64.3 A.cm^{-2} (pulsed operation)[50].

Nevertheless, the issue of all these approaches is that they resort to complex procedures and/or thick buffer layers which strongly limit the design flexibility for further device integration. A thick buffer layer prevents a simple coupling scheme with a photonic circuit embedded in the bottom Si chip. Moreover, driving the current through the dislocation layer is known to dramatically deteriorate the electrical performances[47].

Another solution to manage the strain relaxation without using buffer layers is to decrease the interaction between the grown layer and the substrate. This can be done by using patterned substrates[51] or by growing self-assembled one-dimensional nanostructures such as nanowires, nanoneedles or nanopillars[52–54]. This approach enables the growth of lattice mismatched materials without the formation of dislocations because of the large surface-to-volume ratio in the one-dimensional nanostructure, where the strain can be efficiently and elastically relaxed[55]. Interesting results have been recently achieved by the group of C. Chang-Hasnain in Berkeley[56]. They have demonstrated room temperature lasing of an InGaAs/GaAs core-shell nanopillar with helically propagating cavity modes (see Fig. 1-9).

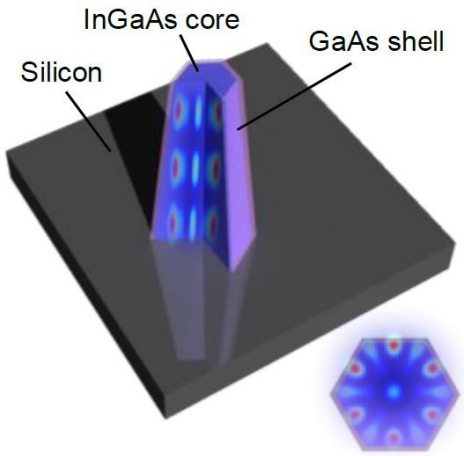

Fig. 1-9: III-V nanopillar grown on Si with an helically optical mode. From Ref. 58.

Due to the very small laser volume (6.10^{-13} cm^{-3}), this approach is exciting for ultimate integration of light source. Nevertheless, it faces various challenges. Electrically pumped lasers are missing even if light-emitting diodes with complex metallic contacts technology have been

shown[57]. Moreover, (111) oriented Si substrate are often used to favor the vertical growth of the III-V structure. The control of the growth direction on more conventional (001) Si substrate is still challenging.

1.3 The pseudomorphic approach

The issue of the lattice-mismatch between III-V semiconductors and Si is often given as the main reason which has prevented the development of III-V laser on Si. To avoid the plastic relaxation which is the cause of device performances degradation, the layers can be grown coherently (pseudomorphically). This means that the in-plane lattice constant of the layers have to remain equal to the substrate lattice constant.

Fig. 1-10 is a zoom picture of Fig. 1-4 showing that GaP and AlP are the binary III-V semiconductors that have the smallest lattice-mismatch to Si (only 0.37 % for GaP/Si and 0.69 % for AlP/Si). Nevertheless, with a non-zero lattice-mismatch, a layer starts to relax plastically above the so-called critical thickness. Obviously, the smaller is the lattice-mismatch, the larger is the critical thickness. For GaP/Si, this value has been estimated to be in the range between 40 nm and 100 nm[59–61]. A laser structure (including active zone and cladding layers) usually requires a larger thickness (between 2 and 3 µm). Thus, compounds with even smaller lattice-mismatch to Si are needed.

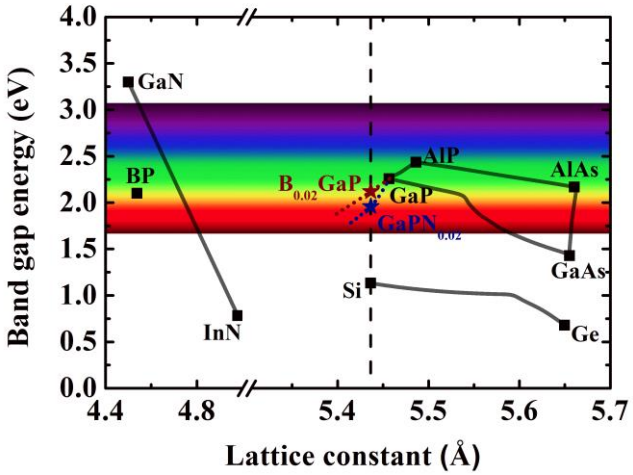

Fig. 1-10: Bandgap energy of semiconductors as a function of their lattice constant. The blue (red) dotted line represents the dilute nitride (boron) GaPN (BGaP) alloy and highligths the perfect lattice-matching of $GaPN_{0.02}$ ($B_{0.02}GaP$) with Si.

A perfect lattice-matching can be achieved with the incorporation of a small amount of nitrogen (2.2 % in GaP and 3.8 % in AlP at room temperature). Note that the lattice parameters of GaP, AlP and Si don't have the same variation with temperature. This difference in thermal expansion coefficient should be compensated during the growth. Another solution is the use of boron. This second route is not studied in this thesis. Few reasons will be given in the following. The pseudomorphic approach which is studied in this thesis thus consists in developing laser structures with lattice-matched layers based on GaP(N) and AlP(N) related compounds. We will now briefly detail the various challenges of this approach.

1.3.1 Growth challenges

Even if the pseudomorphic approach is theoretically expected to result in a "defect free" structure, it still faces two main challenges: the III-V/Si interface and the growth of dilute nitride based laser device. These points are considered in the thesis work of Tra Nguyen Thanh, which has been jointly performed with the present work. Now we just briefly mention a few points related to this approach.

1.3.1.1 III-V/Si interface

Due to the amorphous character of SiN, a perfectly lattice-matched $GaPN_{0.02}$ crystal cannot be directly grown on Si substrate. The commonly widespread strategy is thus to grow a thin (below the critical thickness) GaP buffer layer on Si followed by a lattice-matched laser structure based on dilute nitride alloys[62,63].

Worldwide intense researches have been devoted to improve the crystalline quality of the GaP/Si interface and several research groups are on the verge to obtain defect-free GaP-on-Si pseudo-substrate[64–70]. This is actually not straightforward because a defect-free growth means the control and reduction of classical defects such as 3D growth, stacking faults or microtwins, but also of heterogeneous growth specific defects such as anti-phase boundaries (APB) and interfacial charge effects. The suppression (or at least annihilation) of these defects can be achieved by an advanced optimization of the growth conditions[64,66,67]. The preparation of the Si surface, in order to have a clean, flat and bi-atomic height stepped surface instead of mono-atomic steps, is one of the critical points, because it can totally prevent the APB formation. The use of Si(100) substrates which are slightly misoriented by a few degrees toward the [110]

direction is a route that has been followed by many research groups to favor Si bi-atomic height steps, even if this goal can be reached using conventional Si (001) substrates and carefully selecting the substrate residual misorientation[66,67,70,71].

The Foton laboratory strategy is to independently deal with the issues of GaP/Si interface and development of the III-V laser structure on GaP. This thesis is exclusively devoted to the development of the III-V laser structure, and that is the reason why many results are presented on GaP substrates in order to avoid the defects inherent to the GaP/Si interface.

1.3.1.2 Dilute nitride growth

The growth of dilute nitride alloys is very different from the growth of other III-V alloys. Two main reasons can be highlighted:

- The crystal structure for the endpoints binary semiconductors (zinc-blende for phosphides and arsenides and wurzite for nitrides) is different. This results in a very large miscibility gap, which means that the alloys are difficult to obtain without phase separation.
- The equilibrium solid solubility of nitrogen is extremely low in phosphides as well as arsenides ([N] < 10^{16} cm^{-3} in bulk GaP and [N] < 10^{14} cm^{-3} in bulk GaAs at T = 900 K)[72].

In this context, efficient incorporation of nitrogen requires far from equilibrium growth conditions which are the case when using molecular beam epitaxy (MBE) or metal-organic chemical vapor deposition (MOCVD). From the sixties to the nineties, the incorporation of nitrogen in GaP or GaAs was limited to doping regimes ([N] < 10^{19} cm^{-3}). The incorporation of a few percents of nitrogen in GaAs by MOCVD was achieved by the NTT labs in Japan in 1992[73]. In the same time, the incorporation of a few percents of nitrogen in GaP by MBE was demonstrated by Baillargeon *et al.*[74]. Since, the N incorporation techniques have been improved, especially with the use of novel N precursors for MOCVD (Dimethylhydrazine)[75] or specially designed plasma N_2 source for MBE[76,77].

Although many research groups have studied the growth of many dilute nitride alloys (GaAsN, GaPN, GaInAsN, GaAsPN, GaInAsSbN …) for the past fifteen years, achieving homogeneous and defect-free crystalline layers is still challenging. In dilute nitride alloys, the role of defects on the electronic and optical properties is enhanced, as compared to other semiconductors, due to the intrinsically large difference in size and chemical mismatch between

the N atom and the other V elements such as P or As. These defects give rise to deep levels in the band gap of alloys, which can act as limiting factor of optical properties. This issue has been intensively studied both from the theoretical[78,79] and experimental[80–82] points of view. Among the various N induced defects, N interstitials, Ga vacancies, Ga interstitials, As antisites have been experimentally identified in Ga(In)AsN, GaPN or GaAsPN alloys. The defects density can be reduced by optimizing the growth conditions or performing post-growth annealing[81,83,84]. But a general feature remains: the defects density tends to increase with the increasing of the N content. This is a result of both higher probability of generating such point defects and higher tendency in generating dislocations due to strain. Although N incorporation as high as 16 % has been reported in GaPN[85], reasonable concentrations for the optical devices we are developing in this thesis are limited to a few percents (< 6 %)[86,87].

1.3.2 Electronic structure challenges

We have seen at the beginning of this chapter that Si is not suitable for efficient laser emission because of its indirect band gap. Unfortunately, GaP and AlP also exhibit indirect band gaps. One of the main challenges of this thesis is thus to propose an efficient active zone.

The nitrogen incorporation, in dilute regimes, is known to strongly modify the electronic band structure and consequently the optical properties of arsenide, phosphide or antimonide alloys. A general feature that has been demonstrated in all dilute nitride alloys is the strong reduction of the band gap with increasing N content, the so-called giant band gap bowing[88–93].

The use of a dilute nitride alloy (GaInAsN) as a gain medium was first proposed by Kondow *et al.*[94]. Indeed, this alloy can be lattice-matched to GaAs substrate and has enabled to reach lasing emission at the wavelength of 1.3 μm on GaAs. For the pseudomorphic integration on Si, an alloy with a smaller lattice constant is required. We have seen that GaPN can adress the issue of lattice-mismatch. It has also been claimed that the incorporation of nitrogen in the $GaP_{1-x}N_x$ alloy would allow to reach a direct band gap for $x > 0.5$ %[95]. Unfortunately, the nature of the band gap of GaPN is more complicated than a simple indirect-direct crossover and has been the subject of many controversies in the past decade. The issue is even more crucial for the GaAsPN alloy, for which much less studies exist. Yet, the only pseudomorphic laser structures demonstrated on Si are based on GaAsPN QW[96]. The aim of Chapter 3 is to provide both

theoretical and experimental understandings of this alloy in order to give some routes for the improvements of laser characteristics.

Another challenge is to investigate other nanostructures for the active zone, which may be an alternative to poorly efficient GaAsPN QW existing laser structures. Moreover, the maximum of the emission wavelength reported for such structures with reasonable N content is equal to 980 nm[97], which is not yet in the transparency window of Si (above 1.1 μm). The use of quantum dots is proposed because it allows the coherent growth of smaller band gaps materials nanostructures with larger lattice mismatch. Furthermore, due to their 0D confinement properties, lower threshold currents have been demonstrated, in comparison to their QW counterparts[98]. The InGaAsN/GaP QD system has been proposed by Fukami *et al.* as a good candidate[99]. Nevertheless, very few studies have been performed on both InGaAsN/GaP QD and nitrogen-free InGaAs/GaP QD system.

Finally, another critical point for laser devices is the choice of cladding layers, whose role is to increase the overlap between the electromagnetic field and the gain region. In laser devices on GaAs substrate, AlGaAs cladding layers have been extensively used, because the incorporation of Al is known to strongly reduce the refractive index and AlAs and GaAs are quasi lattice-matched. By analogy, AlGaP based alloys are considered in this work. But the striking difference with the AlAs/GaAs system is the type-II band alignment for AlP/GaP[100]. This feature has to be carefully considered because it can reduce the confinement of carriers in the active zone.

1.3.3 Context of the pseudomorphic approach and positioning of Foton laboratory

Even if several research teams are working on the pseudomorphic approach, two of them can be highlighted, as they have succeeded in demonstrating operating devices on silicon.

The first one is installed in Philipps University Marburg, Germany, with a commercial showcase through the NAsP III/V GmbH Company. The first breakthrough demonstrated by this team was the achievement of room temperature lasing under electrical injection of GaAsPN quantum wells on GaP substrate in 2006[101]. Although the laser characteristics which are shown are limited (pulsed operation and a high threshold current density of 4 $kA.cm^{-2}$)[97]; this is, to our knowledge, the only demonstration of lasing on GaP substrate. After having optimized the

GaP/Si interface[64], they recently gave a demonstration of GaAsPN QWs lasing on Si substrate up to 150 K both optically and electrically[96], and measured optical gain up to 300 K[102]. Nitrogen is only incorporated in the quantum wells. The lattice-matching of barriers and cladding layers to Si, is ensured by the incorporation of boron in respectively BGaAsP and BGaP alloys. This growth strategy is conditioned by the use of MOCVD as the growth technique. Indeed, the compositional control and uniformity of dilute nitride layers is known to be harder to achieve with MOCVD as compared to MBE growth techniques; the most efficient dilute nitride based devices (GaInNAs/GaAs lasers[103] and tandem solar cells[104]) were presently demonstrated with MBE. On the contrary, the incorporation of boron is more efficient with MOCVD thanks to the use of triethyl boron precursor[105]. In the case of MBE, it is still challenging because of the very low vapor pressure of solid B which requires very high cells temperature[106].

The second team is based in Toyohashi University of Technology, Japan. They first demonstrated significant reduction of GaP-Si induced defects density in pseudomorphic layers in 1998[107] by using an alternated growth procedure. This procedure is still being optimised[66,108]. They achieved the MBE growth of GaPN lattice-matched to Si[109]. They demonstrated room temperature LED devices on Si based on InGaPN/GaPN double heterostructure[110] and GaAsN/GaPN QW[111], They finally demonstrated the ability to drive a GaPN LED by a p-type metal oxide semiconductor field effect transistor (MOSFET) on Si[112], which was the first demonstration of real on-chip photonic integration, in the pseudomorphic integration.

In this context, the FOTON laboratory started studying the growth of III-V heterostructures on GaP substrates by MBE in 2007. The incorporation of nitrogen has been enabled since 2009. Finally, a UHV-CVD (Ultra High Vacuum Chemical Vapor Deposition) chamber for the growth of group IV semiconductors has been installed during this thesis. The aim of this chamber is to grow a Si buffer layer with a surface as perfect as possible (with double atomic steps) prior to the growth of the III-V structure. A III-V solid source MBE chamber is connected through a ultra-high vacuum transfer tunnel. Group-III elements (Al, Ga and In) are generated from conventional effusion cells. Group-V elements (P, As, and Sb) are provided by using valved cracker cells. Nitrogen is supplied using a valved RF plasma N_2 source. Finally, Be (p-type) and Si (n-type) are used as dopant sources. Fig. 1-11 shows a schematic of the UHVCVD-MBE growth cluster. The choice of the pseudomorphic approach was not conditioned

only by the need to integrate laser on Si. Indeed, since 2011, the FOTON laboratory has also been studying the development of multi-junction solar cells based on a Si bottom cell and a lattice-matched GaAsPN top cell[61,113]. Finally, the growth of GaP on Si is expected to be interesting for the integration of nonlinear optical functions. Indeed, GaP is an excellent candidate for second-order nonlinear processes because of its large indirect bandgap (2.35 eV), its large nonlinear susceptibility (45 pm.V^{-1})[114] and its large thermal conductivity (1.1 W.cm^{-1}.K^{-1}).

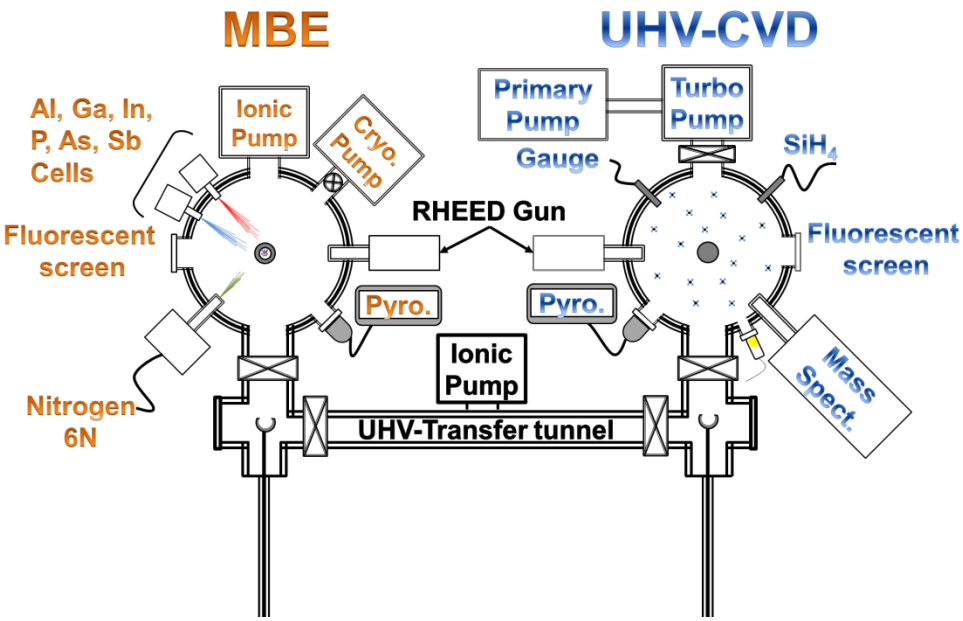

Fig. 1-11: UHVCVD-MBE growth cluster for III-V on Si integration. From Ref. 70.

1.4 Conclusion

In summary, we have seen that many approaches are worldwide proposed to demonstrate a laser on Si, each of them with its own benefits and drawbacks. None of them has clearly been standing out for now and complementary routes are most likely to emerge depending on the applications. The hybrid integration of III-V lasers on Si by bonding is probably going to address the medium volume applications of inter-chips optical communications. For VLSI applications, a monolithic laser is more desirable. The pseudomorphic approach may be one of the solutions as it prevents the high defect densities encountered in the growth of lattice-mismatched layers on Si. Nevertheless, it needs to deal with both growth challenges and efficient laser design. This latter point is developed in the following chapters.

References of Chapter 1

[1] J. Bardeen and W.H. Brattain, Phys. Rev. **74**, 230 (1948).
[2] Int. Technol. Roadmap Semicond. Itrs (2012).
[3] T. Tsuchizawa, K. Yamada, H. Fukuda, T. Watanabe, J. Takahashi, M. Takahashi, T. Shoji, E. Tamechika, S. Itabashi, and H. Morita, Ieee J. Sel. Top. Quantum Electron. **11**, 232 (2005).
[4] N. Daldosso, M. Melchiorri, F. Riboli, M. Girardini, G. Pucker, M. Crivellari, P. Bellutti, A. Lui, and L. Pavesi, J. Light. Technol. **22**, 1734 (2004).
[5] M. Ziebell, D. Marris-Morini, G. Rasigade, J.-M. Fédéli, P. Crozat, E. Cassan, D. Bouville, and L. Vivien, Opt. Express **20**, 10591 (2012).
[6] G.T. Reed, G. Mashanovich, F.Y. Gardes, and D.J. Thomson, Nat Photon **4**, 518 (2010).
[7] P. Chaisakul, D. Marris-Morini, M.-S. Rouifed, G. Isella, D. Chrastina, J. Frigerio, X. Le Roux, S. Edmond, J.-R. Coudevylle, and L. Vivien, Opt. Express **20**, 3219 (2012).
[8] Y.-H. Kuo, Y.K. Lee, Y. Ge, S. Ren, J.E. Roth, T.I. Kamins, D.A.B. Miller, and J.S. Harris, Nature **437**, 1334 (2005).
[9] L. Vivien, J. Osmond, J.-M. Fédéli, D. Marris-Morini, P. Crozat, J.-F. Damlencourt, E. Cassan, Y. Lecunff, and S. Laval, Opt. Express **17**, 6252 (2009).
[10] O. Fidaner, A.K. Okyay, J.E. Roth, R.K. Schaevitz, Y.-H. Kuo, K.C. Saraswat, J.S. Harris, and D.A.B. Miller, Ieee Photonics Technol. Lett. **19**, 1631 (2007).
[11] D. Liang and J.E. Bowers, Nat. Photon. **4**, 511 (2010).
[12] W.P. Dumke, Phys. Rev. **127**, 1559 (1962).
[13] M.A. Green, J. Zhao, A. Wang, P.J. Reece, and M. Gal, Nature **412**, 805 (2001).
[14] M.J. Chen, J.L. Yen, J.Y. Li, J.F. Chang, S.C. Tsai, and C.S. Tsai, Appl. Phys. Lett. **84**, 2163 (2004).
[15] N. Daldosso and L. Pavesi, Laser Photonics Rev. **3**, 508 (2009).
[16] L. Dal Negro, M. Cazzanelli, B. Danese, L. Pavesi, F. Iacona, G. Franzò, and F. Priolo, J. Appl. Phys. **96**, 5747 (2004).
[17] L. Pavesi, L.D. Negro, C. Mazzoleni, G. Franzò, and F. Priolo, Nature **408**, 440 (2000).
[18] S. Yerci, R. Li, and L. Dal Negro, Appl. Phys. Lett. **97**, 081109 (2010).
[19] A. Anopchenko, A. Marconi, M. Wang, G. Pucker, P. Bellutti, and L. Pavesi, Appl. Phys. Lett. **99**, 181108 (2011).
[20] H. Rong, A. Liu, R. Jones, O. Cohen, D. Hak, R. Nicolaescu, A. Fang, and M. Paniccia, Nature **433**, 292 (2005).
[21] H. Rong, Y.-H. Kuo, S. Xu, A. Liu, R. Jones, M. Paniccia, O. Cohen, and O. Raday, Opt. Express **14**, 6705 (2006).
[22] R.N. Hall, G.E. Fenner, J.D. Kingsley, T.J. Soltys, and R.O. Carlson, Phys. Rev. Lett. **9**, 366 (1962).
[23] N. Holonyak and S.F. Bevacqua, Appl. Phys. Lett. **1**, 82 (1962).
[24] H. Wada and T. Kamijoh, Ieee Photonics Technol. Lett. **8**, 173 (1996).
[25] A.W. Fang, H. Park, O. Cohen, R. Jones, M.J. Paniccia, and J.E. Bowers, Opt. Express **14**, 9203 (2006).
[26] G. Roelkens, D. Van Thourhout, R. Baets, R. Nötzel, and M. Smit, Opt. Express **14**, 8154 (2006).
[27] M. Lamponi, S. Keyvaninia, C. Jany, F. Poingt, F. Lelarge, G. de Valicourt, G. Roelkens, D. Van Thourhout, S. Messaoudene, J.-M. Fedeli, and G.H. Duan, Ieee Photonics Technol. Lett. **24**, 76 (2012).

[28] D. Liang, M. Fiorentino, T. Okumura, H.-H. Chang, D.T. Spencer, Y.-H. Kuo, A.W. Fang, D. Dai, R.G. Beausoleil, and J.E. Bowers, Opt. Express **17**, 20355 (2009).
[29] M. Paniccia, Nat. Photonics **4**, 498 (2010).
[30] P. Cheben, R. Soref, D. Lockwood, and G. Reed, Adv. Opt. Technol. **2008**, 1 (2008).
[31] J. Weertman and J.R. Weertman, *Elementary Dislocation Theory* (Macmillan, 1964).
[32] J.W. Matthews and A.E. Blakeslee, J. Cryst. Growth **27**, 118 (1974).
[33] J. Liu, L.C. Kimerling, and J. Michel, Semicond. Sci. Technol. **27**, 094006 (2012).
[34] R.E. Camacho-Aguilera, Y. Cai, N. Patel, J.T. Bessette, M. Romagnoli, L.C. Kimerling, and J. Michel, Opt. Express **20**, 11316 (2012).
[35] P. Moontragoon, R.A. Soref, and Z. Ikonic, J. Appl. Phys. **112**, 073106 (2012).
[36] M.T. Currie, S.B. Samavedam, T.A. Langdo, C.W. Leitz, and E.A. Fitzgerald, Appl. Phys. Lett. **72**, 1718 (1998).
[37] J.P. van der Ziel, R.D. Dupuis, R.A. Logan, and C.J. Pinzone, Appl. Phys. Lett. **51**, 89 (1987).
[38] M. Razeghi, M. Defour, R. Blondeau, F. Omnes, P. Maurel, O. Acher, F. Brillouet, J.C. C-Fan, and J. Salerno, Appl. Phys. Lett. **53**, 2389 (1988).
[39] M. Sugo, H. Mori, Y. Sakai, and Y. Itoh, Appl. Phys. Lett. **60**, 472 (1992).
[40] T. Egawa, Y. Murata, T. Jimbo, and M. Umeno, Photonics Technol. Lett. Ieee **9**, 872 (1997).
[41] T. Yamada, M. Tachikawa, T. Sasaki, H. Mori, and Y. Kadota, Appl. Phys. Lett. **70**, 1614 (1997).
[42] I.J. Luxmoore, R. Toro, O.D. Pozo-Zamudio, N.A. Wasley, E.A. Chekhovich, A.M. Sanchez, R. Beanland, A.M. Fox, M.S. Skolnick, H.Y. Liu, and A.I. Tartakovskii, Sci. Reports **3**, (2013).
[43] K. Samonji, H. Yonezu, Y. Takagi, K. Iwaki, N. Ohshima, J.K. Shin, and K. Pak, Appl. Phys. Lett. **69**, 100 (1996).
[44] Z. Mi, J. Yang, P. Bhattacharya, G. Qin, and Z. Ma, Proc. Ieee **97**, 1239 (2009).
[45] B. Gobaut, J. Penuelas, J. Cheng, A. Chettaoui, L. Largeau, G. Hollinger, and G. Saint-Girons, Appl. Phys. Lett. **97**, 201908 (2010).
[46] S.H. Huang, G. Balakrishnan, A. Khoshakhlagh, L.R. Dawson, and D.L. Huffaker, Appl. Phys. Lett. **93**, 071102 (2008).
[47] J.R. Reboul, L. Cerutti, J.B. Rodriguez, P. Grech, and E. Tournié, Appl. Phys. Lett. **99**, 121113 (2011).
[48] L. Cerutti, J.B. Rodriguez, and E. Tournie, Ieee Photonics Technol. Lett. **22**, 553 (2010).
[49] H. Liu, T. Wang, Q. Jiang, R. Hogg, F. Tutu, F. Pozzi, and A. Seeds, Nat. Photonics **5**, 416 (2011).
[50] A. Lee, Q. Jiang, M. Tang, A. Seeds, and H. Liu, Opt. Express **20**, 22181 (2012).
[51] C.V. Falub, H. von Känel, F. Isa, R. Bergamaschini, A. Marzegalli, D. Chrastina, G. Isella, E. Müller, P. Niedermann, and L. Miglio, Science **335**, 1330 (2012).
[52] T. Mårtensson, C.P.T. Svensson, B.A. Wacaser, M.W. Larsson, W. Seifert, K. Deppert, A. Gustafsson, L.R. Wallenberg, and L. Samuelson, Nano Lett. **4**, 1987 (2004).
[53] J. Tatebayashi, A. Lin, P.S. Wong, R.F. Hick, and D.L. Huffaker, J. Appl. Phys. **108**, 034315 (2010).
[54] M.H.H. Alouane, N. Chauvin, H. Khmissi, K. Naji, B. Ilahi, H. Maaref, G. Patriarche, M. Gendry, and C. Bru-Chevallier, Nanotechnology **24**, 035704 (2013).
[55] M. Montazeri, M. Fickenscher, L.M. Smith, H.E. Jackson, J. Yarrison-Rice, J.H. Kang, Q. Gao, H.H. Tan, C. Jagadish, Y. Guo, J. Zou, M.-E. Pistol, and C.E. Pryor, Nano Lett. **10**, 880 (2010).
[56] R. Chen, T.-T.D. Tran, K.W. Ng, W.S. Ko, L.C. Chuang, F.G. Sedgwick, and C. Chang-Hasnain, Nat. Photonics **5**, 170 (2011).

[57] L.C. Chuang, F.G. Sedgwick, R. Chen, W.S. Ko, M. Moewe, K.W. Ng, T.-T.D. Tran, and C. Chang-Hasnain, Nano Lett. **11**, 385 (2011).
[58] R. Chen, T.-T.D. Tran, K.W. Ng, W.S. Ko, L.C. Chuang, F.G. Sedgwick, and C. Chang-Hasnain, in *Integr. Photonics Res. Silicon Nanophotonics* (Optical Society of America, 2010), p. PDIWI2.
[59] Y. Takagi, Y. Furukawa, A. Wakahara, and H. Kan, J. Appl. Phys. **107**, 063506 (2010).
[60] O. Skibitzki, F. Hatami, Y. Yamamoto, P. Zaumseil, A. Trampert, M.A. Schubert, B. Tillack, W.T. Masselink, and T. Schroeder, J. Appl. Phys. **111**, 073515 (2012).
[61] S. Almosni, C. Robert, T. Nguyen Thanh, C. Cornet, A. Létoublon, T. Quinci, C. Levallois, M. Perrin, J. Kuyyalil, L. Pedesseau, A. Balocchi, P. Barate, J. Even, J.M. Jancu, N. Bertru, X. Marie, O. Durand, and A. Le Corre, J. Appl. Phys. **113**, 123509 (2013).
[62] K. Momose, H. Yonezu, Y. Fujimoto, Y. Furukawa, Y. Motomura, and K. Aiki, Appl. Phys. Lett. **79**, 4151 (2001).
[63] T. Nguyen Thanh, C. Robert, W. Guo, A. Létoublon, C. Cornet, G. Elias, A. Ponchet, T. Rohel, N. Bertru, A. Balocchi, O. Durand, J.S. Micha, M. Perrin, S. Loualiche, X. Marie, and A. Le Corre, J. Appl. Phys. **112**, 053521 (2012).
[64] K. Volz, A. Beyer, W. Witte, J. Ohlmann, I. Németh, B. Kunert, and W. Stolz, J. Cryst. Growth **315**, 37 (2011).
[65] A. Létoublon, W. Guo, C. Cornet, A. Boulle, M. Véron, A. Bondi, O. Durand, T. Rohel, O. Dehaese, N. Chevalier, N. Bertru, and A. Le Corre, J. Cryst. Growth **323**, 409 (2011).
[66] K. Yamane, T. Kawai, Y. Furukawa, H. Okada, and A. Wakahara, J. Cryst. Growth **312**, 2179 (2010).
[67] T.J. Grassman, M.R. Brenner, S. Rajagopalan, R. Unocic, R. Dehoff, M. Mills, H. Fraser, and S.A. Ringel, Appl. Phys. Lett. **94**, 232106 (2009).
[68] X. Yu, P.S. Kuo, K. Ma, O. Levi, M.M. Fejer, and J.S. Harris, J. Vac. Sci. Technol. B Microelectron. Nanometer Struct. **22**, 1450 (2004).
[69] M. Sadeghi and S. Wang, J. Cryst. Growth **227-228**, 279 (2001).
[70] T. Quinci, J. Kuyyalil, T.N. Thanh, Y.P. Wang, S. Almosni, A. Létoublon, T. Rohel, K. Tavernier, N. Chevalier, O. Dehaese, N. Boudet, J.F. Bérar, S. Loualiche, J. Even, N. Bertru, A. Le Corre, O. Durand, and C. Cornet, J. Cryst. Growth **380**, 157 (2013).
[71] B. Kunert, I. Németh, S. Reinhard, K. Volz, and W. Stolz, Thin Solid Films **517**, 140 (2008).
[72] I. Ho and G.B. Stringfellow, J. Cryst. Growth **178**, 1 (1997).
[73] M. Weyers and M. Sato, Appl. Phys. Lett. **62**, 1396 (1993).
[74] J.N. Baillargeon, K.Y. Cheng, G.E. Hofler, P.J. Pearah, and K.C. Hsieh, Appl. Phys. Lett. **60**, 2540 (1992).
[75] E. Bourret-Courchesne, Q. Ye, D.. Peters, J. Arnold, M. Ahmed, S.J.. Irvine, R. Kanjolia, L.. Smith, and S.. Rushworth, J. Cryst. Growth **217**, 47 (2000).
[76] H. Carrère, A. Arnoult, A. Ricard, and E. Bedel-Pereira, J. Cryst. Growth **243**, 295 (2002).
[77] M.A. Wistey, S.R. Bank, H.B. Yuen, H. Bae, and J.S. Harris Jr., J. Cryst. Growth **278**, 229 (2005).
[78] S.B. Zhang and S.-H. Wei, Phys. Rev. Lett. **86**, 1789 (2001).
[79] K. Laaksonen, H.-P. Komsa, T.T. Rantala, and R.M. Nieminen, J. Phys. Condens. Matter **20**, 235231 (2008).
[80] I.A. Buyanova, W.M. Chen, and C.W. Tu, J. Phys. Condens. Matter **16**, S3027 (2004).
[81] D. Dagnelund, I.A. Buyanova, X.J. Wang, W.M. Chen, A. Utsumi, Y. Furukawa, A. Wakahara, and H. Yonezu, J. Appl. Phys. **103**, 063519 (2008).

[82] D. Dagnelund, J. Stehr, A. Yu. Egorov, W.M. Chen, and I.A. Buyanova, Appl. Phys. Lett. **102**, 021910 (2013).
[83] Y. Jin, R.M. Jock, H. Cheng, Y. He, A.M. Mintarov, Y. Wang, C. Kurdak, J.L. Merz, and R.S. Goldman, Appl. Phys. Lett. **95**, 062109 (2009).
[84] Y.-J. Kuang, S.-W. Chen, H. Li, S.K. Sinha, and C.W. Tu, J. Vac. Sci. Technol. B Microelectron. Nanometer Struct. **30**, 02B121 (2012).
[85] W.G. Bi and C.W. Tu, Appl. Phys. Lett. **69**, 3710 (1996).
[86] C. Cornet, T. Nguyen Thanh, T. Quinci, S. Almosni, T. Rohel, J. Kuyyalil, A. Rambaud, A. Létoublon, N. Bertru, O. Durand, and A. Le Corre, Appl. Phys. Lett. **101**, 251906 (2012).
[87] J. Kuyyalil, T. Nguyen Thanh, T. Quinci, S. Almosni, A. Létoublon, T. Rohel, N. Bertru, A. Le Corre, O. Durand, and C. Cornet, J. Cryst. Growth **377**, 17 (2013).
[88] X. Liu, S.G. Bishop, J.N. Baillargeon, and K.Y. Cheng, Appl. Phys. Lett. **63**, 208 (1993).
[89] L. Malikova, F.H. Pollak, and R. Bhat, J. Electron. Mater. **27**, 484 (1998).
[90] W.G. Bi and C.W. Tu, J. Appl. Phys. **80**, 1934 (1996).
[91] H. Naoi, Y. Naoi, and S. Sakai, Solid-State Electron. **41**, 319 (1997).
[92] N.Q. Thinh, I.P. Vorona, M. Izadifard, I.A. Buyanova, W.M. Chen, Y.G. Hong, H.P. Xin, and C.W. Tu, Appl. Phys. Lett. **85**, 2827 (2004).
[93] G. Ungaro, G. Le Roux, R. Teissier, and J.-C. Harmand, Electron. Lett. **35**, 1246 (1999).
[94] M. Kondow, T. Kitatani, S. Nakatsuka, M.C. Larson, K. Nakahara, Y. Yazawa, M. Okai, and K. Uomi, Ieee J. Sel. Top. Quantum Electron. **3**, 719 (1997).
[95] I.A. Buyanova, G. Pozina, J.P. Bergman, W.M. Chen, H.P. Xin, and C.W. Tu, Appl. Phys. Lett. **81**, 52 (2002).
[96] S. Liebich, M. Zimprich, A. Beyer, C. Lange, D.J. Franzbach, S. Chatterjee, N. Hossain, S.J. Sweeney, K. Volz, B. Kunert, and W. Stolz, Appl. Phys. Lett. **99**, 071109 (2011).
[97] N. Hossain, S.J. Sweeney, S. Rogowsky, R. Ostendorf, J. Wagner, S. Liebich, M. Zimprich, K. Volz, B. Kunert, and W. Stolz, Electron. Lett. **47**, 931 (2011).
[98] N.N. Ledentsov, M. Grundmann, F. Heinrichsdorff, D. Bimberg, V.M. Ustinov, A.E. Zhukov, M.V. Maximov, Z.I. Alferov, and J.A. Lott, Ieee J. Sel. Top. Quantum Electron. **6**, 439 (2000).
[99] F. Fukami, K. Umeno, Y. Furukawa, N. Urakami, S. Mitsuyoshi, H. Okada, H. Yonezu, and A. Wakahara, Phys. Status Solidi C **8**, 322 (2011).
[100] K. Adomi, N. Noto, A. Nakamura, and T. Takenaka, J. Cryst. Growth **124**, 570 (1992).
[101] B. Kunert, A. Klehr, S. Reinhard, K. Volz, and W. Stolz, Electron. Lett. **42**, 601 (2006).
[102] N. Koukourakis, C. Bückers, D.A. Funke, N.C. Gerhardt, S. Liebich, S. Chatterjee, C. Lange, M. Zimprich, K. Volz, W. Stolz, B. Kunert, S.W. Koch, and M.R. Hofmann, Appl. Phys. Lett. **100**, 092107 (2012).
[103] S. Illek, B. Borchert, G. Ebbinghaus, A.Y. Egorov, and H. Riechert, in *2000 Int. Conf. Indium Phosphide Relat. Mater. 2000 Conf. Proc.* (n.d.), pp. 537–540.
[104] D.B. Jackrel, S.R. Bank, H.B. Yuen, M.A. Wistey, J.S. Harris, A.J. Ptak, S.W. Johnston, D.J. Friedman, and S.R. Kurtz, J. Appl. Phys. **101**, 114916 (2007).
[105] B. Kunert, S. Zinnkann, K. Volz, and W. Stolz, J. Cryst. Growth **310**, 4776 (2008).
[106] N. Urakami, F. Fukami, H. Sekiguchi, H. Okada, and A. Wakahara, J. Cryst. Growth **378**, 96 (2013).
[107] Y. Takagi, H. Yonezu, K. Samonji, T. Tsuji, and N. Ohshima, J. Cryst. Growth **187**, 42 (1998).
[108] K. Yamane, T. Kobayashi, Y. Furukawa, H. Okada, H. Yonezu, and A. Wakahara, J. Cryst. Growth **311**, 794 (2009).

[109] Y. Furukawa, H. Yonezu, K. Ojima, K. Samonji, Y. Fujimoto, K. Momose, and K. Aiki, Jpn. J. Appl. Phys. **41**, 528 (2002).
[110] S.Y. Moon, H. Yonezu, Y. Furukawa, S.M. Kim, Y. Morita, and A. Wakahara, Jpn. J. Appl. Phys. **44**, 1752 (2005).
[111] K. Umeno, Y. Furukawa, A. Wakahara, R. Noma, H. Okada, H. Yonezu, Y. Takagi, and H. Kan, J. Cryst. Growth **311**, 1748 (2009).
[112] K. Yamane, K. Noguchi, S. Tanaka, Y. Furukawa, H. Okada, H. Yonezu, and A. Wakahara, Appl. Phys. Express **3**, 074201 (2010).
[113] J.F. Geisz, J.M. Olson, D.J. Friedman, K.M. Jones, R.C. Reedy, and M.J. Romero, in *Conf. Rec. Thirty-First Ieee Photovolt. Spec. Conf. 2005* (IEEE, 2005), pp. 695– 698.
[114] H. Takahashi, M. Ohashi, T. Kondo, N. Ogasawara, Y. Shiraki, and R. Ito, Jpn. J. Appl. Phys. **33**, L1456 (1994).

Chapter 2

Theoretical challenges

In this chapter, we present the challenges and requirement for accurately calculating the optical properties of semiconductor structures grown on Si(001). To this end, a precise description of the whole electronic structure, including strain effects, is required. We focus on the peculiarities of the dilute nitride alloys and their numerical modeling. Finally, we demonstrate some advantages of the $sp^3d^5s^*$ tight-binding model through simulations on model structures.

2.1 Introduction to the band structure calculations

To improve the design of optoelectronics devices, understanding of both optical and electronic properties of semiconductors structures is needed. The first prerequisite is an accurate modeling of the band structures of bulk materials and related heterostructures including the calculation of energy subbands and wave functions. Then one can extract the featured optical parameters such as the interband transitions and oscillator strengths which give access to the spectral functions: absorption and gain spectra, complex dielectric responses, refractive indexes. In addition, many body effects (electron-hole correlations) can also be simulated[1].

In this context, several theoretical methods based on the time-independent Schrödinger approximation* were developed in the last four decades of the 20th century. The characteristic equation is:

$$H\psi(r) = E\psi(r) \qquad 2\text{-}1$$

* By solving the Schrödinger equation, we mean finding the total or a part of the eigenvalues spectrum E_n and their corresponding eigenvectors $\psi_n(r)$.

where H is the Hamiltonian operator and E is the energy associated with the wave function of the electronic system $\psi(r)$.

For heavy atoms, the exact solution of Eq. 2-1 is impossible and approximations are needed. To this scope, numerical methods can be divided into two main groups as summarized on Fig. 2-1.

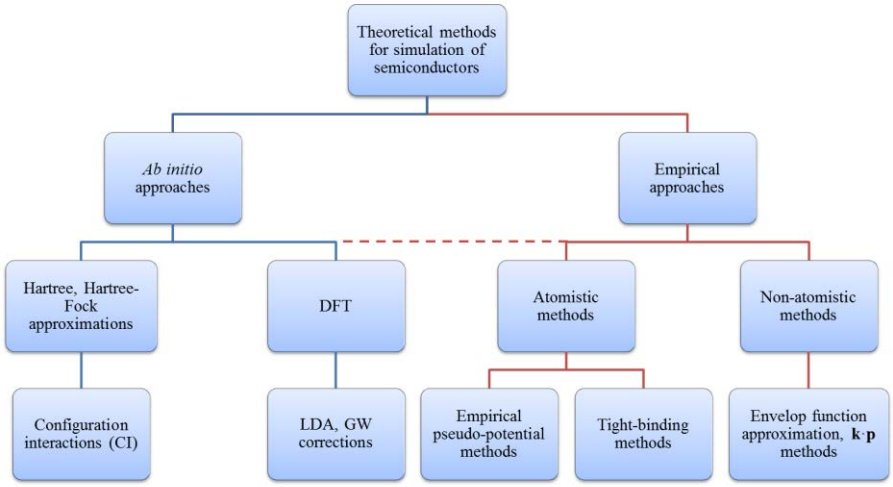

Fig. 2-1: Theoretical methods for calculating the band structure of semiconductors.

The first one relies solely on first principles laws of physics without introducing any empirical parameters. These methods are called *ab initio* approaches. For instance, methods such as Hartree or Hartree-Fock approximations simplify the many-electron system by considering electrons as independent particles or by adding an exchange term. The most commonly used method for solids is the density functional theory (DFT) in which the many-electron system is replaced by an equation acting on the functional of the electronic density[2,3]. The exact exchange-correlation function is however unknown for solids and various approximations are considered. The interaction between electrons can be reasonably taken into account in the frame of the local density approximation (LDA) or Generalized Gradient Approximation (GGA) to predict properties related to the ground state. This method is thus known to be well suited to predict the structural properties of a system in its ground state. On the contrary, the calculation of electronic or optical properties is still unsatisfactory. The band gaps of semiconductors are largely underestimated. For example, InAs is predicted to be a semi-metal. This issue can be partially

overcome by applying many-body perturbation theory and the so-called GW correction[4] (in which G refers to the Green's function and W to the dynamically screened Coulomb interaction). Unfortunately, the heavy computational effort added by this correction is dramatic and this method remains limited to few atoms (few thousands of atoms without the GW correction). *Ab initio* approaches are thus useful tools when focusing on ground state properties of small heterostructures, electronic properties of bulk materials, or first qualitative simulations but they go out of use when simulating complex systems encountered in devices such as nanostructures or alloys.

The limitations of *ab initio* methods can be bypassed by empirical approaches. Indeed, larger systems can generally be considered with these approaches but they require an adjustment of a more or less high number of parameters to fit experimental data or *ab initio* results for bulk materials. We can distinguish atomistic and non-atomistic approaches. In atomistic approaches, the empirical pseudo-potential method (EPM)[5] and the tight-binding (TB)[6] method are known as the two approaches providing the more accurate description of the electronic band structure of semiconductors. And yet, their starting points are totally opposite. In pseudo-potential methods, a nearly free electron is considered and its wave function is decomposed on a plane wave basis. The influence of the ions and other electrons is considered as a potential $V(r)$ which is the empirical parameter. On the opposite, in the tight-binding method, the electrons are considered as tightly bound to their nuclei. The wave function results from the overlapping of the orbitals composing the wave function of each atom. The empirical character of this method comes from the choice of the overlap parameters. With the increase of high-performance computing, both methods are now able to deal with systems containing several millions of atoms[7,8].

On the other hand, in order to simulate electronic and optical devices, simple, economical computing-resources-consuming and non-atomistic methods, such as $\mathbf{k}\cdot\mathbf{p}$ and envelope function approximation, have been developed[9–12]. The $\mathbf{k}\cdot\mathbf{p}$ method is a symmetry based perturbation method used to describe the band structure near a given $\mathbf{k_0}$ point of the Brillouin zone. The electronic wave function is expanded onto the $\mathbf{k_0}$ Bloch functions basis. Nevertheless, because this basis is infinite, considering a finite number of Bloch functions drives to an approximated resolution. For example, when considering eight Bloch functions (in the so-called eight-band $\mathbf{k}\cdot\mathbf{p}$ model[13]), only 20 % of the Brillouin zone is satisfactorily described. This is not a

problem for most of optical devices in which semiconductors have direct band gaps (GaAs, InP, InAs), because most of physical phenomena occur near the band edges. This reason, combined with the fact that the optical matrix elements can be used as input parameters, explains why the **k**·**p** method has been, for years, the most successful method to describe the electronic band structure in optical devices. Nevertheless, in our case we consider semiconductor materials with indirect band gaps such as GaP. Thus, the eight-band **k**·**p** method is insufficient. Recently, it has been shown that increasing the number of bands explicitly included in the **k**·**p** theory up to thirty is enough to give a satisfactory description of the zone edge conduction valleys[14]. Thus, the band structures of indirect gap semiconductors such as Si or Ge were successfully reproduced. However, because of the inherent difficulty in a 30-band Hamiltonian parameterization, derived models are for the time being only restricted to periodic systems with high degree of symmetry such as bulk[14], quantum wells[15] or superlattices[16]. Moreover, the extension of this method for heterostructures suffers from the underlying envelope approximation, i.e. common zone center Bloch functions are assumed for all the materials.

2.2 Modeling the semiconductor band structure and the pseudomorphic integration onto Si

In this part, we present some challenges for the pseudomorphic approach: the use of indirect band gap semiconductors, strain effects and the giant bowing of dilute nitrides.

2.2.1 GaP and AlP

In the pseudomorphic approach, GaP and AlP play an important role because their lattice constant is close to that of Si. Most of III-V compounds crystallize in the zinc blende structure characterized by T_d space group symmetry. This is the case for GaP and AlP although these materials have very recently attracted attention[17,18] for their ability to cristallize also in the wurtzite phase. This Ph.D. dissertation is only dedicated to cubic semiconductors symmetry whose elementary cell is schematically shown in Fig. 2-2(a). From the experimental side, the lattice constants of GaP and AlP are known precisely: 5.4505 Å and 5.4672 Å respectively (at room temperature). The reciprocal space can be limited to the first Brillouin zone as shown in Fig. 2-2(b).

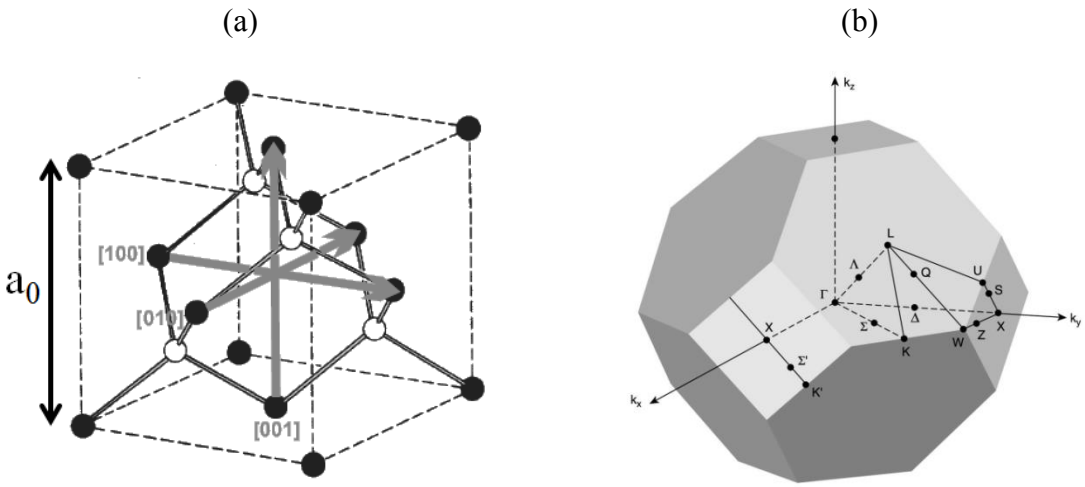

Fig. 2-2: (a) Zinc blende crystalline structure. (b) First Brillouin zone and high symmetry points.

Among high symmetry points, three of them are of particular interest for the description of the electronic properties of semiconductors:

- Γ point (0,0,0)
- 6 equivalent X points $\frac{2\pi}{a_0}(\pm 1,0,0), \frac{2\pi}{a_0}(0,\pm 1,0)$, $\frac{2\pi}{a_0}(0,0,\pm 1)$
- 8 equivalent L points $\frac{2\pi}{a_0}(\pm 0.5,\pm 0.5,\pm 0.5)$

Fig. 2-3 shows the band structures of bulk GaP and AlP. The valence band maximum is located at the Γ point for both semiconductors. On the other hand, their conduction band minimum lies near the X point and the fundamental transition is indirect in k-space in the two cases.

The indirect band gap $E_g^X = X_{6c} - \Gamma_{8v}$ and the direct band gap $E_g^\Gamma = \Gamma_{6c} - \Gamma_{8v}$ have been well measured and calculated and the commonly accepted values[20] are summarized in Table 2-1.

	GaP	AlP
E_g^X (eV)	2.35 (0 K) / 2.26 (300 K)	2.52 (0K) / 2.45 (300K)
E_g^Γ (eV)	2.89 (0 K) / 2.78 (300 K)	3.63 (0K) / 3.56 (300 K)

Table 2-1: First indirect and direct band gaps of bulk GaP and AlP.

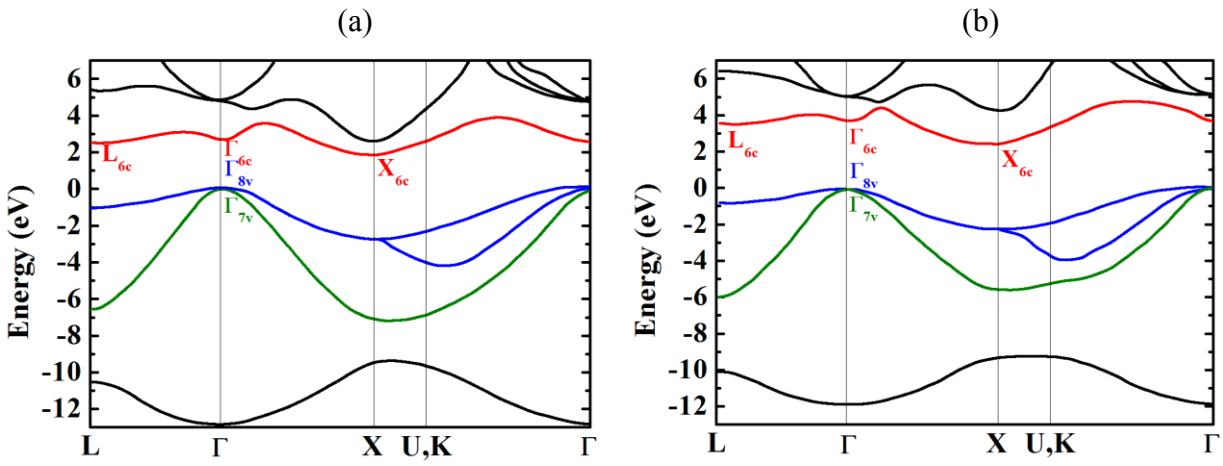

Fig. 2-3: Band structure of (a) bulk GaP and (b) bulk AlP reproduced from Ref. 19.

The case of the second indirect band gap $E_g^L = L_{6c} - \Gamma_{8v}$ is not as well documented especially for AlP but we will retain that the values of E_g^L are between E_g^X and E_g^Γ with $E_g^L \approx 2.7$ eV for GaP and $E_g^L \approx 3.5$ eV for AlP.

Because GaP and AlP low energy band gaps are indirect, these materials obviously cannot be used as an optical gain medium. On the opposite, direct band gap compounds such as GaAs are more suitable. Nevertheless, in the pseudomorphic approach, the layers must be grown coherently, which has two main consequences:

i. The mismatched layers must be accommodated below the critical thickness. Given the lattice-mismatching of GaAs, InP or InAs onto Si, only nanostructures or more complicated alloys are expected to match to some extent.
ii. The strain accumulated in these layers is expected to have a strong impact on the electronic band structures. This point will be stressed in the following.

2.2.2 Strain effects on the electronic band structure of GaAs on GaP(001)

In this part, we provide a general consideration of strain effects on the electronic band structure dealing with GaAs onto GaP (001). This example is of particular importance for FOTON laboratory because the nanostructures investigated are mainly based on GaAs compounds (for instance: GaAsPN QWs or InGaAs QDs). The influence of the substrate, Si or GaP, is secondary for strain consideration because their lattice constants are similar. Si(001) is

here considered so that the $\vec{z} = \langle 001 \rangle$ direction will always be considered as the growth direction in the rest of the manuscript.

2.2.2.1 Strain effects in zinc blende crystals

Strain in a crystal can be defined as the relative lattice displacement created by the structure deformation. In most of cases, these displacements are much smaller than the lattice constant of the crystal so that the strain can be described by the second order symmetric strain tensor:

$$\bar{\bar{\varepsilon}} = \begin{pmatrix} \varepsilon_{xx} & \varepsilon_{xy} & \varepsilon_{xz} \\ \varepsilon_{xy} & \varepsilon_{yy} & \varepsilon_{yz} \\ \varepsilon_{xz} & \varepsilon_{yz} & \varepsilon_{zz} \end{pmatrix} \qquad 2\text{-}2$$

This tensor has only six different terms so that it is more common to write it as a one dimensional array:

$$\bar{\varepsilon} = \begin{pmatrix} \varepsilon_{xx} & \varepsilon_{yy} & \varepsilon_{zz} & \varepsilon_{xy} & \varepsilon_{yz} & \varepsilon_{xz} \end{pmatrix}^t \qquad 2\text{-}3$$

In the same way, the stress tensor $\bar{\tau}$ can be defined. In the framework of the linear continuum elasticity (LCE) theory, $\bar{\tau}$ and $\bar{\varepsilon}$ are linked by the Hooke's law:

$$\bar{\tau} = \bar{\bar{C}}\bar{\varepsilon} \qquad 2\text{-}4$$

in which $\bar{\bar{C}}$ is the elastic stiffness tensor. In the case of zinc blende crystals, $\bar{\bar{C}}$ can be defined with only three linearly independent constants C_{11}, C_{12} and C_{44}:

$$\bar{\bar{C}} = \begin{pmatrix} C_{11} & C_{12} & C_{12} & 0 & 0 & 0 \\ C_{12} & C_{11} & C_{12} & 0 & 0 & 0 \\ C_{12} & C_{12} & C_{11} & 0 & 0 & 0 \\ 0 & 0 & 0 & C_{44} & 0 & 0 \\ 0 & 0 & 0 & 0 & C_{44} & 0 \\ 0 & 0 & 0 & 0 & 0 & C_{44} \end{pmatrix} \qquad 2\text{-}5$$

2.2.2.2 Examples of strain

The simplest deformation is the purely hydrostatic strain in which $\varepsilon_{xx} = \varepsilon_{yy} = \varepsilon_{zz}$ and $\varepsilon_{xy} = \varepsilon_{xz} = \varepsilon_{yz} = 0$. This strain is related to a volume variation:

$$\frac{\Delta V}{V} = \varepsilon_{xx} + \varepsilon_{yy} + \varepsilon_{zz} \qquad 2\text{-}6$$

When a layer with a lattice constant a is grown pseudomorphically on a substrate with a lattice constant a_0, the strain is not purely hydrostatic. Indeed, the substrate imposes the in-plane lattice constant of the layer to be $a_{\parallel} = a_0$, but in the growth direction the layer is likely to relax with an out-of-plane lattice constant $a_{\perp}$. In this biaxial strain configuration, we have thus:

$$\varepsilon_{xx} = \varepsilon_{yy} = \frac{a_{\parallel} - a}{a} = \frac{a_0 - a}{a} \text{ and } \varepsilon_{zz} = \frac{a_{\perp} - a}{a}$$
$$\text{and } \varepsilon_{xy} = \varepsilon_{xz} = \varepsilon_{yz} = 0 \qquad 2\text{-}7$$

Considering Hooke's law and writing the absence of stress in the *z* direction, ε_{zz} and $\varepsilon_{xx} = \varepsilon_{yy}$ can be linked through the relation:

$$\varepsilon_{zz} = -2\frac{C_{12}}{C_{11}}\varepsilon_{xx} \qquad 2\text{-}8$$

This biaxial strain state is often encountered in the case of two dimensional films such as QW grown coherently on a (001) substrate[21].

The case of QD is more complicated because the crystal can relax in the three directions and the strain is no longer homogeneous in the structure. The non-diagonal terms of the strain tensor are related to non-zero shear strain. This more complex case requires adequate methods to describe the strain profiles as discussed in next sections. Nevertheless, in all situations, one can always decompose an arbitrary strain tensor in three parts:

$$\begin{pmatrix} \varepsilon_{xx} & \varepsilon_{xy} & \varepsilon_{xz} \\ \varepsilon_{xy} & \varepsilon_{yy} & \varepsilon_{yz} \\ \varepsilon_{xz} & \varepsilon_{yz} & \varepsilon_{zz} \end{pmatrix} = \frac{1}{3}\begin{pmatrix} \varepsilon_{xx}+\varepsilon_{yy}+\varepsilon_{zz} & 0 & 0 \\ 0 & \varepsilon_{xx}+\varepsilon_{yy}+\varepsilon_{zz} & 0 \\ 0 & 0 & \varepsilon_{xx}+\varepsilon_{yy}+\varepsilon_{zz} \end{pmatrix}$$
$$+\frac{1}{3}\begin{pmatrix} 2\varepsilon_{xx}-(\varepsilon_{yy}+\varepsilon_{zz}) & 0 & 0 \\ 0 & 2\varepsilon_{yy}-(\varepsilon_{xx}+\varepsilon_{zz}) & 0 \\ 0 & 0 & 2\varepsilon_{zz}-(\varepsilon_{xx}+\varepsilon_{yy}) \end{pmatrix} \qquad 2\text{-}9$$
$$+\begin{pmatrix} 0 & \varepsilon_{xy} & \varepsilon_{xz} \\ \varepsilon_{xy} & 0 & \varepsilon_{yz} \\ \varepsilon_{xz} & \varepsilon_{yz} & 0 \end{pmatrix}$$

where the first term refers to the hydrostatic part of the strain, the second one to the uniaxial part in [001] directions and the third one to the shear part in [111] directions. Now we present how the electronic band structure depends on the crystal strain state.

2.2.2.3 The linear deformation potential theory

The linear deformation potential theory is a very simple symmetry-based and useful method to determine the evolution of the band structure with strain[22]. It assumes that the band shift and energy splitting can be described in first approximation by a linear relation involving the strain tensor components and few constants called deformation potentials. Group theory can qualitatively predict these evolutions[23]. We describe these relations focusing on the conduction-band-minimum at the Γ, X and L points and for the valence-band-maximum.

We consider the case of GaAs strained on GaP(001). When unstrained, GaAs is a direct band gap semiconductor. The direct and indirect band gaps reported in Ref.[20] are summarized in Table 2-2.

E_g^L (eV)	E_g^Γ (eV)	E_g^X (eV)
1.815	1.519	1.981

Table 2-2: Indirect and direct band gaps of bulk unstrained GaAs (at 0 K). From Ref. 20.

The lattice constant of GaAs is 5.6533 Å. Thus when pseudomorphically grown on GaP ($a_0 = 5.4505$ Å), it results in a compressive strain of:

$$\varepsilon_{xx} = \varepsilon_{yy} = \frac{a_0 - a}{a} = -0.036 \text{ and } \varepsilon_{zz} = -2\frac{C_{12}}{C_{11}}\varepsilon_{xx} = 0.033$$

where $C_{11} = 122.1$ GPa and $C_{12} = 56.6$ GPa[20].

a) Effect of the hydrostatic strain

The hydrostatic strain shifts the energy levels in proportion to the volume variation $\frac{\Delta V}{V} = \varepsilon_{xx} + \varepsilon_{yy} + \varepsilon_{zz} = -0.039$. The Γ and L conduction-band energies are shifted upwards whereas the X conduction valleys and the Γ valence band maximum shift downwards. The situation is schematized in Fig. 2-4.

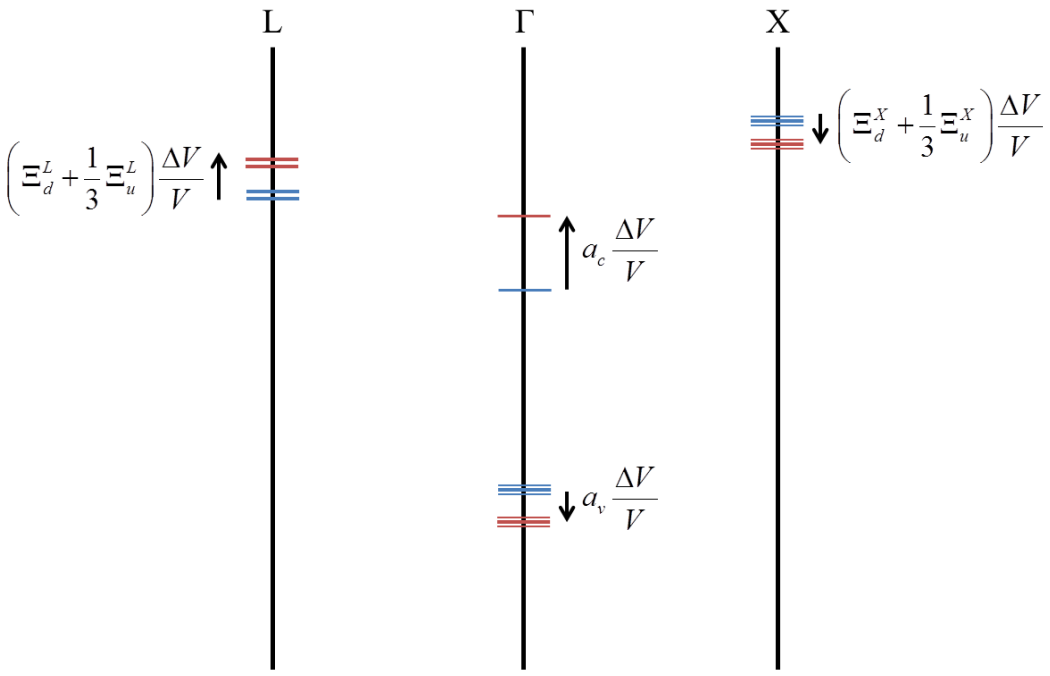

Fig. 2-4: Effect of the hydrostatic strain on bulk GaAs. The unstrained (hydrostatically strained) case is shown as blue (red) lines.

The typical values of the deformation potentials are summarized in Table 2-3. Using these numerical values, the conduction band minima are found to follow the Γ-L-X order as in the unstrained case, but these minima are now closer in energy.

a_c (eV)	a_v (eV)	b (eV)	$\Xi_d^X + \frac{1}{3}\Xi_u^X$ (eV)	$\Xi_d^L + \frac{1}{3}\Xi_u^L$ (eV)	Ξ_u^X (eV)
7.17	1.16	-2.0	1.7	-2.0	6.5

Table 2-3: Deformation potentials of GaAs. From Ref. 20,24.

b) Effect of the uniaxial strain part

The uniaxial part of the biaxial strain (see Fig. 2-5) yields a splitting of the Γ valence-band-maximum into the heavy holes (HH) and light holes (LH) states whereas the X conduction levels are splitted into the X_{XY} and X_Z bands. No effect occurs at the L point for symmetry reasons.

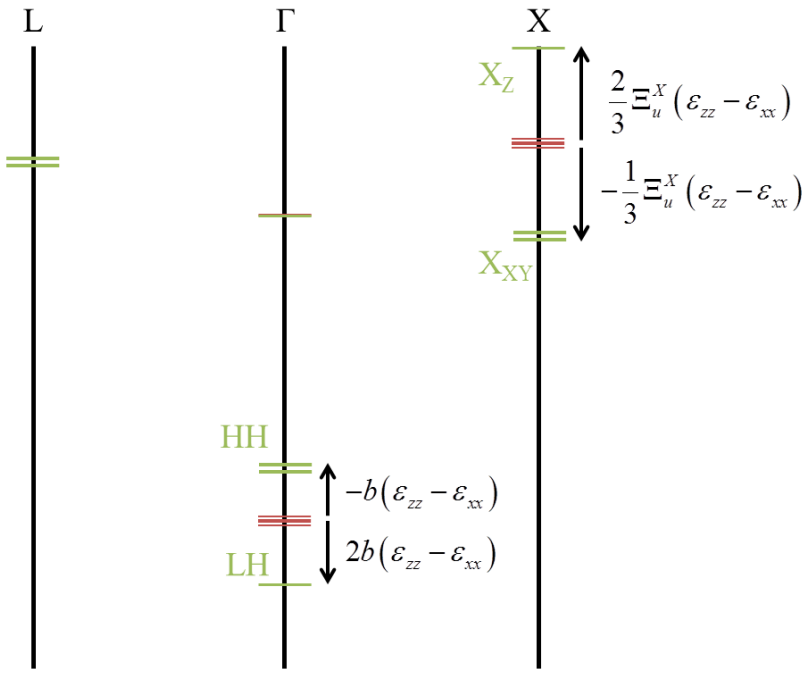

Fig. 2-5: Adding effect of the uniaxial strain. The hydrostatically (biaxially) strained case is shown as red (green) lines.

Interestingly, the conduction band minima order is now found to be X_{XY}-Γ-L-X_Z with $\Gamma - X_{XY} = 30$ meV and $L - \Gamma = 100$ meV. Thus, when it is biaxially strained on a GaP substrate, the band gap of bulk GaAs is borderline indirect/direct. Note that the same conclusions have been drawn by Prieto *et al.*[25].

This example proves that the lateral conduction bands (X and L) must be taken into account in any theoretical model dealing with nanostructures grown on GaP(001). This consequently rules out the eight-band **k**·**p** model.

2.2.3 Modeling the dilute nitrides

Another theoretical challenge related to the pseudomorphic approach is the use of III-V-N alloys. Indeed, their properties considerably differ from the ones of classical III-V alloyed crystals. Providing a correct description has been the subject of many controversies in the past decade.

2.2.3.1 The band gap problem

In conventional alloys, the variations of the band gap with the composition can be described by a quadratic dependence. For instance, for ternary $AB_{1-x}C_x$ with a common cation A and two different anions B and C, the band gap is defined by:

$$E_g(AB_{1-x}C_x) = (1-x)E_g(AB) + x\,E_g(AC) - b\,x(1-x) \qquad 2\text{-}10$$

where $E_g(AB)$ and $E_g(AC)$ are the band gaps of the binary compounds and b is a parameter called the bowing coefficient. b is usually positive, which means that the band gap of the alloy is smaller than the linear interpolation. A typical b value is about 1 eV in conventional ternaries. On the opposite, in dilute nitride alloys, experimental results suggest that a unique bowing coefficient cannot be used over a wide range of compositions[20]. Moreover their values are much larger than for conventional alloys. For example, in $GaAs_{1-x}N_x$ Toivonen *et al.* have reported values up to 26 eV for $x<0.01$[26], justifying the qualification of "huge band gap bowing".

To understand this feature and the theories that have been developed to model it, we have to firstly deal with the doping regime.

2.2.3.2 Nitrogen isoelectronic impurity

First studies on the nitrogen incorporation in GaP or GaAs were conducted in the 60s[27] with a content limited to the doping regime (~10^{17} cm^{-3}). Thomas and Hopfield demonstrated that substituting a phosphor by a nitrogen in GaP induces an impurity bound exciton just below the band gap energy[27]. The creation of this bound state does not occur in other isolectronic

substitution cases such as As in GaP. The singularity of the N behavior can be explained by a strong short-range potential close to the N atom which creates this bound state. This short-range potential results from the strong difference of the electronegativity between N and P (39 % whereas it is only 0.4 % for As and P). Thus, N can easily attract an electron and becomes negatively charged. Then a hole can be attracted by a Coulombic interaction to form the bound exciton. Another reason to explain the N ability to form a short-range potential is its small size compared to P atoms. This results in a local strain field effect which enhances the short-range potential[28]. The observation of a similar N state in GaAs:N has been proved more than eighteen years later[29]. The reason for this late evidence is that contrary to GaP where an isolated N atom creates a bound state in the band gap, the N state is above the conduction band of GaAs. Thus, its optical signature has been highlighted only under hydrostatic pressure[29].

When the N doping concentration is slightly increased (between 10^{18} and 10^{20} cm^{-3}), two N atoms can be statistically located at closer anion sites. In this case, new bound states related to these nitrogen pairs are created and their energy depends on the distance between both N atoms[27,30,31].

The "dilute nitride" terminology corresponds to alloys with larger N concentrations (a few percent). The theoretical descriptions of these alloys are all based on these bound states and their possible interactions with the bands of the host material. We now detail the main ones.

2.2.3.3 The band anti-crossing model

a) A simple two-level model

Because of its extreme simplicity, the band anti-crossing model (BAC) is undoubtedly the most popular model for the description of dilute nitride alloys. It has first been proposed by Shan *et al.* to describe GaInAsN alloys[32], but it has been derived for other dilute nitride alloys[33] and even for other highly mismatched alloys such as III-V-Bi[34] or II-VI-O[35] alloys.

It describes the interaction between an N-related spatially localized level E_N and the delocalized level E_M related to the conduction band edge of the host material (GaInAs in the original paper of Shan *et al.*[32]). The Hamiltonian related to this two-level problem is simply given by:

$$H_{BAC} = \begin{pmatrix} E_M & V_{MN} \\ V_{MN} & E_N \end{pmatrix} \qquad 2\text{-}11$$

where V_{MN} is a coupling term. The diagonalization of this Hamiltonian gives rise to two eigenvalues as shown in Fig. 2-6:

$$E\pm = (E_N + E_M \pm \left[(E_N - E_M)^2 + 4V_{MN}^2 \right]^{1/2}) / 2 \qquad 2\text{-}12$$

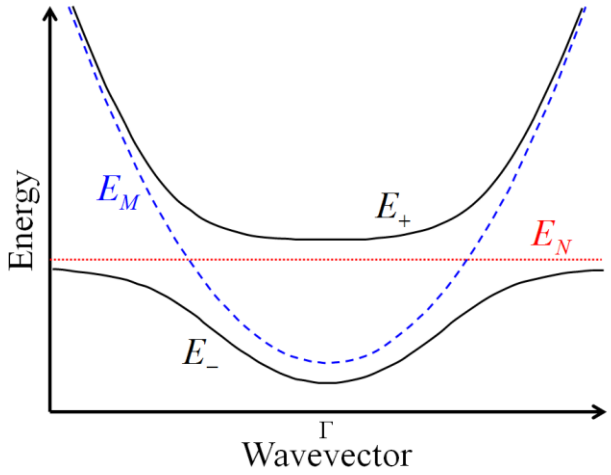

Fig. 2-6: BAC interpretation of the creation of E_- and E_+ new conduction bands in Ga(In)AsN alloy.

The new conduction band edge becomes E_-. The effect of N on the valence bands is neglected[32] and the monotonous reduction of the band gap with N increase is explained by a coupling term V_{MN} which depends on the N composition x with $V_{MN} = C_{MN}\sqrt{x}$ [36].

The other feature described by the BAC theory is the appearance of the second conduction band E_+ whose energy increases with increasing N. Photoreflectance measurements have brought experimental evidences on the existence of a similar level[32] and have justified the rightness of the BAC model for many people. Nevertheless, it suffers from a lack of a firm theoretical basis. Firstly, its description is limited to a small reciprocal space region close to the Γ point[33], while experimental evidences have been brought on the effect of N incorporation at large k vectors[37–40]. Secondly, only one localized level is considered, while N is known to introduce many localized states related to isolated, pairs or more complex clusters of N atoms. Thus, it fails when describing features such as the effective mass of Ga(In)AsN alloy which is underestimated by the BAC model[41].

b) Extensions of the BAC model

To deal with these limitations, various refinements of the simple two level BAC model have been proposed. The group of E.P. O'Reilly has proposed to introduce a second localized level related to a N-N pair resulting in a three-level BAC Hamiltonian[42,43]:

$$H_{BAC} = \begin{pmatrix} E_M & V_{MN} & V_{MNN} \\ V_{MN} & E_N & 0 \\ V_{MNN} & 0 & E_{NN} \end{pmatrix} \qquad 2\text{-}13$$

A *n*-band Hamiltonian has also been proposed by Vaughan and Ridley[44].

Nevertheless, the issue of the BAC model validity over the entire Brillouin zone still remains, although Wu *et al.* have proposed to introduce a k-dependence in the coupling parameter. Moreover, while a relative consensus has been achieved about the values of the E_N and C_{MN} parameters in bulk GaAsN or GaPN[45], a unique parameterization of the quaternary GaAsPN alloy is still lacking[46]. Finally, some authors have chosen to refine the model by adding some arbitrary dependences on N concentration, pressure or temperature in E_N, C_{MN} or E_M [43,47–49], transforming the BAC as a fitting tool rather than a model providing comprehensive elements.

The case of nanostructures has also been dealt with. The confinement in a GaAsN/GaAs QW can be evaluated by applying a finite-depth square-well model with taking the effective mass in the QW from the BAC calculation. A more refined method is to modify the eight-band **k·p** model to include the two additional BAC bands and thus forming a ten-band **k·p** Hamiltonian[50]. This model has been widely used for dilute nitride QW[51] as well as dilute nitride QD[52]. Nevertheless, it still suffers from the eight-band **k·p** method limitation to the Brillouin zone center, which has already been mentioned in a previous section.

2.2.3.4 Polymorphous models

The peculiarity of dilute nitride alloys is the enhanced role of heterogeneity and localization. A theoretical modeling of these effects requires atomistic methods associated with the computing in a supercell to handle a large number of atoms. The use of large unit cells is essential because of the small N concentration and the need to model a realistic statistical distribution of the large variety of local configurations.

a) Empirical pseudo-potential method

An EPM description of both GaAsN and GaPN alloys has been proposed by Kent and Zunger in 2001[53]. They have calculated the energetic position of the isolated N level as well as the N pairs and more complex N clusters in the doping regime of GaP:N and GaAs:N. This study has pointed out a striking difference between GaAs:N and GaP:N. As shown in Fig. 2-7, all the localized levels related to isolated N, NN pairs, N triplets or N chains are located below the conduction band minimum (CBM) of GaP. On the opposite, the isolated N and most of NN pairs levels are located above the CBM of GaAs. The case of clusters and chains containing more than two N atoms is found similar in both GaAs:N and GaP:N with related levels being located deeper in the band gap when the number of N atoms increases.

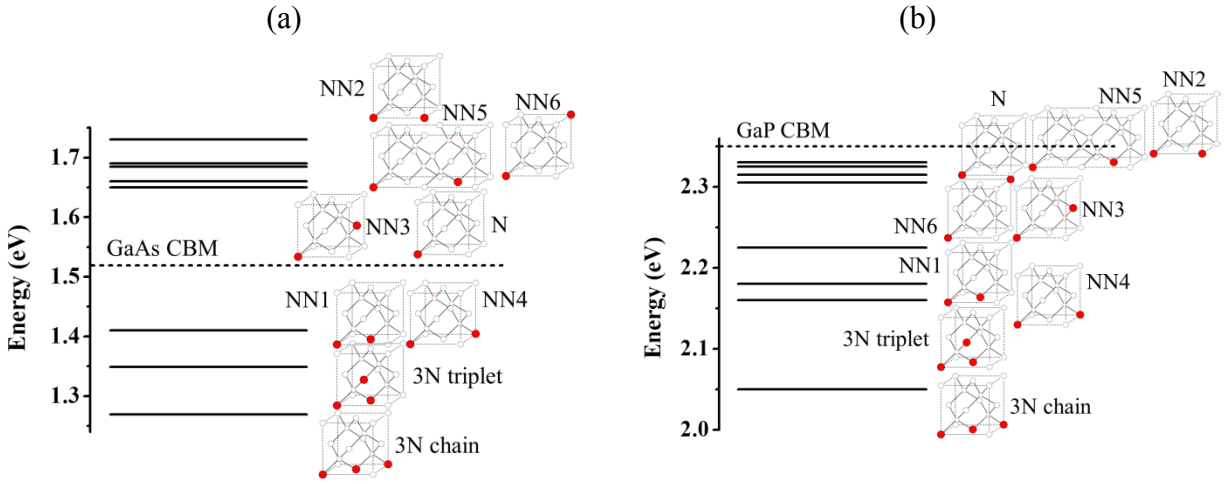

Fig. 2-7: Position of nitrogen related levels in (a) GaAs and (b) GaP as calculated by Kent and Zunger[53]. The isolated N level as well as the sixth first NNi pairs are shown (with i meaning the i^{th} nearest neighbors). 3N triplet and chain clusters are also shown. More than 3N clusters are deeper in energy. N atoms are represented by red atoms.

Additionally, the incorporation of N is found to break the translational symmetry of the host crystal perturbing the conduction states of the host crystal not only at the Γ point but also at the L and X points. The reduction of the conduction band minimum is explained by repulsion between these perturbed host states. With increasing N content, the conduction band minimum swallows the deepest cluster states and the wave function results thus in a mix of localized and more delocalized levels. In this sense, the BAC model is in qualitative agreement, excepted that coupling does not occur between only one localized level and the Γ conduction band of the host material but rather between various conduction band states and various localized cluster states.

b) Tight-binding method

Another famous description has been provided by E.P. O'Reilly using a supercell TB model[41,54–56]. The energies of the isolated N level, NN pairs and clusters are calculated in agreement with the EPM model in GaAsN and GaPN. The strength of this work is to explain the striking behavior of GaAsN and GaPN by an interaction between the conduction band state of the host material and a linear combination of isolated nitrogen states (LCINS). Each N atom in a disordered supercell is associated with an isolated N state which can couple not only with the conduction band state but also with other isolated N states. The fractional Γ character of the conduction band edge is found to be satisfactorily described by the two level BAC model. Indeed, because the isolated N level is above the CBM of GaAs, the conduction band edge of GaAsN is mainly "Γ-like", with a fractional Γ character decreasing from 100 % to nearly 50 % when the N content increases. Nevertheless, it can pass slightly under 50 % when the conduction band edge becomes close to the energies of clusters located inside the band gap. This effect is also responsible of the non-monotonic variation of the electron effective mass with N content in GaAsN[41]. On the opposite, because the N levels are located below the CBM of GaP, the conduction band edge of GaP is mainly "N-like", but with a fractional Γ character globally increasing with the N content and spread over the various N-related levels[55].

2.2.3.5 Recent ab initio considerations and conclusions on GaPN and GaAsN alloys

Several studies have questioned the actual role of the conduction band state of the host material in the optical band gap narrowing effect. The works of Zhang *et al.*[57–59] have claimed that the band gap bowing observed in GaPN is due to the formation of an N impurity band. Moreover, recent *ab initio* simulations have suggested that the red-shifting of the conduction band edge may be explained by the broadening of the N impurity levels[60] which are likely to interact, through zigzag chains on the {110} planes[61], when the N concentration increases.

The large variety of models which have attempted to describe GaAsN and GaPN alloys and the controversies that their conclusions have been kindling, highlights the difficulty in bringing out clear conclusions. Nevertheless, all these models agree on the conclusion that the different behaviors between GaAsN and GaPN are explained by the difference of the host material band gap nature (direct for GaAs and indirect for GaP) and by the position of the N-related level relative to the conduction band (above the conduction band of GaAs and below

that of GaP). Taking the BAC view of Fig. 2-8, we will retain that the CBM of GaAsN has a majority Γ character whereas the CBM of GaPN keeps a majority N-localized character.

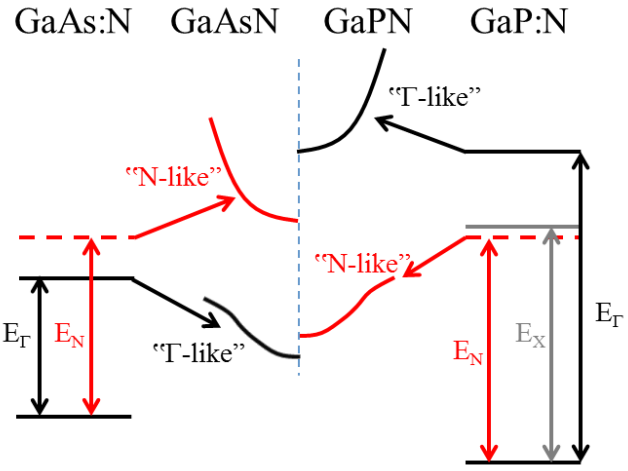

Fig. 2-8: Difference between GaAsN and GaPN conduction band characters. Most of the models agree on the nature of the CBM. The actual nature of the upper conduction band depends on models. Here the BAC view is presented.

In our case, modeling the quaternary alloy GaAsPN is of crucial interest. We can wonder if it is more similar to GaAsN or GaPN and what is the effect of strain. Very few studies have dealt with this issue. Polymorphous models have not been employed because of their computational complexity. Meanwhile, the ten-band **k·p** model has been used for GaAsPN QW but it suffers from the lack of biaxial strain effects or lateral valleys consideration[48,62,63]. We will now show how TB approaches can bring out solutions to the issues of strain effects, lateral valleys consideration and modeling of quaternary dilute nitride alloys.

2.3 The tight-binding model

2.3.1 Fundamentals of the method

The aim of this section is to briefly introduce the main concepts of the TB approaches. Further details can be found in the textbooks of W.A. Harrison[64] and P. Yu and M. Cardona[65].

The TB method is derived from the Hückel theory which describes the formation of orbitals in molecules[66]. A classical description is presented in Fig. 2-9. Two identical atoms, namely A and B, are described by atomic orbitals. When the atoms are close enough, the atomic orbitals can overlap and molecular orbitals are formed. In Fig. 2-9, the simplest case of *s*

spherical orbitals is shown. The two molecular orbitals are called σ, one being symmetric through the two atoms permutation (bonding orbital) and the other being anti-symmetric (antibonding orbital).

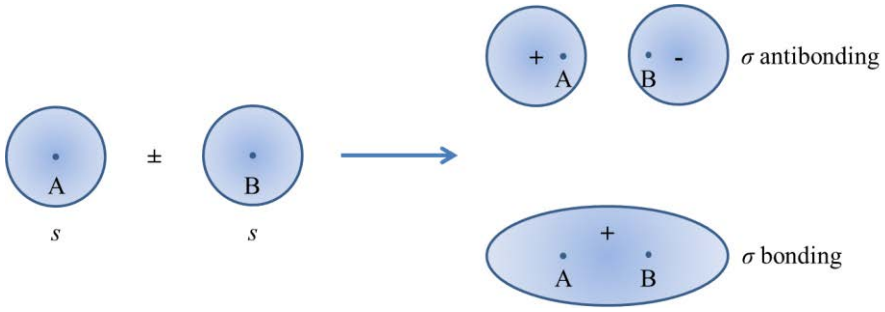

Fig. 2-9: Overlap of two *s* atomic orbitals to form *σ* molecular orbitals.

This hybridization of atomic orbitals is described by an empirical Hamiltonian. For this simple case, the Hamiltonian can be written in the basis of the two atomic orbitals:

$$H = \begin{pmatrix} E_s & V \\ V & E_s \end{pmatrix} \qquad 2\text{-}14$$

with E_s the atomic orbital energy and V the coupling term. The eigenvalues give the energies of both σ molecular orbital ($E_s \pm V$). Similar formations also occur for p or d orbitals, and interactions between orbitals of different type have also to be considered.

The derivation of the TB theory for periodic crystals was first proposed by F. Bloch in 1929[67], and mathematically formalized by Slater and Koster in 1954[6]. The formalism is based on the Löwdin orbitals basis[68], which has the advantage of being orthonormal and conserving the symmetries of the original atomic orbitals. The TB Hamiltonian matrix elements can be written as:

$$H_{\kappa l,\kappa' l'} = \frac{1}{N}\sum_{j,j'} e^{i\vec{k}(\vec{r}_{jl}-\vec{r}_{j'l'})} \left\langle \phi_\kappa(\vec{r}-\vec{r}_{jl}) \middle| \hat{H} \middle| \phi_{\kappa'}(\vec{r}-\vec{r}_{j'l'}) \right\rangle \qquad 2\text{-}15$$

where $\phi_\kappa(\vec{r}-\vec{r}_{jl})$ denotes the κ^{th} Löwdin orbital of the atom localized on the l^{th} site of the j^{th} unit cell, $\hat{H}$ is the Hamiltonian of the entire crystal and N is the number of primitive cells. Because the explicit form of the Löwdin orbitals is not known, these matrix elements cannot be calculated. In the empirical TB model, they are treated as disposable parameters chosen to reproduce the main

features of the band structure. The number of linearly independent parameters can be reduced by considering two approximations: the two-center approximation and the nearest neighbors' approximation. The first approximation consists in neglecting in $\left\langle \phi_\kappa(\vec{r}-\vec{r}_{jl}) \middle| \hat{H} \middle| \phi_{\kappa'}(\vec{r}-\vec{r}_{j'l'}) \right\rangle$ the terms involving an element of $\hat{H}$ centered on an atom different from the two atoms denoted by (j,l) and (j',l'). The second approximation consists in neglecting the interaction between atoms which are not nearest neighbors. The number of adjustable parameters (the on-site energies and the two-center integrals) depends on the size of the chosen orbitals basis. We now detail the chronology which has been driving to the use of the state-of-the-art $sp^3d^5s^*$ basis.

The first basis developed by Harrison[64] is formed by four Löwdin orbitals with s, p_x, p_y and p_z symmetry and requires nine different parameters. Fig. 2-10(a) shows the band structure of bulk GaAs calculated with this sp^3 model and the parameters of Chadi and Cohen[69]. The valence band features and the direct band gap energy are satisfactorily reproduced. The fact that the valence electrons for group-III and group-V atoms are only s or p explains this success. Nevertheless, the energies of the X and L conduction bands cannot be reproduced. The basis has been extended a first time by Vogl *et al.*[70] by adding an effective unoccupied orbital of s symmetry, called the s^* state. The sp^3s^* model requires thirteen parameters. As shown on Fig. 2-10(b), the energies of the X and L conduction band minima are correctly reproduced, but the effective mass at these points are still in poor agreement with experiments. The solution has been finally brought by Jancu *et al.* in 1998[71], who has completed the basis with the five d orbitals: d_{xy}, d_{yz}, d_{xz}, $d_{x^2-y^2}$, $d_{3z^2-r^2}$. The $sp^3d^5s^*$ model requires thirty-three parameters. The band structure of GaAs simulated with this model is shown on Fig. 2-10(c) and correctly reproduces both valence bands and conduction bands up to 10 eV above the Fermi level in the entire Brillouin zone.

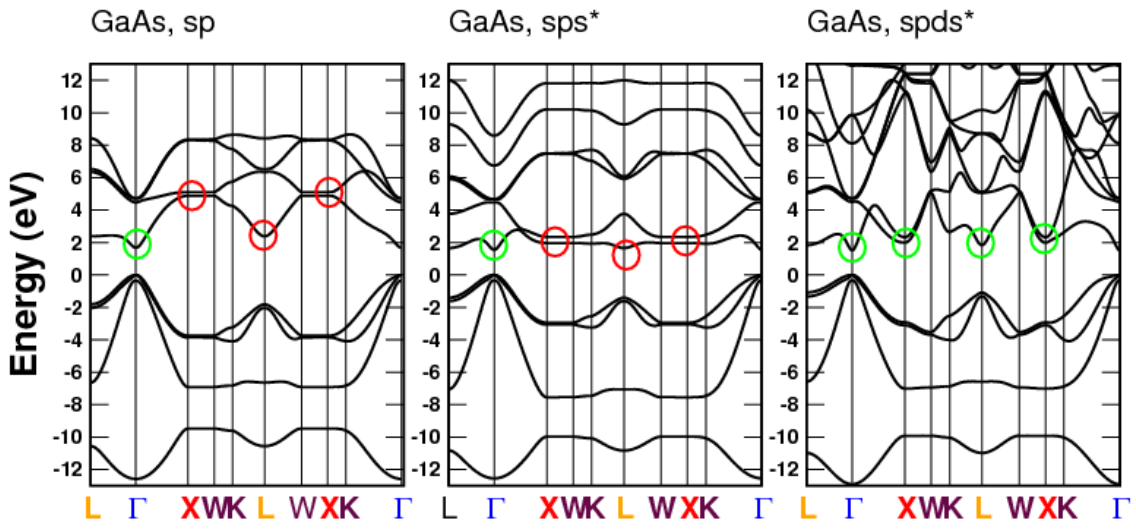

Fig. 2-10: Comparison of GaAs TB band structures obtained for various basis sizes: (a) sp^3, (b) sp^3s^*, (c) $sp^3d^5s^*$. Green and red circles indicate the correct and incorrect energy-band dispersion.

The determination of parameters has been performed by Jancu *et al.*[71]. The general idea is to start from the free electron band structure in an empty zinc-blende lattice. This band structure simply consists in the parabolic dispersion of the free electron which is folded in the first Brillouin zone of the zinc-blende structure. In this fictive structure, the on-site energies and the two-center integrals can be analytically determined. This set of parameters has then been derived to yield starting values in a fitting procedure of all binary III-V semiconductors. The results of Fig. 2-10 are given for the three basis sizes. In the sp^3 and sp^3s^* models, the conduction bands are very delocalized in the k-space (very localized in the real space). On the opposite, in the $sp^3d^5s^*$ model, the highest conduction bands do not strongly differ from the free electron structure. Obviously, this feature agrees with the pseudopotential picture where semiconductor highest conduction band structures display a nearly free-electron character and justify a posteriori the use of the empty lattice parameters set as starting values.

2.3.2 Heterostructures and strain

2.3.2.1 Heterostructures

One of the advantages of the TB method is that it can easily deal with heterostructures containing several semiconductors compounds. Nevertheless, the $sp^3d^5s^*$ model does not contains an energy reference which could be common to all the semiconductors. This is a result of the incompleteness of the $sp^3d^5s^*$ basis which neglect the interactions with the deep atomic

electronic states. These interactions would manifest mostly as a shift of the absolute energies of band extrema. Thus, it can be introduced by an additional parameter known as the unstrained valence band offset (VBO) which can be determined by experimental techniques such as X-ray photoemission spectroscopy (XPS) or by *ab initio* calculations[20,72–75]. The discrepancy between values reported in the literature shows the difficulty of the choice of relevant VBO. But we have to note that this difficulty is not inherent to the TB approach. For example, the same choice has to be made in the **k**·**p** parameterization and atomistic pseudopotentials.

Another general difficulty encountered in the modeling of heterostructures is the identification of the high symmetry points. In the case of a bulk material made of a zinc-blende III-V material, the primitive cell is rhomboedral and composed of two atoms (the anion A and the cation C) and the first Brillouin zone is that of Fig. 2-2(b) which is reproduced in Fig. 2-11(a) by blue lines. We now consider the simplest heterostructure made of the periodic stack represented on Fig. 2-11(b).

An alternation in the z direction of single monolayers of two different semiconductors (C_1A_1 and C_2A_2) is considered. The primitive cell is now tetragonal and contains eight atoms. The first Brillouin zone of this $(C_1A_1)_1/(C_2A_2)_1$ superlattice is shown in Fig. 2-11(b) by red lines. The X_Z point defined by the coordinates $\frac{2\pi}{a}(0,0,1)$ is outside the first Brillouin zone of the superlattice. But it can be merged with the Γ point of the upper adjacent Brillouin zone. This geometrical phenomenon named band folding, has major consequences on the results of band structure calculation and also optical activity. In this case, the study at the Γ point gives the electronic states related to both Γ and X_Z points of the original Brillouin zone.

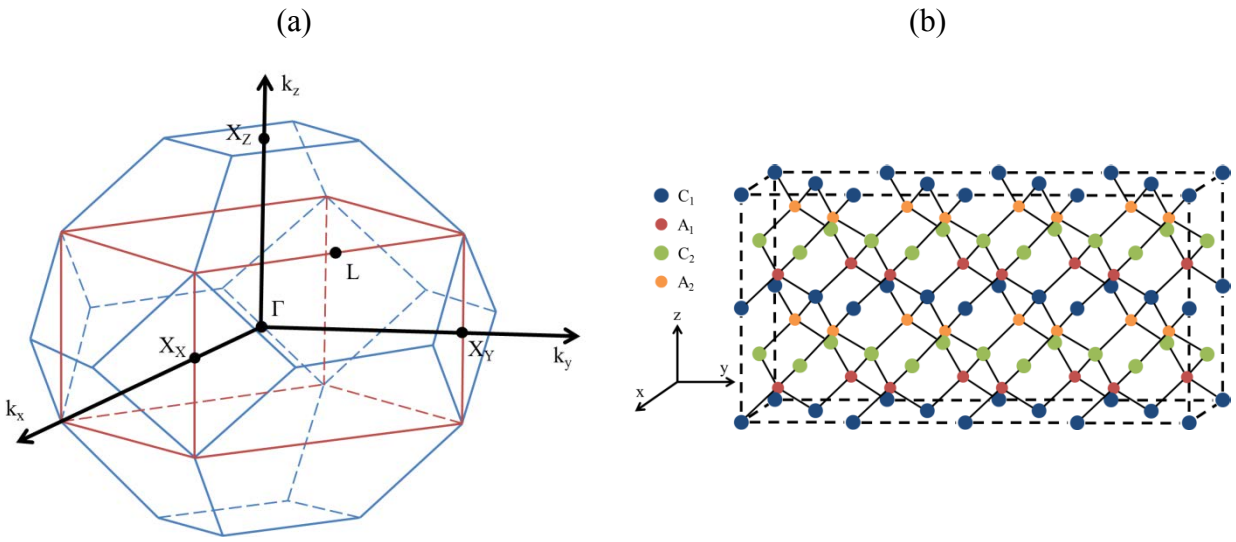

Fig. 2-11: (a) First Brillouin zone of the rhomboedral two atoms cell (blue lines) and first Brillouin zone of the superlattice $(C_1A_1)_1/(C_2A_2)_1$ shown in (b) (red lines).

2.3.2.2 Strain

Another important effect which has to be taken into account in the modeling of heterostuctures is the strain effect. We have seen in section 2.2.2 how strain can be considered in a macroscopic scale by the strain tensor and the deformation potential theory. In an atomistic method such as the TB approaches, these concepts are transferred to the atomistic scale by considering the variations of bond lengths and angles. A first prerequisite is thus to calculate these bond lengths and angles.

A first strategy consists in calculating the macroscopic strain tensor from the continuum elasticity theory and then to deduce the bond lengths and angles. Obviously, this approach neglect the local strain effects encountered in alloys or at interfaces of heterostructures. The second strategy uses an atomistic elasticity in which the elastic energy is described by two potentials V_1 and V_2 acting on bond lengths $\boldsymbol{R_{ij}}$ and bond angles Θ_{ijk}:

$$E = \sum_{i,\mathrm{j}} V_1 \boldsymbol{R_{ij}} + \sum_{i,j,k} V_2 \Theta_{ijk} \qquad \text{2-16}$$

The most commonly used potentials are Keating's potentials from the valence force field (VFF) model[76]. In its original version, the VFF model is defined by two constants often denoted α and β, which are defined to fit the macroscopic elastic constants. Nevertheless, we have seen in section 2.2.2.1 that in the zinc-blende structure, three elastic constants, namely C_{11}, C_{12} and C_{44}

are needed to define the elastic stiffness tensor. Thus, it is impossible to fit these three elastic constants with only two parameters. In the following, we use a traditional approach which consists in using the α, β parameters to reproduce the bulk elastic constants C_{11} and C_{12}, while committing a substantial error on the C_{44} value. This can be justified in our case because C_{44} is related to shear strain in [111] directions, while we are focusing exclusively on structures grown in the [001] direction. Even, for [001] grown QD, it has been demonstrated that this fitting procedure is the most relevant[77]. Nevertheless, we will keep in mind that it is not always true. For example, Niquet have chosen to fit the bulk modulus $K = \frac{(C_{11}+2C_{12})}{3}$ and C_{44} for his modeling of [111] nanowires[78]. Another solution is to extend the VFF model by adding terms related to bond stretch coupling, bond bending stretching coupling or highest order bond stretching terms[79,80]. It enables to reproduce additional features such as the dependence of the Young's modulus with pressure or to better simulate optical phonons dispersion.

Fig. 2-12 shows a comparison of bond lengths in a $(GaAs)_4/(GaP)_4$ superlattice grown on a GaP (001) substrate calculated by both LCE and VFF methods. Obviously, the values are constant with the LCE model, but we see that it is in satisfactory agreement with the VFF calculation excepting a slight discrepancy at the interfaces (below 0.08 %). This effect is also predicted by DFT calculations. This example shows that at least for two dimensional nanostructures, the LCE method can be efficiently used.

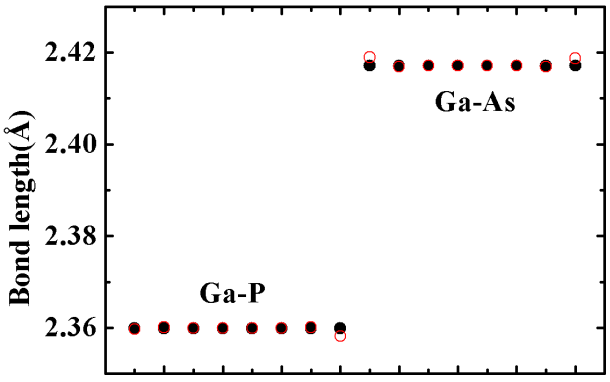

Fig. 2-12: Bond lengths in a $(GaAs)_4/(GaP)_4$ superlattice grown on GaP substrate calculated by the linear continuum elasticity (LCE) model (black filled circles) and the VFF model (red empty circles).

Knowing the relaxed bond lengths and angles, the TB parameters have to be adjusted. The bond angles distortions are incorporated in the phase factors of the Hamiltonian matrix

elements whereas the bond lengths are used to scale the two-center integrals using a generalization of the Harrison's law[64]:

$$ij\kappa(d) = ij\kappa(d_0)\left(\frac{d_0}{d}\right)^{n_{ij\kappa}} \qquad 2\text{-}17$$

where $ij\kappa = \left\langle \phi_\kappa(\vec{r}-\vec{r}_i)\middle|\hat{H}\middle|\phi_{\kappa'}(\vec{r}-\vec{r}_j)\right\rangle$ are the two-center integrals, d (d_0) is the strained (unstrained) bond length. In the original law of Harrison, the $n_{ij\kappa}$ exponents are taken equal to 2 from electrostatic considerations of the two-center integrals[64]. Here we use the values determined by Jancu *et al.* to fit the pressure dependent variation of high symmetry states[71].

2.3.3 Alloys

We have seen in a previous section how to find the TB parameters for bulk binary III-V compounds. We will now discuss the case of alloys. This section is exclusively devoted to "classical" alloys and we will deal with dilute nitrides in a next part.

A rigorous way to simulate alloys in the TB approach is to consider a supercell in which the atoms are randomly distributed. Obviously, the larger is the cell, the better is the description of local configurations variety, and the larger is the number of exact compositions really accessible. Contrary to *ab initio* approaches, the TB method is able to deal with supercells of million atoms. Nevertheless we try to limit their use as much as possible because it creates complications. Firstly, the c.p.u. time increases with the number of atoms. Secondly, a large cell induces a reduced Brillouin zone and consequently the interpretation of the folded band structure is difficult. To illustrate the last point, one can imagine an indirect band gap semiconductor with an X conduction-band-minimum. If one uses a very large supercell, many points in the [100] direction, whose energy is smaller than the Γ-conduction band minimum, are folded onto the Γ point. Thus, in order to yield a correct direct band gap energy and reproduce the true Γ states, a large number of eigenvalues are needed. The determination of effective masses is also complicated by this phenomenon. Obviously, solutions exist to circumvent this difficulty such as the careful analysis of the wave function associated with each state (a Γ and X conduction state can be distinguished by the weight of the *s*, *p* and *d* orbitals) or the calculation of the optical oscillator strength related to each transition. Unfolding is also possible by appropriate methods[81]

such as the majority representation method of A. Zunger[82] but it has not been implemented in the TB code yet.

We aim at providing a simpler and quicker tool, compatible with modeling of complex structures. Using a linear interpolation between the parameters of the binary compounds composing the alloy can be a first step. But, obviously it cannot reproduce the experimental band gap bowings. The strategy developed in this thesis is to model alloys by a linear interpolation of all TB parameters but allowing for a parabolic contribution of the relevant parameters (the on-site energies and the two-center integrals between *s* orbitals and between *p* orbitals). This results in six different bowing parameters. Fig. 2-13 demonstrates an excellent agreement between the direct and indirect band gaps of ternary AlGaAs calculated with this method and the experimental values given by Vurgaftman[20]. We have also shown the calculation of the first transition energy at the Γ point calculated with a randomly distributed cell containing 64-atoms. This is again a good justification for the interpolated method.

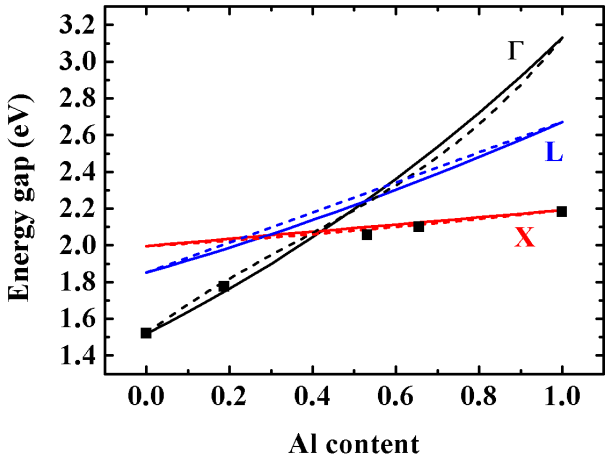

Fig. 2-13: Direct and indirect band gaps of the AlGaAs alloy as a function of Al content. Solid lines represent the calculation made with the TB model and the interpolated TB parameters procedure. Dashed lines represent the band gaps with the bowing parameters of Vurgaftman[20]. Black points show the first transition calculated with a 64-atoms supercell at the Γ point of the supercell Brillouin zone. In the composition range where the alloy is direct, this transition corresponds to the direct band gap, whereas it corresponds to the X indirect band gag in the composition range where the alloy is indirect, due to band folding.

We would like to point out that these bowing parameters are not completely independent from a material to the other. Indeed, the bowing parameters have been originally defined for each atom. This important feature enables us to reproduce all ternary alloys including Al, Ga, In, P, As, and Sb atoms, with only six bowing parameters per atoms. Moreover, quaternary and quinary

can also be modeled without changing the parameters. Fig. 2-14 shows the direct band gap of the AlGaInAs alloy for compositions supplying lattice-matching to InP substrate. Again, the agreement with the experimental values given by Vurgaftman[20] is very good.

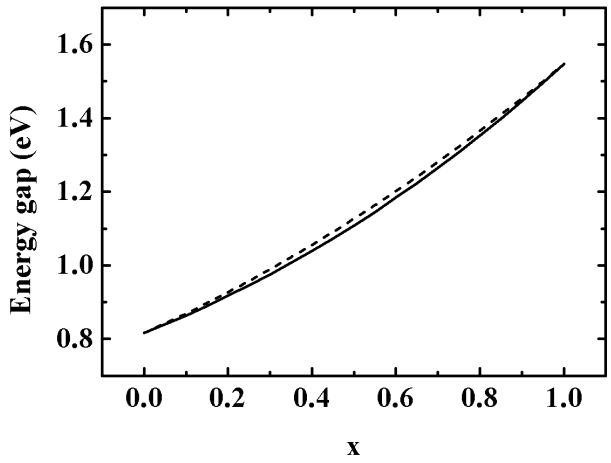

Fig. 2-14: Direct band gap of $(Ga_{0.47}In_{0.53}As)_{1-x}(Al_{0.48}In_{0.52}As)_x$ quaternary alloy lattice matched to InP, calculated with the interpolated TB model (solid lines) and from Vurgaftman[20] (dashed lines).

One may be tempted to criticize the large number of parameters in our model (8 on-site energies, 21 two-center integrals, 12 strain parameters and 6 bowing parameters), but it is important to mention that their values are all compatible with the physical origin of these parameters and are easily transferable between common-anion or common-cation compounds.

2.4 Simulation of QW/QD nanostructures

We now deal with the modeling of nanostructures. Before presenting in chapters 3 and 4 results on (GaAsP(N)/GaP QW, InGaAs/GaP QD), the TB model must be validated on benchmark structures.

2.4.1 2D nanostructures: superlattices and quantum wells

$(GaAs)_n/(AlAs)_n$ [001] superlattices grown lattice-matched on GaAs substrate provide a stringent test for evaluating the performance of *ab initio* and empirical approaches because the conduction-band minimum (CBM) occurs at different k-points other than Γ as function of period n. The unit cell for n=2 is shown in Fig. 2-15(a). The slight strain in AlAs is calculated with the LCE model. The VBO between GaAs and AlAs is taken from recent *ab initio* calculations[75]. The on-site energies are shifted in accordance with this VBO except for the As atoms at the interfaces

which are shifted by a half of the VBO because these atoms are involved in both Ga-As and Al-As bonds. The calculated band structure is shown in Fig. 2-15(b). The results are in excellent agreement with both pseudo-potentials calculations and experimental data as shown by the values of energy gaps summarized in Table 2-4.

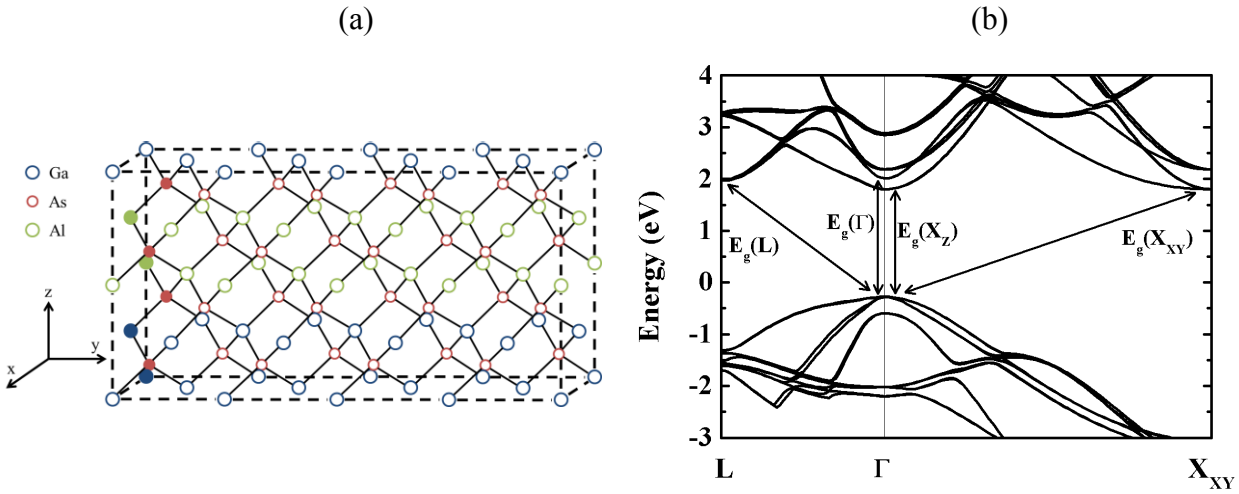

Fig. 2-15: (a) $(GaAs)_2/(AlAs)_2$ [001] superlattice. The atoms of the unit cell are filled. (b) TB calculation of the band structure.

	TB	EPM	Experimental		TB	EPM	Experimental
$E_g(\Gamma)$ (eV)	2.281	2.15	2.3	$E_g(X_{XY})$ (eV)	2.072	2.10	2.066
$E_g(L)$ (eV)	2.241	2.25		$E_g(X_Z)$ (eV)	2.071	2.10	2.082

Table 2-4: Direct and indirect band gap energies for $(GaAs)_2/(AlAs)_2$ superlattice. EPM results are taken from Ref. 5 and experimental data from Ref. 83,84.

QW can be simulated in the same way, with a large number of monolayers in the barrier. We present the simulation of a 8 nm thick GaAs QW embedded in $Al_{0.2}Ga_{0.8}As$ barriers. A $(GaAs)_{28}/(Al_{0.2}Ga_{0.8}As)_{40}$ superlattice is created and the first conduction and valence states at the Γ point are calculated. This structure is direct and type-I and can also be calculated with the eight-band **k·p** model. The values found by both methods are reported in Table 2-5 and are found in very good agreement. The charge densities are also presented.

	k·p	TB	TB square wave function		**k·p**	TB	TB square wave function
e2	1.625	1.637	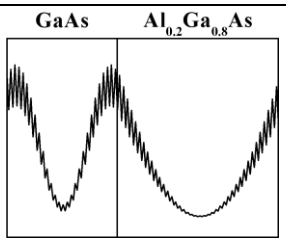	hh2	-0.045	-0.048	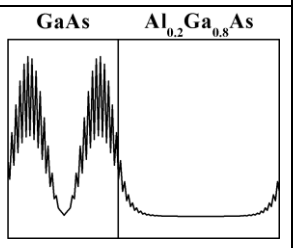
e1	1.551	1.552	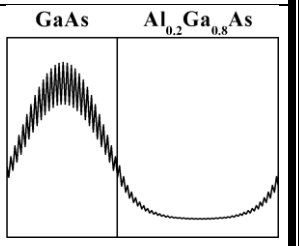	hh3	-0.098	-0.100	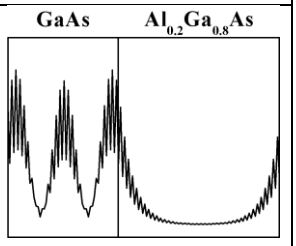
hh1	-0.010	-0.012	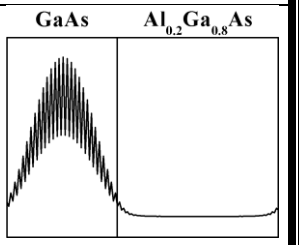	lh2	-0.106	-0.106	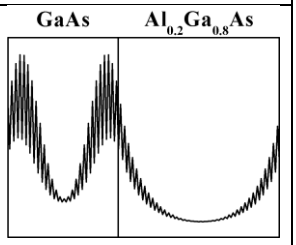
lh1	-0.031	-0.030	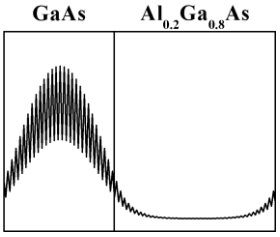				

Table 2-5: Energies in eV of the (doubly degenerated due to spin) confined electron and hole states in a $GaAs/Al_{0.2}Ga_{0.8}As$ QW calculated by both k·p and TB models. 0 eV corresponds to the VBM of unstrained bulk GaAs.

2.4.2 0D nanostructures: embedded quantum dot

The simulation of III-V QD adds another difficulty because the translation symmetry is broken in the three dimensions. Thus, unless carefully considering the effects of rotation symmetry, the entire volume of the dot has to be simulated. The dimensions of such a system are about few nm in height and a few 10 nm in diameter corresponding to a total of a few 10^5 atoms. Moreover, these QDs are embedded in a barrier material which has to be considered in the simulation, leading to a cell size of about millions of atoms. Dealing with such a high number of atoms has been possible for a few years thanks to the huge advances in parallel computing. The group of G. Klimeck is developing a software tool namely NEMO3D and NEMO5 based on a

$sp^3d^5s^*$ TB model which simulate systems up to 10^8 atoms running in parallel architectures with 100,000 cores[8,85]. In this thesis, we have used a supercell TB code developed through a collaboration with M. Nestoklon from the Ioffe Institute and R. Benchamekh, L. Bernardi and P. Voisin from the LPN (Laboratoire de Photonique et de Nanostructures). This code has been here tested, for the first time for structures of million atoms.

2.4.2.1 Numerical aspects

An initial cell is first built with all atoms, regularly placed on the sites of an unstrained zinc blende structure with the substrate lattice constant. The atomic positions are then relaxed with the VFF method. The boundary conditions are guaranteed by periodic conditions on the three supercell basis vectors. To model the strain imposed by the substrate, the two in-plane supercell basis vectors are set fixed during the VFF relaxation. Only the third out-of-plane vector is able to relax. The elastic strain is minimized through a conjugate gradient algorithm with the atomic positions being the variables.

The TB Hamiltonian is then created. In the $sp^3d^5s^*$ basis, each atom is described by 20x2 orbitals (with the factor 2 for the spin). Thus, the size of the matrix for a N-atom supercell is 40N-by-40N. For a supercell of million atoms, manipulating and stocking such a large matrix would be problematic. But, thanks to the nearest neighbors' approximation, most of the matrix elements are zero. The numerical problem consists thus in finding the eigenvalues and the eigenvectors of a sparse matrix. Obviously, diagonalizing the matrix to find all the eigenvalues is often unnecessary and time-consuming. Instead, the lowest eigenvalues are found with a Lanczos algorithm[86]. In a band structure problem, the eigenvalues of interest are at energies around the band gap rather than the lowest eigenvalues. Nevertheless, finding the eigenvalues of the matrix H around a given energy E_{ref} can be reduced to finding the lowest eigenvalues of the matrix $(H-E_{ref})^2$. This technique is called the folded spectrum method[7,87]. Other similar techniques can be used such as the shift inverse method.

Using this code, we have been able to calculate the electronic band structure of a supercell with a number of atoms up to 1,073,741 atoms. It is important to mention that this upper limit is not due to memory overflow, but rather to some mathematical libraries that have

not been intended to manipulate 64-bit integers. This issue should be resolved soon, but 1,073,741 atoms are enough to model a relatively small QD with its barrier.

2.4.2.2 Test on an InAs/InP QD

A cone-shape InAs/InP QD is chosen as a test structure and results are compared with an eight-band **k·p** simulation. The height of the QD is 6 lattice constants (about 3.5 nm) and the diameter is 42 lattice constants (about 25 nm).

a) Strain calculation

The VFF result is compared with the strain calculation performed with the LCE and finite element method. It is convenient to do this comparison with the strain tensor elements language. Thus, the atomic positions have to be linked to a local strain tensor. This is performed with the method of Pryor *et al.*[88]: for each atom, the distorted edges of the tetrahedron formed by its four nearest neighbors are calculated and compared to the unstrained case to deduce the local strain tensor. The strain components $\varepsilon_{hydro} = \varepsilon_{xx} + \varepsilon_{yy} + \varepsilon_{zz}$ and $\varepsilon_{biax} = 0.5(\varepsilon_{xx} + \varepsilon_{yy}) - \varepsilon_{zz}$ are shown on Fig. 2-16 along the [001] direction through the cone tip.

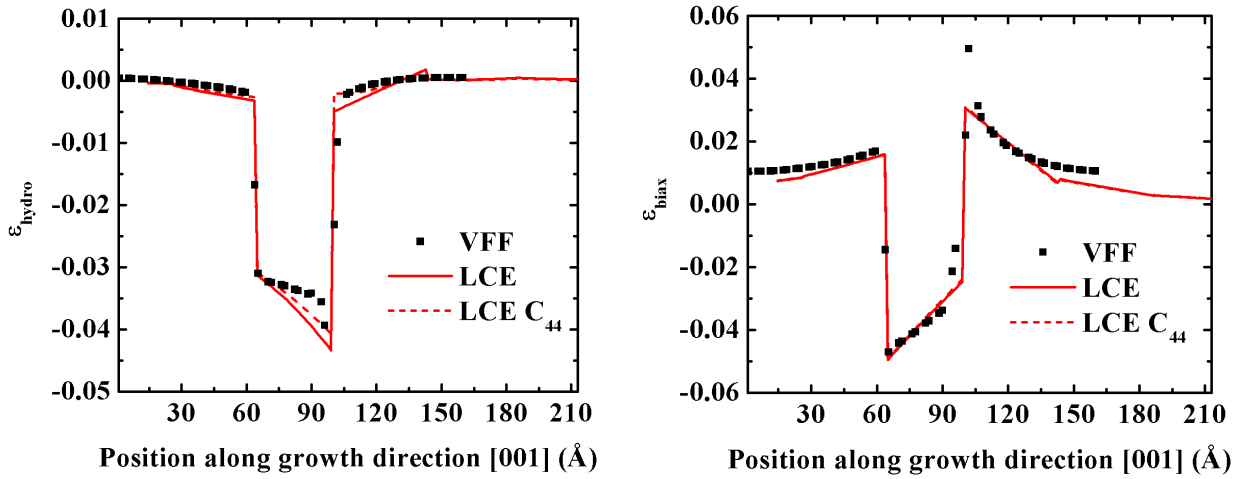

Fig. 2-16: Hydrostatic and biaxial part of the strain in a cone shape InAs/InP QD along the [001] direction through the tip.

Both models are in qualitative agreement, but the discrepancies may be due to various reasons. First, we have shown in section 2.3.2.2, that in the traditional VFF model, C_{44} cannot be fitted by the VFF parameters. For InAs and InP, the underestimation of C_{44} by the VFF model is 18 % and 15 % respectively. These are actually the worst cases compared to other

semiconductors[89]. The calculation with the LCE method with the incorrect value of C_{44} (given by the VFF) is shown on Fig. 2-16 and provide a better agreement with the VFF at least for the hydrostatic part. Secondly, contrary to the VFF model, the LCE does not match with strain at interfaces[88]. Moreover, the situation at the cone tip is the worst case because the strain components analytically diverge in the LCE theory[89]. Thirdly, the LCE assume a linear regime which is true only for infinitesimal strain[89]. Fourthly, for the LCE simulation, an axial approximation is used[90], to keep a $C_{\infty v}$ symmetry even for the deformed QD. Obviously, this $C_{\infty v}$ does not match with the zinc-blende structure, but this approximation will turn out to be very useful in the next section when the electronic band structure with the eight-band **k**·**p** model will be calculated. Finally, it is worth pointing out that the boundary conditions are different for both models. In the LCE simulation, the lower boundary of the calculation box is set displacements fixed to reproduce the substrate whereas the upper limit is set stress free and is thus able to deform (see Fig. 2-17(a)). In the VFF model, the boundary conditions are less realistic and are defined by periodic conditions on the three supercell basis vectors. The two in-plane vectors are set fixed during the relaxation whereas the out-of-plane vector is free to relax (see Fig. 2-17(b)). Because the strain field is relatively long range the size of the supercell must be checked to avoid a strain-induced coupling with the QD of adjacent supercells. Lee *et al.* have demonstrated that the buffer thicknesses (below and above the QD) have to be at least as large as the QD height[91]. This condition is fulfilled here (1.8 times the QD height) and we can check that the hydrostatic strain is converging to zero at the interfaces.

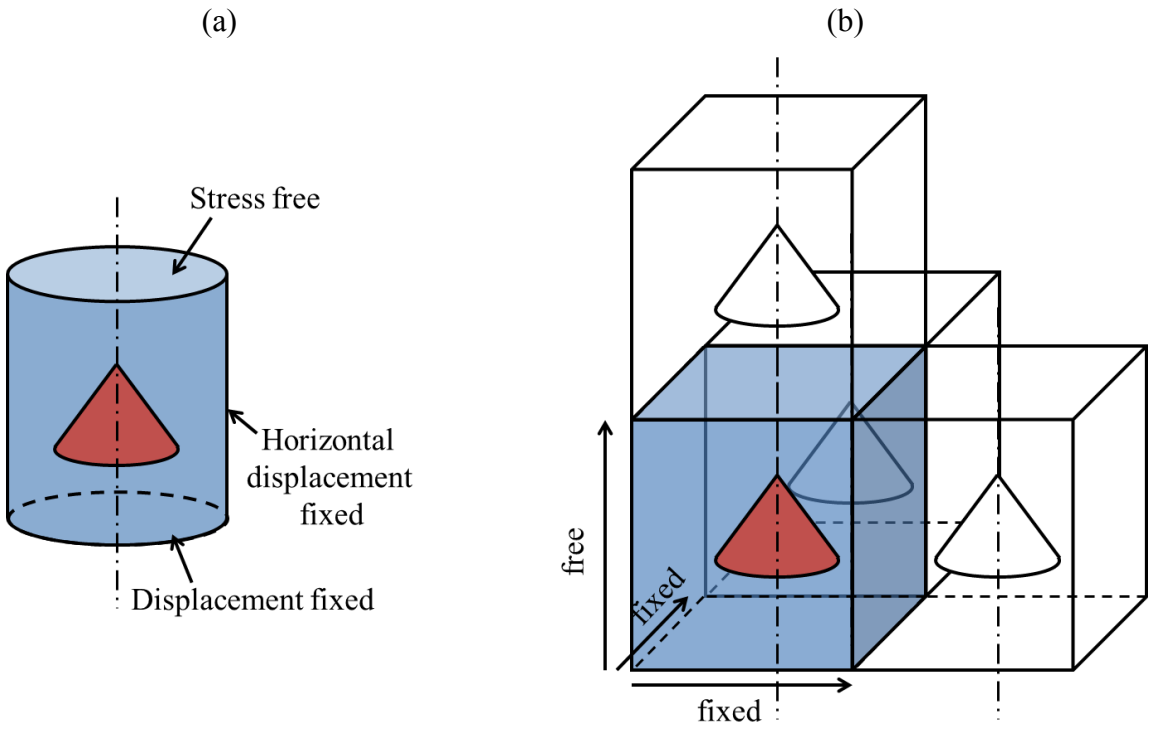

Fig. 2-17: Boundary conditions for the strain calculation in our (a) LCE model and (b) VFF model.

Keeping in mind that none of both models is ideal, we estimate that the present strain simulation is relevant and provides an excellent input for the calculation of the electronic band structure of InAs/InP QDs.

b) Electronic band structure

In this section we compare the results given by the TB model and the eight-band **k·p** model. Because this **k·p** model will also be used in chapter 4, we are now briefly presenting its specificities.

*i. The axial approximation for the 8-band **k·p** model*

For readers interested in the **k·p** theory, wide descriptions of the method can be found in the complete references (Chuang[21] or Fishman[92]). In the case of nanostructures, the elements of the **k·p** Hamiltonian depend on the spatial coordinates. For QD, tri-dimensional solving is required. Nevertheless, it has been shown that the problem can be considerably simplified using an axial symmetry[93,94]. Using the cylindrical coordinates (r,φ,z), the problem is now bi-dimensional (only depending on r and z). This assume that all the components are invariant through the rotation around the [001] axis. Two approximations are needed to conserve

this $C_{\infty v}$ symmetry. The first one has been mentioned in the previous section and consists in replacing the elastic moduli $C_{66} = C_{44}$ by an effective modulus $\overline{C}$ in the expression of the elastic stiffness tensor obtained by an arbitrary rotation around the *z* axis[90,94].

$$\overline{\overline{C}} = \begin{pmatrix} C'_{11} & C'_{12} & C_{12} & 0 & 0 & 0 \\ C'_{12} & C'_{11} & C_{12} & 0 & 0 & 0 \\ C_{12} & C_{12} & C_{11} & 0 & 0 & 0 \\ 0 & 0 & 0 & C_{44} & 0 & 0 \\ 0 & 0 & 0 & 0 & C_{44} & 0 \\ 0 & 0 & 0 & 0 & 0 & \overline{C} \end{pmatrix} \qquad \text{2-18}$$

with $C'_{11} = \frac{C_{11} + C_{12}}{2} + \overline{C}$, $C'_{12} = \frac{C_{11} + C_{12}}{2} - \overline{C}$ and $\overline{C} = \frac{C_{11} - C_{12}}{2} + \left(C_{44} - \frac{C_{11} - C_{12}}{2} \right) d$.

The second approximation is on the shear deformation term in the Bir Pikus Hamiltonian (R_ε in the notation of Chuang[21]). The Hamiltonian is kept in a block diagonal form by replacing in R_ε the deformation potentials *b* and *d* by a mean value[94]. It has been demonstrated that this approximation provides satisfactory results for QD systems where a conic geometry can be assumed (InAs/InP (001)[95], InAsSb/GaAsSb[96]).

ii. Results

The first four confined electron and hole levels calculated by both methods are presented on Table 2-6. The energies of the electron levels are found to be in excellent agreement. A slight discrepancy (19 meV) is found for the first hole level. We attribute this difference to the approximations related to the **k**·**p** method and the slight difference in the calculation of strain, as discussed previously. It is important to mention that the nature of the states is also in perfect agreement, with a first electron confined state with S symmetry (e1), followed by the two states with P symmetry (e2 and e3) and states with D symmetry (e4 and upper states which are not shown here). The same order is found for the first hole states which are majoritarily HH. Finally, our results are also in good agreement with the TB calculation of Zieliński, who has simulated a QD with the same dimensions but with a lens shape[77,97].

	k·p	TB	TB square wave function		**k·p**	TB	TB square wave function
e4	1.010	1.012	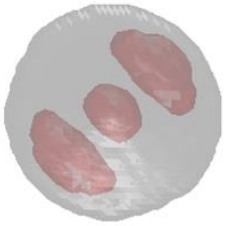	hh1	-0.049	-0.068	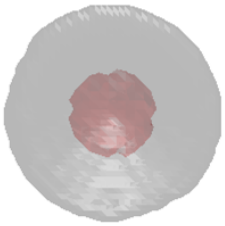
e3	0.948	0.954	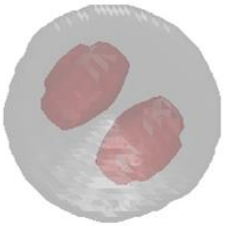	hh2	-0.080	-0.093	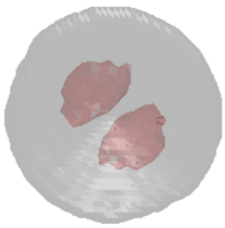
e2	0.947	0.950	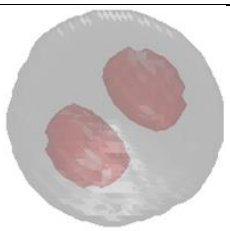	hh3	-0.081	-0.094	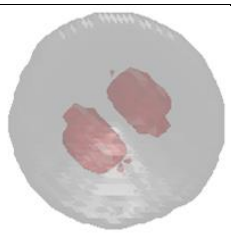
e1	0.876	0.878	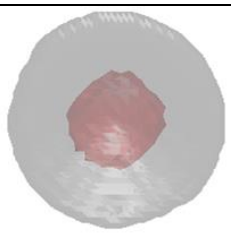	hh4	-0.104	-0.108	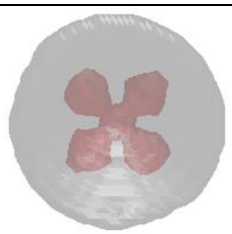

Table 2-6: Energies in eVof the first four (doubly degenerated due to spin) confined electron and hole states in a InAs/InP QD calculated by both k·p and TB models. 0 eV corresponds to the VBM of unstrained bulk InAs. 80 % of the electronic probability density is inside the red surface.

2.5 Dilute nitrides

In section 2.3.3, we have presented an interpolation method for modeling the TB parameters of alloys. This is justified when atoms are similar. But nitrogen is different both in size and electronegativity from other usual anions (e.g. As) and consequently the scheme of section 2.3.3 does not apply for III-V-N . Resorting to supercells seems to be inescapable. Nevertheless, a simpler strategy, proposed by Shtinkov *et al.*[98], consists in adding a s_N orbital to the TB basis. This state represents a nitrogen-related level with a spherical symmetry consistent with the EPM calculations of Kent and Zunger[53]. Because nitrogen essentially affects the Γ

conduction band, the more relevant two-center parameter is $s_c s_N \sigma$ which describes the interaction of the additional N-related anion orbital with the nearest cation *s* orbitals. All the other additional two-center parameters are set to zero. The interest of this approximation is that one can model a dilute nitride from the same TB parameters than the host material with only two additional parameters: the energy of the s_N state, E_s^N and the coupling parameter $s_c s_N \sigma$. In this way, it is very similar to the two-level BAC model, but with the additional advantage of providing a description of the band structure in the entire Brillouin zone.

E_s^N is set with regard to VBO to fix the position of the nitrogen level independent of the host material[75]. $s_c s_N \sigma$ is chosen to match results with E_+ and E_- transitions in the BAC model, which are known to fit well with experimental data[20]. For example, the parameters for GaAsN and GaPN are set to:

$$E_s^N = 1.65 \text{ eV and } s_c s_N \sigma = -1.04\sqrt{x} \text{ eV for } GaAs_{1-x}N_x$$

$$E_s^N = 2.19 \text{ eV and } s_c s_N \sigma = -1.09\sqrt{x} \text{ eV for } GaP_{1-x}N_x$$

The $s_c s_N \sigma$ parameter is found to have a very similar value in both GaAsN and GaPN, which is not surprising because, in both cases, it represents the coupling between the anion N-related orbital and the Ga nearest neighbors' *s*-orbitals.

Fig. 2-18(a) represents the band structure of bulk GaPN calculated with the present model. For an infinitesimally low N composition, the band structure consists in the band structure of bulk GaP and a N-localized level located just below the CBM. When increasing N content, this N-level evolves toward a partially delocalized conduction band with a CBM at the Γ point. The GaP Γ point is shifted up as predicted by the BAC model. For GaAsN (Fig. 2-18(b)), the N-level is just above the CBM of GaAs. Consequently, the CBM of GaAsN evolves from the GaAs CBM. For both cases, the valence bands and the X conduction-band valleys are not affected by nitrogen because of symmetry reasons. On the opposite, the L-derived states are slightly affected. Turcotte *et al.*[99,100] have shown that these behaviors are consistent with spectroscopic ellipsometry measurements of E_1 and E_2 critical points[101].

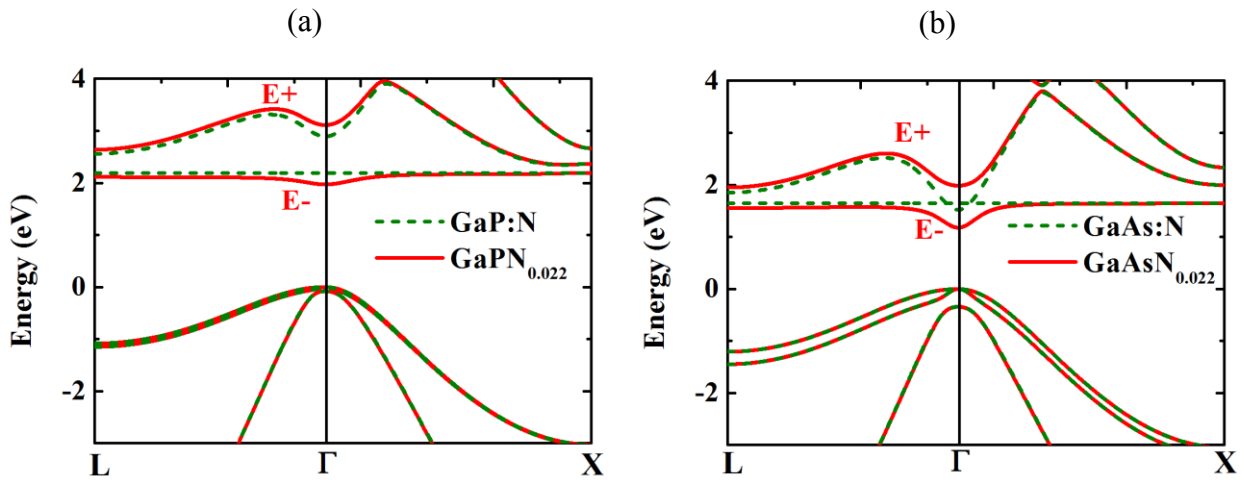

Fig. 2-18: Band structure of (a) GaPN and (b) GaAsN calculated with the $sp^3d^5s^*s_N$ model for N content of 2.2 % (red solid lines) and infinitesimally low (green dashed lines).

Fig. 2-19 shows the first (Γ_-) and second (Γ_+) direct transitions of GaPN and GaAsN calculated with the $sp^3d^5s^*s_N$ TB model. It perfectly reproduces the BAC results which are known to fit with experimental data[45].

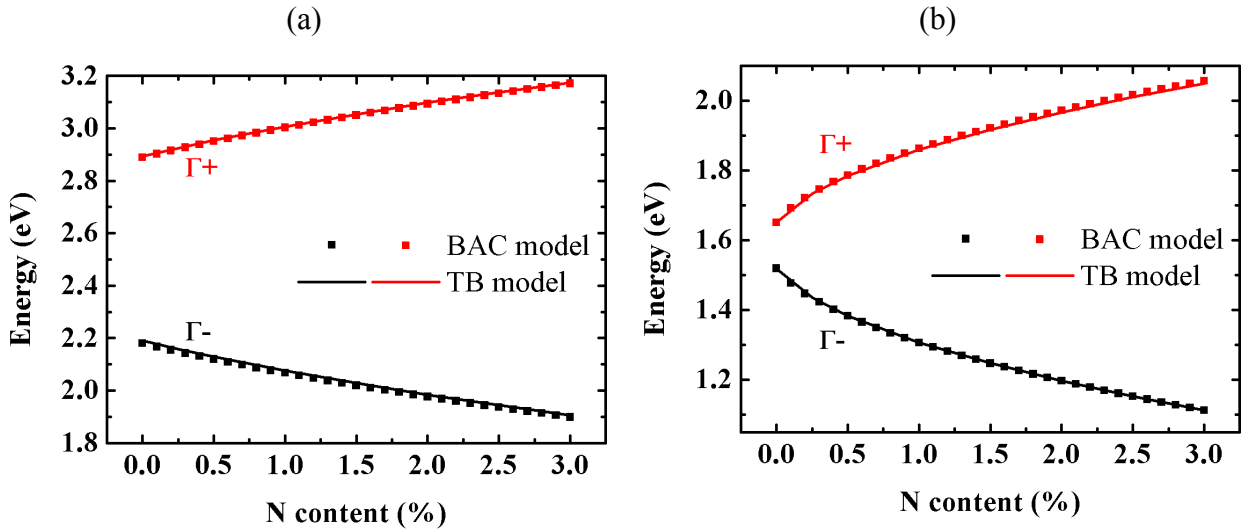

Fig. 2-19: First and second direct transitions of bulk (a) GaPN and (b) GaAsN as a function of N content calculated with the $sp^3d^5s^*s_N$ TB model. The values obtained with the 2-level BAC are shown for comparison. The BAC parameters are taken from Ref. 45.

2.6 Optical properties

2.6.1 Coupling to an electromagnetic field

When a semiconductor is illuminated with light, the Hamiltonian can be written:

$$H \simeq H_0 + H' = \frac{\boldsymbol{p}^2}{2m_0} + V(\boldsymbol{r}) - \frac{e}{m_0}\boldsymbol{A}\cdot\boldsymbol{p} \qquad 2\text{-}19$$

where $H' = -\frac{e}{m_0}\boldsymbol{A}\cdot\boldsymbol{p}$ is the light-induced perturbed term, $\boldsymbol{A}$ is electromagnetic vector potential and $\boldsymbol{p}$ the momentum operator. Please note that the highest order term in $\boldsymbol{A}^2$ is neglected because it is often much smaller than the linear term in $\boldsymbol{A}$. A prerequisite to the calculation of optical properties is to know the $H'_{vc}(\boldsymbol{k}) = \langle \psi_v(\boldsymbol{r},\boldsymbol{k}) | H'(\boldsymbol{r},\boldsymbol{k}) | \psi_c(\boldsymbol{r},\boldsymbol{k}) \rangle$ matrix elements. This term can be written by:

$$H'_{vc}(\boldsymbol{k}) = -\frac{e}{m_0}\boldsymbol{A}\cdot\langle \psi_v(\boldsymbol{r},\boldsymbol{k}) | \boldsymbol{p} | \psi_c(\boldsymbol{r},\boldsymbol{k}) \rangle \qquad 2\text{-}20$$

in which $\boldsymbol{p}_{vc}(\boldsymbol{k}) = \langle \psi_v(\boldsymbol{r},\boldsymbol{k}) | \boldsymbol{p} | \psi_c(\boldsymbol{r},\boldsymbol{k}) \rangle$ is called the momentum matrix element. It can be shown that $\boldsymbol{p}_{vc}(\boldsymbol{k})$ can be written by[102]:

$$\boldsymbol{p}_{vc}(\boldsymbol{k}) = \frac{m_0}{i\hbar}\langle \psi_v(\boldsymbol{r},\boldsymbol{k}) | \nabla_{\boldsymbol{k}} H(\boldsymbol{k}) | \psi_c(\boldsymbol{r},\boldsymbol{k}) \rangle \qquad 2\text{-}21$$

Thus, the momentum matrix elements can be calculated using a k-derivation of the TB Hamiltonian[103]. From Eq. 2-15, it is obvious that $\boldsymbol{p}_{vc}(\boldsymbol{k})$ can be finally written by:

$$\boldsymbol{p}_{vc}(\boldsymbol{k}) = \frac{1}{N}\frac{m_0}{\hbar}\sum_{j,j'} e^{i\boldsymbol{k}(\boldsymbol{r}_{jl}-\boldsymbol{r}_{j'l'})}(\boldsymbol{r}_{jl}-\boldsymbol{r}_{j'l'})\langle \phi_\kappa(\boldsymbol{r}-\boldsymbol{r}_{jl}) | \hat{H} | \phi_{\kappa'}(\boldsymbol{r}-\boldsymbol{r}_{j'l'}) \rangle \qquad 2\text{-}22$$

It is worth mentioning that these momentum matrix elements can be calculated without adding any new parameters.

Another common quantity is the dimensionless oscillator strength that can be written as a function of the direction of the optical field:

$$f(\hat{e}) = \frac{2}{m_0} \frac{\left|\hat{e} \cdot \boldsymbol{p}_{vc}(\boldsymbol{k})\right|^2}{\left(E_c(\boldsymbol{k}) - E_v(\boldsymbol{k})\right)} \qquad 2\text{-}23$$

where $\hat{e}$ is a unit vector in the direction of the optical electric field and $E_v(\boldsymbol{k})$ and $E_c(\boldsymbol{k})$ are the energies of the initial and final states.

2.6.2 Absorption in a bulk semiconductor

An electron initially at state $E_v(\boldsymbol{k})$ can be promoted at state $E_c(\boldsymbol{k})$ with the absorption of a photon of energy E at a transition rate given by the Fermi's golden rule:

$$W_{cv}(E, \boldsymbol{k}) = \frac{2\pi}{\hbar} \left|H'_{vc}(\boldsymbol{k})\right|^2 \delta\left(E_c(\boldsymbol{k}) - E_v(\boldsymbol{k}) - E\right) \qquad 2\text{-}24$$

Only transitions between an initial state and a final state with the same $\boldsymbol{k}$ are considered because the photon has negligible wave vector amplitude. The absorption is then given by summing on $\boldsymbol{k}$, all the transition rates:

$$\alpha(E) = \frac{\pi \hbar e^2}{n_r c \varepsilon_0 m_0{}^2 E} \int \frac{d^3k}{(2\pi)^3} \left|\hat{e} \cdot \boldsymbol{p}_{vc}(\boldsymbol{k})\right|^2 \delta\left(E_c(\boldsymbol{k}) - E_v(\boldsymbol{k}) - E\right)\left(f_v - f_c\right) \qquad 2\text{-}25$$

where n_r is the static refractive index. f_v and f_c are the occupation functions of the valence and conduction states. At the thermodynamic equilibrium and at 0 K, the valence bands are completely occupied ($f_v = 1$) and the conduction bands are completely empty ($f_c = 0$). In practice, the integral is transformed into a finite sum. The Brillouin zone is meshed into 10000 $\boldsymbol{k}$ points and the Dirac function is replaced by a Gaussian broadening in order to get a smooth spectrum. The absorption spectrum is finally given by:

$$\alpha(E) = \frac{\pi \hbar e^2}{n_r c \varepsilon_0 m_0{}^2 E} \sum_{v,c,k} \frac{\Delta^3 k}{(2\pi)^3} \left|\hat{e} \cdot \boldsymbol{p}_{vc}(\boldsymbol{k})\right|^2 \frac{1}{\sigma\sqrt{2\pi}} \exp\left(-\frac{\left(E_c(\boldsymbol{k}) - E_v(\boldsymbol{k}) - E\right)^2}{2\sigma^2}\right) \qquad 2\text{-}26$$

where $\sigma = 5$ meV is the Gaussian broadening.

Fig. 2-20 shows the calculated absorption spectrum of bulk GaAs at 0 K. It shows a good agreement with experiment at 300 K. The slight discrepancy can be explained by the difference in temperature which results in both red-shifting and broadening of the absorption spectrum at 300 K.

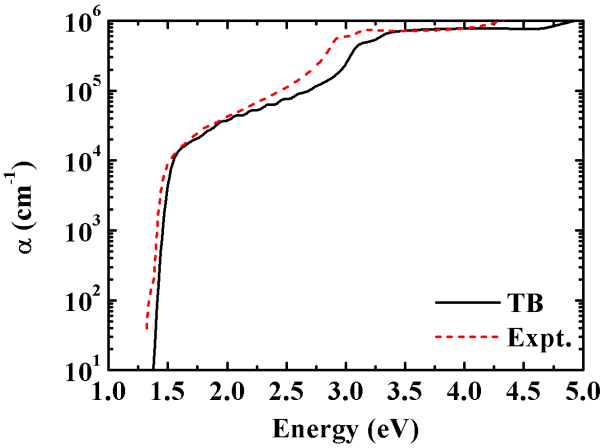

Fig. 2-20: Absorption of bulk GaAs calculated with the TB model (black solid line) at 0 K and experimental data (red dashed line) at 300 K from Ref. 104,105.

2.6.3 Complex dielectric function

In the same way, the complex dielectric function $\varepsilon = \varepsilon_0(\varepsilon_r + i\varepsilon_i)$ can be calculated. The imaginary part can be written by:

$$\varepsilon_i(E) = \frac{1}{4\pi\varepsilon_0}\left(\frac{2\pi\hbar e}{m_0 E}\right)^2 \int \frac{d^3k}{(2\pi)^3} \left|\hat{e}\cdot \boldsymbol{p}_{vc}(\boldsymbol{k})\right|^2 \delta\left(E_c(\boldsymbol{k}) - E_v(\boldsymbol{k}) - E\right) \qquad 2\text{-}27$$

The real part can then be deduced from the Kramers-Kronig relation:

$$\varepsilon_r(E) = 1 + \frac{4\pi e^2}{4\pi\varepsilon_0 m_0} \int \frac{d^3k}{(2\pi)^3} \frac{2\hbar^2}{m_0(E_c(\boldsymbol{k}) - E_v(\boldsymbol{k}))} \frac{\left|\hat{e}\cdot \boldsymbol{p}_{vc}(\boldsymbol{k})\right|^2}{(E_c(\boldsymbol{k}) - E_v(\boldsymbol{k}))^2 - E^2} \qquad 2\text{-}28$$

The refractive index is calculated by:

$$n = \left(\frac{\left(\varepsilon_r^{\,2} + \varepsilon_i^{\,2}\right)^{\frac{1}{2}} + \varepsilon_r}{2}\right)^{\frac{1}{2}} \qquad 2\text{-}29$$

The comparison with experimental data is shown in Fig. 2-21. A significant discrepancy appears above 4 eV which is due to the fact that excitonic effects are not taken into account in

this TB model[106]. Nevertheless, the calculation of the refractive index in the transparent region ($n \simeq \sqrt{\varepsilon_r}$), which is of great interest for the design of our laser structure, agrees very well with experimental measurements.

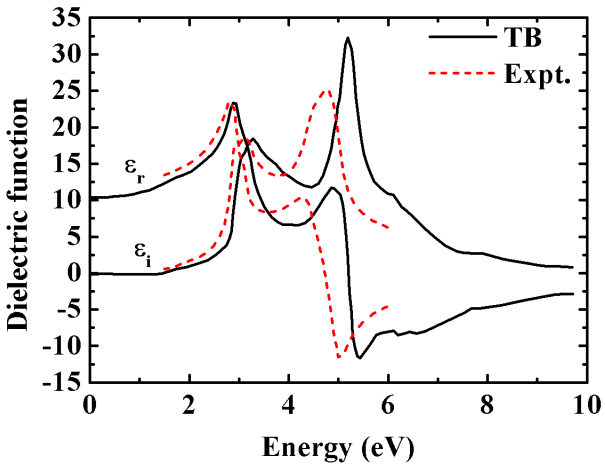

Fig. 2-21: Real and imaginary part of the dielectric function of bulk GaAs calculated with the TB model (black solid line) at 0 K and experimental data (red dashed line) at 300 K from Ref. 104.

2.6.4 Gain spectrum

The calculation of the gain spectrum is very similar to the absorption:

$$g(E) = C_0 \int \frac{d^3k}{(2\pi)^3} \left|\hat{e} \cdot \boldsymbol{p}_{vc}(\boldsymbol{k})\right|^2 \delta\left(E_c(\boldsymbol{k}) - E_v(\boldsymbol{k}) - E\right)\left(f_c(E_c(\boldsymbol{k}), E_{fn}, T) - f_v(E_v(\boldsymbol{k}), E_{fp}, T)\right) \quad 2\text{-}30$$

where:

$$C_0 = \frac{\pi \hbar e^2}{n_r c \varepsilon_0 m_0^{\,2} E} \quad 2\text{-}31$$

We have now, non-equilibrium conditions with a partial filling of the conduction bands and a partial emptying of the valence bands. The occupation functions f_v and f_c are the Fermi-Dirac distributions:

$$f_{v,c}\left(E_{v,c}, E_{fp,n}, T\right) = \frac{1}{1 + \exp\left(\frac{E_{v,c} - E_{fp,n}}{k_B T}\right)} \quad 2\text{-}32$$

$E_{fp,n}$ are the quasi-Fermi levels for holes and electrons and are calculated by numerically solving:

$$N = \int_{E_{CBM}}^{+\infty} D(E) f_c(E, E_{fn}, T) dE$$
$$P = \int_{-\infty}^{E_{VBM}} D(E) f_v(E, E_{fp}, T) dE \qquad 2\text{-}33$$

where N and P are the free electrons and free holes densities (with $N = P$ to guarantee charge neutrality) and $D(E)$ is the density of states.

Similarly, the gain can be calculated for a QW with a thickness L.

$$g(E) = C_0 \frac{1}{L} \int \frac{d^2k}{(2\pi)^2} \left| \hat{e} \cdot \boldsymbol{p}_{vc}(\boldsymbol{k}) \right|^2 \delta\left(E_c(\boldsymbol{k}) - E_v(\boldsymbol{k}) - E\right)$$
$$\left(f_c(E_c(\boldsymbol{k}), E_{fn}, T) - f_v(E_v(\boldsymbol{k}), E_{fp}, T)\right) \qquad 2\text{-}34$$

In practice, the Brillouin zone is meshed and a Gaussian broadening is added. For direct band gap QW, we can restrict the mesh to a zone near the Γ point. Fig. 2-22 shows the gain spectra for a $(GaAs)_{8nm}/Al_{0.2}Ga_{0.8}As$ QW for various carrier densities.

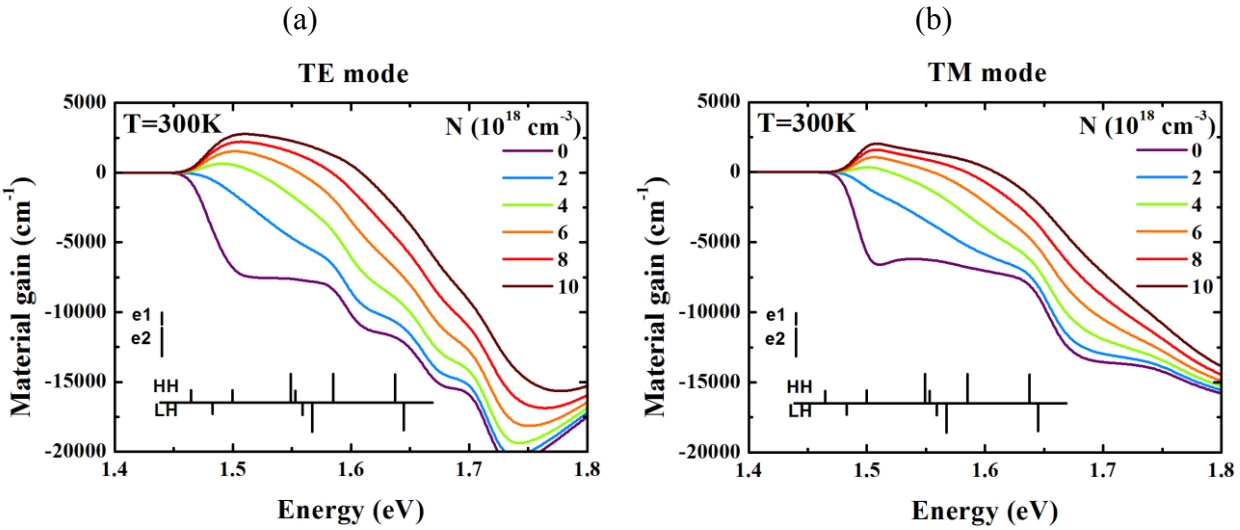

Fig. 2-22: Material gain for (a) TE and (b) TM polarization in a $(GaAs)_{8nm}/Al_{0.2}Ga_{0.8}As$ QW calculated with the TB model for various N=P carrier densities.

The gain depends on the polarization mode. Transverse electric (TE) mode corresponds with the electric optical field oriented in a direction in the growth plane whereas the transverse magnetic (TM) mode corresponds with the electric optical field oriented perpendicular to the growth plane. Good agreement is found with the results found in classical laser books[107,108], both for maximum gain and carrier density threshold.

2.6.5 Optical properties in a quantum dot

The concept of absorption in cm^{-1} for a QD system can only be defined when considering the volume density of QD. For a QD we prefer to calculate the radiative lifetime for a given optical transition[109]:

$$\tau_{rad} = \frac{2\pi\varepsilon_0 m_0 c^3 \hbar^2}{n_r e^2 \left(E_c - E_v\right)^2 f_{eff}} \qquad 2\text{-}35$$

where f_{eff} is the effective oscillator strength which is calculated by integrating the oscillator strength $f(\hat{e})$ over the unit sphere:

$$f_{eff} = \int_0^{\pi}\int_0^{2\pi} f(\hat{e})\sin\varphi d\theta d\varphi \qquad 2\text{-}36$$

An effective refractive index n_r has to be considered to take into account the difference between the QD material and the barrier material. Thränhardt *et al.*[110] have demonstrated that it can be written:

$$n_r = \frac{9n_{barrier}^5}{\left(2n_{barrier}^2 + n_{QD}^2\right)^2} \qquad 2\text{-}37$$

For the InAs/InP QD simulated in section 2.4.2.2, the **k·p** and the TB models give similar value for the radiative lifetime of the ground optical transition (1.2 ns for **k·p** and 1.3 ns for TB).

We define the absorption spectrum in arbitrary units by calculating the oscillator strength as a function of energy for TE and TM polarizations. A Gaussian broadening is added to take into account the homogeneous broadening of levels. Fig. 2-23 presents the comparison between **k·p** and TB results for the InAs/InP QD. The slight discrepancy on the energy transitions mainly results from the discrepancy between the calculated hole energies (see Table 2-6). The TM spectra slightly differ but is should be noticed that the TM optical activity is much less intense than the TE one, and strongly depends on very small LH components of the hole wavefunctions which are less well described in the **k·p** method.

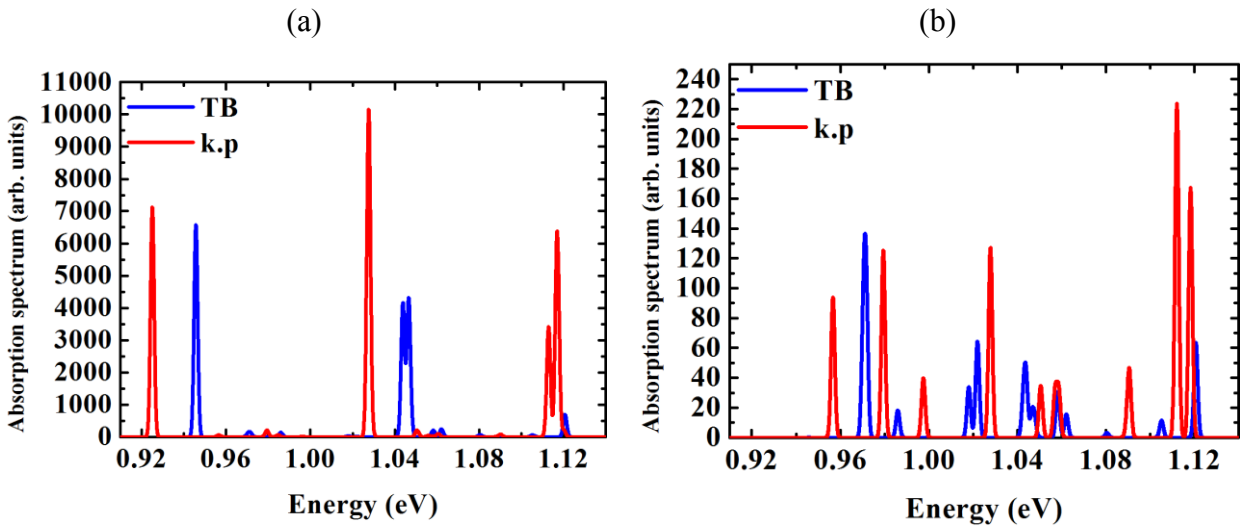

Fig. 2-23: Absorption spectrum of the cone-shaped InAs/InP defined in section 2.4.2.2 calculated with the k·p and TB methods for the (a) TE and (b) TM polarizations. The TB calculation considers the first four electron and hole levels (each being doubly degenerated due to spin) whereas the k·p calculation considers the first six electron and hole levels (each being doubly degenerated due to spin).

2.7 Conclusions

In conclusion, we have highlighted the difficulties of modeling our semiconductors structures for the pseudomorphic approach. The first difficulty comes from the use of indirect band gap semiconductors: GaP and AlP. Even for nanostructures based on direct band gap semiconductors (GaAs), the compressive strain induced by the growth on GaP or Si substrate may result in a strong proximity of various conduction states coming from various Brillouin zone points. The second difficulty is the modeling of the non-classical dilute nitride alloys. We have shown that the extended $sp^3d^5s^*$ TB model provides solutions for both issues. In order to get the simplest model as possible, we have presented two strategies to model classical alloys and dilute nitrides. We will use these methods in the following chapters in order to explain the experimental measurements.

References of Chapter 2

[1] R. Ben Chamekh, Fonctions D'onde Locales Dans Le Formalisme Des Liaisons Fortes, Thèse Université Pierre et Marie Curie - Paris VI, 2012.
[2] P. Hohenberg and W. Kohn, Phys. Rev. **136**, B864 (1964).
[3] P. Rinke, A. Qteish, J. Neugebauer, C. Freysoldt, and M. Scheffler, New J. Phys. **7**, 126 (2005).
[4] L. Hedin, Phys. Rev. **139**, A796 (1965).
[5] K.A. Mäder and A. Zunger, Phys. Rev. B **50**, 17393 (1994).
[6] J.C. Slater and G.F. Koster, Phys. Rev. **94**, 1498 (1954).
[7] A. Canning, L.W. Wang, A. Williamson, and A. Zunger, J. Comput. Phys. **160**, 29 (2000).
[8] G. Klimeck, S.S. Ahmed, H. Bae, N. Kharche, S. Clark, B. Haley, S. Lee, M. Naumov, H. Ryu, F. Saied, M. Prada, M. Korkusinski, T.B. Boykin, and R. Rahman, Electron Devices Ieee Trans. **54**, 2079 (2007).
[9] G. Dresselhaus, A.F. Kip, and C. Kittel, Phys. Rev. **98**, 368 (1955).
[10] J.M. Luttinger and W. Kohn, Phys. Rev. **97**, 869 (1955).
[11] E.O. Kane, J. Phys. Chem. Solids **1**, 249 (1957).
[12] G. Bastard and J.A. Brum, Ieee J. Quantum Electron. **22**, 1625 (1986).
[13] C.R. Pidgeon and R.N. Brown, Phys. Rev. **146**, 575 (1966).
[14] S. Richard, F. Aniel, and G. Fishman, Phys. Rev. B **70**, 235204 (2004).
[15] S. Richard, F. Aniel, and G. Fishman, Phys. Rev. B **72**, 245316 (2005).
[16] S. Boyer-Richard, F. Raouafi, A. Bondi, L. Pédesseau, C. Katan, J.-M. Jancu, and J. Even, Appl. Phys. Lett. **98**, 251913 (2011).
[17] A. De and C.E. Pryor, Phys. Rev. B **81**, 155210 (2010).
[18] S. Assali, I. Zardo, S. Plissard, D. Kriegner, M.A. Verheijen, G. Bauer, A. Meijerink, A. Belabbes, F. Bechstedt, J.E.M. Haverkort, and E.P.A.M. Bakkers, Nano Lett. (2013).
[19]*Landolt-Börnstein Intrinsic Properties of Group IV Elements and III-V, II-VI and I-VII Compounds* (1987).
[20] I. Vurgaftman, J.R. Meyer, and L.R. Ram-Mohan, J. Appl. Phys. **89**, 5815 (2001).
[21] S.L. Chuang, *Physics of Optoelectronic Devices* (John Wiley & Sons, Incorporated, 1995).
[22] J. Bardeen and W. Shockley, Phys. Rev. **80**, 72 (1950).
[23] G.L. Bir and G.E. Pikus, *Symmetry and Strain-Induces Effects in Semiconductors* (Israel Program for Scientific Translations, 1974).
[24] S. Adachi, *GaAs and Related Materials: Bulk Semiconducting and Superlattice Properties* (World Scientific, 1994).
[25] J.A. Prieto, G. Armelles, M.-E. Pistol, P. Castrillo, J.P. Silveira, and F. Briones, Appl. Phys. Lett. **70**, 3449 (1997).
[26] J. Toivonen, T. Hakkarainen, M. Sopanen, and H. Lipsanen, J. Cryst. Growth **221**, 456 (2000).
[27] D.G. Thomas and J.J. Hopfield, Phys. Rev. **150**, 680 (1966).
[28] J.W. Allen, J. Phys. C Solid State Phys. **4**, 1936 (1971).
[29] D.J. Wolford, J.A. Bradley, K. Fry, and J. Thompson, in (Proceedings of the 17th International Conference on the Physics of Semiconductors, San Francisco, California, USA, August 6-10, 1984, 1985), p. 627.
[30] E. Cohen and M.D. Sturge, Phys. Rev. B **15**, 1039 (1977).
[31] X. Liu, M.-E. Pistol, L. Samuelson, S. Schwetlick, and W. Seifert, Appl. Phys. Lett. **56**, 1451 (1990).
[32] W. Shan, W. Walukiewicz, J.W. Ager, E.E. Haller, J.F. Geisz, D.J. Friedman, J.M. Olson, and S.R. Kurtz, Phys. Rev. Lett. **82**, 1221 (1999).

[33] J. Wu, W. Shan, and W. Walukiewicz, Semicond. Sci. Technol. **17**, 860 (2002).
[34] K. Alberi, J. Wu, W. Walukiewicz, K.M. Yu, O.D. Dubon, S.P. Watkins, C.X. Wang, X. Liu, Y.-J. Cho, and J. Furdyna, Phys. Rev. B **75**, 045203 (2007).
[35] W. Shan, W. Walukiewicz, J.W. Ager, K.M. Yu, J. Wu, E.E. Haller, Y. Nabetani, T. Mukawa, Y. Ito, and T. Matsumoto, Appl. Phys. Lett. **83**, 299 (2003).
[36] W. Shan, K.M. Yu, W. Walukiewicz, J.W. Ager, E.E. Haller, and M.C. Ridgway, Appl. Phys. Lett. **75**, 1410 (1999).
[37] M. Kozhevnikov, V. Narayanamurti, C.V. Reddy, H.P. Xin, C.W. Tu, A. Mascarenhas, and Y. Zhang, Phys. Rev. B **61**, R7861 (2000).
[38] H.M. Cheong, Y. Zhang, A. Mascarenhas, and J.F. Geisz, Phys. Rev. B **61**, 13687 (2000).
[39] M.J. Seong, A. Mascarenhas, and J.F. Geisz, Appl. Phys. Lett. **79**, 1297 (2001).
[40] B. Fluegel, A. Mascarenhas, A.J. Ptak, S. Tixier, E.C. Young, and T. Tiedje, Phys. Rev. B **76**, 155209 (2007).
[41] A. Lindsay and E.P. O'Reilly, Phys. Rev. Lett. **93**, 196402 (2004).
[42] S. Fahy and E.. O'Reilly, Phys. E Low-Dimens. Syst. Nanostructures **21**, 881 (2004).
[43] S.B. Healy, A. Lindsay, and E.P. O'Reilly, Optoelectron. Ieee Proc. **151**, 397 (2004).
[44] M.P. Vaughan and B.K. Ridley, Phys. Rev. B **75**, 195205 (2007).
[45] I. Vurgaftman and J.R. Meyer, J. Appl. Phys. **94**, 3675 (2003).
[46] R. Kudrawiec, J. Appl. Phys. **101**, 116101 (2007).
[47] P.J. Klar, H. Gr ning , W. Heimbrodt, J. Koch, F. H hnsdor f, W. Stolz, P.M.A. Vicente, and J. Camassel, Appl. Phys. Lett. **76**, 3439 (2000).
[48] B. Kunert, K. Volz, J. Koch, and W. Stolz, Appl. Phys. Lett. **88**, 182108 (2006).
[49] J. Chamings, S. Ahmed, A.R. Adams, S.J. Sweeney, V.A. Odnoblyudov, C.W. Tu, B. Kunert, and W. Stolz, Phys. Status Solidi B **246**, 527 (2009).
[50] A. Lindsay, S. Tomic, and E.P. O'Reilly, Solid-State Electron. **47**, 443 (2003).
[51] M. Gladysiewicz, R. Kudrawiec, J.M. Miloszewski, P. Weetman, J. Misiewicz, and M.S. Wartak, J. Appl. Phys. **113**, 063514 (2013).
[52] J. Chen, W.J. Fan, Q. Xu, X.W. Zhang, S.S. Li, and J.B. Xia, Superlattices Microstruct. **52**, 618 (2012).
[53] P.R.C. Kent and A. Zunger, Phys. Rev. B **64**, 115208 (2001).
[54] A. Lindsay and E.P. O'Reilly, Phys. E Low-Dimens. Syst. Nanostructures **21**, 901 (2004).
[55] C. Harris, A. Lindsay, and E.P. O'Reilly, J. Phys. Condens. Matter **20**, 295211 (2008).
[56] E.P. O'Reilly, A. Lindsay, P.J. Klar, A. Polimeni, and M. Capizzi, Semicond. Sci. Technol. **24**, 033001 (2009).
[57] Y. Zhang, B. Fluegel, A. Mascarenhas, H.P. Xin, and C.W. Tu, Phys. Rev. B **62**, 4493 (2000).
[58] Y. Zhang, B. Fluegel, M.C. Hanna, J.F. Geisz, L.-W. Wang, and A. Mascarenhas, Phys. Status Solidi B **240**, 396 (2003).
[59] B. Fluegel, Y. Zhang, J.F. Geisz, and A. Mascarenhas, Phys. Rev. B **72**, 073203 (2005).
[60] H.-X. Deng, J. Li, S.-S. Li, H. Peng, J.-B. Xia, L.-W. Wang, and S.-H. Wei, Phys. Rev. B **82**, 193204 (2010).
[61] V. Virkkala, V. Havu, F. Tuomisto, and M.J. Puska, Phys. Rev. B **88**, 035204.
[62] Y.-H. Zhu, H.-Y. Yu, and W.-J. Fan, Appl. Phys. Lett. **98**, 121112 (2011).
[63] N. Koukourakis, C. Bückers, D.A. Funke, N.C. Gerhardt, S. Liebich, S. Chatterjee, C. Lange, M. Zimprich, K. Volz, W. Stolz, B. Kunert, S.W. Koch, and M.R. Hofmann, Appl. Phys. Lett. **100**, 092107 (2012).
[64] W.A. Harrison, *Elementary Electronic Structure* (World Scientific, 1999).
[65] P. Yu and M. Cardona, *Fundamentals of Semiconductors - Physics and Materials Properties*.

[66] E. Hückel, Z. Für Phys. **70**, 204 (1931).
[67] F. Bloch, Z. Für Phys. **52**, 555 (1929).
[68] P.-O. L wdin, J . Chem. Phys. **18**, 365 (1950).
[69] D.J. Chadi and M.L. Cohen, Phys. Status Solidi B **68**, 405 (1975).
[70] P. Vogl, H.P. Hjalmarson, and J.D. Dow, J. Phys. Chem. Solids **44**, 365 (1983).
[71] J.-M. Jancu, R. Scholz, F. Beltram, and F. Bassani, Phys. Rev. B **57**, 6493 (1998).
[72] S.-H. Wei and A. Zunger, Phys. Rev. Lett. **59**, 144 (1987).
[73] S.-H. Wei and A. Zunger, Appl. Phys. Lett. **72**, 2011 (1998).
[74] C.G. Van de Walle and J. Neugebauer, Nature **423**, 626 (2003).
[75] Y.-H. Li, A. Walsh, S. Chen, W.-J. Yin, J.-H. Yang, J. Li, J.L.F. Da Silva, X.G. Gong, and S.-H. Wei, Appl. Phys. Lett. **94**, 212109 (2009).
[76] P.N. Keating, Phys. Rev. **145**, 637 (1966).
[77] M. Zieliński, Phys. Rev. B **86**, 115424 (2012).
[78] Y.M. Niquet, Phys. Rev. B **74**, 155304 (2006).
[79] A.J. Williamson, L.W. Wang, and A. Zunger, Phys. Rev. B **62**, 12963 (2000).
[80] H. Fu, V. Ozoliņš, and A. Zunger, Phys. Rev. B **59**, 2881 (1999).
[81] T.B. Boykin and G. Klimeck, Phys. Rev. B **71**, 115215 (2005).
[82] L.-W. Wang, L. Bellaiche, S.-H. Wei, and A. Zunger, Phys. Rev. Lett. **80**, 4725 (1998).
[83] W. Ge, W.D. Schmidt, M.D. Sturge, L.N. Pfeiffer, and K.W. West, J. Lumin. **59**, 163 (1994).
[84] R. Cingolani, L. Baldassarre, M. Ferrara, M. Lugarà, and K. Ploog, Phys. Rev. B **40**, 6101 (1989).
[85] S. Steiger, M. Povolotskyi, H.-H. Park, T. Kubis, and G. Klimeck, Ieee Trans. Nanotechnol. **10**, 1464 (2011).
[86] D.S. Watkins, *The Matrix Eigenvalue Problem: GR and Krylov Subspace Methods* (SIAM, 2007).
[87] L.-W. Wang and A. Zunger, J. Chem. Phys. **100**, 2394 (1994).
[88] C. Pryor, J. Kim, L.W. Wang, A.J. Williamson, and A. Zunger, J. Appl. Phys. **83**, 2548 (1998).
[89] O. Stier, M. Grundmann, and D. Bimberg, Phys. Rev. B **59**, 5688 (1999).
[90] J. Even, F. Doré, C. Cornet, L. Pedesseau, A. Schliwa, and D. Bimberg, Appl. Phys. Lett. **91**, 122112 (2007).
[91] S. Lee, F. Oyafuso, P. von Allmen, and G. Klimeck, Phys. Rev. B **69**, 045316 (2004).
[92] G. Fishman, *Semi-conducteurs : les bases de la théorie k.p* (Ecole Polytechnique, 2010).
[93] M. Tadić, F.M. Peeters, and K.L. Janssens, Phys. Rev. B **65**, 165333 (2002).
[94] J. Even, F. Doré, C. Cornet, and L. Pedesseau, Phys. Rev. B **77**, 085305 (2008).
[95] C. Cornet, A. Schliwa, J. Even, F. Doré, C. Celebi, A. Létoublon, E. Macé, C. Paranthoën, A. Simon, P.M. Koenraad, N. Bertru, D. Bimberg, and S. Loualiche, Phys. Rev. B **74**, 035312 (2006).
[96] F. Doré, Emetteurs à Îlots Quantiques Pour Le Moyen-infrarouge, Thèse INSA Rennes, 2008.
[97] M. Zieliński, M. Korkusiński, and P. Hawrylak, Phys. Rev. B **81**, 085301 (2010).
[98] N. Shtinkov, P. Desjardins, and R.A. Masut, Phys. Rev. B **67**, 081202 (2003).
[99] S. Turcotte, N. Shtinkov, P. Desjardins, R.A. Masut, and R. Leonelli, J. Vac. Sci. Technol. Vac. Surfaces Films **22**, 776 (2004).
[100] N. Shtinkov, S. Turcotte, J.-N. Beaudry, P. Desjardins, and R.A. Masut, J. Vac. Sci. Technol. Vac. Surfaces Films **22**, 1606 (2004).
[101] G. Leibiger, V. Gottschalch, M. Schubert, G. Benndorf, and R. Schwabe, Phys. Rev. B **65**, 245207 (2002).
[102] L.C. Lew Yan Voon and L.R. Ram-Mohan, Phys. Rev. B **47**, 15500 (1993).

[103] T.B. Boykin and P. Vogl, Phys. Rev. B **65**, 035202 (2001).
[104] D.E. Aspnes and A.A. Studna, Phys. Rev. B **27**, 985 (1983).
[105] E.D. Palik, *Handbook of Optical Constants of Solids* (Academic Press, 1985).
[106] B. Arnaud and M. Alouani, Phys. Rev. B 63, 085208 (2001).
[107] P.S. Zory, *Quantum Well Lasers* (Academic Press, 1993).
[108] W.W. Chow, S.W. Koch, and M. Sargent, *Semiconductor-laser Physics* (Springer-Verlag, 1994).
[109] G.W. p't Hooft, W.A.J.A. van der Poel, L.W. Molenkamp, and C.T. Foxon, Phys. Rev. B **35**, 8281 (1987).
[110] A. Thränhardt, C. Ell, G. Khitrova, and H.M. Gibbs, Phys. Rev. B **65**, 035327 (2002).

Chapter 3

Study of GaAsPN quantum well based structures

In this chapter, we study the optical properties of dilute nitride structures based on bulk GaPN and GaAsPN as well as GaAsPN/GaP(N) QW. The development of GaAsPN QW based laser structures is discussed. In particular, the AlGaP alloy is studied as a potential candidate for cladding layers.

3.1 Optoelectronic properties of bulk Ga(As)PN dilute nitride alloys

3.1.1 Bulk GaPN

3.1.1.1 From nitrogen doping to dilute nitride regime

A good starting point to understand the role of nitrogen in the optical properties of GaPN alloys is the detailed experimental study of Zhang *et al.*[1]. Fig. 3-1 presents the evolution of low temperature PL spectrum for the GaPN alloy from very low N content (doping regime) up to 0.9 %. In the doping regime, sharp lines are observed. The theoretical study (chapter 2) shows that an isolated N atom in a GaP matrix results in a bound exciton state located just below the conduction band minimum (CBM). Similarly, NN pairs also give rise to excitonic bound states whose energies, which have been theoretically calculated by Kent and Zunger[2] (see Fig. 2-7), depend on the spacing between the two N atoms. In the GaP crystal, all these states are localized below the CBM. The sharp lines observed in Fig. 3-1 are indeed attributed to radiative recombinations involving these localized N levels and phonon replica. Despite the indirect band gap of GaP, a relatively high optical efficiency is thus found when it is N-doped. Indeed, the

localized N centers break the translational symmetry of the crystal and relax the wave vector conservation requirement for optical transitions. Nevertheless, this very low incorporation regime is probably not the most relevant for our applications because the lattice-matching of GaPN alloy to Si requires a larger N content (around 2.2 %). Moreover, we will show that the optical efficiency can be increased when increasing N content. But it is worth mentioning that this regime has historically been used in green LED applications since the 60s[3].

When increasing the N content beyond 0.24 %, the PL spectrum progressively evolves from a sharp line spectrum to a broad peak. The energy of the maximum PL intensity red shifts and the integrated PL intensity increases. In the following, we only consider this higher incorporation regime, and call it "dilute nitride regime".

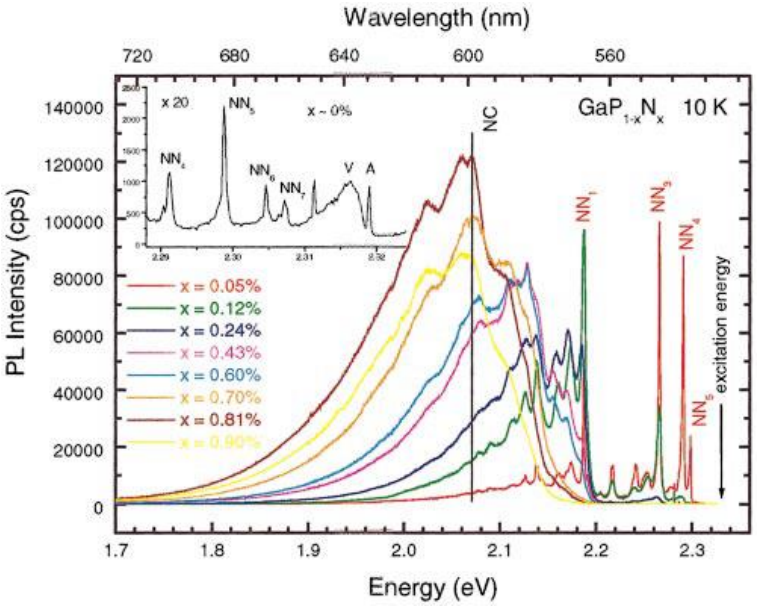

Fig. 3-1: Low temperature PL study of Zhang *et al.*[1] for bulk GaPN in the very low N composition range.

3.1.1.2 The dilute regime

Experimental studies have been performed on GaPN/GaP layers grown using a Solid-Source Molecular Beam Epitaxy (SSMBE). A 100 nm thick GaP buffer layer is first grown at 580 °C, followed by a 100 nm thick GaPN layer. A 10 nm GaP capping layer is finally overgrown. The N composition in the GaPN layer is controlled by growth temperature, growth rate, phosphorus beam equivalent pressure and N plasma cell parameters (N_2 flow rate, RF power and valve opening). For readers interested in growth details, the growth procedure is described in

Ref.[4]. The N content is deduced from high resolution X-ray diffraction (HRXRD) (measurements performed in the framework of T. Nguyen Thanh and S. Almosni's PhD thesis). The GaPN layer thickness is limited to 100 nm to avoid plastic relaxation. Nevertheless, when N content is larger than 3.9 %, the GaPN layer is found to be partially relaxed due to the larger lattice-mismatch with the GaP substrate[4].

The samples are first analyzed by continuous-wave PL. Experiments have been carried out with a 405 nm continuous-wave laser diode source, yielding a maximum power density roughly estimated to 80 $W.cm^{-2}$. The samples have been set in a helium bath closed-cycle cryostat to study PL from 10 K to room temperature.

Fig. 3-2 presents the room temperature PL of GaPN samples with various N compositions from 0.47 % to 2.37 %. Please notice that we do not observe any discrete features in the lowest N contents of 0.47 % and 0.68 % as observed in Fig. 3-1 because the spectra are taken at 300 K. A first striking feature is the monotonous red-shift of the PL peak when increasing N content. This behavior follows the trend already observed in Fig. 3-1 and is obviously due to the giant band gap bowing effect usually encountered in dilute nitride alloys[5–12]. The origins of this effect have already been discussed in chapter 2; i.e. according to the view of Kent and Zunger[2] (see section 2.2.3.4), N forms perturbed host conduction states which shift down in energy when increasing the N content.

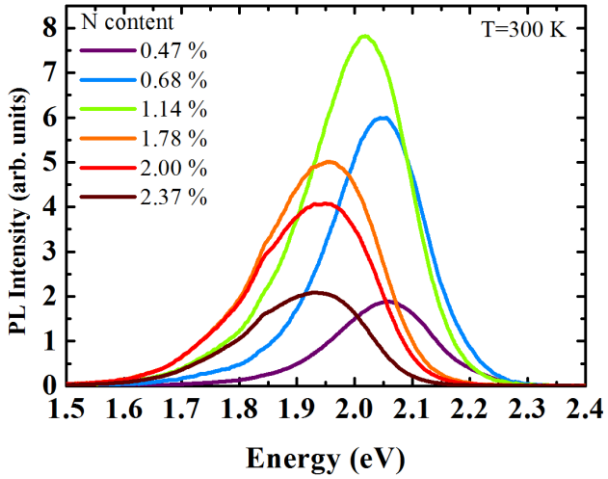

Fig. 3-2: Room temperature PL spectra of GaPN layer as a function of N content. The excitation density is roughly estimated to be 80 $W.cm^{-2}$.

The position of the PL peak as a function of N content is summarized in Fig. 3-3(a). We assume that at room temperature, the energy of the PL peak roughly corresponds to the alloy band gap energy (the transition between the lowest perturbed host conduction state in the picture of Kent and Zunger[2] and the valence band maximum). We will see that it is not true at low temperature. Therefore, 20 meV error bars have been added to take into account this assumption. The dilute nitride alloy band gap can be calculated at T=0 K with the $sp^3d^5s^*s_N$ TB model presented in chapter 2. The results are displayed in Fig. 3-3(a) by the red line, and are in good agreement with experimental data assuming a temperature red-shift of 50 meV (measured in Ref.[13] by absorption experiments).

Another striking feature observed in Fig. 3-2 is the variation of the PL intensity with N content. The PL intensity first increases when increasing the N content from 0.47 % to 1.14 % and then decreases when incorporating more nitrogen. Obviously, the PL intensity depends on the structural quality, which can differ when the growth conditions are changed. But, Fig. 3-3(b) shows that there exists a strong correlation between the integrated PL intensity and the N content.

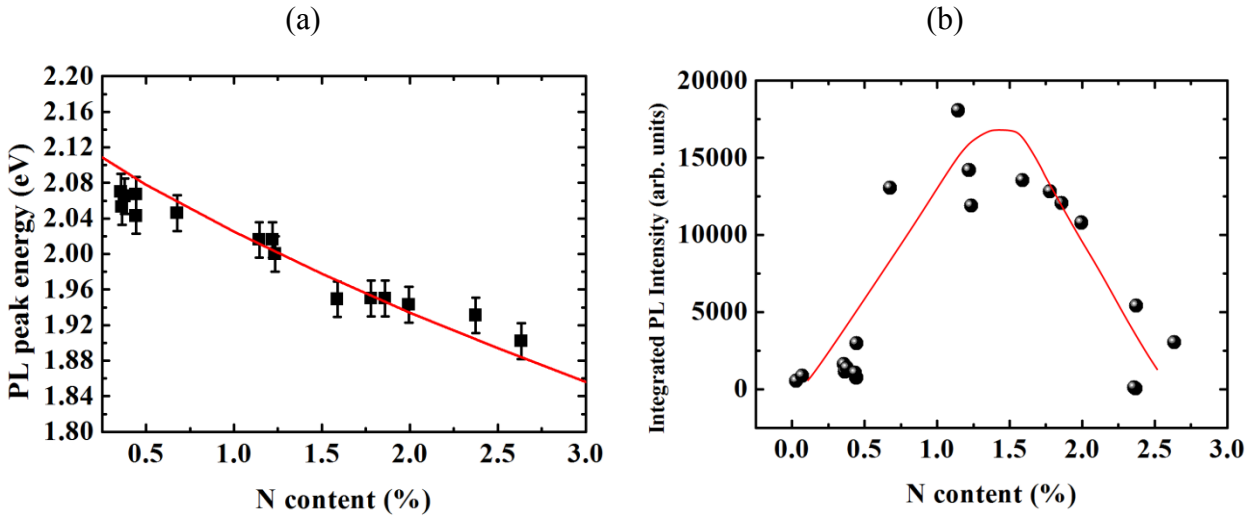

Fig. 3-3: (a) Energy of the maximum room temperature PL intensity as a function of N content. The red line is the calculated band gap with the $sp^3d^5s^*s_N$ TB model. The calculation is performed at 0 K and a red-shift of 50 meV is considered between 0 K and room temperature. (b) Room temperature integrated PL intensity as a function of N content. The red line is a guide to the eye.

The increasing recombination efficiency for N contents below 1.5 % can be explained by the nature of the alloy conduction band edge. In GaPN, the N-levels are located below the conduction band minimum (CBM) of GaP. When increasing the N content, these N levels are coupled with the CBM of GaP and more strongly with the Γ CBM. In the simple two-level **k·p**

BAC picture, the CBM of GaPN has such a mixed character. The fractional Γ character is given by[14]:

$$|a_\Gamma|^2 = \frac{1}{2}\left(1-\left(1+\frac{4C_{MN}^2 x}{(E_N-E_M)^2}\right)^{-1/2}\right)$$

when keeping the notations of chapter 2. In the $sp^3d^5s^*s_N$ TB model, a similar quantity is defined by calculating the relative contribution of the s_N orbital to the CBM wave function and taking the fraction $1-s_N$[15]. Fig. 3-4 shows that in GaPN, this fractional Γ character increases when increasing N. This simple calculation explains why the PL intensity is enhanced when increasing N content in bulk GaPN (at least below a given concentration roughly equal to 1.5 %).

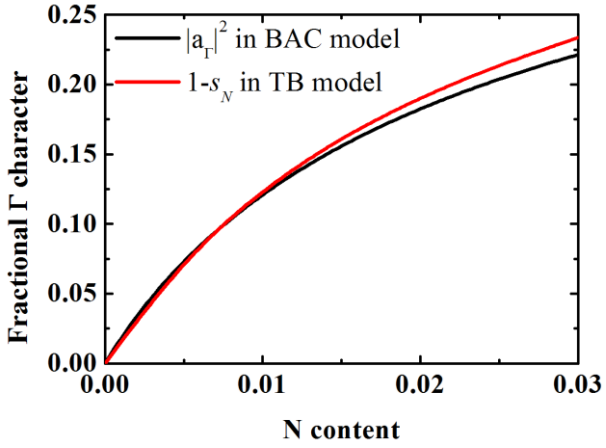

Fig. 3-4: Fractional Γ character in bulk GaPN calculated with the 2-levels BAC model and the $sp^3d^5s^*s_N$ TB model as a function of N content. For the BAC model, the commonly used values E_M=2.89 eV, E_N=2.18 eV and C_{MN}=3.05 eV are considered[16]. The parameters for the TB calculation are defined in chapter 2.

The reason why the PL intensity does not increase in the whole N content range is that N incorporation also generates non-radiative defects in the layer[17]. We have reported N incorporation up to 6 %[4,18], but in this case the additional effect of plastic relaxation prevents any detection of a PL signal.

The PL peak shape is another striking feature in dilute nitride alloys. In the room temperature PL spectra of Fig. 3-2, one can already notice that the low energy tail is longer than the high energy tail. Fig. 3-5 shows the normalized PL intensity of a $GaP_{0.98}N_{0.02}$ layer at 10 K. The spectrum exhibits an asymmetric line shape with a sharp high energy cutoff and an

exponential low energy tail. This behavior is classically attributed to disorder effects. For example, random fluctuations in alloy composition result in a smearing of band edges and in an extended density of states into the band gap. This effect is not inherent to dilute nitride alloys and have been reported in GaAlAs[19], SiGe[20] or GaAsP[21] alloys. But it is strongly enhanced in the dilute nitride case because the emission energy strongly depends on the alloy composition. Because the high energy tail is enhanced by thermal filling of the bands, the asymmetric shape is more pronounced at low temperature (Fig. 3-5) than at room temperature (Fig. 3-2). The localization potential can be estimated by fitting the low energy tail with a single exponential $\propto \exp(E / E_{loc})$. In classical alloys, E_{loc} is about 7-10 meV[19–21]. But in dilute nitride alloys large values of 50-100 meV are found[22]. For the spectrum of Fig. 3-5 the localization potential is found to be 75 meV.

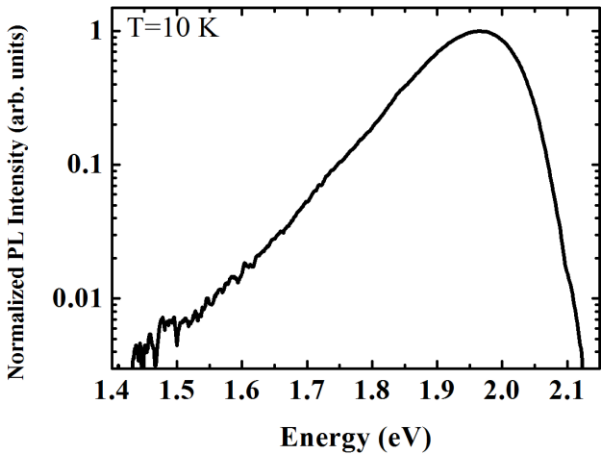

Fig. 3-5: Low temperature PL spectrum of a $GaP_{0.972}N_{0.018}$ layer with an excitation density of 50 $W.cm^{-2}$.

The dependence of the PL spectrum on the excitation density is presented in Fig. 3-6. The energy of the PL peak is found to exhibit a logathmic blue shift with increasing the excitation density (Fig. 3-6(a)). The integrated PL intensity has a nearly linear variation as a function of excitation density (Fig. 3-6(b)). These features are attributed to the gradual filling of energy states resulting from localized centers due to alloy fluctuations in the low energy band tail. The radiative recombinations in this band tail are expected to be the dominant mechanism which is responsible for the PL in this whole excitation density range. Indeed, a saturation of the localized states density, would yield additional recombinations from the band edges and a change in the slopes in Fig. 3-6 would be expected[23]. Thus, the energy of the band gap of this GaPN layer may be at a slightly higher energy than the position of the PL peak measured at 10 K. Actually, it has

been demonstrated by many authors that the position of the PL peak at low temperature differs from the band gap energy that can be measured by absorption, PLE or photoreflectance experiments[13,22,24,25]. This phenomenon is called the Stokes shift.

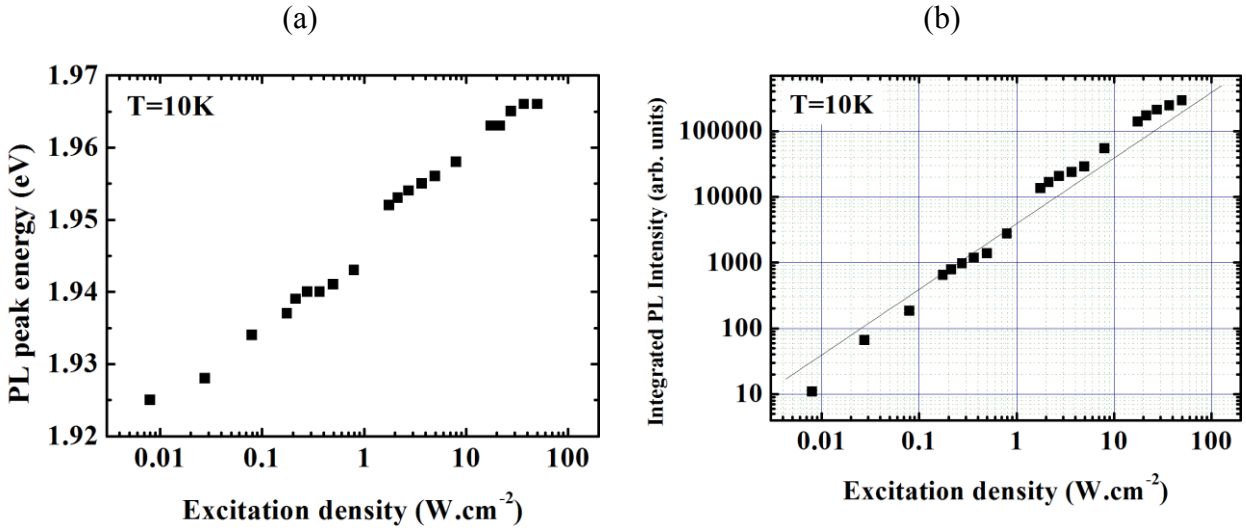

Fig. 3-6: Excitation power density dependence of (a) the PL peak energy and (b) the integrated PL intensity. The thin black line is a guide to the eye to match with an expected linear variation. The temperature is 10 K.

Additional information is obtained from time resolved photoluminescence (TRPL) experiments performed in collaboration with the group of X. Marie in LPCNO (Toulouse). GaPN being known to exhibit long decay times on the order of 100 ns[25–28], the chosen experimental setup (presented in Appendix B) has a repetition rate equal to 4 MHz. The experiments are performed at 10 K to limit the effects of non-radiative channels.

Fig. 3-7(a) presents the streak camera image of a $GaP_{0.979}N_{0.021}$ layer. One can recognize the low energy tail due to disorder effects. But at short times, the PL spectrum also extends slightly on the high energy side. The PL dynamics is analyzed for three detection energies marked by the arrows in Fig. 3-7(a). The dynamics of the low energy tail is detected at 1.82 eV (blue arrow). The corresponding PL decay shown in Fig. 3-7(b) exhibits a mono-exponential behavior with a decay time of 131 ns. When detecting at a higher energy of 1.95 eV (green arrow), corresponding to the maximum PL intensity, the PL dynamics remains similar. The behavior is also mono-exponential with a slight decrease of the decay time to 103 ns. On the contrary, for a detection energy at 2.08 eV, corresponding to the high energy side (black arrow), the PL dynamic is strongly non-mono exponential. At least three exponential decays are required to fit the curve. This behavior has also been observed in (In)GaAsN[22,29]. The long decay times are

characteristic of recombination in the localized centers created by alloy fluctuations. The faster dynamics observed on the high energy side is usually attributed to a delocalized character with band-to-band transitions and relaxation processes toward localized states[22].

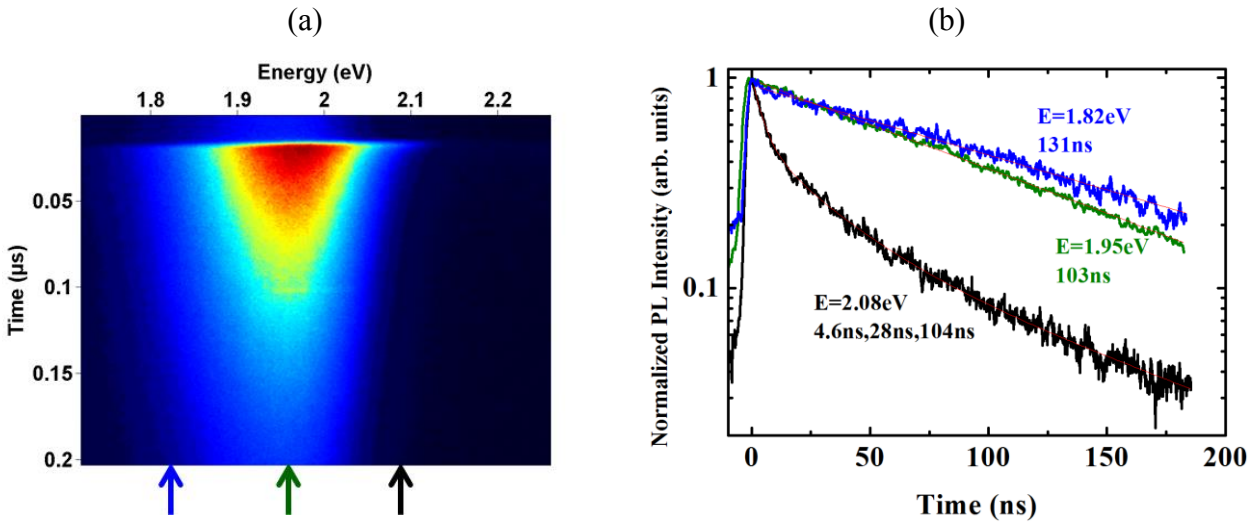

Fig. 3-7: (a) Streak camera image of a $GaP_{0.979}N_{0.021}$ layer at 10 K and (b) PL dynamics at selected energies marked by colored arrows. The thin red lines show the exponential fit. The excitation density is 2000 W.cm^{-2} and the repetition rate is 4 MHz.

In TRPL experiments, the main difference between bulk GaPN and bulk (In)GaAsN[22,29] is the characteristic measured decay times. In (In)GaAsN, the measured decay times related to localized excitons are at least one order of magnitude smaller than the one measured in GaPN. Our interpretation relies on the nature of the CBM which is more "Γ-like" in (In)GaAsN, due to the direct band gap nature of the (In)GaAs host material.

To summarize, we have highlighted the main optical properties of bulk GaPN. The low temperature PL is dominated by optical transitions related to excitons localized in N-alloy fluctuations. This results in a low energy tail on the PL spectrum. The recombination at the GaPN band gap is only visible at short times under high pumping. The measured decay times in the low energy tail are as long as 100 ns which suggest that the Γ character of the GaPN CBM remains limited as compared with bulk (In)GaAsN. These two features are detrimental for laser applications. A large density of localized states below the band gap may increase the transparency threshold and a low transition rate may result in a low material gain. O'Reilly *et al.* has even claimed that GaPN is not suitable as an active laser material[30]. Nevertheless, the $GaP_{0.98}N_{0.02}$ alloy can be useful for the barrier material in a laser structure because thick layers

can be grown lattice-matched to Si. However, in the case of $GaP_{0.98}N_{0.02}$ barrier material, electronic states involved into carrier mobility and carrier injection to the active zone may be mostly related to alloy states. The role of localized states in the carrier injection will be studied in section 3.3. Moreover, this ternary alloy does not allow any degree of freedom for band engineering in laser structure because the N concentration is fixed by the lattice-matching condition which consequently fixes the band gap (about 1.92 eV at room temperature). In order to get a further degree of freedom, the study of bulk dilute nitride alloys has been extended to the quaternary GaAsPN alloy.

3.1.2 Bulk GaAsPN

The study of bulk GaAsPN alloys is also interesting for the development of tandem solar cells on Si, which is the essential work of S. Almosni's PhD work. Indeed, it has been shown that the theoretical maximum efficiency of a tandem solar cell based on a Si bottom cell with a band gap of 1.1 eV is obtained with a top cell with a band gap of 1.7 eV[18,31]. For this application, the chosen GaAsPN alloy must satisfy both conditions of perfect lattice-matching to Si (to allow the growth of thick layers) and a band gap of 1.7 eV. Another dilute nitride quaternary alloy (InGaPN) is expected to fulfill these conditions. Fig. 3-8 shows the band gap energy calculated with the TB model for the GaAsPN (InGaPN) alloy as a function of As (In) and N contents to keep a perfect lattice-matching to Si. Obviously, because the N content is experimentally limited to a few percents, the study of the GaAsPN quaternary alloy as a bulk material is relevant in the small As content range (few percents). According to these calculations, the use of InGaPN for the top solar cell would require a slightly larger N content than in GaAsPN. Moreover, the fractional Γ character is the same for both alloys with band gap at 1.7 eV ($1 - s_N = 0.31$). Given this result and that InN bonds are usually difficult to deal with from the growth point of view[32], we have only studied the GaAsPN alloy.

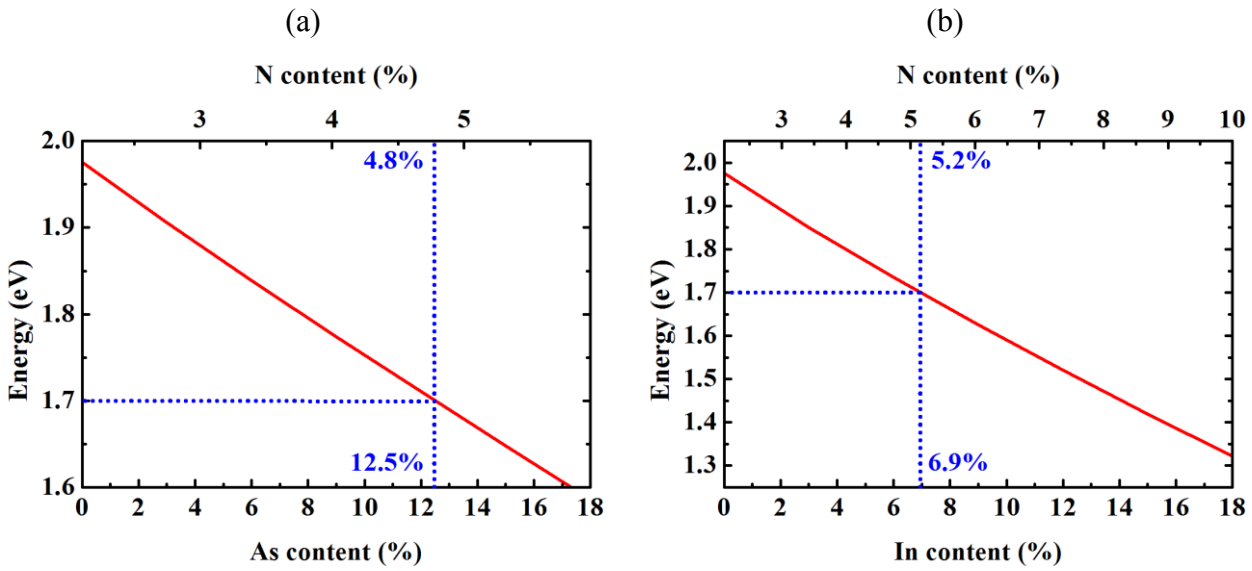

Fig. 3-8: TB calculation of the band gap of quaternary alloys (a) GaAsPN and (b) InGaPN guaranteeing the perfect lattice-matching to Si.

The GaAsPN layer studied in this part is grown on an undoped GaP substrate after the deposition of a 100 nm thick GaP buffer. A 10 nm thick GaP capping layer is added. A very small lattice-mismatch of 0.02 % is achieved by growing at a temperature of 480 °C, with a growth rate of 0.2 ML.s^{-1} and by adjusting the As flow[18] to maintain a low As incorporation of a few percents. The exact composition cannot be unambiguously determined by HRXRD because of the presence of three group-V elements[33].

Fig. 3-9 shows the TRPL results for bulk GaAsPN at 10 K. The trends are very similar to Fig. 3-7 for bulk GaPN. The main difference is the red-shift of the emission energy due to the As incorporation. The decay times measured on Fig. 3-9(b) are also slightly smaller. The band to band transitions observed on the high energy side at short times are also more visible.

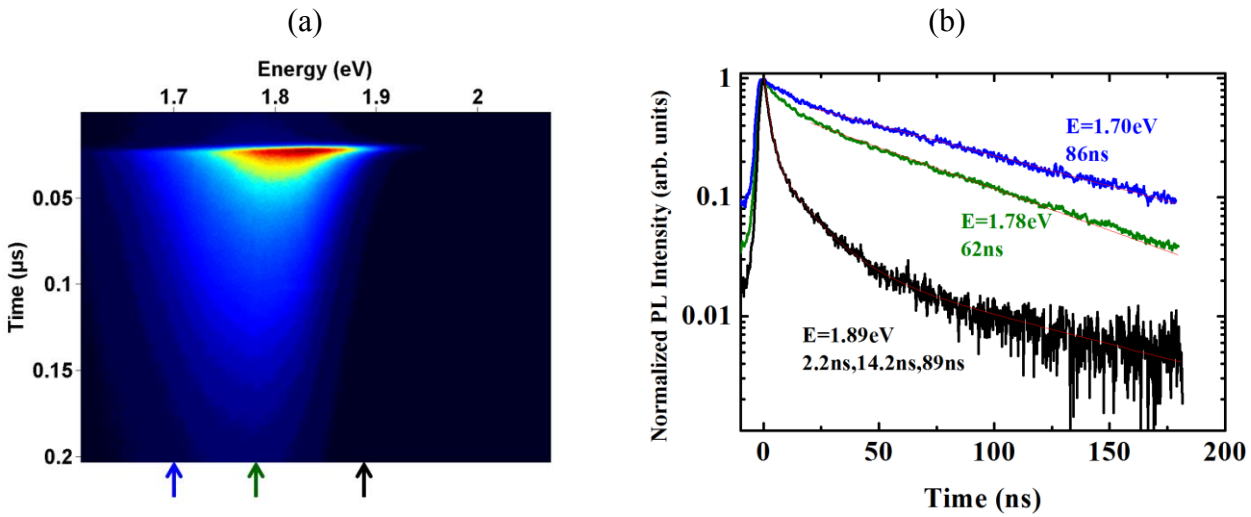

Fig. 3-9: (a) Streak camera image of bulk GaAsPN at 10 K and (b) PL dynamics at selected energies marked by colored arrows. The thin red lines show the exponential fit. The excitation density is 3500 W.cm^{-2} and the repetition rate is 4 MHz.

This sample is also studied by TRPL as a function of temperature. Fig. 3-10(a) shows the time-integrated PL spectra as a function of temperature. The position of the PL peak is plotted in Fig. 3-10(b).

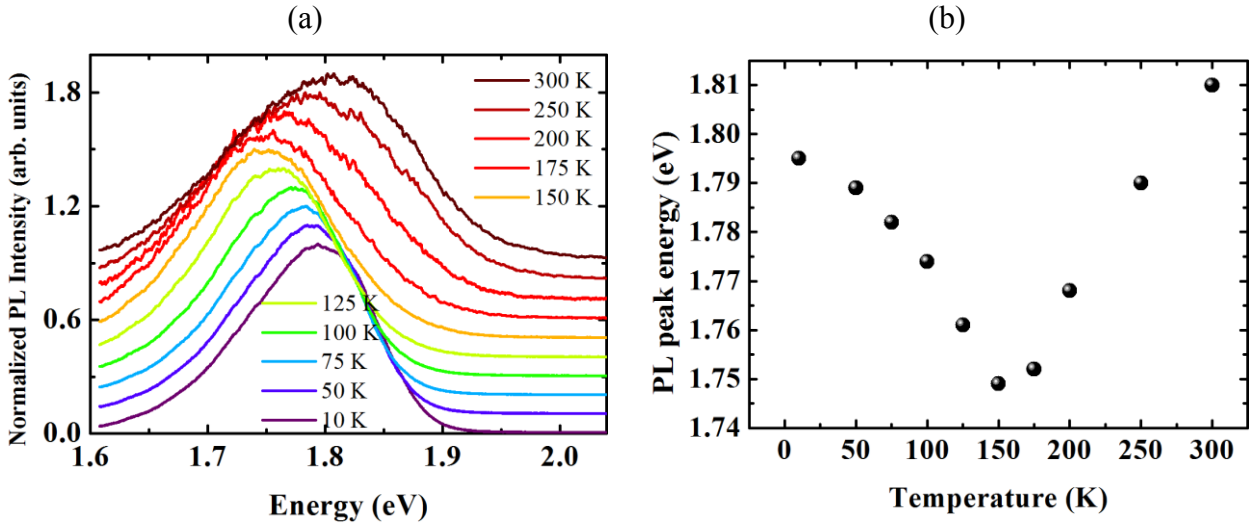

Fig. 3-10: (a) Normalized time-integrated PL intensity at various temperature. An offset of 0.1 is added between the spectra for clarity. (b) Position of the maximum time-integrated PL intensity as a function of temperature.

From 10 K to 150 K, the PL peak is dominated by recombination of localized excitons. Above 150 K, the PL peak blue-shifts and broadened on the high energy side. The localized carriers get enough thermal energy and begin to escape into the delocalized states. This phenomenon is common in disordered structure and is called the S-shape behavior[34–37]. It is important to notice

that the last portion of the S curve (the red shift at high temperature) is not visible in Fig. 3-10(b) because experiments have been performed up to 300 K. We will provide a more detailed analysis about this phenomenon in the study of GaAsPN QW (see section 3.3.3).

The PL dynamics is also strongly affected by temperature. Fig. 3-11(a) shows the variation of the decay time as a function of temperature. Because the energy integrated PL dynamic is strongly multi-exponential, the mean decay time is estimated by measuring the ratio between intensities just after and just before the laser pulse.

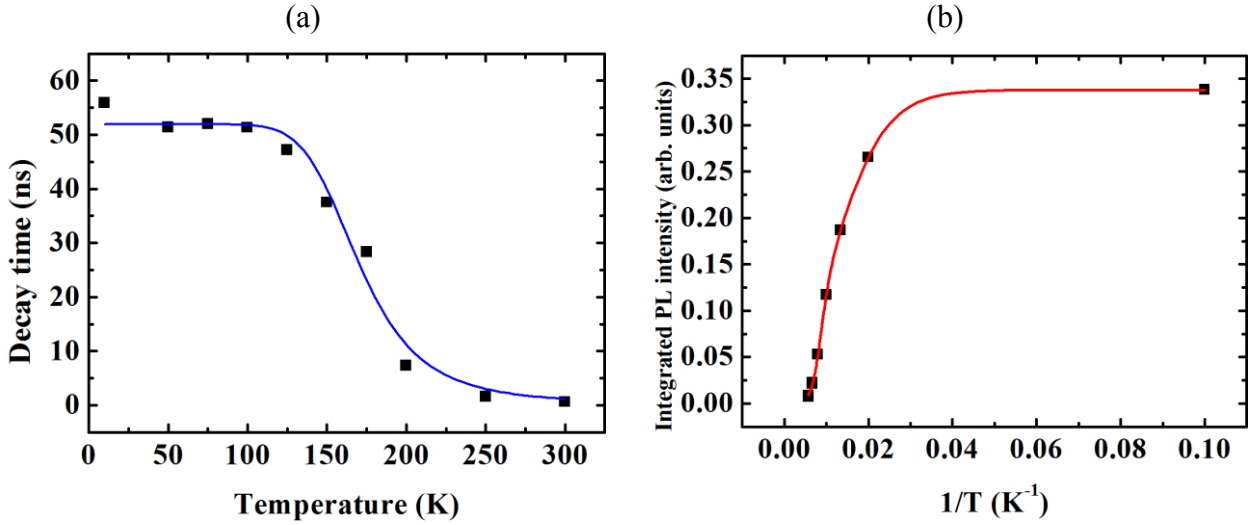

Fig. 3-11: (a) Decay time of bulk GaAsPN as a function of temperature. The blue line is a guide to the eye. (b) Integrated PL as a function of inverse temperature. The red line shows the fit with an Arrhenius law with two activation energies.

The decay time is strongly reduced above 150 K which is due to the escape of excitons from localized states. When the carriers are delocalized, they are also likely to meet a defect where they recombine non-radiatively. Consequently the PL intensity is quenched by heating. Fig. 3-11(b) shows the temperature dependence of the integrated PL intensity. The experimental data can be well fitted by an empirical Arrhenius law involving two activation energies:

$$I = \frac{I_0}{1 + \alpha_1 \exp\left(\frac{-E_{a1}}{kT}\right) + \alpha_2 \exp\left(\frac{-E_{a2}}{kT}\right)}$$

where α_1 and α_2 are related to carriers escape efficiencies toward non-radiative levels. The two activation energies are found to be 13 meV and 83 meV. Interestingly, the first one corresponds

to a temperature of 150 K which is in very good agreement with the observation made in Fig. 3-10(b) where the PL mechanism strongly change at this temperature.

3.2 Study of GaAsP/GaP quantum wells

Increasing As content is expected to both increase the Γ character of the CBM and decrease the band gap. Unfortunately, it also increases the lattice constant and thus requires a larger N incorporation to satisfy the lattice-matching condition needed to grow thick layers. Nevertheless, a tolerance on the lattice-mismatch can be accepted when growing thin layers; i.e. below a given critical thickness. In this way, the section 3.3 is devoted to the study of GaAsPN QW with a large As content (above 70 %) that can be grown coherently but compressively strained on Si substrate. We first attempt to understand the properties of nitrogen free GaAsP/GaP QW.

The structures studied in this section have been grown at 580 °C using GSMBE on non-intentionally doped GaP(001) substrate. The stack consists of a 360 nm thick GaP buffer layer, on which five 2.7 nm thick $GaAs_{0.7}P_{0.3}$ QW (composition estimated by HRXRD measurements) separated by 30 nm thick GaP barriers are grown. Finally a 20 nm thick GaP capping layer covers the whole heterostructure.

Fig. 3-12 shows the temperature dependence of the PL spectrum for the GaAsP/GaP QW heterostructure. The experimental setup is the same as in section 3.1 (cw laser diode emitting at 405 nm). The maximum emission intensity observed at 1.96 eV at low temperature is red-shifted by 50 meV between 12 K and 300 K. The low–temperature spectrum exhibits a second feature 30 meV below the main peak as already observed in similar structures[38].

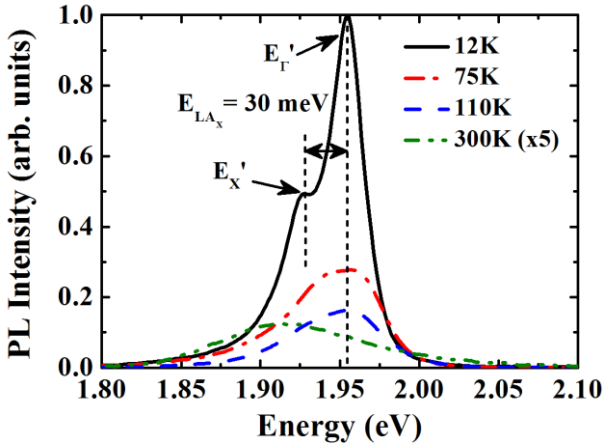

Fig. 3-12: Temperature dependent cw-PL spectra of GaAsP/GaP QW structure from 12K to 300 K. E_Γ' and E_X' are reported at 12K and are separated by zone-edge LA phonon energy (30 meV). The phonon replica reveals wave function mixing over indirect and direct states.

The PL dynamics extracted from TRPL measurements is shown in Fig. 3-13. The experimental setup used in this part is described in Appendix A. The repetition rate is 80 MHz. The decay times are found to be much longer than the repetition period of the laser (12 ns) even at room temperature. These observations are related to small radiative transition rates but also to small non-radiative recombinations.

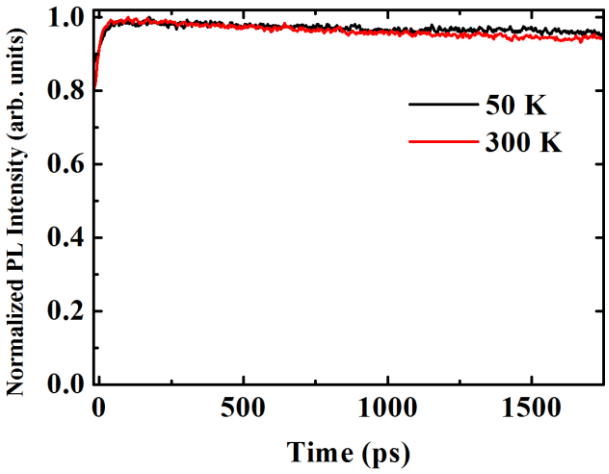

Fig. 3-13: PL dynamics of GaAsP/GaP QW at 50 K and 300 K. The repetition rate is 80 MHz. The excitation density is estimated to be about 700 W.cm^{-2}.

The nature of the interband transitions in GaAsP/GaP QW is investigated using the TB model. Fig. 3-14 represents the electronic band structure of the resulting QW, composed of 10 $GaAs_{0.7}P_{0.3}$ monolayers biaxially strained and embedded into GaP barriers. Conduction band and valence band energy variations are represented along the Λ and Δ directions of the QW Brillouin

zone. The first Γ→Γ and X_{XY}→Γ transition energies are found equal to $E_Γ$=2.23 eV and E_X=1.97 eV respectively. The latter is consistent with the PL spectrum (Fig. 3-12). The indirect character is also consistent with the observed very long decay time. Room temperature luminescence efficiency is explained by a mixing of "X" and "Γ" like bulk Bloch wave function in the E_X QW electronic wave function due to interface disorder[21,39,40]. The main experimental PL peak at an energy $E_Γ$'=1.96 eV corresponding to E_X in Fig. 3-14 is thus associated with a Γ→Γ -like transition originating from the Γ Bloch wave function component. The E_X' feature in Fig. 3-12 is a phonon replica which is associated with the transition X→Γ, i.e. originating from the X Bloch wavefunction component. For this component, emission of zone edge LA phonon is necessary for the conservation of k momentum during the emission process, leading to LA_X energy offset (E_X'=E_X-E_{LAX}) with E_{LAX}=29 meV[38].

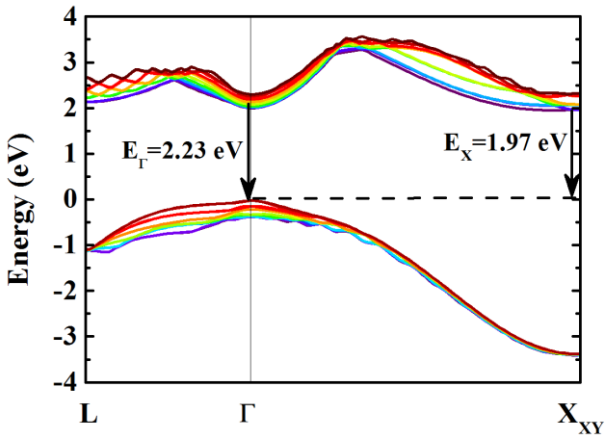

Fig. 3-14: Tight-binding simulation of electronic band structure of 8 $GaAs_{0.7}P_{0.3}$ monolayers biaxially strained on GaP. The first Γ→Γ and X_{XY}→Γ transitions are reported.

3.3 Study of GaAsPN/GaP(N) quantum wells

The study of GaAsPN QW is of paramount importance because these QW are up to now the nanostructure choice for the active zone leading to the best results in lasing operation (electrically pumped lasers have been reported on GaP[41] (at room temperature) and on Si[42] (below 150 K)).

3.3.1 First experimental observations

To highlight the effect of nitrogen incorporation, a similar nitrogen-containing structure has been grown with growth conditions strictly identical to those described in section 3.2. The

360 nm thick GaP buffer layer is replaced by a 300 nm thick GaP buffer layer followed by a 60 nm thick $GaP_{0.995}N_{0.005}$ layer. The 30 nm thick GaP barriers between the wells are replaced by 30 nm thick $GaP_{0.995}N_{0.005}$ barriers and the five QW are now composed of $GaAs_{0.6975}P_{0.2975}N_{0.005}$ alloy. The composition of $GaP_{0.995}N_{0.005}$ layers has been estimated from HRXRD measurements. On the contrary the composition of QW cannot be estimated unambiguously. We have simply assumed that at this low N content (N=0.5 %), the incorporation is the same in both barrier and QW and that the presence of atomic N at the surface of the sample during the growth has no influence on the As/P relative incorporation so that the As/P concentration ratio is similar in both GaAsPN and GaAsP samples (section 3.2).

Fig. 3-15 presents the temperature dependent cw-PL spectra of the GaAsPN/GaPN QW. Two main peaks are now distinguishable. The peak at lowest energies corresponds to GaAsPN QW, while the strong luminescence of the GaPN barriers is now clearly visible at low temperature. Comparison between Fig. 3-12 and Fig. 3-15 reveals the spectacular effects of the incorporation of nitrogen. Firstly, the peak originating from the QW strongly red-shifts from 1.96 eV for GaAsP to 1.72 eV for GaAsPN (at 12 K) due to the giant band gap bowing effect. Secondly, the intensity of the QW peak is slightly increased as compared to Fig. 3-12 (the same arbitrary units are used and experiments have been performed in the same conditions). The peak shape is also strongly changed. The FWHM at low temperature increases from 34 meV for GaAsP (including the phonon replica) to 105 meV for GaAsPN. The broadening mainly occurs on the low energy side due to the band tail of localized states. Finally, with increasing temperature, GaAsPN peak intensity overtakes that of GaPN, which suggests a good carrier confinement in QW at room temperature.

Fig. 3-16 presents the TRPL dynamics of the GaAsPN QW peak at 50 K. The streak camera image of Fig. 3-16(a) is very similar to what has been observed in bulk GaPN and GaAsPN (see Fig. 3-7 and Fig. 3-9) with a long decay time for the low energy tail and a shorter dynamic for the band to band recombination. Nevertheless, the decay times are shorter than in the bulk GaPN and GaAsPN materials studied in previous sections. Indeed, the decay time in the low energy tail can be estimated around 12 ± 2 ns.

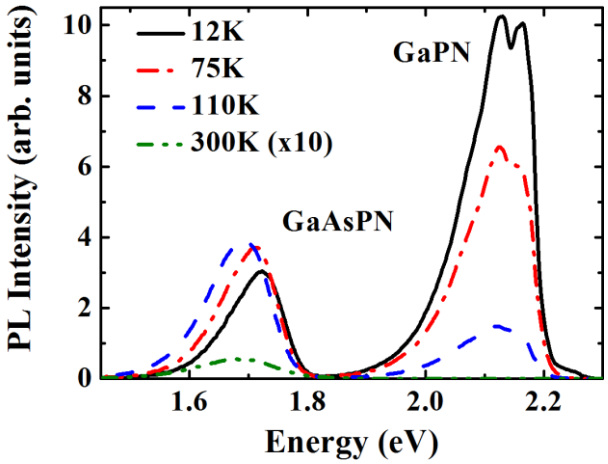

Fig. 3-15: Temperature dependent cw-PL spectra of $GaAs_{0.6975}P_{0.2975}N_{0.005}/GaP_{0.995}N_{0.005}$ QW structure from 12 to 300 K. The same arbitrary units than those of Fig. 3-12 are used.

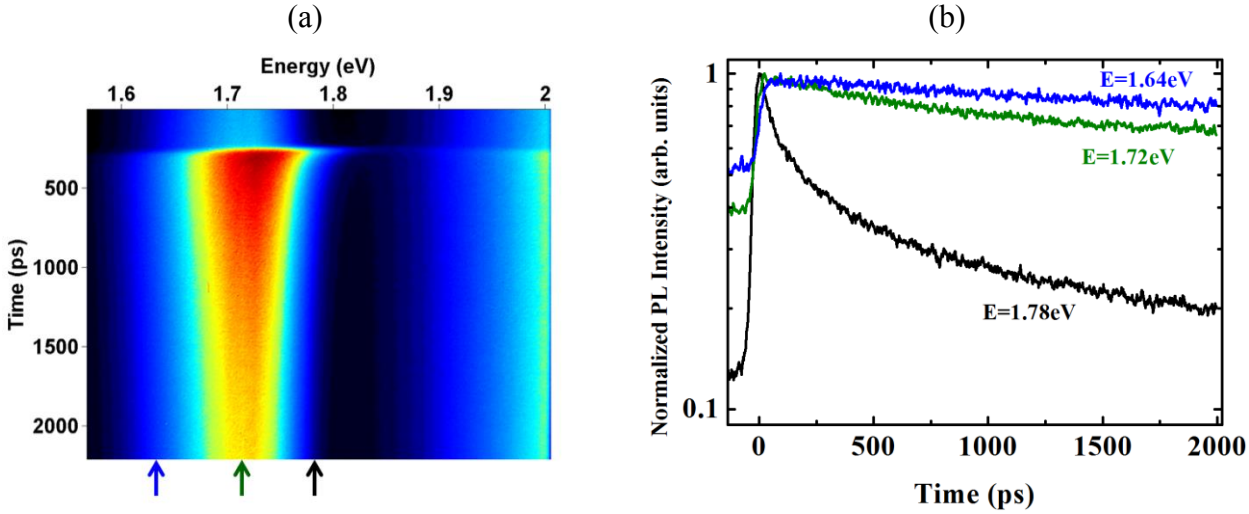

Fig. 3-16: (a) Streak camera image of $GaAs_{0.6975}P_{0.2975}N_{0.005}/GaP_{0.995}N_{0.005}$ QW at 10 K and (b) PL dynamics at selected energies marked by colored arrows. The excitation density is 700 W.cm^{-2} and the repetition rate is 80 MHz.

3.3.2 Theoretical study of the electronic band structure of GaAsPN/GaPN QW

Comprehensive elements can be brought by simulating the electronic band structure of GaAsPN/GaPN QW with the $sp^3d^5s^*s_N$ TB model. First of all, it is necessary to understand the role of both As content and strain on the nature of the CBM in the GaAsPN alloy. Indeed, as underlined in section 3.1, the character of the CBM in dilute nitride alloys depends on the nature of the host material band gap (indirect or direct) and on the position of the N-related level relative to the CBM.

3.3.2.1 Simulation of strained bulk GaAsPN

Fig. 3-17 shows the calculated valence and conduction bands of GaAsP:N alloys in the N doping regime as a function of the As content for two configurations: unstrained (dashed lines) and strained on Si (001) (solid lines). The N concentration is set to be infinitesimally low and the N-level is represented by the dash-dotted line. The energy reference is the VBM of bulk GaP. We find a direct-indirect band gap crossover in the unstrained GaAsP alloy occurring for about 50 % of As content, in agreement with experiment[43]. The position of the N-level relative to the conduction band is located 170 meV under the X point of unstrained GaP and 131 meV above the Γ point of unstrained GaAs. The L-band is not represented for clarity. The CBM of unstrained $GaAs_yP_{1-y}$ crosses the N-level for $y \approx 0.75$ and the maximum separation between the N-level and the conduction band edge of unstrained $GaAs_yP_{1-y}$ is obtained for $y \approx 0.45$. This is consistent with the early results of Groves *et al.*[44]. For GaAsP:N strained on Si (001) , the VBM states are heavy-hole like. The degeneracy of X conduction bands states is also lifted with an upper Xz level and lower Xxy valleys as a direct consequence of the compressive strain. The Γ CBM is found above the Xxy CBM for all composition range, in agreement with the results of Prieto *et al.* for the case of GaAs strained layer on GaP(001) which is reported to be slightly indirect[45] close to the X-point. The N-level is insensitive to strain as in reported previous works[46,47] and lies below the CBM of strained GaAsP whatever the As content.

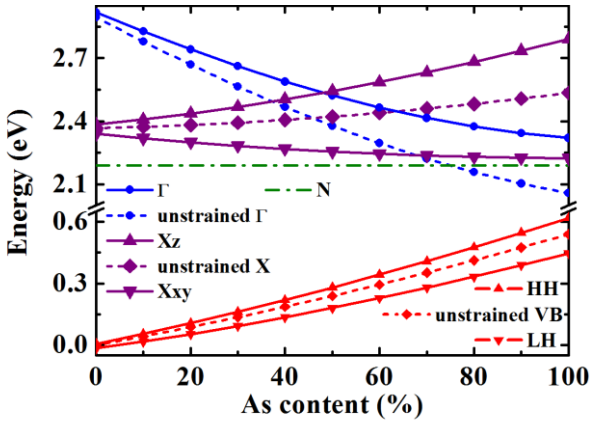

Fig. 3-17: Conduction band and valence bands of bulk GaAsP:N with a N concentration infinitesimally low at 0 K. Dashed lines represent the unstrained case, solid lines represent the biaxially strained case, and the green dash-dotted line represents the position of the N-level. The L band is not represented for clarity.

Fig. 3-18 shows the effect of N concentrations on the Γ conduction band levels in the diluted regime. As predicted by the **k·p** BAC model, the N level interacts with the Γ band of the host strained material to form two subbands Γ- and Γ+. The other bands are not represented for clarity because the energy shifts with respect to the positions in Fig. 3-17 are weak. We just briefly describe the major features. The valence bands, and the Xxy and Xz conduction valleys, are only affected by the weak decrease of the compressive strain due to the nitrogen incorporation. Finally, the L conduction band states have a similar but weaker behavior than the Γ state leading to the coupling of the host material L-bands and the N-related level, and the appearance of two bands, namely L+ and L−. The relative contribution of the s_N orbital to the Γ− and Γ+ wave functions is also shown in Fig. 3-18 for various N and As contents. The Γ− wave function evidences a predominant s_N character as a consequence of the lower energetic position of the N-level relative to the Γ band of strained GaAsP (see Fig. 3-17). This striking result is in contradiction with recent papers[33,48] where the biaxial strain or lateral valleys are not taken into account. The second number given in Fig. 3-18, is the effective mass in the (100) direction. The Γ− band evidences a strong effective mass because of its N character but it decreases with N content because of the position of the N level below the Γ band of the host material. The decreasing of the effective mass with increasing N content has been recently proposed as an interpretation of the observed reduced energy scale of the compositional disorder in GaAsPN QW when increasing N content[49,50]. According to Fig. 3-17 and Fig. 3-18 it is the consequence of the N level located below the CBM of the strained GaAsP host material.

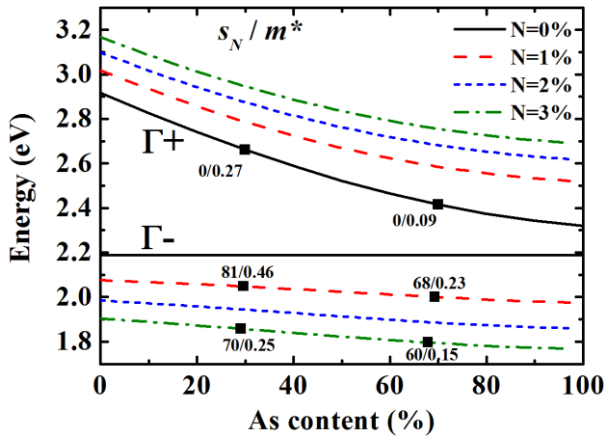

Fig. 3-18: Γ- and Γ+ conduction bands for bulk GaAsPN biaxially strained at different nitrogen concentrations at 0 K. The energy reference is the same as in Fig. 3-17. The percentage of s_N contribution to the wave function is represented by the first number. The second number is the effective mass in the (100) direction in units of free electron mass m_0.

3.3.2.2 Simulation of GaAsPN/GaPN QW

Fig. 3-19 shows the calculated band structure of a 2.7 nm thick $GaAs_{0.6975}P_{0.2975}N_{0.005}$ QW with $GaP_{0.995}N_{0.005}$ barrier strained on GaP (001) close to Brillouin zone center. The envelope wave functions of the first conduction and valence subbands are represented in the two insets on the left. The envelope wave functions of the CBM and VBM of the barrier are plotted in the insets on the right evidencing a type-I in real space. Only one electron state is found to be confined in the QW whith a confinement energy of 34 meV, whereas four hole levels are confined (two HH states and two LH states) with a confinement energy of 346 meV for the first hole level. The ground energy transition in the well is equal to 1.78eV. This energy is in very good agreement with the high energy feature observed at short times in the streak camera image of Fig. 3-16(a).

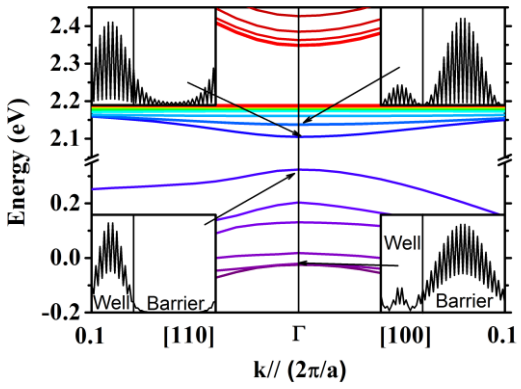

Fig. 3-19: Band structure of a 2.7 nm thick ($GaAs_{0.6975}P_{0.2975}N_{0.005}$/$GaP_{0.995}N_{0.005}$) QW biaxially strained on GaP substrate at 0 K. The envelope wave functions of the conduction and valence band extrema for the well and the barrier are represented in the insets. The energy reference is the same as in Fig. 3-17.

3.3.3 Temperature dependent PL experiments

As reported in section 3.1.2 (Fig. 3-10), the bulk GaAsPN PL spectrum exhibits unusual behavior with temperature. Similar temperature dependent PL experiments have been performed on GaAsPN/GaPN QW below 300 K in a cryostat but also above room temperature using a hot plate. Fig. 3-20(a) presents the energy of the cw-PL peak from 10 K to 600 K. Please notice that the strong uncertainty on the measurement of the temperature above 300 K prevents any quantitative analysis in this temperature range. Nevertheless, the data points clearly follow the S-shape behavior that has been reported in all dilute nitride QW[37,51,52]. At 10 K, the photogenerated carriers are trapped in local potential minima which are close to the region where

they have been excited. When increasing the temperature, the carriers become more mobile and thermalize to the lowest localized states. This results in the strong red-shift observed up to 150 K. Above 150 K, carriers get enough thermal energy to detrap from the localized states and start to recombine into extended states which are higher in energy. This results in a blue-shift of the PL peak between 150 K and 300 K. Above 300 K, the PL peak red-shifts following the more usual trend of a Varshni law which describe the temperature dependence of the band gap in many semiconductors[53].

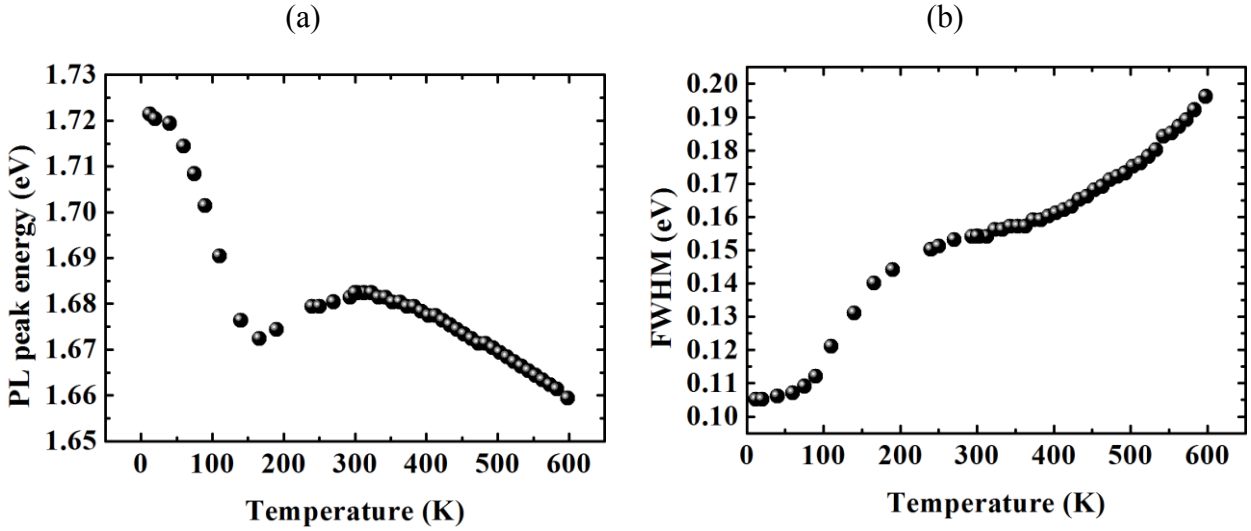

Fig. 3-20: (a) Position of the PL peak of GaAsPN/GaPN QW as a function of temperature. (b) FWHM as a function of temperature. The excitation density is 80 W.cm^{-2}.

Simultaneously to the S-shape behavior, the FWHM is expected to exhibit unusual temperature dependence. Fig. 3-20(b) presents our measurements on GaAsPN/GaPN QW. The FWHM is found to monotonously increase when increasing temperature but with a clear plateau between 250 K and 350 K. This behavior is strongly different from what is usually observed in similar disordered systems. Indeed, it has been observed in GaInAsN/GaAs QW[54] as well as in GaAsPN/GaP QW[37] that the PL linewidth is maximum for a temperature equal or slightly higher than the temperature for which the PL peak energy is a local minimum corresponding to the maximum Stokes shift (150 K in Fig. 3-20(a)).

Several theoretical models have been proposed to describe both S-shape and FWHM behaviors[34,36,55,56]. The model of Baranovskii *et al.*[55] uses a Monte Carlo simulation to calculate the temperature induced hopping of excitons in a density of states of spatially distant localized centers. The crux of this model is the choice of the density of localized states. Because of the

exponential low-energy tail of the PL spectrum, an exponential density of states $\propto \exp(E / E_{loc})$ is often considered. The same authors[54] have demonstrated that according to this model E_{loc} is related through universal relations to the FWHM at T = 0 K ($FWHM(0) \simeq 2.5E_{loc}$), the temperature at which the Stokes shift is maximum ($T \simeq 0.8E_{loc} / k_B$) and the temperature at which the FWHM is maximum ($T \simeq 1.1E_{loc} / k_B$). With the low energy tail of the PL spectrum, we measure E_{loc} = 46 meV. A similar value of 40 meV has been measured by Karcher *et al.* in GaAsPN/GaP QW[37]. The theoretical value of FWHM at low T is $FWHM(0) \simeq 2.5E_{loc}$ = 115 meV which is in good agreement with the measured value of 105 meV. Nevertheless, the experimental Stokes shift is maximum at 150 K and should correspond to a localization energy of 16 meV which is far below the expected value of 46 meV. Such a discrepancy between different measurements of the localization energy has already been observed and has been attributed to the existence of two different length scales for the disorder[37,57]. In bulk GaAsBi, a first length is attributed to alloy fluctuations and long range whereas a second length is attributed to clustering effects and short range disorder. Thickness fluctuations have been proposed as the origin of the long range disorder in GaAsPN/GaP QW[37]. Karcher *et al.*[37] have proposed that the shape of the density of states related to this second disorder is also exponential. Nevertheless the important difference in our observations comes from the FWHM which exhibits a plateau instead of a maximum. Actually, it has been demonstrated that a Gaussian density of states can be responsible of a saturation of the FWHM above a given temperature[55]. We can thus propose that in the present study, two scales of disorder exist with one being better described by a Gaussian density of states.

Other interesting behaviors can be observed on the integrated PL intensities of both GaAsPN QW and GaPN barriers (Fig. 3-21). From 10 K to 150 K, the intensity of GaPN barriers quenches while the intensity of GaAsPN QW increases. This effect occurs because carriers are trapped in the localized centers of GaPN barriers at very low temperature. But when the temperature is increased, both carrier mobility in GaPN and carrier capture by the GaAsPN QW are enhanced which results in an increase of the QW PL intensity.

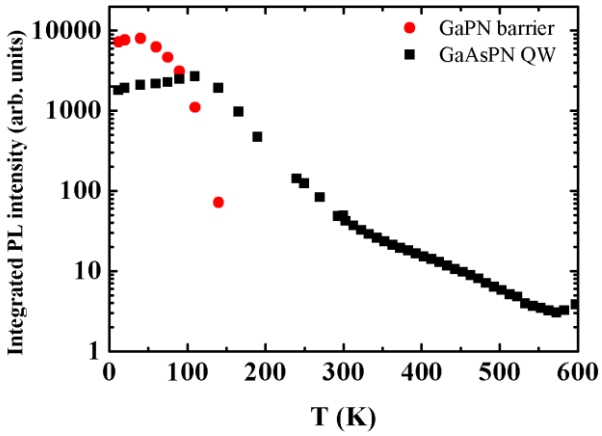

Fig. 3-21: Integrated PL intensity of GaAsPN QW and GaPN barriers as a function of temperature.

3.3.4 Effects of nitrogen content and QW thickness

The $GaAs_{0.7}PN_{0.005}/GaPN_{0.005}$ QW structure studied in sections 3.3.1 to 3.3.3 is strongly influenced by disorder effects. Moreover, the emission wavelength is 740 nm which is far below the transparency window of Si (> 1.1 µm). In this section, we study the effects of QW thickness and composition on both disorder effects and emission wavelength.

Fig. 3-22 presents the room temperature PL spectra of the $GaAs_{0.7}PN_{0.005}/GaPN_{0.005}$ QW structure of previous sections (black line) and of a similar (same thickness and same number of QW) QW structure with a higher N and As content (red line). Here again, the determination of As and N contents is tricky. We estimate the As content to be around 88 % (determined from the comparison of the energy of the PL peak of a nitrogen free structure with the TB calculation). The N content is estimated around 1.5 %. The PL peak is strongly red-shifted to around 1.4 eV (900 nm) due to both higher As and N content. The localization energy (measured with the slope of the low energy tail at low temperature) is slightly reduced to 37 meV. It is important to mention that this structure has been grown under different growth conditions (by SSMBE) that may affect the disorder scale, but this is consistent with the recent results of Jandieri *et al.* who has demonstrated that increasing the N content reduces the disorder effects[49,50]. Unfortunately, Fig. 3-22 also shows that the PL intensity is strongly reduced in this structure. It may come from three reasons. Firstly, a higher N content results in a higher density of point defects. Secondly, the compressive strain is stronger in the $GaAs_{0.88}PN_{0.015}$ QW which can result in extended defects like dislocations. Finally, even though the disorder is expected to be smaller in the

$GaAs_{0.88}PN_{0.015}$ QW structure, the carrier mobility is enhanced and the sensitivity to defects increases.

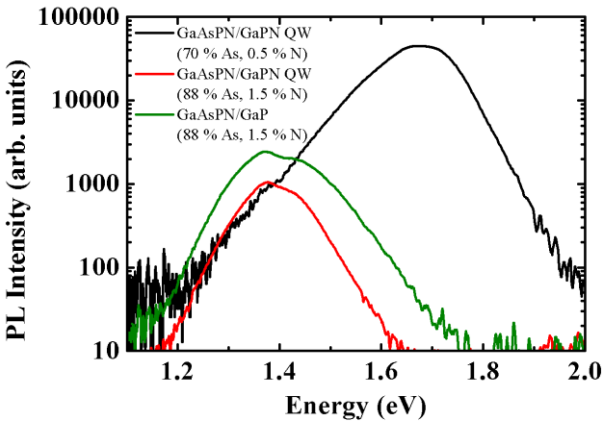

Fig. 3-22: Room temperature PL spectra of five 2.7 nm thick GaAsPN/GaP(N) QW with various N and As composition. The splitting of the peak at 1.37 eV is an artifact of our spectrometer.

The incorporation of N in the barriers is an additional source of luminescence efficiency reduction. Indeed, from the results of section 3.3.1, we may expect that the density of states associated to localized states modify the carrier mobility and capture to the QW. Moreover, incorporation of N in the barriers may also create additional defects in the barriers and reduce the electron confinement in the QW as compared to N free barriers structure. The room temperature PL spectrum of $GaAs_{0.88}PN_{0.015}$/GaP QW is shown in Fig. 3-22 by the green line. This structure has been grown under strictly the same conditions than the $GaAs_{0.88}PN_{0.015}$/$GaPN_{0.015}$ QW structure excepting that the N valve has been closed during the barriers' growth. The integrated PL intensity is increased by a factor of 3.

Fig. 3-23(a) presents the influence of the GaAsPN QW thickness on the optical properties. In this section, a single GaAsPN QW is studied. Three samples corresponding to three different QW thicknesses have been grown under strictly similar growth conditions. Nevertheless, we cannot be sure that the composition is strictly identical in the three QW. Indeed, it has recently been proposed that the N incorporation is enhanced by an increased surface roughness[58]. A thicker QW may result in a rougher surface due to the partial strain relaxation and thus to a larger N incorporation. Fig. 3-23(a) shows that increasing the QW thickness decreases the room temperature PL peak energy due to the reduced quantum confinement effect (and a possible larger N content). Nevertheless, it also reduces the integrated PL intensity. The insert of

Fig. 3-23(a) represents the normalized PL intensity in a semilog scale. The localization energy measured by the slope of the low energy tail is found to be similar in the 1.4 nm thick and in the 2.2 nm thick QW but it is significantly reduced for the 3.3 nm thick QW. This can be due to a larger N content but also to the reduced sensitivity to thickness fluctuations when the thickness increases.

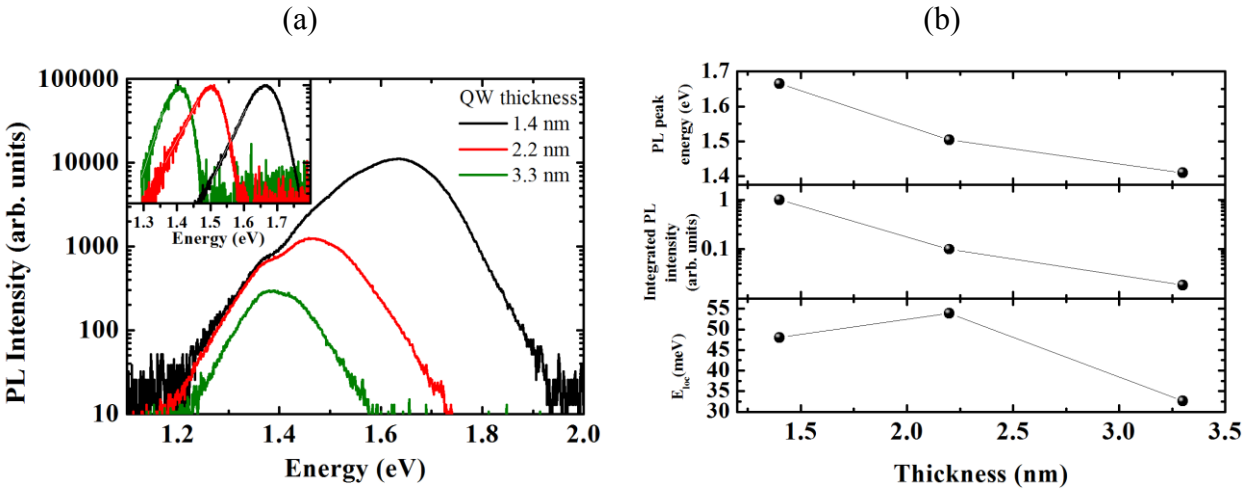

Fig. 3-23: (a) Room temperature PL spectra of a single GaAsPN/GaP QW as a function of the QW thickness. The insert show the normalized PL intensity at 10 K. The splitting of the peak at 1.37 eV is an artifact of our spectrometer. (b) Energy of the PL peak at 10 K, integrated PL intensity at room temperature and localization energy at 10 K for a single GaAsPN/GaP QW as a function of thickness.

3.3.5 Carrier dynamics in GaAsPN QW

In this section we analyze more in details the dynamics of recombination and injection of carriers in GaAsPN/GaP QW. The structure studied in this section consists of 5 $GaAs_{0.88}PN_{0.015}$/GaP QW.

Fig. 3-24(a) presents the time dependence of the total TRPL intensity (energy integrated) of GaAsPN QW as a function of the excitation density. The dynamics exhibits strong non-monoexponential behavior which cannot be fitted with less than triple exponential decays using three independent time constants. The contribution of fast decay components increases at highest excitation densities. Such an observation has already been made by Jandieri *et al.*[59]. In the framework of Monte Carlo simulations, they have interpreted this behavior as the result of a competition between the slow radiative recombination of localized excitons and the fast capture by non radiative centers. Fig. 3-24(b) shows the corresponding time-integrated TRPL intensity as a function of excitation density in a logarithm scale (black square points). The variation is found

to be sub-linear. This behaviour is consistent with the hypothesis of a non-radiative process which is enhanced by the carrier density. But it could also be related to a decrease of the capture efficiency with increasing carrier density. Actually, the PL maximum intensity, which is detected just after the laser pulse, is found to be slightly over-linear with the excitation density (red circle points in Fig. 3-24(b)), which rules out this second hypothesis. To provide an explanation of the over-linearity, we need to analyse the results as a function of energy.

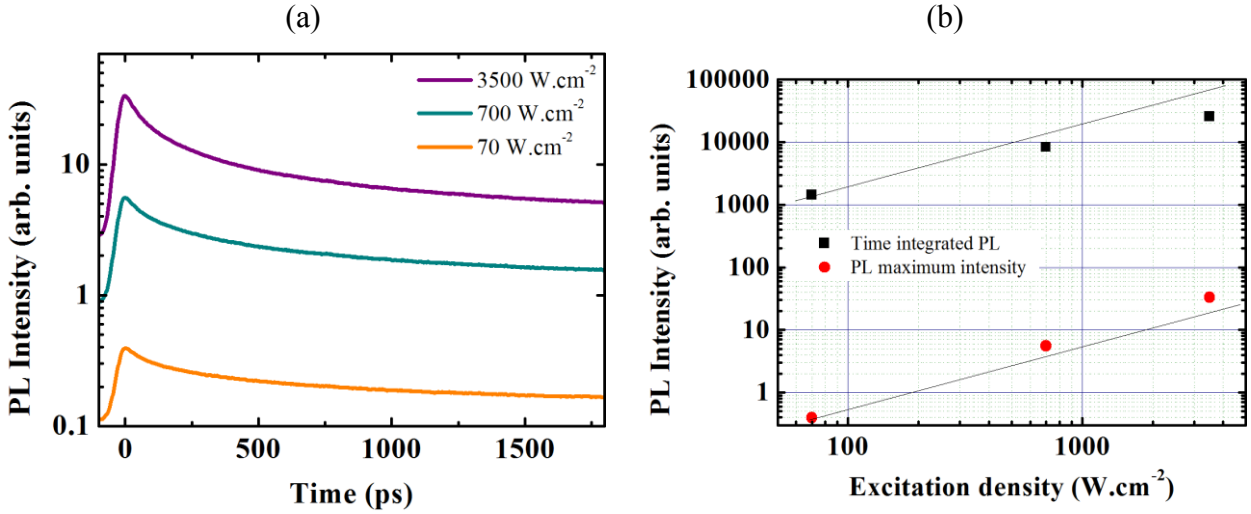

Fig. 3-24: (a) Total PL (energy integrated) dynamics of GaAsPN/GaP QW as a function of excitation density. (b) Time integrated PL intensity as a function of excitation power density (black square points) and PL maximum intensity (just after the laser pulse) (red circle points). The thin black line is a guide to the eye to match with an expected linear variation. The temperature is 10 K and the repetition rate is 80 MHz.

The interpretation of Jandieri *et al.*[59] relies on the hypothesis that both radiative localized states and delocalized states contribute to the energy integrated spectrum with the same radiative recombination rate and that the fast dynamics observed at short times is due to a capture of delocalized excitons by non radiative centers. According to this picture, the radiative localized states have to be saturated at high excitation density to enhance the capture by non radiative defects. Nevertheless, there is no study showing this saturation effect of radiative localized states. Fig. 3-25(b) presents the PL dynamics at 10 K for the highest excitation density used in these experiments (3500 W.cm^{-2}) and for the four detection energies marked by the colored arrows in the streak image of Fig. 3-25(a). No saturation effect is clearly visible even on the low energy side (blue curve).

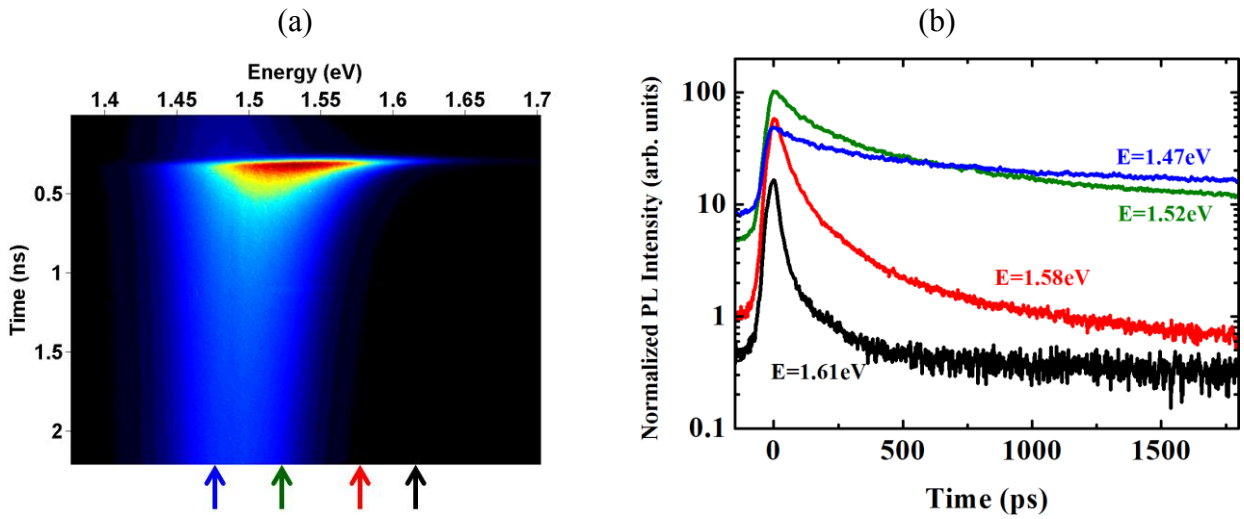

Fig. 3-25: (a) Streak camera image of GaAsPN/GaP QW at 10 K and (b) PL dynamics at selected energies marked by colored arrows. The excitation density is 3500 W.cm^{-2} and the repetition rate is 80 MHz.

The PL maximum intensity at selected energies (just after the laser pulse) is plotted in Fig. 3-26 as a function of excitation density. The blue triangle points (corresponding to the lowest detection energy marked by the blue arrow) follow a linear trend which seems to disagree with a saturation effect.

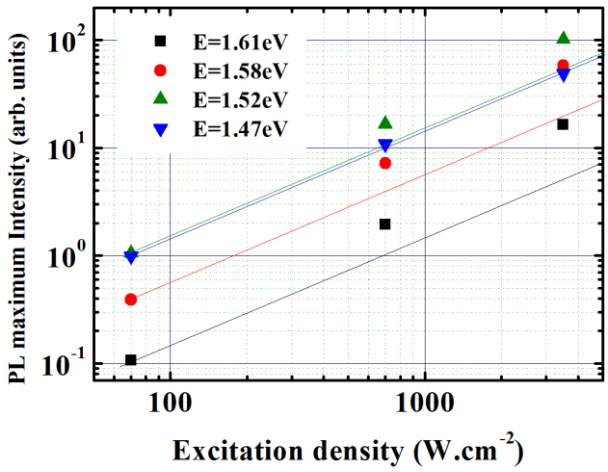

Fig. 3-26: PL maximum intensity (just after the laser pulse) at selected energies marked by colored arrows in Fig. 3-25(a). The thin lines are guides to the eye to match with an expected linear variation.

Nevertheless, the PL maximum intensity for the higher energy states (shown by green, red and black points) is found to be over-linear. The degree of over-linearity increases with increasing the detection energy. Thus, the linearity observed on the lowest energy state can be a sign of a partial saturation because it does not follow the over-linearity trend. It is important to mention that our excitation density range is much lower by at least one order of magnitude than the one employed

by Jandieri *et al.*[59]. Moreover, their QW are excited quasi-resonantly whereas we excite the structure in the GaP barriers where some carriers are expected to be lost. This can explain that the saturation effect is only partial in our case.

Now we have to explain the over-linearity trend, observed on the high energy states in Fig. 3-26 but also for the energy integrated study in Fig. 3-24(b). We can retain three reasons for this behavior. First, capture efficiency may be enhanced by the carrier density; i.e. a Auger assisted relaxation for example. Fig. 3-27 shows the PL rising for the four detection energies and the three excitation densities. The smallest temporal resolution that can be achieved with the experimental setup is 6 ps, but this is enough to roughly compare the rise times at different energies and excitation densities. The rise time does not seem to depend on the excitation density, which may exclude an enhanced capture efficiency with increasing the carrier density. Another interesting result (Fig. 3-27) is that the rise time increases for lower energy states. For the detection energy of 1.475 eV (blue arrow in Fig. 3-25(a)), the rise time is around 30 ps and larger for the highest detection energy (20 ps, black arrow in Fig. 3-25(a)). A possible explanation is that an exciton has to hop between spatially distant (but close) localized states to reach a low energy localized state[60]. The lower is the energy of the final localized state, the longer is this mechanism.

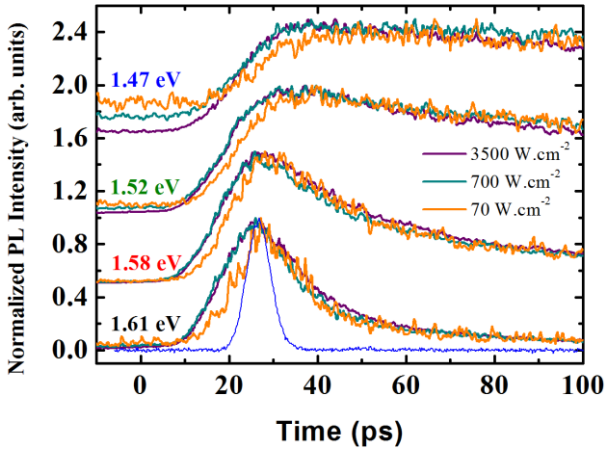

Fig. 3-27: Normalized PL rising of GaAsPN/GaP QW at selected energies show on the left and as a function of excitation density. An offset of 0.5 between the spectra at different energy is added for clarity. The thin blue line is the impulse response showing a temporal resolution of 6 ps.

A second possible reason for the over-linearity of the energy integrated PL maximum intensity (Fig. 3-24(b)) is that the highest energy states may be more radiatively efficient than the

lowest ones. Because the highest energy states are more populated at high excitation density, their contribution to the PL spectrum may be more significant. Nevertheless, Jandieri *et al.*[59] have obtained a better description of their time integrated PL spectra by taking equal lifetimes for localized and free excitons in their Monte-Carlo simulation. Moreover, it cannot explain the over-linearity at selected energies observed in Fig. 3-26.

A third more likely explanation relies on the fact that the barrier composition is not the one of pure GaP, but corresponds to a significant N fraction. Indeed, a broad PL peak extends from 1.8 eV to 2.3 eV at low temperature (see Fig. 3-28). This effect can be due to the exodiffusion of N atoms from the QW to the barrier, which may not be neglected considering the high growth temperature (580 °C) and the small size of the N atom. Thus, a significant number of carriers that are photo-created in the barrier are trapped by the N related localized states in the vicinity of the QW. Increasing the excitation density may lead to a saturation of these barrier localized states and consequently to an enhanced capture by the QW. The number of carriers in the QW thus increases over-linearly with the excitation density.

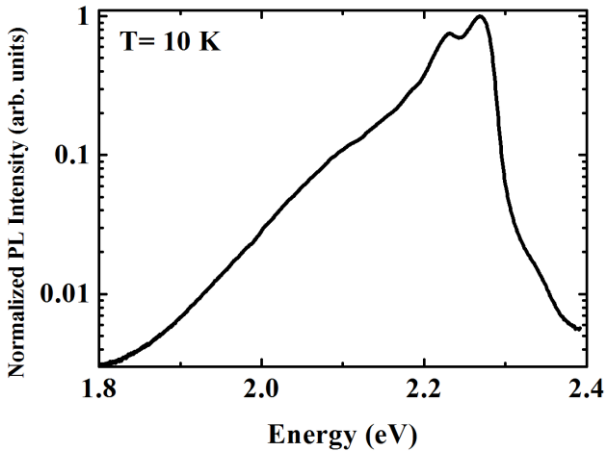

Fig. 3-28: Time integrated PL intensity of the GaP barrier. The excitation density is 3500 W.cm^{-2} and the temperature is 10 K.

The role of temperature is highlighted by the streak camera images taken at 100 K and 300 K (Fig. 3-29). The dynamics at 100 K is very similar to what has been observed at 10 K in Fig. 3-25(a). This proves that most of the carriers stay trapped in the low energy tail even at 100 K. On the contrary, the streak image of Fig. 3-29(b) taken at 300 K shows that the excitons get enough thermal energy to be transferred to states lying at higher energies. The role of non-

radiative states is enhanced as proved by the quenching of the decay time. The same trends have been observed by Baranowski *et al.* in InGaAsN/GaAs QW[61].

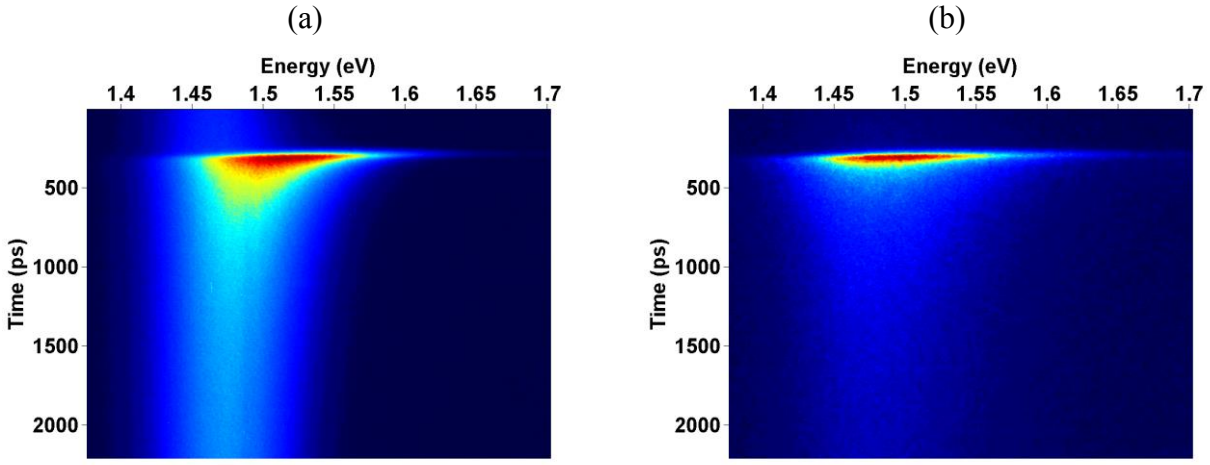

Fig. 3-29: Streak camera image of GaAsPN/GaP QW at (a) 100 K and (b) 300K. The excitation density is 700 W.cm^{-2} and the repetition rate is 80 MHz.

To summarize, this study shows that the radiative localized states and the non radiative states play an important role on the carrier dynamic in GaAsPN QW. Increasing the N content may decrease the influence of the radiative localized states as demonstrated by Jandieri *et al.*[49]. Increasing the QW thickness may have similar effect as shown in Fig. 3-23. Nevertheless, it may also enhance the role of non radiative defects. The composition in the barrier material has also consequences on the injection of carriers in the QW. Due to both radiative localized states and non radiative defects, GaAsPN/GaPN QW structures seems to be limited for laser applications Nevertheless, it is worth mentioning that the structures which have been studied in this thesis are as-grown structures. A post-growth annealing is expected to reduce both the disorder effect and the density of non-radiative states, as observed by many authors in dilute nitride systems[62].

3.4 Toward GaAsPN QW-based light emitters

In this section, we present the required steps for the development of GaAsPN QW based laser structures on both GaP and Si substrates. The composition of the QW is discussed through the theoretical study of the material gain. The cladding layers are also studied and the results on doping and contacts are presented. We first present the simplest case of light emitting diodes (LED) on GaP substrate.

3.4.1 Light emitting diodes

As both structures studied in sections 3.2 and 3.3.1 exhibit strong room temperature PL, two LED have been fabricated with the same $GaAs_{0.7}P_{0.3}$/GaP and $GaAs_{0.6975}P_{0.2975}N_{0.005}$/$GaP_{0.995}N_{0.005}$ active areas on n-doped GaP substrate. In both cases, active areas are grown between two 300 nm-thick doped-GaP layers with a nominal dopant concentration of 5.10^{18} cm^{-3} (Si for n-type and Be for p-type) by GSMBE. Annular metallic contacts with a diameter of 300 µm and a width of 50 µm are built using AuZn/Au/Ni deposition for p-type, and In deposition for n-type.

Electroluminescence (EL) at room temperature is obtained for both diodes as shown in Fig. 3-30 by black lines. Obviously, the differences between the GaAsP and the GaAsPN spectra are the same as what has been observed in PL spectra (Fig. 3-12 and Fig. 3-15), i.e. a strong red shift and a larger FWHM when N is incorporated. Intensity is also multiplied by a factor of about 6, making the red spot visible with the naked eye; even at a low excitation current (<1 mA).

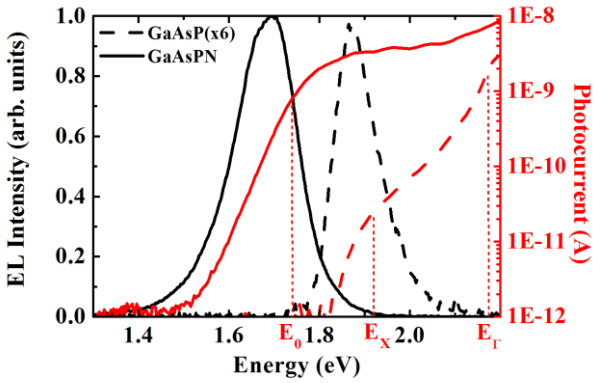

Fig. 3-30: Room temperature photocurrent (red lines) of $GaAs_{0.7}P_{0.3}$/GaP (dashed lines) and $GaAs_{0.6975}P_{0.2975}N_{0.005}$/$GaPN_{0.005}$ (solid lines) diodes superimposed on electroluminescence spectra (black lines). The indirect and the direct transitions calculated by TB simulations in sections 3.2 and 3.3.2.2 and corrected from temperature shifting (50meV) are indicated by vertical dotted lines.

Photocurrent experiments have also been performed on both diodes. The experimental setup is described in Appendix C. The results are compared to EL spectra in Fig. 3-30. The energies of the direct and/or indirect transitions calculated by the TB model in Fig. 3-14 and Fig. 3-19 and corrected from temperature shifting of 50 meV correspond to the observed absorption edges. The incorporation of nitrogen shifts the absorption edge towards lower energies but also enhances PC intensity by two orders of magnitude: PC at the first transition energies is 1.3 nA for

GaAsPN (at E_0 on Fig. 3-30) and only 24 pA for GaAsP (at E_X on Fig. 3-30). Moreover, the absorption profile shape is clearly modified. For GaAsPN QW, the steplike behaviour of the PC is attributed to a two-dimensional joint density of states and a pseudo-direct bandgap. We clearly see a softer PC increase for the GaAsP QW, which is consistent with its indirect transition character. It is followed by the direct transition at higher energy and the indirect transition in the GaP barriers.

Even if room temperature EL has been demonstrated, the LED structure is far from being optimized. Fig. 3-31 presents the I(V) characteristics at room temperature for a forward bias. When limiting the current to 20 mA, a threshold voltage of 2.8 V can be estimated, but when looking to the full current range (up to 100 mA in Fig. 3-31), a threshold voltage of 6 V is estimated. We believe that these effects are partially due to the metal-semiconductor contacts which are only partially ohmic.

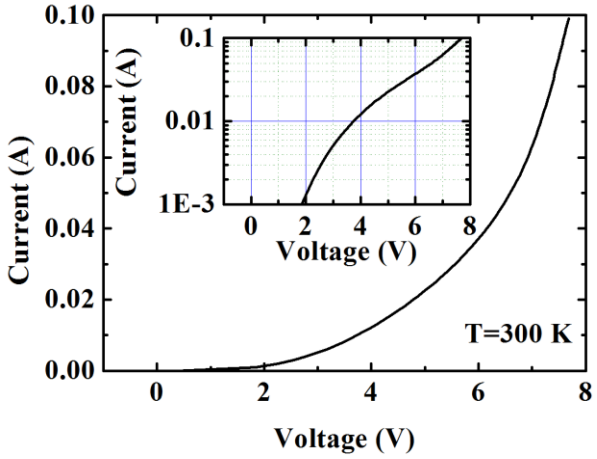

Fig. 3-31: Room temperature I(V) curve of the GaAsPN QW LED. The insert shows the I(V) curve in a semi logarithmic scale.

3.4.2 Contacts and doping

The quality of metallic contacts has been greatly improved by S. Almosni in the framework of his PhD thesis work dedicated to the development of GaAsPN-based solar cells. Ohmic specific contacts of 1.7 x 10^{-5} Ω.cm^2 and 1.3 x 10^{-5} Ω.cm^2 have been achieved on n-type and p-type GaP substrates respectively. For the n-type contact, the stack is $Ni_{5nm}/Au_{45nm}/Ge_{45nm}/Au_{55nm}/Ni_{35nm}/Au_{50nm}$[63]. For the p-type contact, the stack is $Pd_{30nm}/Au_{2nm}/Zn_{70nm}/Au_{2nm}/Pd_{200nm}$[64]. Both contacts are annealed 2 minutes at 550 °C by rapid thermal annealing (RTA).

n-doped and p-doped GaP has also been grown by SSMBE. The highest n-doping (with Si dopants) has been measured at 3 x 10^{18} cm^{-3} by both C(V) and Hall techniques. The highest p-doping (with Be dopants) has been measured at 1 x 10^{18} cm^{-3}. Further studies are in progress to increase these doping concentrations.

3.4.3 Material gain in a GaAsPN QW based structure

We have studied in details in the previous sections the optical properties of GaAsPN QW but we have not dealt with the issue of the material gain yet. It is now analyzed for a structure reported in the literature which exhibits a lasing effect[65]. The material gain is calculated with the TB model for a 8 nm thick $GaAs_{0.92-x}P_{0.08}N_x$ QW with GaP barriers on GaP substrate[66]. Results for TE polarization, room temperature and various N concentrations are presented in Fig. 3-32 (the carrier density is 3.2 x 10^{12} cm^{-2}). No positive gain in TM polarization has been calculated at this carrier density.

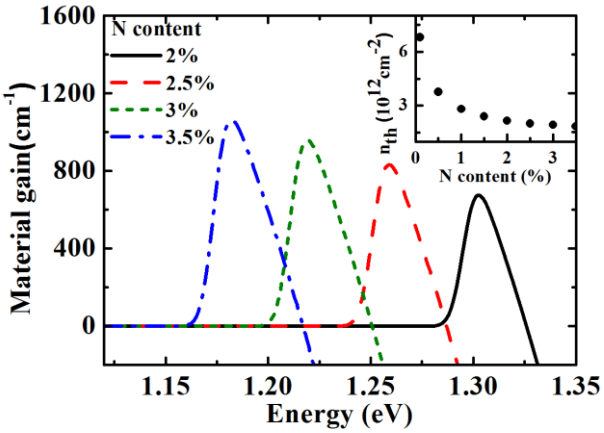

Fig. 3-32: Material gain for TE polarization at 300K for a 8 nm thick $GaAs_{0.92-x}P_{0.08}N_x$/GaP QW on GaP substrate for a carrier density of 3.2 x 10^{12} cm^{-2}. The band structure is calculated at 0 K and a shift of 50 meV is assumed to get the band structure at 300 K. The inset represents the transparency threshold as a function of N content.

Experimentally, the energy position of the gain maximum has been reported at 1.30 eV at 293 K for a N composition assumed to be equal to 3.5%[65]. Nevertheless, as already mentioned and as quoted by the same authors[33], the experimental determination of GaAsPN quaternary alloy composition is very difficult. According to our calculations, a maximum gain at 1.30 eV rather matches with a somewhat lower N content between 2% and 2.5%. Taking into account mirror losses and optical confinement factor, a lower limit for the material gain of about 240 cm^{-1} has been proposed experimentally. The theoretical calculation leads to a maximum value in the

650-1050 cm^{-1} range. The discrepancy is probably associated to additional losses for the experimental structure, related to the material itself, like interstitial non radiative N centers or barrier intraband recombinations.

A good point is that these calculated gains are similar to those encountered in unstrained InGaAs/InP or GaAs/AlGaAs systems[67]; despite the partial N-character of the conduction band edge which reduces the oscillator strength (see Fig. 3-18). Increasing N content is found to increase the maximum of the gain because of the enhancement of the Γ character in the conduction band wave function. Moreover, the issue of low oscillator strength is compensated by the conduction band large effective mass which result in a large density of states. Nevertheless, this large effective mass may have dramatic consequences on transparency thresholds. The influence of N concentration on the transparency threshold is illustrated in the inset of Fig. 3-32. The transparency threshold increases dramatically as the N content decreases as a result of conduction band large effective mass.

We remind that our TB model does not take into account the disorder effects which have been experimentally highlighted in section 3.3. These disorder effects may increase the transparency threshold because the localized states composing the low energy tail of the PL do not participate to the material gain and have to be saturated before populating the conduction band edge. Thus, Borck *et al.*[65] have observed that the laser peak at 20 K is located on the high energy side of the PL spectrum. Experimentally, the lasing effect requires an excitation density up to 2.0 x 10^{13} photons.cm^{-2} (by optical pumping) which is one order of magnitude higher than the transparency threshold calculated in Fig. 3-32. A said before, this can be attributed to the optical losses and to the disorder induced high density of localized radiative states below the band gap. Nevertheless, because it has been demonstrated that the disorder effects are reduced when increasing the N content[49,50], we can expect to reduce the threshold densities by incorporating more N.

In conclusion, increasing the N content in GaAsPN QW may have several advantages: increasing the material gain, reducing the transparency threshold for an ordered system, reducing the disorder effects and thus decreasing even more the transparency threshold, and finally increasing the emission wavelength to get closer to the transparency window of Si. But

unfortunately it also deteriorates the crystalline quality of the material thus increasing the optical losses.

3.4.4 Cladding layers

The first role of cladding layers is to increase the overlap between the electromagnetic field and the gain medium. To this purpose, the chosen material must have a low refractive index as compared to the refractive index of the active zone. Moreover, because cladding layers are generally thick layers, a coherent growth requires a quasi-perfect lattice-matching to the substrate (Si or GaP). In the following, we study the AlGaP alloy as a possible candidate on GaP substrate. Indeed, by analogy with the GaAs/AlGaAs laser system, the incorporation of Al is expected to lower the refractive index while keeping a similar lattice constant to GaP. First, we have to check that thick AlGaP layers can be grown pseudomorphically onto GaP substrate.

3.4.4.1 Structural properties

AlGaP layers are grown on n-doped GaP substrate using SSMBE. The growth is performed at 580 °C with a growth rate set to 0.7 ML.s^{-1}. After the growth of a 230 nm thick GaP buffer layer, a 300 nm thick AlGaP layer is grown. The Al composition is fixed by the flux ratio between Ga and Al species. Three samples with different Al contents are processed.

The strain relaxation is analyzed by HRXRD reciprocal space mapping (RSM) around the (224) GaP Bragg reflection. For a detailed description of the experimental setup and measurement techniques, readers are encouraged to look at references[4,68–70]. Fig. 3-33 represents the RSM for the three different Al contents. The reflection peak related to the AlGaP layer is shifted down and vertically aligned with the (224) GaP reflection in the reciprocal space map. This indicates that the AlGaP layer remains coherently grown on GaP substrate for the three different Al contents. The relative position of the AlGaP peak to the GaP substrate peak is used to calculate the out-of-plane lattice constant and to deduce the Al content. The three samples contain 37 %, 57 % and 83 % of Al respectively.

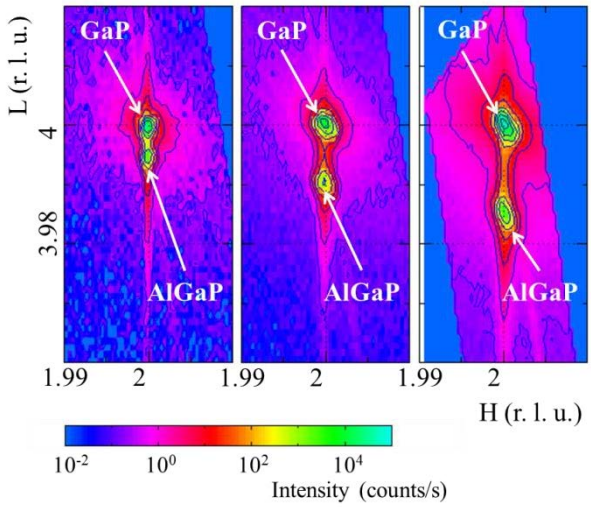

Fig. 3-33: RSM around the (224) Bragg reflection of 300 nm thick AlGaP layers grown on GaP substrate. From the left to the right, the Al content increase.

The thicknesses required for cladding layers are generally larger than 300 nm. Fig. 3-34 shows the RSM of a 1 µm thick $Al_{0.66}Ga_{0.34}P$ layer grown on GaP substrate. Here again, the coherent growth is demonstrated.

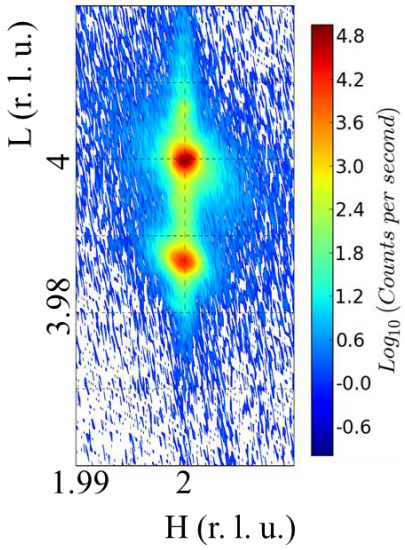

Fig. 3-34: RSM around the (224) Bragg reflection of a 1 µm thick AlGaP layer grown on GaP substrate.

3.4.4.2 Optical properties

Spectroscopic ellipsometry (SE) experiments are performed to measure the effective dielectric function $\langle\varepsilon\rangle = \langle\varepsilon_r\rangle + i\langle\varepsilon_i\rangle$ of the 300 nm thick AlGaP layers grown on GaP substrate.

The measurements are performed at room temperature using a Horiba Jobin-Yvon Uvisel 2 phase-modulated ellipsometer. SE data in the range 0.6 – 6 eV are measured with an incidence angle of 70°. Fig. 3-35(a) shows the experimental data (circles) for the $Al_{0.57}Ga_{0.53}P$/GaP sample. Oscillations are observed below 3.4 eV and are associated to interferences for the energy range where the film is transparent.

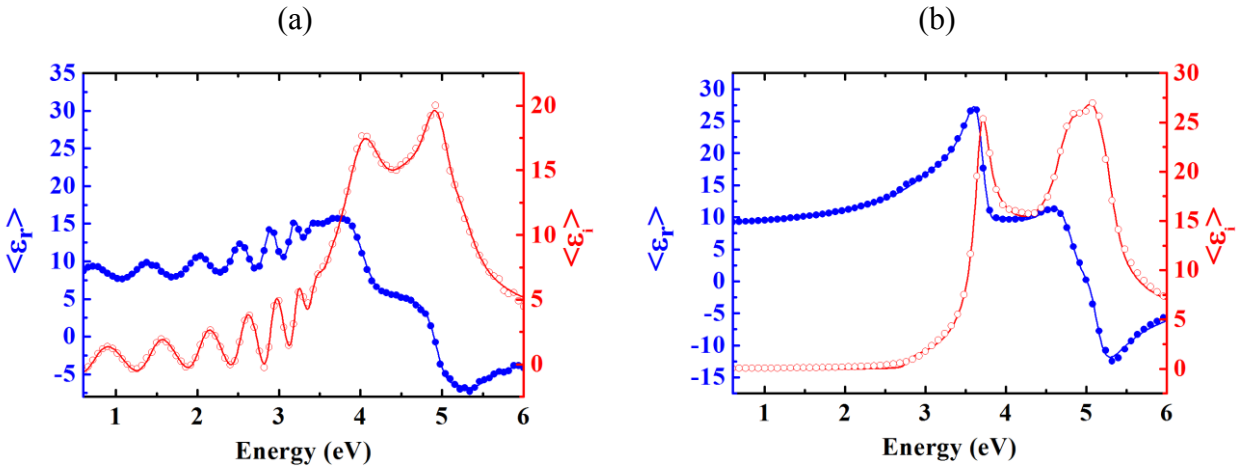

Fig. 3-35: Real (blue filled circles) and imaginary (red open circles) parts of the measured effective dielectric function of (a) the $Al_{0.57}Ga_{0.53}P$/GaP sample and (b) GaP substrate. Solid lines show the fit.

To get the dielectric function of the AlGaP layer and deduce the refractive index in this energy range, a spectroscopic model has to be constructed. First, a parametric dispersion model is used to describe the dielectric function of AlGaP layer on the whole experimental energy range [0.6 eV – 6 eV]. Many models have been proposed to describe dielectric functions of semiconductors. However, correctly describing indirect semiconductors like GaP or AlP over a large energy region is tricky. Adachi's model[71] is known to yield a reasonable agreement for semiconductor alloys in the region below the fundamental band gap whereas oscillator ensembles[72–74] better describe the critical points above the fundamental band gap. In this study, the dispersion model is based on Kato-Adachi model[75] below the fundamental band gap. The critical points above the fundamental band gap are described by four Tauc-Lorentz oscillators[72]. The initial parameters are determined by a fit on measured dielectric function on GaP substrate. Fig. 3-35(b) shows the fit with this model to the experimental spectrum of GaP. This dispersion model is then introduced in a four phase geometric model (ambient air/surface roughness/AlGaP layer/GaP substrate). For each sample, the AlGaP layer thickness is measured by ω-2θ XRD scan and this value is used as an initial guess to fit the ellipsometry spectra. Surface roughness is

modeled by the effective medium approximation[76] between AlGaP and void. The roughness layer in the geometric model also account for an eventual surface native oxide[77]. The calculated roughness does not exceed 20 Å which is consistent with AFM analysis on epitaxial layers. The model correctly fits the experimental data as shown by solid lines in Fig. 3-35(a).

The extracted imaginary part of the dielectric function for the different $Al_xGa_{1-x}P$ layers is shown in Fig. 3-36. The results are consistent with the measurements of Choi *et al.*[78]. The direct band gap E_0 (Γ_{15}- Γ_1) is found to linearly increase with the Al content: E_0(eV) = 2.96 + 0.66x. The critical point E_1 (L_3-L_1) also linearly increases with the Al content: E_1(eV) = 3.69 + 0.60x. Several critical points are expected to yield contributions around the 5 eV spectral region, but it is hard to distinguish them. We can qualitatively assert that the maximum of the peak in the E_2 spectral region is nearly fixed in energy in agreement with the results of Choi *et al.*[78].

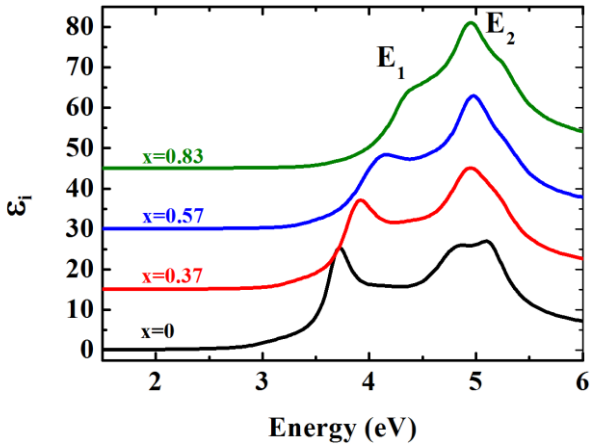

Fig. 3-36: Imaginary part of the measured dielectric function of $Al_xGa_{1-x}P$ alloy for x=0, 0.37, 0.57, 0.83. An offset of 15 between spectra has been added for clarity.

The refractive index of AlGaP is finally deduced for the different Al contents. The results are represented in Fig. 3-37 by square points in the energy range where a lasing emission is possible. It shows a significant lowering of the refractive index when the Al content increases. For example, at 850 nm (1.46 eV), which is a typical emission wavelength of GaAsPN/GaP QW, the refractive index follows roughly a linear law $n(Al_xGa_{1-x}P) = 3.17 - 0.31x$. Extrapolating this law to x=1, we find a refractive index of 2.86 for AlP which is in good agreement with the measurements of Jung *et al.*[79] (2.83) and Monemar[80] (2.78).

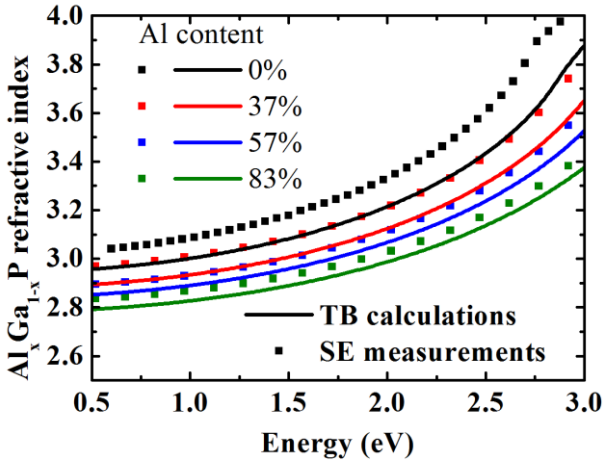

Fig. 3-37: Experimental (filled square) and theoretical (solid lines) refractive index of $Al_xGa_{1-x}P$.

The refractive index of the AlGaP alloy can also be calculated theoretically with the TB model as presented in chapter 2. The calculated refractive index is shown in Fig. 3-37 for the three Al contents and GaP. The discrepancy between theoretical and experimental results does not exceed 3 %. This may be explained by two reasons. The calculations are performed at 0 K and the excitonic correction is not taken into account in the TB model. These two corrections should yield a blue shift of the theoretical results and reduce the discrepancy with experimental results.

3.4.4.3 Band alignments

Cladding layers also play an important role in the injection of carriers in the active zone. Fig. 3-38 presents the band alignment of the AlGaP alloy with GaP calculated with the TB model and the VBO taken from *ab initio* calculations[81]. The effect of strain is negligible when grown on GaP substrate because of the small lattice mismatch between GaP and AlP (0.3%). The band alignment is type-II with a confinement of holes in the Γ valence band of GaP and electrons in the X conduction band of AlGaP, as demonstrated in several papers[82–87]. For the AlP/GaP heterojunction the conduction and valence band offsets are 0.53 eV and 0.41 eV respectively.

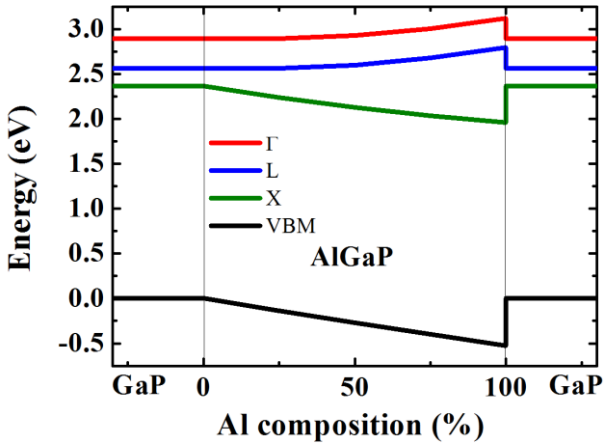

Fig. 3-38: Band alignment of AlGaP alloy biaxially strained on GaP as a function of Al content calculated with the TB model at 0 K.

This band alignment may be dramatic in a laser structure composed of a GaAsPN/GaP QW active zone embedded in AlGaP cladding layers grown on GaP substrate such as the one of Hossain *et al.*[41]. Indeed, it creates a potential barrier for the electrons at the AlGaP/GaP heterojunction. Fig. 3-39 shows the band alignment of such a laser structure. The composition and width of GaAsPN/GaP QW are designed to emit around 850 nm at room temperature according to the TB simulation. The Al content in the cladding layers is fixed at 25 % similarly to the structure of Hossain *et al.*[41]. The width of the GaP barriers and AlGaP cladding layers are discussed in the next section. We remind that the CBM of GaP barriers and AlGaP cladding layers is X-type whereas the CBM of GaAsPN QW is a mixing of Γ and N character. The green circle in the conduction band shows the 130 meV potential barrier that electrons need to overcome to enter the active zone. The structure also exhibits a 140 meV potential barrier for holes from a GaP-p++ contact layer (if the substrate is n-doped) or from the GaP-p substrate (if the substrate is p-doped) to the AlGaP-p+ cladding layer. This second potential barrier is probably less dramatic than the first one because the GaP can be heavily doped in this zone to help the holes to travel into the whole structure. It is however more dangerous to heavily dope the zone of the electron potential barrier because it is closer to the optical field and thus may lead to additional optical losses.

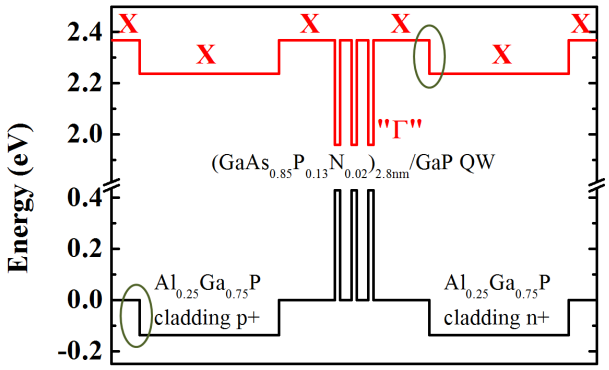

Fig. 3-39: Band alignment of a laser structure composed of GaAsPN/GaP QW embedded in AlGaP cladding layers grown on GaP substrate. The structure theoretically emits around 850 nm at room temperature. The green circles represent potential barriers for carriers. The band alignment is calculated at 0 K.

A possible solution is a composition graded cladding layer to soften the potential barrier. Nevertheless, it should also reduce the confinement of the optical mode in the active zone. Another solution is to replace the GaP barrier material by a lower conduction band material which can be grown lattice-matched to the GaP substrate. The quaternary GaAsPN alloy (with low As content) experimentally studied in section 3.1.2 is a potential candidate. Fig. 3-40 presents the band alignment of the AlGaP alloy with the GaAsPN alloy (keeping the perfect lattice-matching to GaP condition). It shows that depending on Al composition in AlGaP cladding layers, an adequate couple of (As, N) content can be used for the GaAsPN barrier material in order to suppress the potential barrier for electrons.

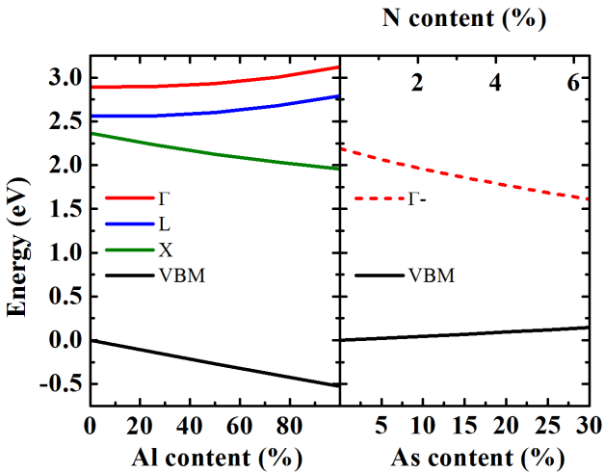

Fig. 3-40: Band alignment of AlGaP alloy (left) with the quaternary GaAsPN alloy (right) perfectly lattice-matched to GaP calculated with the TB model at 0 K. For the GaAsPN alloy, only the VBM and the CBM (mixing of Γ and N character) are represented.

The band alignment of a laser structure with $GaAs_{0.85}P_{0.13}N_{0.02}/GaAs_{0.09}P_{0.89}N_{0.02}$ QW embedded in AlGaP cladding layers is shown in Fig. 3-41. The issue of the potential barrier is now solved but the confinement of electrons in the QW is strongly reduced. The calculated energy difference between the first electron state confined in the QW and the CBM of the barrier material is 60 meV. Nevertheless, it can be enhanced by increasing the N and/or As content in the QW or reducing both N and As contents in the barrier material.

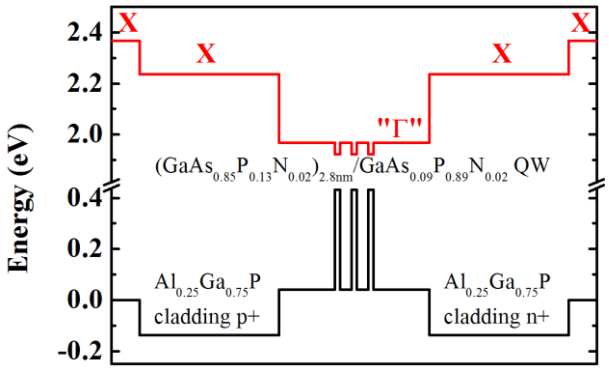

Fig. 3-41: Band alignment of a laser structure composed of $GaAs_{0.85}P_{0.13}N_{0.02}/GaAs_{0.09}P_{0.89}N_{0.02}$ QW embedded in AlGaP cladding layers grown on GaP substrate. The structure theoretically emits around 850 nm at room temperature. The band alignment is calculated at 0 K.

A preliminary growth of such an active area (without the cladding layers) has been performed at 480 °C to ensure a good reproducibility in the composition of the GaAsPN barrier material with a few percent of As and N (see section 3.1.2). A 36 nm thick GaP buffer layer is first grown by SSMBE on an undoped GaP substrate. Then five compressively strained 2.7 nm thick GaAsPN QW with a high As content (around 85 %) are grown. They are separated by 20 nm thick GaAsPN barriers lattice matched to GaP (with a low As content). A 10 nm thick GaP capping layer is finally overgrown. The As content is increased in the QW as compared to the barrier by reducing the growth rate from 0.5 $ML.s^{-1}$ to 0.1 $ML.s^{-1}$ and increasing the As beam equivalent pressure from 3.3 x 10^{-7} Torr to 1.1 x 10^{-6} Torr. 2 s and 5 s growth interruptions under As, P and N are respectively performed before and after the QW growth. Fig. 3-42(a) presents the cw-PL spectrum at 13 K. Both barrier and QW peaks are visible at 1.87 eV and 1.43 eV respectively. At room temperature (Fig. 3-42(b)), the QW peak is still visible whereas the barrier peak vanished indicating an efficient confinement in the QW. Nevertheless, growth improvements should be achieved before using this structure as a laser active zone. Indeed, the

room temperature integrated PL intensity is decreased by a factor of 60 as compared to the GaAsPN/GaP structure of Fig. 3-22.

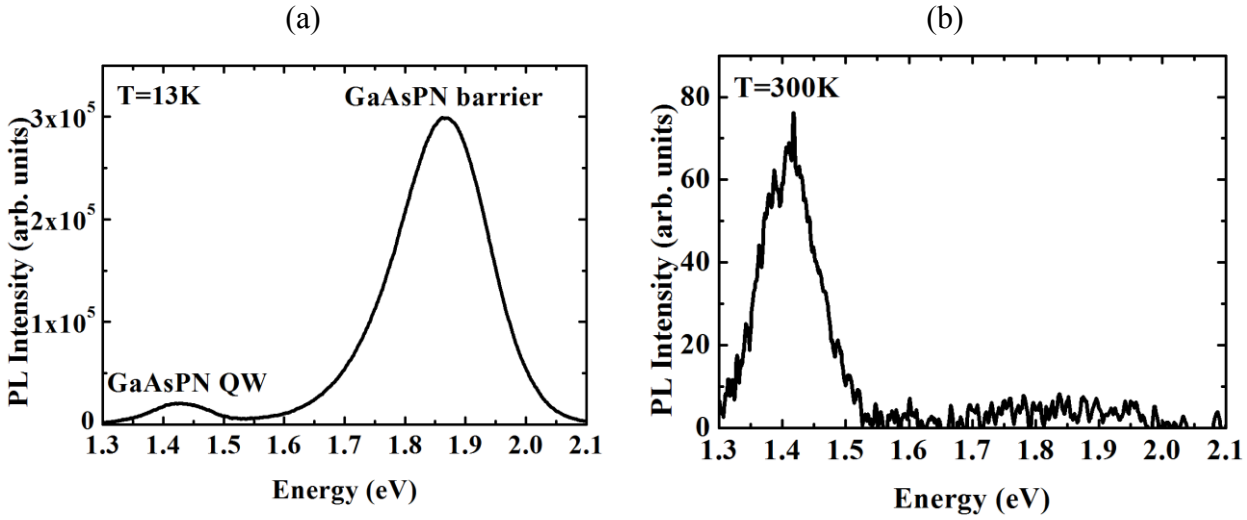

Fig. 3-42: cw-PL spectrum of GaAsPN/GaAsPN QW at (a) 13 K and (b) room temperature.

3.4.4.4 Confinement of the optical mode

In this section, we give additional recommendations for the choice of the thicknesses of both active zone and cladding layers as well as the composition of the cladding layers. First, we estimate the optical confinement factor that can be expected for the active zone, by solving the Maxwell equations in the laser structure and calculating the fraction of the mode which is guided in the active zone:

$$\Gamma = \frac{\int_{\text{active zone}} |E(x,y)|^2 \, dxdy}{\int_{-\infty}^{+\infty} |E(x,y)|^2 \, dxdy}$$

where E is the electric field and z is the direction of propagation for light. We suppose that the optical mode is TE as it corresponds to a higher material gain in Fig. 3-32. We consider only vertical confinement so that the problem becomes one dimensional.

Let us first consider the case of an active zone embedded into AlGaP cladding layers with infinite thickness. We suppose as a first approximation that the refractive index of the active zone is the one of GaP. Please notice that the presence of the GaAsPN QW may slightly increase this refractive index. If the barrier material is bulk GaAsPN, it may also increase the refractive

index as compared to GaP. The wavelength of 850 nm is chosen for the calculation and the refractive index of $Al_xGa_{1-x}P$ is taken with a linear variation of 3.17 – 0.31x as measured in Fig. 3-37. This problem can be easily solved numerically. Fig. 3-43 presents the calculated confinement factor as a function of Al content and for various active zone thicknesses. It shows that a good confinement factor of 70 % can be achieved with an active zone with a thickness of 300 nm and $Al_{0.5}Ga_{0.5}P$ cladding layers.

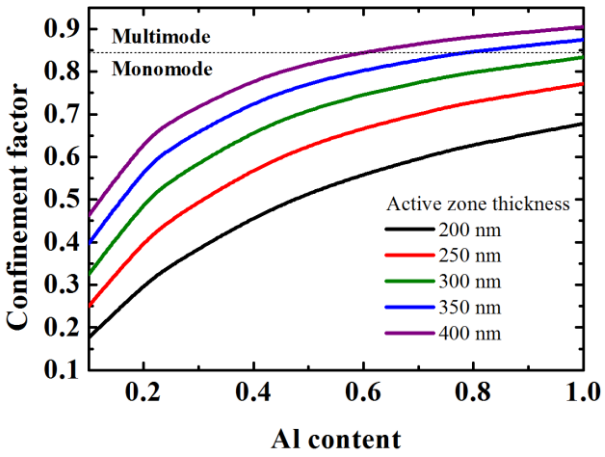

Fig. 3-43: Confinement factor as a function of Al content in AlGaP cladding layers with infinite thicknesses for various thicknesses for the active zone.

The thickness of cladding layers has also to be carefully chosen. The top cladding layers have to be thick enough to limit the strong optical losses that occur if a significant part of the optical mode reaches the top metallic contact. This can be quantified by calculating the ratio between the intensity of the optical mode at the metal/semiconductor interface and the maximum intensity of the mode.

$$R = \frac{\left|E_{metal/semiconductor}\right|^2}{\left|E_{\max}\right|^2}$$

The bottom cladding layer has also to be thick enough to isolate the optical mode from the substrate. Indeed, as similar to GaAs/AlGaAs system, the GaP substrate has the same or just a slighltly lower refractive index than the active zone. Consequently, the light can couple from the active zone into the substrate and result in additional losses. Garmire has calculated the corresponding loss coefficient[88]:

$$\alpha_{leak} \approx \frac{\lambda_0^3 hp^2 \sin^2(hT)\exp(-2pd)}{\pi^3 n\Delta n^2 T}$$

where T is the active zone thickness, d is the bottom cladding layer thickness, h and p are the transverse propagation vectors in the active zone and in the cladding layer respectively. Δn is the difference between the refractive index of GaP and AlGaP.

We have simulated the one-dimensional structure described in Fig. 3-44 by finite element method. The thickness of the active zone is fixed to 300 nm. The same composition x and the same thickness t are used for both top and bottom cladding layers. An absorption coefficient is arbitrarily introduced into the GaP substrate to avoid the simulation to depend on the substrate thickness. The value does not affect the results.

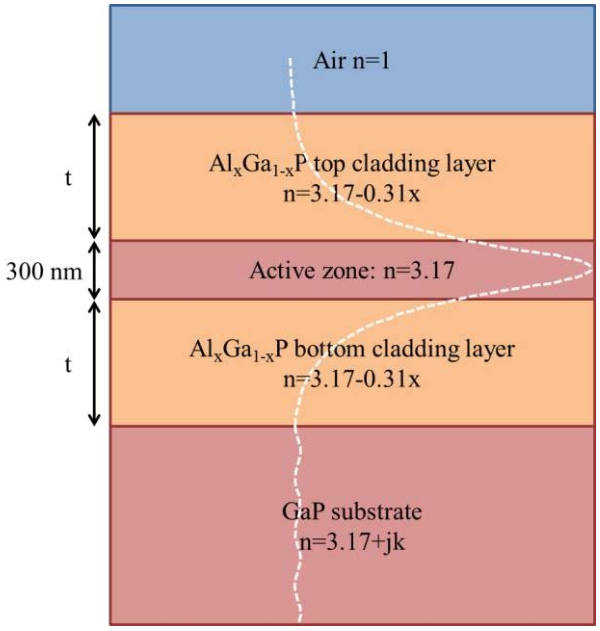

Fig. 3-44: One dimensional structure for the simulation of the optical mode. The composition and the thickness of both cladding layers are keeping identical.

Fig. 3-45 presents the calculation of α_{leak} and R as a function of composition and thickness of cladding layers. It shows that Al content of 50 % with thicknesses of 1 µm should be enough to ensure a good isolation of the optical mode into the structure.

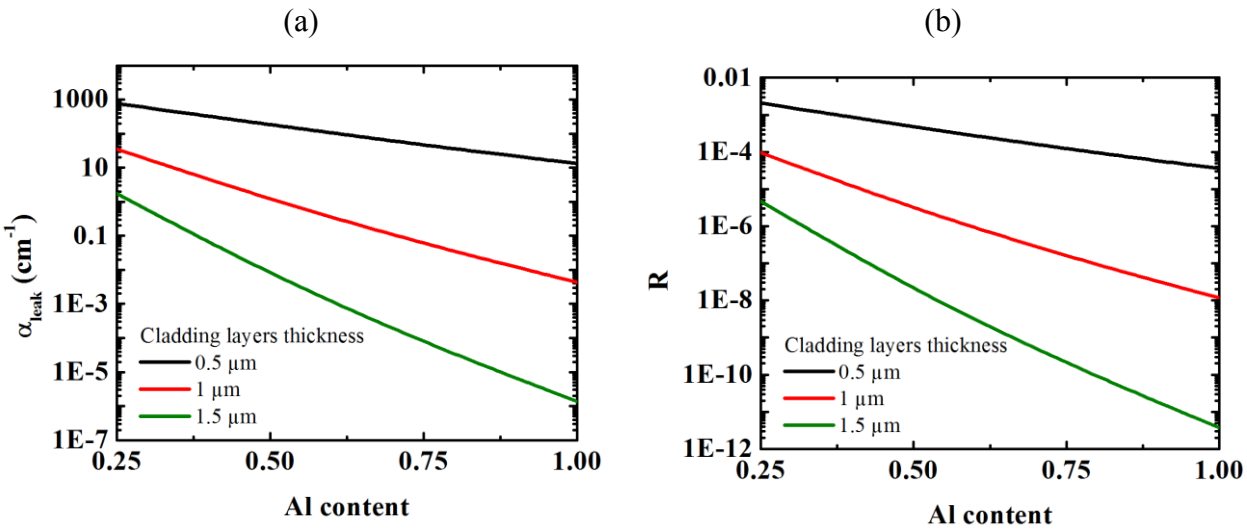

Fig. 3-45: (a) Leakage of the optical mode in the substrate and (b) ratio between the intensity of the optical mode at the interface AlGaP/air and the maximum of intensity as a function of Al content and cladding layers thickness.

3.4.5 GaP substrate vs Si substrate: what does it change?

In this section, we argue about the expected differences in the laser design when a Si substrate is considered rather than a GaP substrate. Finally we present some preliminary results of optical properties of GaAsPN/GaPN QW grown on Si substrate.

Because Si has a smaller lattice constant, thick AlGaP layers cannot be grown pseudomophically. Thus, the incorporation of N to form the AlGaPN alloy is required to preserve the lattice-matching condition. Very few studies exist on this dilute nitride alloy. The growth of quaternary alloy AlGaPN and ternary alloy AlPN has been demonstrated[89,90]. The study of point defects in AlGaPN has also been reported[91]. Recently, Okada *et al.*[92] have obtained a reflectivity of 75 % with a distributed Bragg reflector made of eight pairs of AlPN/GaPN grown on Si substrate.

First, we can wonder about the conduction band alignment of bulk AlGaPN with bulk GaAsPN (keeping the condition of perfect lattice-matching to Si for both alloys). Unfortunately, the band gap of the AlPN alloy is not known and consequently no BAC parameters for this alloy exist. As a first rough estimate, we can calculate the band alignment with the $sp^3d^5s^*s_N$ TB model. The N level and the coupling parameter for AlPN are chosen to be the same as in GaPN. The effect of N on the absolute energy of the AlGaPN CBM is difficult to predict. Indeed, increasing N content may lower the band gap but it also requires a higher Al content to preserve

the lattice-matching condition. Because the direct band gap of the AlGaP host material increases with Al content (see Fig. 3-38), it may have a counter effect on the decreasing of the band gap when increasing both Al and N contents. Fig. 3-46 presents the calculated band alignment of AlGaPN and GaAsPN alloys perfectly lattice-matched to Si. It shows that a type I band alignment may be achieved by correctly choosing the composition in the barrier material (GaAsPN) and in the cladding layer (AlGaPN).

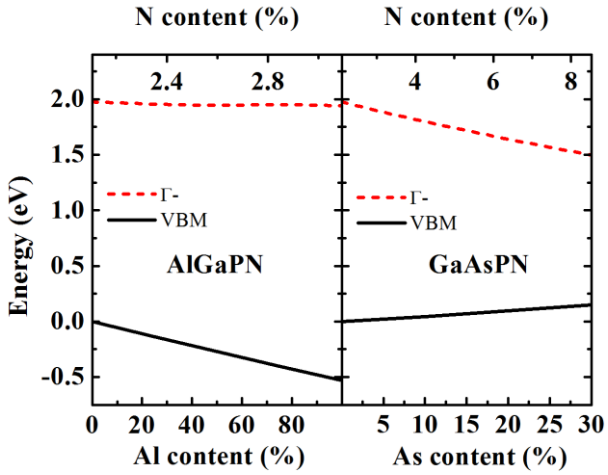

Fig. 3-46: Band alignment of AlGaPN alloy (left) with the quaternary GaAsPN alloy (right) perfectly lattice-matched to Si calculated with the TB model at 0 K.

Secondly, the effect of N on the refractive index in dilute nitride alloys is not well documented. Kanaya *et al.*[93] have presented measurement of the dielectric function of GaPN as a function of N which suggest that the effect of N on the refractive index in the transparency region is small. Moreover, Okada *et al.*[92] have measured the same refractive index in $Al_{0.8}Ga_{0.2}PN$ and in $Al_{0.8}Ga_{0.2}P$ in the near-infrared range.

Thirdly, for an electrically pumped laser structure, the cladding layers need to be doped. This faces two challenges. First, because of its affinity to oxygen, the doping of Al-based alloys requires an adequate choice of growth temperature. Studies are in progress in Foton laboratory to find the best growth conditions to dope AlGaP alloys. Moreover, doping of dilute nitride alloys is known to be trickier as reported by several groups[94,95]. This will require specific investigations in the near future.

Finally, the growth on Si substrate is known to introduce additional defects due to the GaP/Si interface. Nevertheless, room temperature PL of GaAsPN/GaPN QW grown on Si

substrate has been achieved[96]. Two 2.7 nm thick GaAsPN QW with As content around 70 % and N content around 1.5 % separated by a 30 nm thick GaPN barrier have been grown on Si substrate (001). A 60 nm thick GaP buffer layer followed by a 100 nm thick GaPN layer is first grown before the first QW. The capping layer consists in a 30 nm thick GaPN layer followed by a 20 nm thick GaP layer. Fig. 3-47 presents the PL spectra at low temperature showing the peak of both QW and barrier. The inset shows the room temperature PL spectrum of the QW.

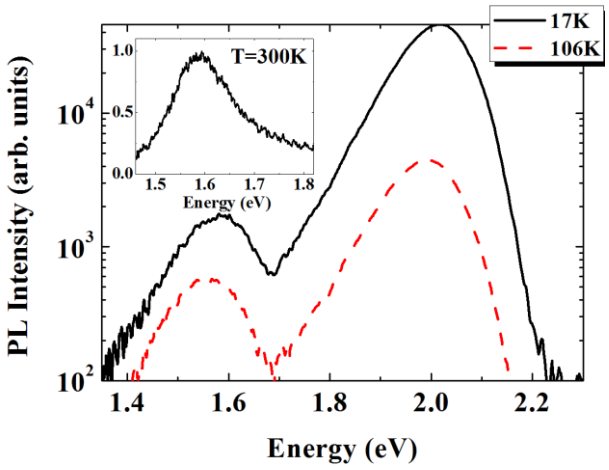

Fig. 3-47: cw-PL spectra at 17 K and 106 K of GaAsPN/GaPN QW grown on Si substrate at 160 nm from the GaP/Si interface. The peak around 1.58 eV is related to QW whereas the peak around 2.02 eV is related to the GaPN barrier. The inset shows the PL spectrum at 300 K.

Nevertheless, this structure is far from being optimized from the growth view. In particular, the GaP/Si interface is not optimized. Moreover the N content in the barrier is not fixed for a perfect lattice matching to Si. It thus results in many defects as shown by the TRPL dynamics in Fig. 3-48. At 10 K, the PL dynamics can be fitted with a double exponential function with two decay times of 140 ps and 1250 ps. At 300 K, these times are dramatically shortened to 30 ps and 180 ps respectively, as a direct consequence of the non radiative channels.

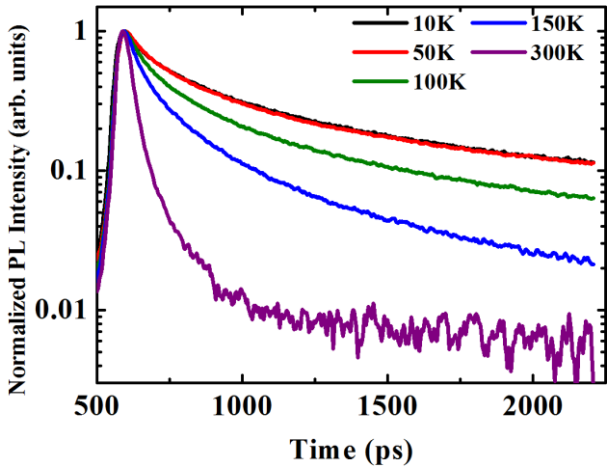

Fig. 3-48: PL dynamics of GaAsPN/GaPN QW grown on Si substrate as a function of temperature. The detection energy corresponds to the peak of the spectrum for a given temperature. The excitation density is 4000 W.cm^{-2} and the repetition rate is 80 MHz.

Nevertheless, this preliminary result highlights the great potentiality of GaAsPN QW to efficiently emit light very close to the Si substrate (160 nm from the GaP/ Si interface), which is a potential advantage of the pseudomorphic approach to easily couple the light into a Si waveguide.

3.5 Conclusion

In conclusion, we have studied dilute nitride alloys for the development of active zone on GaP and Si substrate. Bulk GaAsPN (with low As content) can be grown pseudomorphically onto GaP or Si substrate and allow for a band engineering of the barrier material. The unusual optical properties of dilute nitride structures are observed for bulk GaPN and GaAsPN as well as GaAsPN QW. In particular, the disorder effects result in a density of radiative localized states below the band gap which may have consequences on the threshold current densities in laser structures. Further optimizations are in progress to reduce these effects (composition of QW and barrier materials, QW thickness, post-growth annealing and optimization of growth conditions) which may contribute to decrease the state-of-the art high threshold current densities for such structures (4 kA.cm^{-2} in pulsed mode at room temperature on GaP substrate[41] and 4.4 kA.cm^{-2} in pulsed mode at 120 K on Si substrate[42]). In chapter 4, we will study the potential of InGaAs/GaP QD as an alternative to GaAsPN QW. Finally, the AlGaP(N) alloy has been shown to be a good choice for the cladding layers because of its lower refractive index as compared to GaP. Nevertheless, it requires taking care to the AlGaP/GaP type II band alignment. Elements for band engineering using AlGaP(N) and GaAsPN alloys have been provided.

References of Chapter 3

[1] Y. Zhang, B. Fluegel, A. Mascarenhas, H.P. Xin, and C.W. Tu, Phys. Rev. B **62**, 4493 (2000).
[2] P.R.C. Kent and A. Zunger, Phys. Rev. B **64**, 115208 (2001).
[3] R.A. Logan, Appl. Phys. Lett. **13**, 139 (1968).
[4] J. Kuyyalil, T. Nguyen Thanh, T. Quinci, S. Almosni, A. Létoublon, T. Rohel, N. Bertru, A. Le Corre, O. Durand, and C. Cornet, J. Cryst. Growth **377**, 17 (2013).
[5] U. Tisch, E. Finkman, and J. Salzman, Appl. Phys. Lett. **81**, 463 (2002).
[6] X. Liu, S.G. Bishop, J.N. Baillargeon, and K.Y. Cheng, Appl. Phys. Lett. **63**, 208 (1993).
[7] W. Shan, W. Walukiewicz, K.M. Yu, J. Wu, J.W. Ager, E.E. Haller, H.P. Xin, and C.W. Tu, Appl. Phys. Lett. **76**, 3251 (2000).
[8] H.P. Xin, C.W. Tu, Y. Zhang, and A. Mascarenhas, Appl. Phys. Lett. **76**, 1267 (2000).
[9] W.G. Bi and C.W. Tu, Appl. Phys. Lett. **69**, 3710 (1996).
[10] W.G. Bi and C.W. Tu, Appl. Phys. Lett. **70**, 1608 (1997).
[11] W.G. Bi and C.W. Tu, J. Appl. Phys. **80**, 1934 (1996).
[12] J.-C. Harmand, A. Caliman, E.V.K. Rao, L. Largeau, J. Ramos, R. Teissier, L. Travers, G. Ungaro, B. Theys, and I.F.L. Dias, Semicond. Sci. Technol. **17**, 778 (2002).
[13] G.Y. Rudko, I.A. Buyanova, W.M. Chen, H.P. Xin, and C.W. Tu, Appl. Phys. Lett. **81**, 3984 (2002).
[14] C. Harris, A. Lindsay, and E.P. O'Reilly, J. Phys. Condens. Matter **20**, 295211 (2008).
[15] N. Shtinkov, P. Desjardins, and R.A. Masut, Phys. Rev. B **67**, 081202 (2003).
[16] I. Vurgaftman and J.R. Meyer, J. Appl. Phys. **94**, 3675 (2003).
[17] I.A. Buyanova, W.M. Chen, and C.W. Tu, J. Phys. Condens. Matter **16**, S3027 (2004).
[18] S. Almosni, C. Robert, T. Nguyen Thanh, C. Cornet, A. Létoublon, T. Quinci, C. Levallois, M. Perrin, J. Kuyyalil, L. Pedesseau, A. Balocchi, P. Barate, J. Even, J.M. Jancu, N. Bertru, X. Marie, O. Durand, and A. Le Corre, J. Appl. Phys. **113**, 123509 (2013).
[19] M.D. Sturge, E. Cohen, and R.A. Logan, Phys. Rev. B **27**, 2362 (1983).
[20] L.C. Lenchyshyn, M.L.W. Thewalt, D.C. Houghton, J.-P. Noe-umll, N.L. Rowell, J.C. Sturm, and X. Xiao, Phys. Rev. B **47**, 16655 (1993).
[21] M. Oueslati, M. Zouaghi, M.E. Pistol, L. Samuelson, H.G. Grimmeiss, and M. Balkanski, Phys. Rev. B **32**, 8220 (1985).
[22] I.A. Buyanova, W.M. Chen, G. Pozina, J.P. Bergman, B. Monemar, H.P. Xin, and C.W. Tu, Appl. Phys. Lett. **75**, 501 (1999).
[23] Y.I. Mazur, V.G. Dorogan, M. Schmidbauer, G.G. Tarasov, S.R. Johnson, X. Lu, M.E. Ware, S.-Q. Yu, T. Tiedje, and G.J. Salamo, J. Appl. Phys. **113**, 144308 (2013).
[24] M. Güngerich, P.J. Klar, W. Heimbrodt, G. Weiser, J.F. Geisz, C. Harris, A. Lindsay, and E.P. O'Reilly, Phys. Rev. B **74**, 241202 (2006).
[25] M. Izadifard, J.P. Bergman, I. Vorona, W.M. Chen, I.A. Buyanova, A. Utsumi, Y. Furukawa, S. Moon, A. Wakahara, and H. Yonezu, Appl. Phys. Lett. **85**, 6347 (2004).
[26] I.A. Buyanova, G. Pozina, J.P. Bergman, W.M. Chen, H.P. Xin, and C.W. Tu, Appl. Phys. Lett. **81**, 52 (2002).
[27] H. Yaguchi, S. Miyoshi, H. Arimoto, S. Saito, H. Akiyama, K. Onabe, Y. Shiraki, and R. Ito, Solid-State Electron. **41**, 231 (1997).
[28] T. Niebling, O. Rubel, W. Heimbrodt, W. Stolz, S.D. Baranovskii, P.J. Klar, and J.F. Geisz, J. Phys. Condens. Matter **20**, 015217 (2008).

[29] R.A. Mair, J.Y. Lin, H.X. Jiang, E.D. Jones, A.A. Allerman, and S.R. Kurtz, Appl. Phys. Lett. **76**, 188 (2000).
[30] E.P. O'Reilly, A. Lindsay, P.J. Klar, A. Polimeni, and M. Capizzi, Semicond. Sci. Technol. **24**, 033001 (2009).
[31] S.R. Kurtz, P. Faine, and J.M. Olson, J. Appl. Phys. **68**, 1890 (1990).
[32] V.-M. Korpijärvi, A. Aho, P. Laukkanen, A. Tukiainen, A. Laakso, M. Tuominen, and M. Guina, J. Appl. Phys. **112**, 023504 (2012).
[33] B. Kunert, K. Volz, J. Koch, and W. Stolz, Appl. Phys. Lett. **88**, 182108 (2006).
[34] Q. Li, S.J. Xu, M.H. Xie, and S.Y. Tong, J. Phys. Condens. Matter **17**, 4853 (2005).
[35] M. Latkowska, R. Kudrawiec, F. Janiak, M. Motyka, J. Misiewicz, Q. Zhuang, A. Krier, and W. Walukiewicz, Appl. Phys. Lett. **102**, 122109 (2013).
[36] Q. Li, S.J. Xu, W.C. Cheng, M.H. Xie, S.Y. Tong, C.M. Che, and H. Yang, Appl. Phys. Lett. **79**, 1810 (2001).
[37] C. Karcher, K. Jandieri, B. Kunert, R. Fritz, M. Zimprich, K. Volz, W. Stolz, F. Gebhard, S.D. Baranovskii, and W. Heimbrodt, Phys. Rev. B **82**, 245309 (2010).
[38] M.-E. Pistol, M.R. Leys, and L. Samuelson, Phys. Rev. B **37**, 4664 (1988).
[39] C. Robert, A. Bondi, T. Nguyen Thanh, J. Even, C. Cornet, O. Durand, J.P. Burin, J.M. Jancu, W. Guo, A. Létoublon, H. Folliot, S. Boyer-Richard, M. Perrin, N. Chevalier, O. Dehaese, K. Tavernier, S. Loualiche, and A. Le Corre, Appl. Phys. Lett. **98**, 251110 (2011).
[40] A. Bondi, W. Guo, L. Pedesseau, S. Boyer-Richard, H. Folliot, N. Chevalier, C. Cornet, A. Letoublon, O. Durand, C. Labbé, M. Gicquel, A. Lecorre, J. Even, S. Loualiche, and A. Moreac, Phys. Status Solidi C **6**, 2212 (2009).
[41] N. Hossain, S.J. Sweeney, S. Rogowsky, R. Ostendorf, J. Wagner, S. Liebich, M. Zimprich, K. Volz, B. Kunert, and W. Stolz, Electron. Lett. **47**, 931 (2011).
[42] S. Liebich, M. Zimprich, A. Beyer, C. Lange, D.J. Franzbach, S. Chatterjee, N. Hossain, S.J. Sweeney, K. Volz, B. Kunert, and W. Stolz, Appl. Phys. Lett. **99**, 071109 (2011).
[43] I. Vurgaftman, J.R. Meyer, and L.R. Ram-Mohan, J. Appl. Phys. **89**, 5815 (2001).
[44] W.O. Groves, Appl. Phys. Lett. **19**, 184 (1971).
[45] J.A. Prieto, G. Armelles, M.-E. Pistol, P. Castrillo, J.P. Silveira, and F. Briones, Appl. Phys. Lett. **70**, 3449 (1997).
[46] J. Chamings, S. Ahmed, S.J. Sweeney, V.A. Odnoblyudov, and C.W. Tu, Appl. Phys. Lett. **92**, 021101 (2008).
[47] B. Gil, M. Baj, J. Camassel, H. Mathieu, C.B. à la Guillaume, N. Mestres, and J. Pascual, Phys. Rev. B **29**, 3398 (1984).
[48] Y.-H. Zhu, H.-Y. Yu, and W.-J. Fan, Appl. Phys. Lett. **98**, 121112 (2011).
[49] K. Jandieri, M.K. Shakfa, S. Liebich, M. Zimprich, B. Kunert, C. Karcher, A. Chernikov, K. Volz, W. Stolz, M. Koch, S. Chatterjee, W. Heimbrodt, F. Gebhard, and S.D. Baranovskii, Phys. Rev. B **86**, 125318 (2012).
[50] K. Jandieri, S.D. Baranovskii, B. Kunert, M. Zimprich, S. Liebich, K. Volz, W. Stolz, S. Chatterjee, C. Karcher, W. Heimbrodt, and F. Gebhard, J. Phys. Conf. Ser. **376**, 012021 (2012).
[51] R.J. Potter, N. Balkan, H. Carrère, A. Arnoult, E. Bedel, and X. Marie, Appl. Phys. Lett. **82**, 3400 (2003).
[52] T. Nuytten, M. Hayne, B. Bansal, H.Y. Liu, M. Hopkinson, and V.V. Moshchalkov, Phys. Rev. B **84**, 045302 (2011).
[53] Y.P. Varshni, Physica **34**, 149 (1967).
[54] O. Rubel, M. Galluppi, S.D. Baranovskii, K. Volz, L. Geelhaar, H. Riechert, P. Thomas, and W. Stolz, J. Appl. Phys. **98**, 063518 (2005).

[55] S.D. Baranovskii, R. Eichmann, and P. Thomas, Phys. Rev. B **58**, 13081 (1998).
[56] P.G. Eliseev, P. Perlin, J. Lee, and M. Osiński, Appl. Phys. Lett. **71**, 569 (1997).
[57] S. Imhof, A. Thränhardt, A. Chernikov, M. Koch, N.S. Köster, K. Kolata, S. Chatterjee, S.W. Koch, X. Lu, S.R. Johnson, D.A. Beaton, T. Tiedje, and O. Rubel, Appl. Phys. Lett. **96**, 131115 (2010).
[58] C. Cornet, T. Nguyen Thanh, T. Quinci, S. Almosni, T. Rohel, J. Kuyyalil, A. Rambaud, A. Létoublon, N. Bertru, O. Durand, and A. Le Corre, Appl. Phys. Lett. **101**, 251906 (2012).
[59] K. Jandieri, B. Kunert, S. Liebich, M. Zimprich, K. Volz, W. Stolz, F. Gebhard, S.D. Baranovskii, N. Koukourakis, N.C. Gerhardt, and M.R. Hofmann, Phys. Rev. B **87**, 035303 (2013).
[60] A. Miller and E. Abrahams, Phys. Rev. **120**, 745 (1960).
[61] M. Baranowski, R. Kudrawiec, M. Latkowska, M. Syperek, J. Misiewicz, and J.A. Gupta, Appl. Phys. Lett. **100**, 202105 (2012).
[62] S. Francoeur, G. Sivaraman, Y. Qiu, S. Nikishin, and H. Temkin, Appl. Phys. Lett. **72**, 1857 (1998).
[63] L. Peternai, J. Jakabovič, and M. Michalka, in *9th Int. Work. Apcom* (2003), pp. 157–160.
[64] F. Zhang, D. Zhang, B. Li, E. Liu, F. Liu, and R. Gan, Mater. Sci. Eng. B **48**, 198 (1997).
[65] S. Borck, S. Chatterjee, B. Kunert, K. Volz, W. Stolz, J. Heber, W.W. R hle, N.C. Gerhardt, and M.R. Hofmann, Appl. Phys. Lett. **89**, 031102 (2006).
[66] C. Robert, M. Perrin, C. Cornet, J. Even, and J.M. Jancu, Appl. Phys. Lett. **100**, 111901 (2012).
[67] W.W. Chow, S.W. Koch, and M. Sargent, *Semiconductor-laser Physics* (Springer-Verlag, 1994).
[68] C. Robert, T.N. Thanh, A. Létoublon, M. Perrin, C. Cornet, C. Levallois, J.M. Jancu, J. Even, P. Turban, A. Balocchi, X. Marie, O. Durand, and A. Le Corre, Thin Solid Films **541**, 87 (2013).
[69] P.F. Fewster, *X-ray Scattering from Semiconductors*, 2nd Edition (Imperial College Press, London, 2003).
[70] D.K. Bowen and B.K. Tanner, *High Resolution X-Ray Diffractometry And Topography* (CRC Press, 1998).
[71] S. Adachi, J. Appl. Phys. **66**, 6030 (1989).
[72] G.E. Jellison and F.A. Modine, Appl. Phys. Lett. **69**, 371 (1996).
[73] H. Yao, P.G. Snyder, and J.A. Woollam, J. Appl. Phys. **70**, 3261 (1991).
[74] M. Erman, J.B. Theeten, P. Chambon, S.M. Kelso, and D.E. Aspnes, J. Appl. Phys. **56**, 2664 (1984).
[75] H. Kato, S. Adachi, H. Nakanishi, and K. Ohtsuka, Jpn. J. Appl. Phys. **33**, 186 (1994).
[76] D.E. Aspnes, Thin Solid Films **89**, 249 (1982).
[77] S. Zollner, Appl. Phys. Lett. **63**, 2523 (1993).
[78] S.G. Choi, Y.D. Kim, S.D. Yoo, D.E. Aspnes, D.H. Woo, and S.H. Kim, J. Appl. Phys. **87**, 1287 (2000).
[79] Y.W. Jung, J.S. Byun, S.Y. Hwang, Y.D. Kim, S.H. Shin, and J.D. Song, Thin Solid Films **519**, 8027 (2011).
[80] B. Monemar, Solid State Commun. **8**, 1295 (1970).
[81] Y.-H. Li, A. Walsh, S. Chen, W.-J. Yin, J.-H. Yang, J. Li, J.L.F. Da Silva, X.G. Gong, and S.-H. Wei, Appl. Phys. Lett. **94**, 212109 (2009).
[82] K. Adomi, N. Noto, A. Nakamura, and T. Takenaka, J. Cryst. Growth **124**, 570 (1992).
[83] S. Nagao, T. Fujimori, H. Gotoh, H. Fukushima, T. Takano, H. Ito, S. Koshihara, and F. Minami, J. Appl. Phys. **81**, 1417 (1997).
[84] T. Sugita, N. Usami, and Y. Shiraki, J. Cryst. Growth **188**, 323 (1998).

[85] K. Arimoto, T. Sugita, N. Usami, and Y. Shiraki, Phys. Rev. B **60**, 13735 (1999).
[86] A. Chen and J.M. Woodall, Appl. Phys. Lett. **94**, 021102 (2009).
[87] M.T. Borgström, K. Mergenthaler, M.E. Messing, U. Håkanson, J. Wallentin, L. Samuelson, and M.-E. Pistol, J. Cryst. Growth **324**, 290 (2011).
[88] E. Garmire, Appl. Phys. Lett. **23**, 403 (1973).
[89] V.A. Odnoblyudov and C.W. Tu, Appl. Phys. Lett. **88**, 071907 (2006).
[90] T. Kawai, K. Yamane, Y. Furukawa, H. Okada, and A. Wakahara, Phys. Status Solidi C **8**, 288 (2011).
[91] I.. Vorona, N.. Thinh, I.. Buyanova, W.. Chen, Y.. Hong, and C.. Tu, Phys. B Condens. Matter **340–342**, 466 (2003).
[92] H. Okada, K. Kumagai, T. Kawai, H. Sekiguchi, and A. Wakahara, in *2012 Ieee Photonics Conf. Ipc* (2012), pp. 887–888.
[93] H. Kanaya, H. Yaguchi, Y. Hijikata, S. Yoshida, S. Miyoshi, and K. Onabe, Phys. Status Solidi C 2753 (2003).
[94] Y. Furukawa, H. Yonezu, A. Wakahara, Y. Yoshizumi, Y. Morita, and A. Sato, Appl. Phys. Lett. **88**, 142109 (2006).
[95] M. Kaneko, T. Hashizume, V.A. Odnoblyudov, and C.W. Tu, J. Appl. Phys. **101**, 103707 (2007).
[96] T. Nguyen Thanh, C. Robert, W. Guo, A. Létoublon, C. Cornet, G. Elias, A. Ponchet, T. Rohel, N. Bertru, A. Balocchi, O. Durand, J.S. Micha, M. Perrin, S. Loualiche, X. Marie, and A. Le Corre, J. Appl. Phys. **112**, 053521 (2012).

Chapter 4

Study of InGaAs/GaP quantum dots

In this chapter, we present a detailed (structural, theoretical and optical) study of the InGaAs(N)/GaP QD system. Its potentiality as an alternative to GaAsPN QW for lasing applications is discussed.

4.1 Advantages of quantum dots for laser applications

The use of QD in a laser active zone has first been proposed by Arakawa and Sakaki in 1982[1]. Most of the expected properties of QD laser has been predicted in the 1980's[1,2] although the first QD laser realization is dating from 1994[3–5]. Almost all the QD interesting properties derive from the peculiarities of the density of states (DOS). Indeed, the DOS for 0D systems consists in Dirac peaks at each confined state. Thus, for an equal carrier's density, the optical gain in a QD system is expected to be higher, in comparison to larger dimensionality systems (bulk, quantum well, quantum wire)[2]. Moreover, the population inversion and thus the transparency threshold occur for lower carrier densities in QD systems. Consequently, lower threshold currents have been demonstrated in QD lasers, in comparison to their QW counterparts[6]. In addition, the temperature-sensitivity of this threshold current is known to be reduced[7]. Furthermore, because of the high differential gain, QD laser are expected to present better dynamical properties suitable for a direct modulation of light[8]. Finally, QD present two additional advantages particularly suitable for the pseudomorphic integration on Si. Because the carriers are strongly localized in a small volume, they are less sensitive to defects. And, QD allow the coherent growth of smaller band gap material nanostructures with larger lattice-mismatch, and may be an efficient alternative to dilute nitride QW to reach the transparency window of Si (emission wavelength above 1.1 μm).

Nevertheless, in order to develop an efficient laser structure, QD have to present good structural, electronic and optical properties. To get a large optical gain, the QD density has to be high, but with size dispersion as small as possible. In terms of electronic band structure, direct and type-I transitions are obviously preferred. Finally, radiative lifetimes have to be shorter than non-radiative lifetimes and rising times have to be as short as possible to ensure a good carrier capture.

4.2 Quantum dots on GaP substrate

Various QD systems on GaP have been studied in the past decade. The (In,Ga)P/GaP QD system has been proposed. Gerhard *et al.*[9] have demonstrated high density QD of In-rich $Ga_{0.46}In_{0.54}P$ alloy on GaP (surface density ~1 x 10^{11} cm^{-2}). But only low intensity photoluminescence (PL) signal at 4 K has been observed. InP/GaP QD have also been studied[10,11] and related devices have been developed[12]. However, bandlineups between (In,Ga)P and GaP have been demonstrated to be borderline type-I - type-II and the QD density is low (10^8-10^9 cm^{-2})[13].

The (In,Ga)As(N)/GaP QD, with an appropriate In content, are expected to overcome bandlineups issue[14]. InAs/GaP QD have first been proposed[15,16], but efficient PL has not been achieved because of the plastic relaxation due to the large lattice mismatch (11.2 %). Then, Shamirzaev *et al.*[17] have claimed the demonstration of type-I alignment for GaAs QDs on GaP, but strain relaxation processes and indirect band gap led to PL emission only up to 40 K. The quaternary dilute nitride InGaAsN/GaP QD system has recently attracted much attention. Indeed, the lowest emission energy ever been reported for a QDs system on GaP has been demonstrated with the room temperature photoluminescence of InGaAsN/GaP QD at 1.39 eV[18]. Moreover, Fukami *et al.* have claimed that the transparency window of silicon may be reached when In composition is 50% to approximately 60% and N composition is 1% to approximately 2%[14]. However, the large full width at half maximum (FWHM) (334 meV) has been interpreted as a broad inhomogeneous distribution of the QD size[18].

In this thesis, the InGaAs/GaP QD are studied as a step toward InGaAsN/GaP QD system. In a 2004 report on MOCVD-grown InGaAs/GaP QDs properties, Fuchi *et al.*[19] have measured a PL signal up to 77 K and pointed out the issue of In composition. But the major

progresses have been achieved very recently by a few research groups. In 2010, Song *et al.*[20] have reported the MBE-growth of low density (1.5 x 10^{10} cm^{-2}) $In_{0.5}Ga_{0.5}As$ QD but have shown a PL signal only up to 80 K. We present, in the next sections, the first room temperature PL that has been obtained in our group for a low In content in 2011[21]. Then, Rivoire *et al.*[22] have claimed single emission of type-I $In_{0.5}Ga_{0.5}As$/GaP QD. The first room temperature electroluminescence has been demonstrated by Song and Lee in 2012[23]. Meanwhile, we have presented a detailed study of structural, electronic and optical properties of InGaAs/GaP QD[24,25]. Finally, the group of TU Berlin has recently proposed the MOCVD-grown $In_{0.25}Ga_{0.75}As$/GaP QD system for nanomemory cells applications[26,27].

4.3 Growth and structural properties of InGaAs/GaP QD

4.3.1 Growth details

The (In,Ga)As QD have been grown on both n-doped and undoped GaP(001) substrates using a Gaz-Source Molecular Beam Epitaxy (GSMBE) or a Solid-Source Molecular Beam Epitaxy (SSMBE). The substrate temperature has been nominally set to 580 °C. The influence of the growth temperature will be discussed in section 4.7.1. A GaP buffer layer has been first deposited. It has been n-doped using silicon at 10^{17} cm^{-3} only for STM measurements. Then the QD have been formed with the deposition of 3 monolayers (ML) for SSMBE samples or 4 ML for GSMBE samples with a subsequent 30 s growth interruption under As. The influence of the growth interruption time will be discussed in section 4.7.2. A careful attention has been paid to ensure that QD grown in both MBEs give similar structural and optical properties. Nominal composition of indium has been set to 30 %. For cross-sectional STM (X-STM) and optical measurements, the QD have been capped with a thin 30-nm thick GaP layer whereas for plane-view STM or AFM measurements, no capping layer has been deposited.

4.3.2 Structural properties

Plane-view STM measurements have been performed in collaboration with P. Turban from the University of Rennes 1. Fig. 4-1(a) shows a 800 x 800 nm^2 image of InGaAs/GaP QD. A very high QD density is measured (1.3 x 10^{11} ± 0.2 x 10^{11} cm^{-2}). Such a high density is encountered in well-known QD materials systems such as InAs/InP or InAs/GaAs, which are currently used in high performance laser devices[28,29]. The mean QD height and diameter are equal

to (3.5 ± 1.2) nm and (18.0 ± 3.6) nm respectively. Fig. 4-1(b) presents the statistical correlation between diameter and height. The size homogeneity is found to be not far from the state-of-the art QD in other reference materials systems[28,29]. At least from the structural properties view, our InGaAs/GaP QD are thus suitable for laser applications.

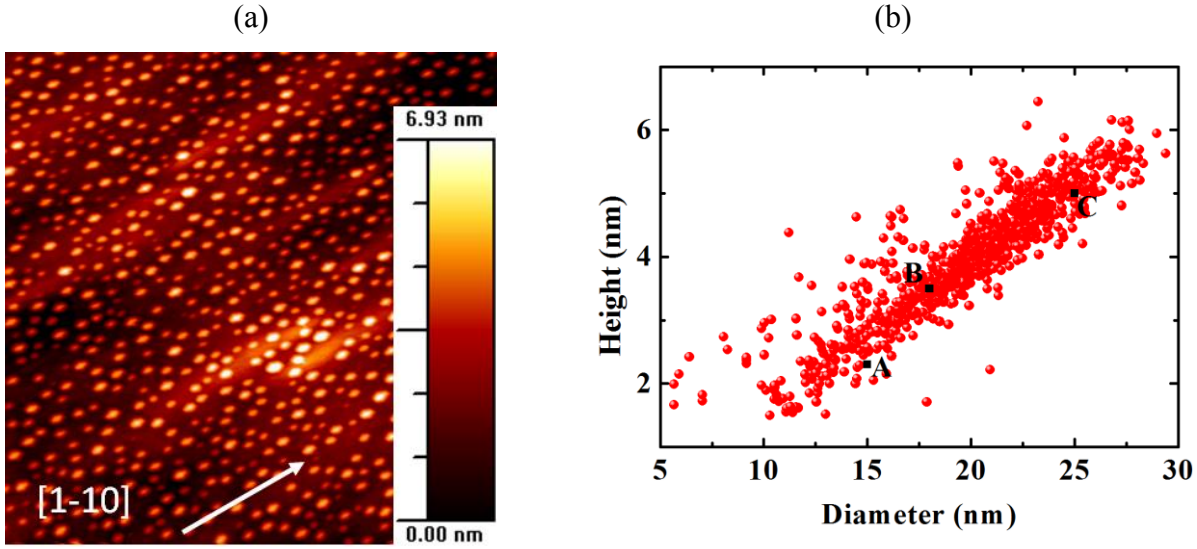

Fig. 4-1: (a) 800 x 800 nm^2 STM image of InGaAs/GaP QD and (b) statistical correlation between diameter and height.

Further details can be brought out with the analysis of single QD morphology. Fig. 4-2(a) presents a 60 x 60 nm^2 STM high-resolution image of the surface with a few QD. Atomic sites with high electronic density are fingerprints of an indium-rich surface. They are observed on top of QD as well as on the base planar surface. The presence of indium reveals the existence of a wetting layer (WL) and thus demonstrates the Stranski-Krastanov (SK) growth mode. The issue of indium composition determination in the QD cannot be solved easily. Indeed, although the nominal composition is 30 %, the effective indium composition depends on indium segregation, indium desorption, or surface energies, which are non-trivial problems and require specific investigations[27,30]. The desorption of In atoms arises when the temperature is higher than 520 °C, but indium incorporation has been reported even at 595 °C during (In,Ga)As/GaAs deposition[31]. The indium incorporation coefficient in InGaAs/GaAs epilayers at this temperature has been measured to be around 40-50 %[32–35], depending on growth conditions. Considering that the indium incorporation is dependent on the strain[33,36], the indium incorporation coefficient in our case (i.e. on GaP substrate) is even lower, which would lead to an indium effective composition below or equal to 15 %. Fig. 4-2(a) inset presents the morphology of a typical small single QD,

and Fig. 4-2(b) presents the morphology of a larger QD. The in-plane anisotropic ratio (between length and width) is reduced from 1.5 (small QD) to nearly 1 (large QD). These values show the relatively low in-plane anisotropy of our QD. The small QD (Fig. 4-2(a)) exhibits six main facets, including (136), (316), $(\bar{1}\bar{3}6)$ and $(\bar{3}\bar{1}6)$ well-defined planes, and two other facets with a more diffuse aspect. In the larger QD of Fig. 4-2(b) the QD presents additional facets, especially well-defined low-index (111) facets. A striking feature that can be highlighted for the smallest QD is the absence of a σ_v plane symmetry that would be expected for conventional QD[37–42]. Instead, QD exhibit a C_2 symmetry which may be an interesting feature for single dot spectroscopy[22], which is beyond the scope of this thesis.

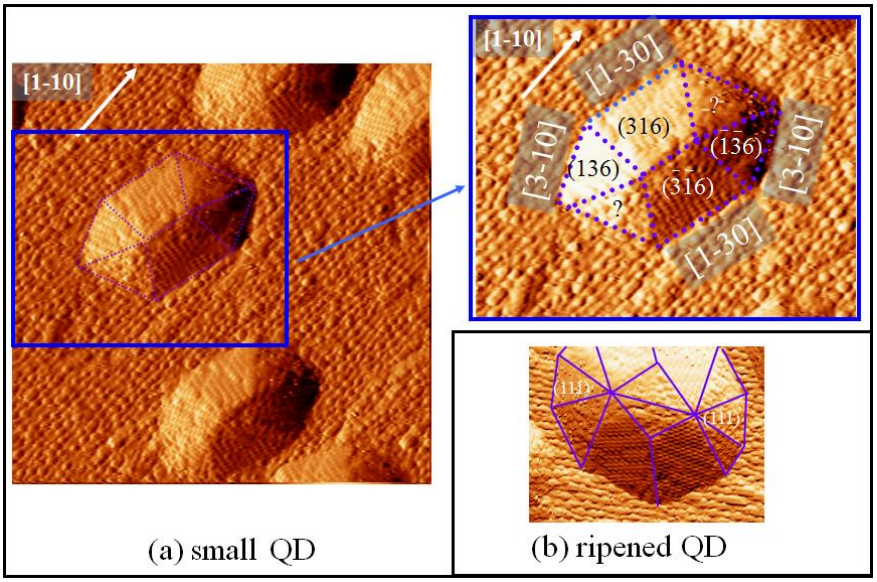

Fig. 4-2: (a) 60 x 60 nm^2 plane-view STM image of not ripened InGaAs QD. A detailed analysis of the image allows the identification of the facets in the inset. (b) The facet analysis for ripened QD shows low-index facets appearing with underlying crystal symmetry.

The main drawback of plane-view images is that it does not embrace the role of the capping layer in the QD shape. X-STM measurements on buried InGaAs/GaP QD have been performed in collaboration with the group of P. Koenraad in TU Eindhoven. Fig. 4-3 shows an image of such a buried QD. Both anisotropic shape and presence of a WL are confirmed. Nevertheless, the dimensions cannot be determined unambiguously because of the uncertainty of the cleaving plan in regard to the middle of the QD. Furthermore, getting a relevant statistical distribution of QD is a hard task. However, the dimensions of the QD of Fig. 4-3 (3.4 nm height and 19.5 nm width) are in good agreement with the mean dimensions determined by plane-view

STM, which can let us reasonably thinking that the capping procedure does not strongly affect the shape.

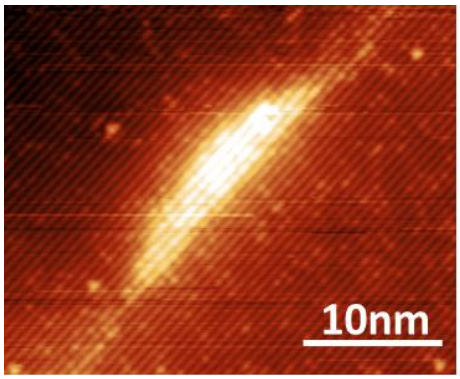

Fig. 4-3: X-STM image of an InGaAs/GaP QD.

4.4 Electronic band structure

In this section, we present a first simulation of the electronic band structure of InGaAs/GaP QD.

4.4.1 Bulk InGaAs

We first calculate the band structure of bulk InGaAs alloy with the TB model presented in Chapter 2. The VBO are taken from recent *ab initio* calculations[43] and are summarized in Table 4-1.

	GaP	GaAs	InAs
VBO (eV)	3.29	3.83	3.9

Table 4-1: VBO taken in the calculation.

Fig. 4-4(a) presents the band alignments of unstrained bulk InGaAs with bulk GaP for an In content between 0 % and 50 %. Obviously, the conduction band minimum is located at the Γ point for the entire In content range. A realistic calculation must however include the effect of large compressive strain (3.7 % for GaAs/GaP and 7.4 % for $In_{0.5}Ga_{0.5}As$/GaP), as the electronic levels are strongly modified by strain (see section 2.2.2). Fig. 4-4(b) shows the band alignments when bulk InGaAs is biaxially strained on GaP. In the valence band, the heavy and light hole states are split by about 200 meV so that in the following, the valence band maximum will be systematically considered of heavy hole type. The case of the conduction band minimum is not trivial. For instance, the simulation leads to the result that GaAs becomes slightly indirect when

strained to be lattice-matched to GaP. For low In content, the Γ, L and X_{XY} conduction bands energies of InGaAs and the X conduction band energy of GaP are located in the same energy window of 150 meV. Thus, the lateral valleys are expected to have a strong influence on the band structure of InGaAs/GaP QDs.

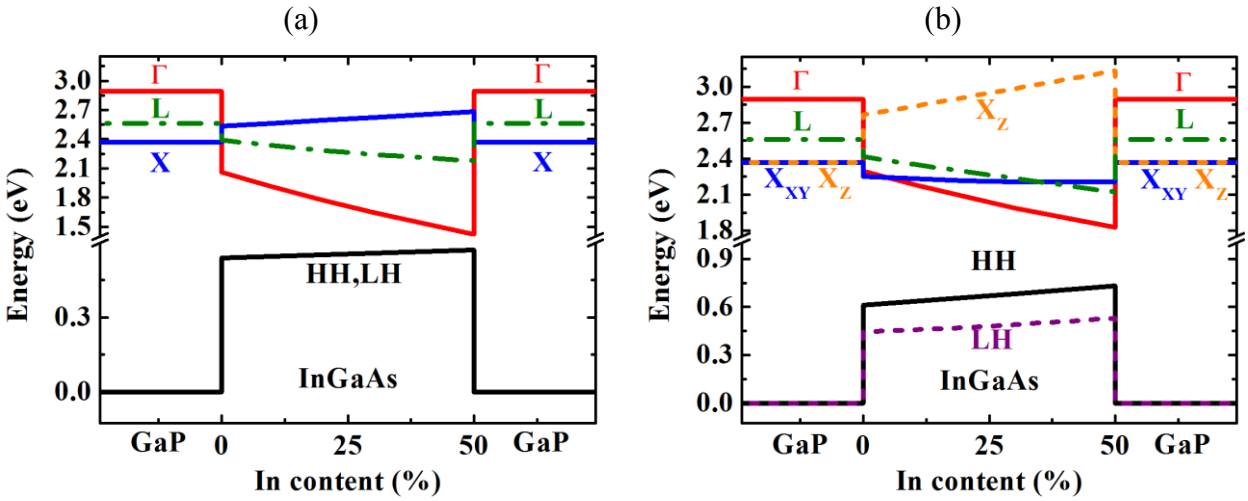

Fig. 4-4: Band alignment and band structure of bulk $In_xGa_{1-x}As$ and GaP in the unstrained case (a) and when $In_xGa_{1-x}As$ is biaxially strained on GaP (b). The calculations are performed at 0 K with the TB model.

4.4.2 First description of the electronic band structure of InGaAs/GaP QD

The electronic band structure of InGaAs/GaP QD can be calculated with the supercell TB model presented in Chapter 2. Nevertheless, for a first description[24], we have chosen to use a simpler strategy which is computationally simpler. A more recent supercell TB simulation using the new version of TB code is presented at the end of this chapter to refine the discussion.

4.4.2.1 Modeling strategy

To calculate the direct optical transition, we actually consider the eight-band **k·p** model. STM results of section 4.3.2 have shown that QD exhibit small in-plane anisotropy. For simulation calculation, we thus assume a full $C_{\infty v}$ symmetry and use the modified Hamiltonian for axial symmetry presented in section 2.4.2.2 for InAs/InP QD. The 75 x 75 nm^2 STM image, shown on Fig. 4-5(a), exhibits InGaAs/GaP QD with approximatively a cone shape. The **k·p** simulation is performed using the geometry defined on Fig. 4-5(b). Three typical dimension sets representative of the inhomogeneous size distributions are summarized in the table of Fig. 4-5(b). The A, B and C geometries correspond to real QD found in the statistical distribution of Fig. 4-1(b). The D geometry is chosen to prospectively study larger QD in order to address the

problem of lowering the emission energy. A typical WL of 1-ML thick is added in the model to account for the SK growth mode.

(a) (b)

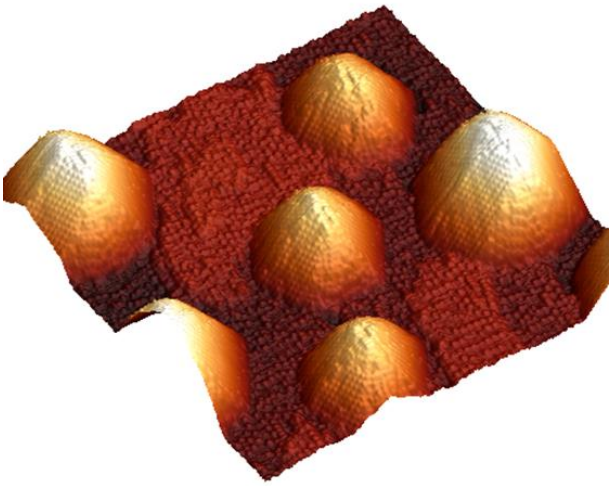

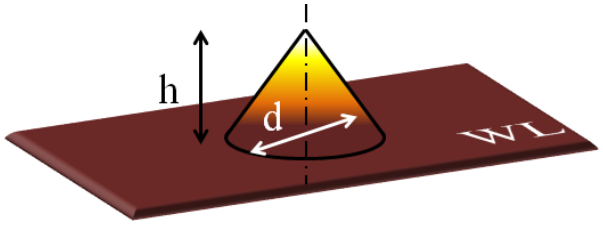

QD geometry	h (nm)	d (nm)
A	2.3	15
B	3.5	18
C	5	25
D	6.5	36

Fig. 4-5: (a) 75 x 75 nm^2 STM 3D plane view of InGaAs QD showing the different size of QD. (b) Cone-shaped QD geometry for the eight band k·p calculations.

To get an estimation of X-like and L-like states energies in the dot, we consider the TB model for a QW to calculate the electronic levels in the X_{XY} and L conduction bands. The equivalent QW is assumed to have a thickness equal to the height of the QD. Disregarding the lateral quantum confinement effect on these bands, we assume that the results are a good approximation of the X-like and L-like states energies for a QD. A justification is provided in Fig. 4-6. The first electronic levels in the Γ, X_{XY} and L valleys are calculated by the TB model for an $In_{0.3}Ga_{0.7}As$/GaP QW as a function of the thickness. It shows that quantum confinement mainly affects the Γ band. The X_{XY} and L are less affected because of their larger effective mass and their smaller conduction band offset with X and L bands of GaP (see Fig. 4-4(b)). The transition associated with the wetting layer can also be simulated by a 1 ML thick QW in TB description.

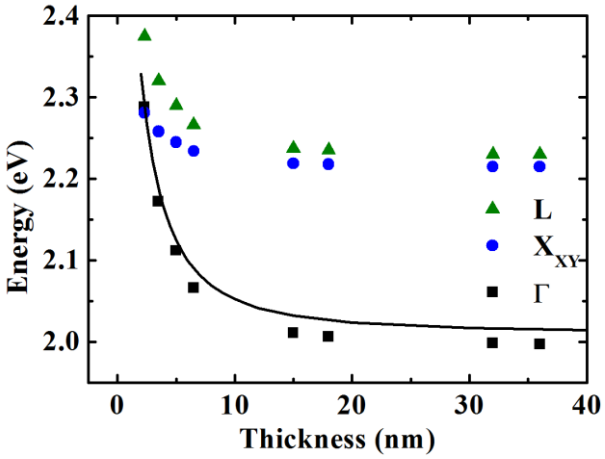

Fig. 4-6: First electronic levels in the Γ, X_{XY} and L valleys for an $In_{0.3}Ga_{0.7}As$/GaP QW as a function of the thickness calculated with the TB model. The first electronic level in the Γ valley calculated with the k·p method is shown by the solid line.

Another point has to be mentioned. The decomposition of QD electronic states in reciprocal space is not so straightforward[44]. Indeed, due to the breaking of translational symmetry, complex band folding occurs in a QD Brillouin zone and **k** is no longer a good quantum number. Thus, the electronic states originating from different points of the Brillouin zone of the parent bulk material are mixed. This first calculation neglects this intervalley electronic coupling in order to calculate the Γ, X and L QD energy levels independently. This coupling effect is more likely to occur when the states are close in energy. We are aware that the states labeled Γ and X in our calculations should be coupled in a more advanced theoretical description (in a supercell TB model for instance). However, for the case of a QW, we can estimate this coupling effect by calculating the confined states in the Γ valley with both models; i.e., eight band **k·p** method for which the conduction band mixing is not taken into account and TB model for which it is. The results of Fig. 4-6 show that both models give approximately the same value (solid black line and black square points) suggesting that conduction band mixing may have a small effect at least on the energetic position of the electronic levels.

4.4.2.2 Results

The results for the four geometries are represented in Fig. 4-7. The case of the smaller QD (type A) is clear. The first Γ-like quantum confined electronic level (calculated by the **k·p** method) lies well above the first X and L levels (calculated by the TB method). The energy separation between the X and the Γ level is found to be 400 meV and 240 meV for In contents of

0 % and 30 % respectively. The X_{XY} and L states of GaP barrier material are even found to be at lower energy than the Γ level of the dot. The radiative emission probability from the Γ-Γ transition is expected to be small for these dots. The case of the wetting layer is similar (see Fig. 4-8). Due to the strong confinement effect, the Γ level of the WL lies above the X_{XY} and L states of both the WL and the GaP barriers. The electronic confinement is even found to be very weak, especially for the X_{xy} and L states (below 10 meV). Thus, except for the HH state, the wave function is not much localized in the WL. For type B QD, the indirect to direct crossover occurs only for In content above 50 %.

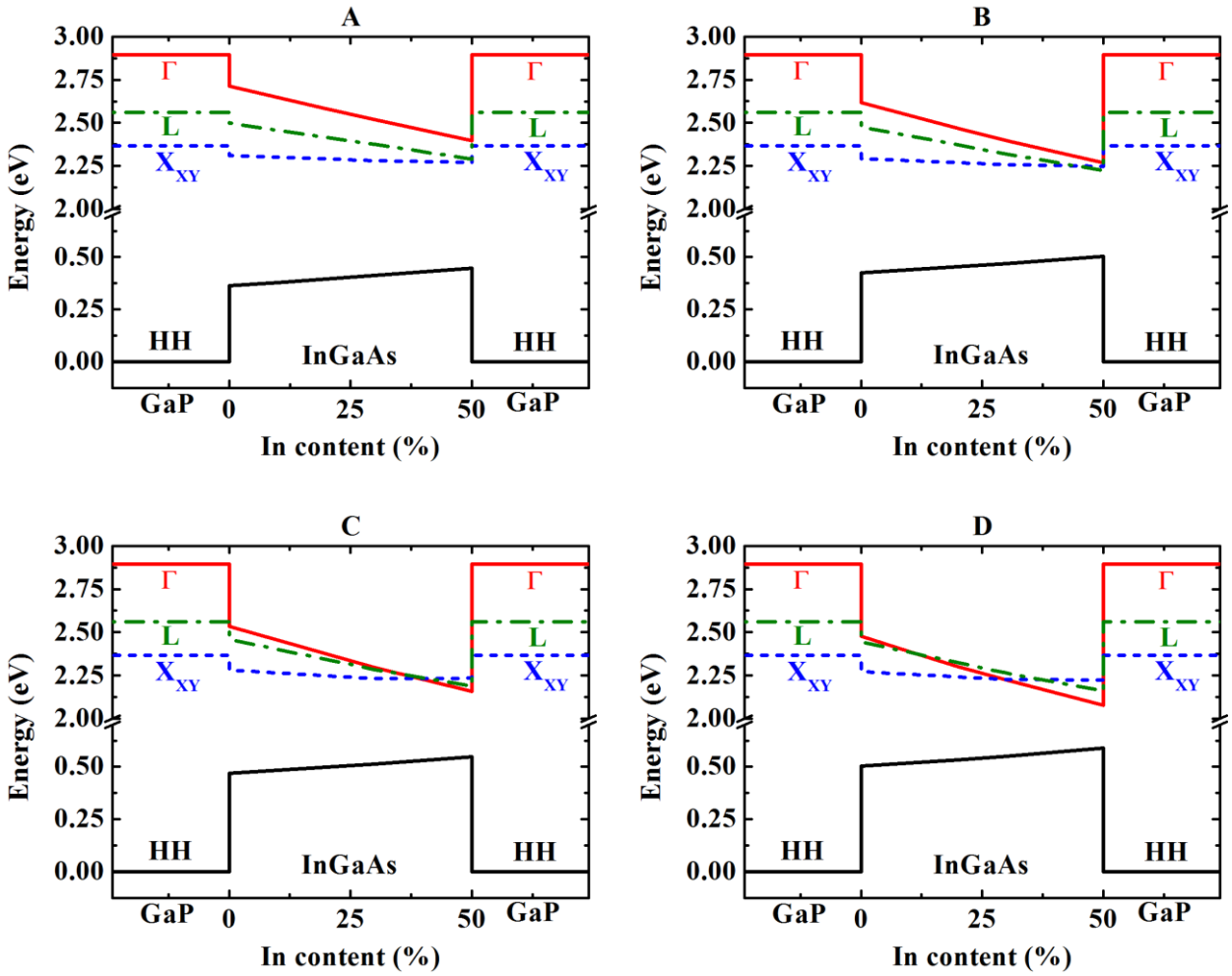

Fig. 4-7: First confined energy levels of $In_xGa_{1-x}As$ QD in Γ, X_{XY} and L conduction bands and in HH valence band and their band alignment with the GaP barrier states for the four geometries defined in Fig. 4-5(b) and as a function of In content. The first electronic level in the Γ valley and the first hole level are calculated with the k·p method. The first electronic levels in the X and in the L valleys are calculated with the TB method. All calculations are performed at 0 K.

The cases of type C and type D QD are somewhat different. Indeed, because of their larger spatial dimensions, the quantum confinement effect on the Γ conduction band is less pronounced. Thus, the lowest conduction band is found to be Γ-like for In content above 39 % for C dots and above 29 % for D dots. If we assume that there is about 15 % of In in our QD, the lowest conduction state is thus X-like. Nevertheless, for bigger dots, the Γ state lies 90 meV above the X state.

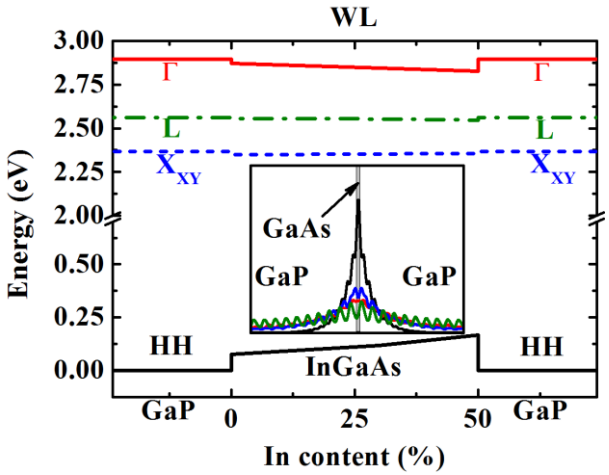

Fig. 4-8: TB calculation of the first confined energy levels in a 1 ML $In_xGa_{1-x}As$ QW embedded in GaP in Γ, X_{XY} and L conduction bands and in HH valence band and their band alignment with the GaP barrier states as a function of In content. The inset shows the square wave function of a 1 ML GaAs QW embedded in GaP. All calculations are performed at 0 K.

4.5 Optical properties

After having qualitatively studied the electronic band structure of $In_xGa_{1-x}As$ /GaP QD, we now present a discussion about their optical properties.

Photoluminescence experiments have been carried out by exciting samples with a 405 nm continuous-wave laser diode. The power density is roughly estimated to be 80 $W.cm^{-2}$. The samples have been set in a helium bath closed-cycle cryostat to study PL from 10 K to room temperature. Measurements have also been performed above room temperature using a hot plate.

4.5.1 A preliminary study

The optical experiments presented in section 4.5 have been performed on three samples corresponding to different growth conditions (Table 4-2).

Sample	S1	S2	S3
MBE apparatus	GSMBE	SSMBE	GSMBE
Growth temperature	580 °C	550 °C	580 °C
InGaAs ML deposited	4	3	4
Growth interruption time	30 s	30 s	180 s
GaP substrate	n-doped	undoped	undoped
GaP Buffer thickness	500 nm	68 nm	500 nm

Table 4-2: Growth details of the three samples used for the optical properties measurements.

The goal of this preliminary study is to make a quick comparison between samples obtained under slightly different growth conditions and to show that similar QD growth processes could be used for the two MBE chambers. Actually, the three samples exhibit optical properties with very similar trends. For example, Fig. 4-9 shows the room temperature PL of the three samples. Each spectrum exhibit two main peaks which are slightly closer in energy for the S1 sample. The larger PL intensity is obtained for S3 sample. It is attributed essentially to a better structural quality.

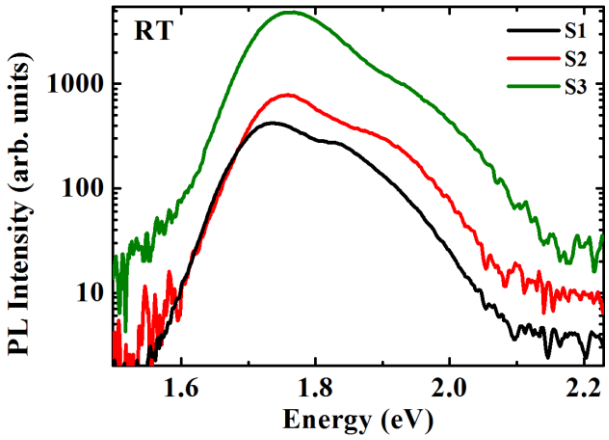

Fig. 4-9: Room temperature PL of the three $In_xGa1_{-x}As$/GaP samples.

It is also interesting to consider the influence of the substrate on the optical properties. Indeed, n-doped GaP substrates are known to exhibit red-luminescence in the 715 nm range, close to the observed QD luminescence peak. Fig. 4-10 shows the room temperature PL of n-doped and undoped GaP substrates on which a GaP buffer is grown. The PL signal is only clearly visible for a n-doped GaP substrate with a thin buffer thickness. The penetration length of the 405

nm-laser in GaP is equal to 126 nm. All the InGaAs QD have thus been grown on either undoped substrate or above a thick enough GaP buffer layer (~500 nm), in order to unambiguously avoid a possible red luminescence from the GaP substrate.

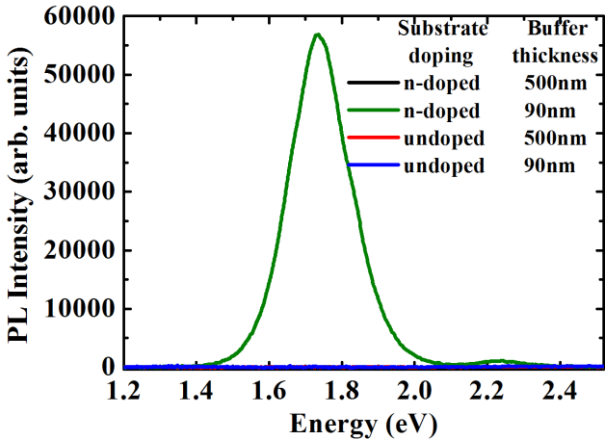

Fig. 4-10: Room temperature PL of GaP substrate (n-doped or undoped) and for two different grown GaP buffer thicknesses. Red luminescence is only observed for n-doped substrate when the buffer layer is thin with respect to the absorption length.

4.5.2 Temperature dependent PL

4.5.2.1 Observations

Fig. 4-11 presents the temperature variation of the $In_xGa_{1-x}As$/GaP QD PL spectrum in the [12 K-375 K] temperature range. The peak shape has a strong evolution from low to high temperature. At 12 K, PL exhibits a single peak centered at 1.78 eV. It is however slightly power dependent and evolves to 1.76 eV at lower excitation power, as will be shown in a section 4.5.4. The full width at half maximum (FWHM) of the PL peak is equal to 100 meV and is attributed to the QD inhomogeneous size distribution. The temperature increase leads to a red shift of the main peak to 1.74 eV at room temperature. At 260 K, a shoulder appears on the high energy side of the spectrum. At 300 K, another optical transition can be clearly distinguished. When increasing the temperature above 300 K, the maximum of PL intensity switches from a low energy (LE) peak to a higher energy (HE) peak.

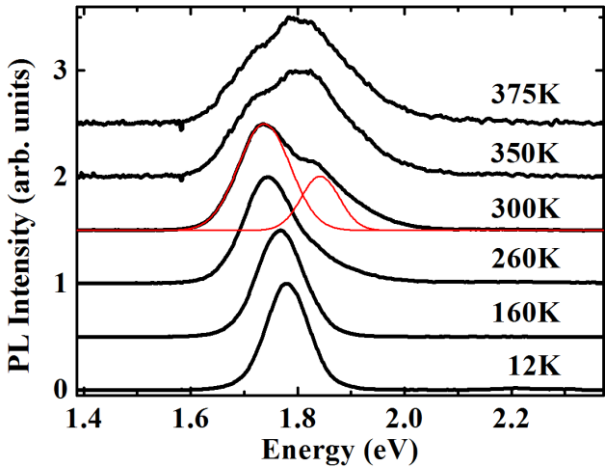

Fig. 4-11: Temperature-dependent PL spectra of sample S1. The intensities are normalized and spectra are shifted by 0.5 in intensity for clarity. The red thin lines show the fit of the two transitions LE and HE by two Gaussian peaks.

The quenching of the QD integrated PL intensity with temperature is represented in Fig. 4-12. The results can be well fitted with an Arrhenius law with two activation energies:

$$I = \frac{I_0}{1 + \alpha_1 \exp\left(\frac{-E_{a1}}{kT}\right) + \alpha_2 \exp\left(\frac{-E_{a2}}{kT}\right)}$$

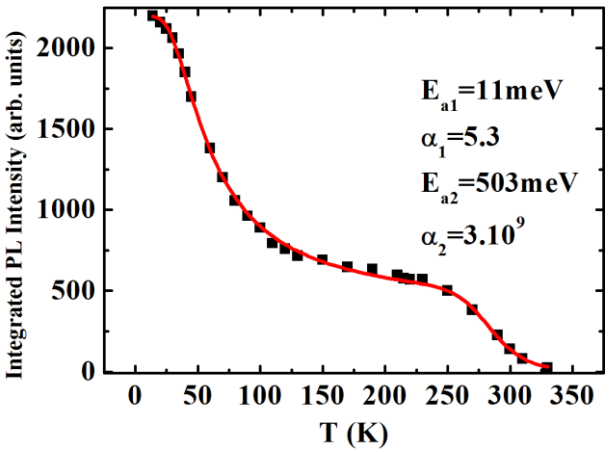

Fig. 4-12: Integrated PL intensity versus inverse temperature of sample S2. The red line shows the fit with an Arrhenius law and two activation energies.

where α_1 and α_2 are related to carriers escape efficiencies from the QD toward non-radiative levels. A first weak activation energy of 11 meV is found, but with a weak α_1 prefactor. Thus, the PL intensity between 12 K and 230 K is only reduced by a factor of 3.8. The second activation

energy ($E_{a2} = 503$ meV) is much larger but the corresponding large α_2 prefactor has a dramatic influence on the QD PL efficiency.

The energies of the LE and HE transitions can be extracted using a double Gaussian fit. The results are shown on Fig. 4-11 for 300 K by thin red lines. The LE transition is found by fitting the low energy side of the PL spectrum by a first Gaussian peak. The HE transition is found by applying the same procedure on the spectrum resulting from the subtraction of the first Gaussian peak from the original PL spectrum. The high energy tail is not fitted and is attributed to the thermal filling of higher energy states. The difference in energy between these two transitions is $E_{HE}-E_{LE}=100$ meV. The integrated intensity related to both transitions is also extracted by taking the areas under both Gaussians. In Fig. 4-13, the ratio between the integrated intensities of the HE peak (A_{HE}) and the LE peak (A_{LE}) is represented on a logarithm scale as a function of $1/k_BT$.

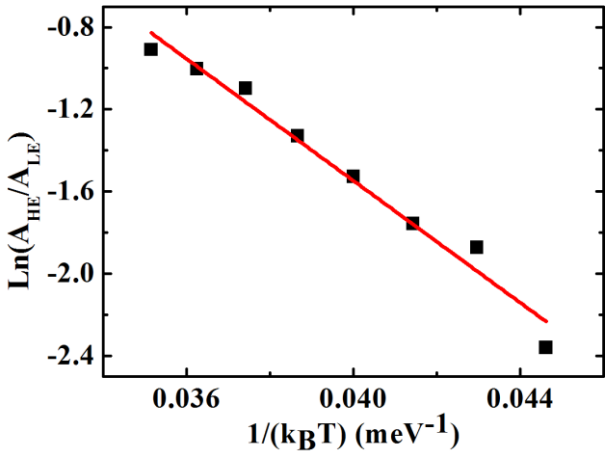

Fig. 4-13: Ratio between the integrated intensities related to the two HE and LE transitions as a function of $(k_BT)^{-1}$ for sample S1. The red line shows a linear fit.

The linear shape of the curve is interpreted as the thermalization of excitons between both states with a ratio:

$$\frac{A_{HE}}{A_{LE}} = \frac{\tau_{LE}}{\tau_{HE}} \exp\left(-\frac{E_A}{k_BT}\right)$$

An activation energy E_A of 140±10 meV is deduced, which is consistent with the difference in energy between the two transitions $E_{HE}-E_{LE}$. The ratio τ_{LE}/τ_{HE} between the radiative lifetimes is found to be 80±30 assuming that both states have the same degeneracy. It shows that the HE optical transition is radiatively more efficient than the LE one. Same trends are found in sample S2 and S3 with slightly larger $E_{HE}-E_{LE}$ and E_A.

Additional features can be analyzed at low temperature. Fig. 4-14 shows the PL spectra between 12 K and 60 K using an intensity logarithmic scale. A broad emission peak with a small intensity is centered at about 2.05 eV. We attribute this peak to the WL. It vanishes above 60 K. The peak located at 2.35 eV is attributed to the GaP substrate emission. Its intensity rapidly quenches with temperature. Meanwhile a slight carrier transfer to the WL is observed. We believe that this peak is attributed to localized levels in the GaP substrate rather than to the GaP barriers. Indeed, it clearly appears only in sample S2 for which the GaP buffer layer is thin. Please note that the large linewidth of this peak is an artifact due to a defect on our spectrometer. Indeed, our commercial fibered spectrograph included an order sorting filter placed near the CCD element. This filter had been damaged on a particular position, leading to an increased scattering of light around 530 nm (~ 2.35 eV). The spectrum taken with a non-damaged spectrometer (see the inset) shows that it corresponds actually to several thin peaks due to the recombination in shallow impurities in GaP substrate and its phonon replica.

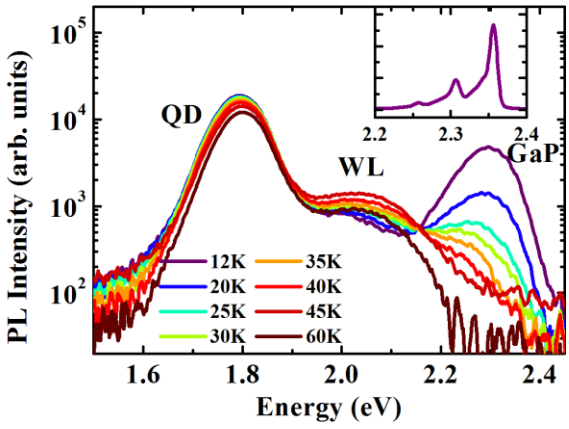

Fig. 4-14: Temperature-dependent PL spectra of sample S2 between 12 K and 60 K. Inset shows the PL of GaP at 12 K with a better resolution spectrometer.

4.5.2.2 Interpretations

These results can be interpreted on the basis of the theoretical results of section 4.4.2.2. Fig. 4-15 shows the transitions between the first X confined level in the QD and the first heavy hole state and between the first Γ confined level in the QD and the first heavy hole state for the geometries A, B and C calculated as a function of In content.

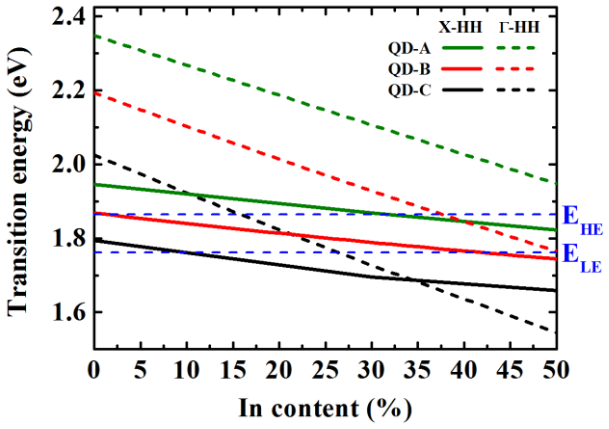

Fig. 4-15: First indirect transition energy (solid lines) and first direct transition energy (dashed lines) calculated as a function of In content for $In_xGa_{1-x}As$ QD with geometry A, B and C. All calculations are performed at 0 K. The energy position of the PL peak E_{LE} at 12 K and $E_{HE}=E_{LE}+100$ meV are shown by horizontal blue lines.

The energy position of the LE PL peak at low temperature (E_{LE}=1.76 eV) is consistent with the calculated indirect transition for QD with geometry C with an In content equal to about x=10 %. The E_{HE} transition is also in reasonable agreement with the direct transition for C QD and for x=15 %. The theoretical model approach presented in section 4.4.2 is however limited. For example, the inhomogeneity in the alloy composition due to In segregation is not taken into account. Nevertheless, we may draw a first conclusion: the LE PL peak at low temperature may result from an indirect transition with an In content x smaller than 15 %. At room temperature, charge carriers get enough thermal energy to activate a second and more efficient optical transition that could be of direct type.

In Fig. 4-12, we have measured two activation energies $E_{a1} = (12 \pm 1)$ meV and $E_{a2} = (503 \pm 90)$ meV. We attribute the second activation energy to the confinement energy of holes in the QD assuming that the confinement energy for the electrons is much smaller. Indeed, in the calculations of Fig. 4-7, for type C QD and x=15 %, we have found a difference between

the HH state of QD and the VBM of GaP equal to 490 meV. The E_{a1} value seems to be too small to be related to the confinement energy of electrons. Indeed, in the calculations of Fig. 4-7, for type C QD and x=15 %, we have found a difference between the X_{XY} state of QD and the X conduction band of GaP of 100 meV. However it could be related to a non-radiative level in the QD. We will come back to this point in the discussion about supercell calculation results in section 4.6.

Moreover, we have attempted to attribute the E_{HE} transition to the first direct transition in the QD. We believe that the PL intensity of the E_{HE} remains weak because the filling of the Γ confined state has low probability. Indeed, the first Γ electronic level is located above the GaP X state for most of QD. But, for the largest QD and with higher local In content, the QD Γ state might be very close to the barrier state. It is also important to mention that our theoretical model does not take into account the Coulombic interaction between holes and electrons. Here, the strong confinement of holes in the QD may enhance the probability of attracting the electrons on electronic levels in the QD.

The peak attributed in Fig. 4-14 to the WL is also consistent with theoretical calculations. Fig. 4-16 shows the ground state emission energy of an $In_xGa_{1-x}As$/GaP QW in the TB description calculated as a function of In content. Because of the experimental uncertainty on the WL thickness, we consider thicknesses equal to 1, 2 and 3 ML. The broad experimental linewidth of the WL PL peak (Fig. 4-14) could be explained by the fluctuation of local thicknesses and In content. Moreover, the WL ground state emission is attributed to an HH confined state and a very weakly confined X_{XY} electronic state (see Fig. 4-8), in agreement with the observed low PL intensity. The very high density of QD may also explain this very low PL intensity[45,46].

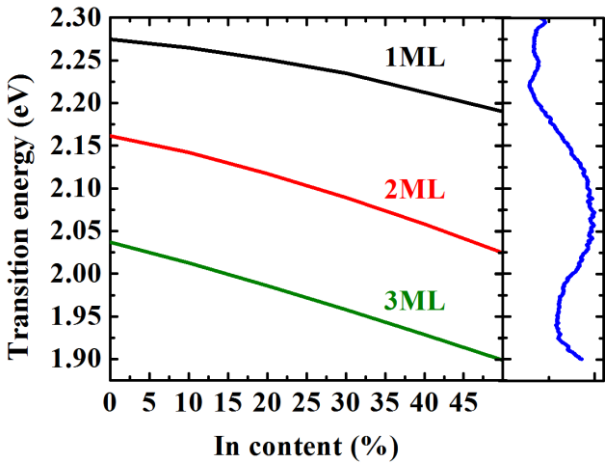

Fig. 4-16: Calculated ground state in the InGaAs WL simulated by considering a 1, 2 or 3 ML thick InGaAs/GaP QW in the TB description. All calculations are performed at 0 K. On the right, the experimental PL spectrum at 40 K is shown (temperature for which the WL intensity is maximized).

Theoretical calculations and temperature dependent PL have allowed us to propose a first interpretation of the optical transitions in the $In_xGa_{1-x}As$ QD using a band alignment model. We now provide additional information obtained from a pressure dependent PL experiment.

4.5.3 Pressure dependent PL

Strain is known to have a deep impact on the band structure of semiconductors (see section 2.2.2). Pressure dependent PL is thus a convenient technique to probe the nature of the optical transitions in QD[11,47]. Pressure dependent experiments have been performed in collaboration with the group of A. Goñi in ICMAB (Barcelona). The experimental setup is presented in Appendix D. The measurements have been performed at room temperature.

Fig. 4-17(a) shows the PL spectra of sample S3 for various values of hydrostatic pressure. The rough data are represented by thin lines. The interference fringes due to multiple reflections of the emitted light between both parallel-plane faces of the polished sample are readily observed. The double very sharp peaks at around 1.78 eV correspond to the ruby luminescence used to determine the pressure. The thick lines show smoothed spectra. The thin black line is a guide for eyes corresponding to the energy of the maximum PL intensity which is plotted in Fig. 4-17(b).

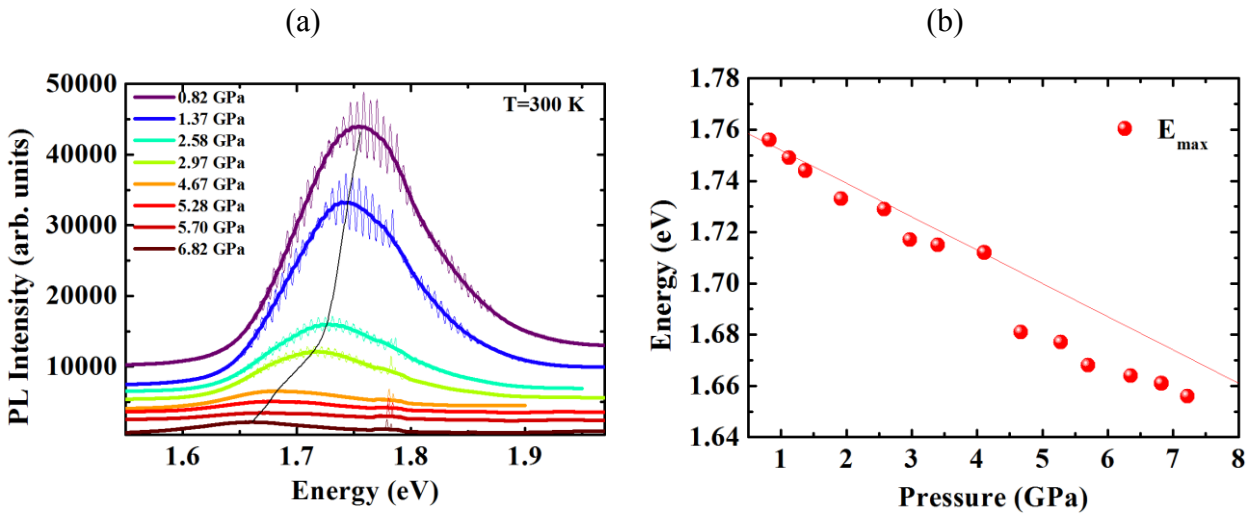

Fig. 4-17: (a) PL spectrum of sample S3 at room temperature as a function of hydrostatic pressure. The rough data are shown by thin lines. The spectra are smoothed (thick lines) to avoid the interference fringes. The thin black line is a guide to the eye to highlight the variation of the energy of the maximum PL intensity E_{max} which is plotted in (b). The thin red line shows an expected linear variation with a pressure coefficient of -13 meV.GPa^{-1}.

A first important result is the monotonic red-shift of the PL peak with increasing pressure. This feature can be understood by considering the effect of a hydrostatic compressive strain on the Γ, X and L bands (see Fig. 2-4). Both direct band gap Γ-Γ and indirect band gap L-Γ should blue-shift with increasing pressure. Here, the observed red-shift unambiguously proves that the PL peak involves X-type conduction states.

At ambient pressure, two peaks LE and HE have been clearly separated (see Fig. 4-11). Here, the HE transition is not clearly observed. An explanation can be proposed based on our assumption of a HE transition of direct type. Indeed, a direct transition is related to a large positive pressure coefficient (for bulk GaAs the pressure coefficient of the direct band gap is around 110 meV.GPa^{-1} [48]). As soon as a slight hydrostatic pressure is applied, the HE transition (if assumed to be a direct transition) may strongly shift up in energy while the LE transition (which is an indirect transition involving X conduction states) shifts down in energy. The intensity ratio between the two transitions follows an exponential law of the level splitting (see Fig. 4-13), it is then not surprising to quench the HE transition for the smallest pressure (0.82 GPa) considered in this study. Another reason is the shift down in energy of the X conduction state of GaP barrier with increasing pressure. When the Γ electronic state of the QD goes above the X state of the GaP barrier, the probability of filling the Γ electronic state of the QD is further strongly reduced.

Another interesting feature is the decrease of the integrated PL intensity with pressure. This behavior can be attributed to a more favorable escape of carriers toward the GaP barrier where they may recombine non-radiatively through defects. In other words, it means that the confinement in the QD decreases with increasing pressure. The pressure coefficient of the indirect band gap of bulk GaP (X-Γ) has been measured to be -13 meV.GPa^{-1} [49]. Thus, the pressure coefficient of the energy of the maximum PL intensity E_{max} should be negative and with an absolute value smaller than 13 meV.GPa^{-1}. If we assume that the energy E_{max} is related to the optical transition between a X_{XY} state and a HH state of the InGaAs QD, the pressure coefficient should be, in first approximation, the pressure coefficient of the indirect band gap of bulk InGaAs. However, neglecting the effect of indium, the pressure coefficient of the indirect band gap of bulk GaAs has also been measured around -13 meV.GPa^{-1} [48]. Actually, a smaller absolute value is expected when taking into account the difference in bulk modulus between GaP and the QD material[11]. Indeed, the bulk modulus of GaP (88 GPa) is higher than the bulk modulus of GaAs (75 GPa) and InAs (58 GPa)[50]. Thus, the compressibility of GaP barrier is smaller than the compressibility of the QD material. The consequence is that the lattice-mismatch between the QD material and the GaP barrier decreases with increasing applied hydrostatic pressure. The X-valley splitting, resulting from the biaxial component of the strain, thus decreases with the external pressure. The situation is summarized in Fig. 4-18 in which the applied pressure is assumed to have effects only on conduction bands. The X band of GaP barrier shifts down at -13 meV.GPa^{-1} (black solid line). The mean X state of (In)GaAs QD also shifts down at -13 meV.GPa^{-1} (black dashed line) and the splitting of X states ΔE_X reduces when increasing pressure. Consequently the shift down of the X_{XY} state (blue line) should be smaller than 13 meV.GPa^{-1} in absolute value.

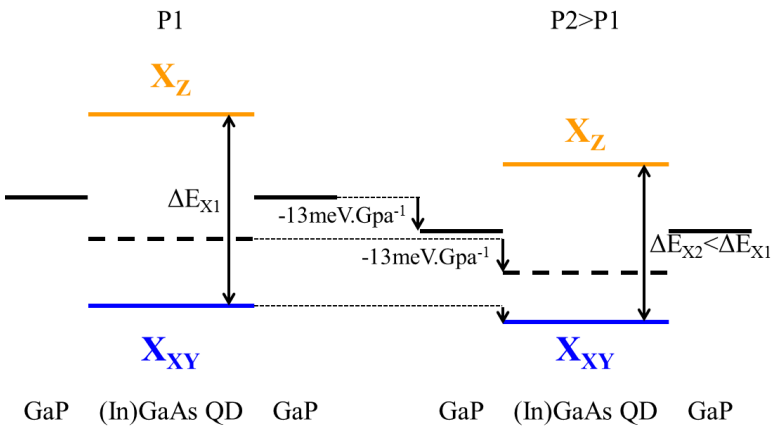

Fig. 4-18: Sketch of the effect of applied pressure on the X band of GaP barrier and X_{XY} and X_Z states of (In)GaAs QD. The dashed line shows the X state of (In)GaAs QD before taking into account the biaxial strain component.

Surprisingly, when looking at Fig. 4-17(b), the energy E_{max} red shifts with pressure at a rate slightly stronger than -13 meV.GPa^{-1} (the thin red line in Fig. 4-17(b) represents the equation $E(eV) = E_{max}(P = 0) - 0.013P$). To explain this result which is in disagreement with the sketch of Fig. 4-18, we can propose that the PL peak is probably composed of several optical transitions. The exact number of transitions cannot be unambiguously resolved as only one maximum is measured for each pressure. In Fig. 4-19(a), four Gaussian peaks are used to fit the PL spectrum at 2.97 GPa, keeping the FWHM of the four Gaussian peaks constant as a function of pressure. In Fig. 4-19(b), the energies of the four Gaussian peaks as a function of pressure are compared to the energy E_{max} of the maximum PL intensity.

The pressure dependence of E_1, E_2, E_3 and E_4 is linear with pressure coefficients between -2 meV.GPa^{-1} and -4 meV.GPa^{-1}. The negative values ensure that these transitions are X-type. Moreover the small values are in agreement with the sketch of Fig. 4-18. Finally, depending on pressure, E_{max} coincides with the points at which a different Gaussian peak is the dominant one and thus can explain the non-linear behavior of E_{max}. For example, at 2.97 GPa (Fig. 4-19(a)), the E_2 peak has the highest intensity. But when increasing pressure above 4.5 GPa, the E_1 peak becomes the dominant one. This can be explained because of the highest confinement energy of the E_1 transition and above 4.5 GPa, the excitons at the E_2 energy are more likely to escape in the GaP barrier.

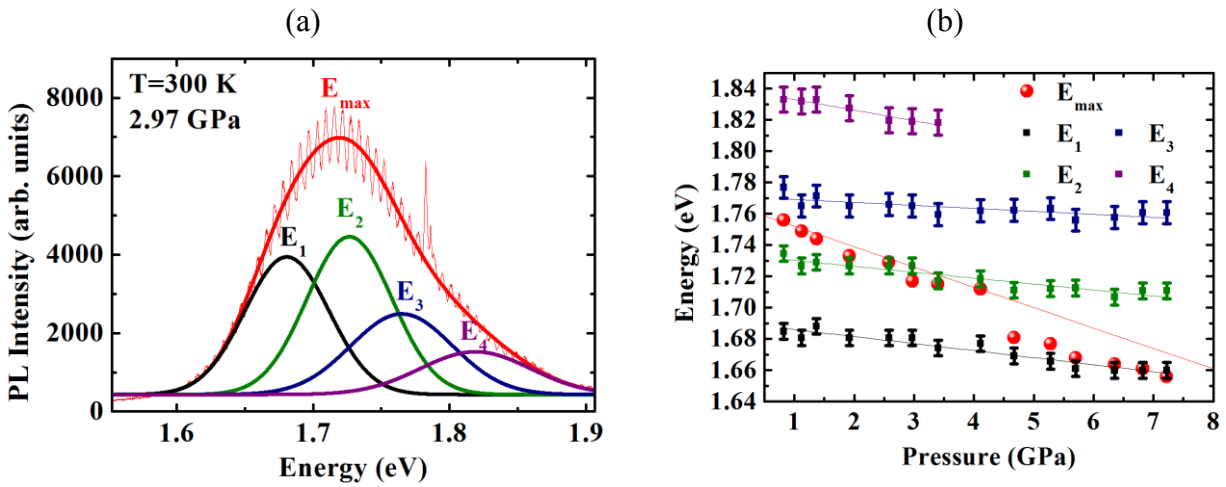

Fig. 4-19: (a) PL spectrum of sample S3 at 2.97 GPa and fitting with four Gaussian peaks centered at E_1, E_2 E_3 and E_4. (b) Pressure dependence of the energies E_{max} of the maximum PL intensity and of the four Gaussian peaks used to fit the spectra. The FWHM of the four Gaussian peaks are kept constant as a function of pressure.

To summarize the pressure dependent PL results, we have demonstrated that the LE peak observed at room temperature involves X conduction states. Although these experiments do not bring an irrefutable evidence of the direct type of the HE transition, they do not exclude it. Finally, at room temperature, the LE peak is possibly a combination of several optical transitions between X conduction states and HH states. We will come back to the possible nature of these various optical transitions in section 4.6.

4.5.4 Excitation power-dependent PL

4.5.4.1 Low temperature experiments

The tuning of the excitation power is a commonly used technique to probe the filling of QD excited states. Unfortunately, the low temperature experimental setup does not enable us to pump the sample with a power density larger than the one (80 $W.cm^{-2}$) used in section 4.5.2. Fig. 4-20 shows the normalized PL spectra at 14 K for excitation densities ranging from 80 $mW.cm^{-2}$ to 80 $W.cm^{-2}$. The HE transition does not appear as a separate peak as it is the case at room temperature (Fig. 4-11). Nevertheless, increasing power density broadens the peak mainly on the high energy side. The energy position of the maximum PL intensity is also found to monotonously and slightly blue-shift with the increase of the power density. Such a behaviour is often attributed to a type-II transition[51,52]. In that case, the peak position is expected to vary linearly with the excitation density to the power of 1/3. The corresponding experimental curve

plotted in the inset of Fig. 4-20 shows that data points clearly deviate from such a law above for power densities larger than 3 W.cm^{-2}. In previous sections we have excluded type-II transitions based on our band structure simulation, but we have to keep in mind that the X conduction band of GaP is still very close to the calculated X confined levels of the QD and its influence cannot be definitively ruled out. The experimental blue-shift may also result from a complex filling of excited states (with mixed X and Γ characters).

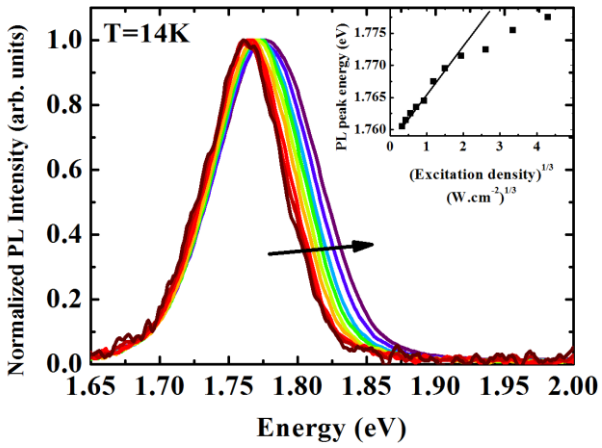

Fig. 4-20: Normalized photoluminescence spectra of sample S1 as a function of excitation density at 14 K. The arrow represents the increasing of excitation density with the following values: 80 mW.cm^{-2}, 180 mW.cm^{-2}, 370 mW.cm^{-2}, 800 mW.cm^{-2}, 1.7 W.cm^{-2}, 3.4 W.cm^{-2}, 7.4 W.cm^{-2}, 17.8 W.cm^{-2}, 37 W.cm^{-2}, and 80 W.cm^{-2}. The insert shows the energy of the PL peak as a function of the cubic root of excitation density. The line is a guide to the eye.

Fig. 4-21 presents the integrated PL intensity plotted in a logarithm scale as a function of the excitation power density. The variation is found to be sub-linear when increasing power density above a few W.cm^{-2} which is related to non-radiative channels increasing as a function of the carrier density such as non-radiative Auger recombinations.

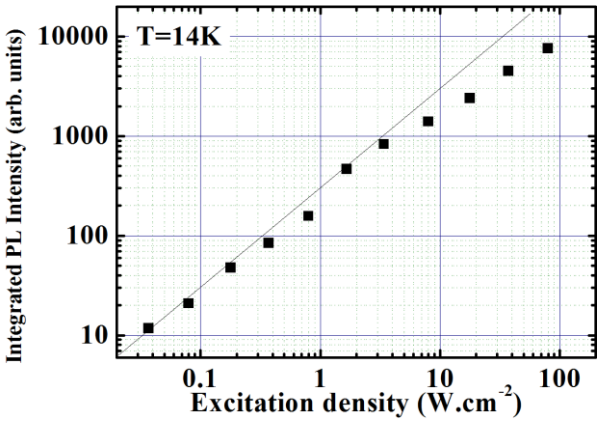

Fig. 4-21: Integrated PL intensity of sample S1 as a function of excitation power density at 14 K. The thin black line is a guide to the eye to match with an expected linear variation.

4.5.4.2 Room temperature experiments

The same excitation power-dependent PL experiments have been performed at room temperature (Fig. 4-22(a)). Additionally, samples have been excited with a larger range of power densities through a x40 microscope objective (Fig. 4-22(b)). In Fig. 4-22, the whole PL spectrum (including LE and HE peak) is integrated. The variation is now found to be over-linear (roughly quadratic) for excitation densities between 10 $W.cm^{-2}$ and 6000 $W.cm^{-2}$. At very high power density, the behavior changes to linear. These features can be explained by the increased contribution of the efficient optical transitions (the HE peak) between 10 $W.cm^{-2}$ and 6000 $W.cm^{-2}$. It is more significant than at low temperature. In the linear regime (very high power density, Fig. 4-22(b)), the non-radiative Auger effects or a saturation of the HE transition may compensate the effect of the over-linear evolution.

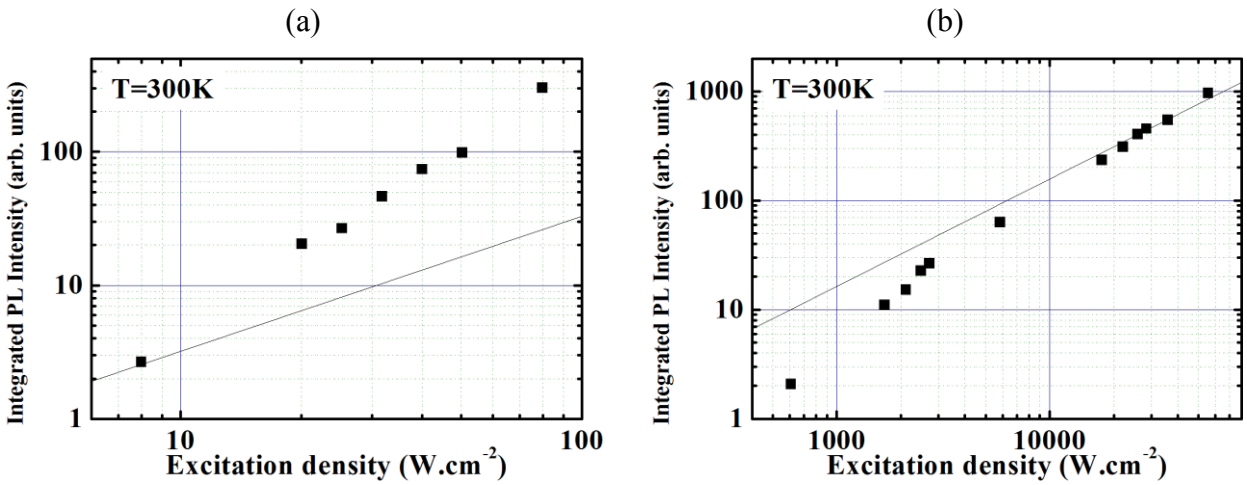

Fig. 4-22: Integrated PL intensity of sample S1 as a function of excitation power density at room temperature. The absolute intensities between both figures are not comparable. The thin black line is a guide to the eye to match with an expected linear variation.

4.5.5 Time-resolved photoluminescence

4.5.5.1 Observations

The dynamics of the recombination and injection of carriers have been investigated through time-resolved photoluminescence spectroscopy in collaboration with the group of X. Marie in LPCNO (Toulouse).

The samples are first analyzed at 10 K with the experimental setup described in Appendix A. The repetition rate is equal to 80 MHz. The mappings of PL intensity as a function of both energy and time are presented in Fig. 4-23(a) and Fig. 4-23(b) for two different excitation power densities. The estimated time-averaged excitation densities are respectively 70 $W.cm^{-2}$ for the low power case (LP) and 4000 $W.cm^{-2}$ for the high power case (HP). When the QDs are excited with a LP density, the PL intensity exhibits a very long decay time independent of the emission energy. When the excitation density is increased (Fig. 4-23(b)), the PL spectrum broadens on the high energy side as observed in Fig. 4-20. The decay time now depends on the emission energy with a shortening on the high energy side.

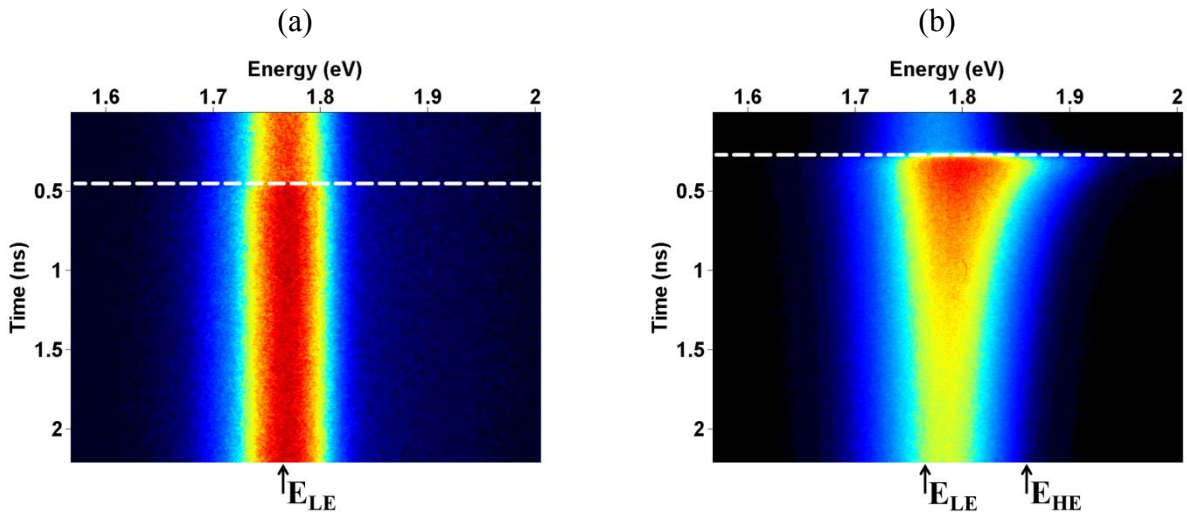

Fig. 4-23: Streak camera image of sample S1 at 10 K with a repetition rate of 80 MHz and for an excitation density of (a) LP=70 W.cm^{-2} and (b) HP=4000 W.cm^{-2}. The white horizontal dashed line marks the instant of the laser pulse.

The results are quantitatively presented in Fig. 4-24 as a function of time. The time-resolved PL intensity is represented at two energies: E_{LE}=1.76 eV and E_{HE}=E_{LE}+100meV=1.86 eV. The corresponding energy positions are shown by arrows on Fig. 4-23. The HE transition energy being not clearly evaluated from the experimental results at this temperature, we choose the E_{HE} energy in order to match the energy splitting between E_{LE} and E_{HE} measured at room temperature (E_{HE}=E_{LE}+100 meV). For the LP case, the decay time is greater than the repetition period of the laser (12 ns) and cannot be quantitatively measured. This supports the interpretation in terms of a LE ground transition corresponding to an indirect type transition. For the LP case, the emission at E_{HE} is not detectable. For the HP case, the time-resolved emission related to the LE transition can be fitted by the sum of a short exponential decay with a lifetime of 770 ps and a constant associated with the very long lifetime of the indirect transition. The physical reason of the shortest time is more complex. It may result from many body effects such as Auger effects due to the high density of electron-hole pairs (above ten per QD). For the HE transition, the emission shows a biexponential decay with short lifetimes of 340 ps and 1700 ps respectively. Here again many body effects and energy relaxation are expected to have an influence on the carriers dynamics[53]. Nevertheless, these short lifetimes are also consistent with a HE transition of direct type.

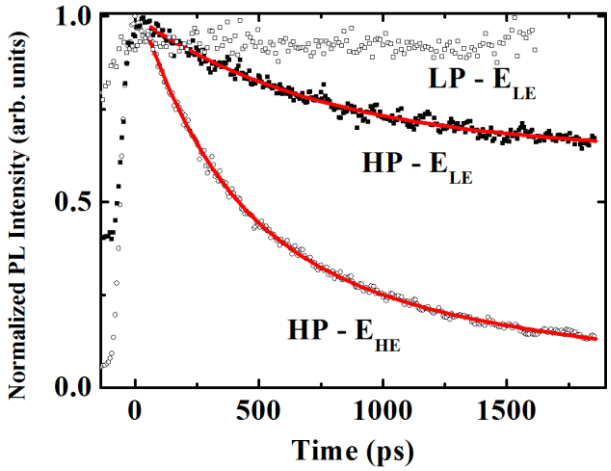

Fig. 4-24: PL dynamics at selected energies (E_{LE}=1.76 eV and E_{HE}=1.86 eV) for two power densities (LP=70 W.cm^{-2} and HP=4000 W.cm^{-2}). Red lines show biexponential fits.

4.5.5.2 Analysis of the LE ground state transition decay

To measure very long decay times, the repetition rate of pulses have been lowered to 0.8 MHz. The experimental setup is presented in Appendix B. Fig. 4-25 presents the PL dynamics at E_{LE} for three excitation power densities.

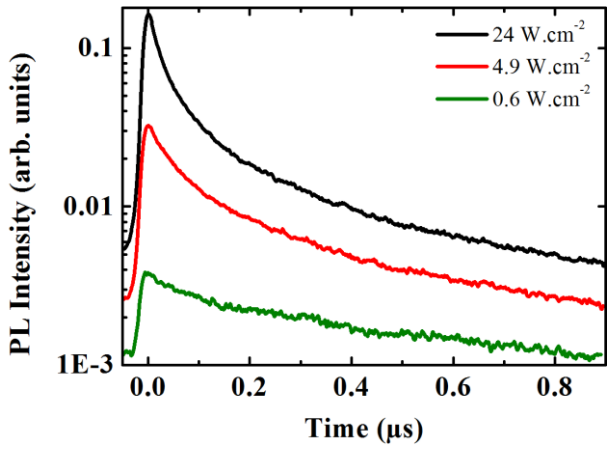

Fig. 4-25: PL dynamic of sample S3 at E_{LE} for three power densities with a repetition rate of 0.8 MHz.

Obviously, the photons density exciting the sample per pulse at 0.8 MHz is equal to the one measured at 80 MHz when the measured power density is divided by a factor 100. But it is important to mention that the initial density of carriers in the sample should be different because at 80 MHz the lifetimes are much larger than the repetition rate and there is an accumulation effect pulse after pulse. The PL dynamic is found to strongly vary with the excitation density. At 0.6 W.cm^{-2}, the PL decay is mono exponential with a decay time of 1.2 µs. When increasing

power, the dynamics speeds up and can no more be fitted with a single exponential. But for the three curves presented in Fig. 4-25, there is always a very slow component of 1.2 ± 0.2 µs.

A general feature of TRPL is that the observed decay time comes from the slower relaxation process in the cascade that lead from the excitation energy to the detection energy. To illustrate that, let us consider a simple model based on a LE level with a radiative lifetime τ_{rad}^{LE} fed by a reservoir (which we do not clarify for now) with a characteristic time $\tau_{res\to LE}$. In this case, the differential equation for the carrier density in the LE level n_{LE} is simply:

$$\frac{dn_{LE}(t)}{dt} = \frac{n_{res}(t)}{\tau_{res\to LE}} - \frac{n_{LE}(t)}{\tau_{rad}^{LE}}$$

where n_{res} is the carrier density in the reservoir. If we assume that all the carriers of the reservoir are injected at the LE level, n_{res} can be written:

$$n_{res}(t) = n_{res}(t=0)\exp\left(-\frac{t}{\tau_{res\to LE}}\right)$$

Considering that $n_{LE}(t=0) = 0$, the analytic solution for n_{LE} is:

$$n_{LE}(t) = \frac{n_{res}(t=0)\tau_{rad}^{LE}}{\tau_{res\to LE} - \tau_{rad}^{LE}}\left[\exp\left(-\frac{t}{\tau_{res\to LE}}\right) - \exp\left(-\frac{t}{\tau_{rad}^{LE}}\right)\right]$$

The density of emitted photons is $s_{LE}(t) = \frac{n_{LE}(t)}{\tau_{rad}^{LE}}$ and two limit cases can be considered:

$$s_{LE}(t) = \frac{n_{res}(t=0)}{\tau_{rad}^{LE}}\left[\exp\left(-\frac{t}{\tau_{rad}^{LE}}\right) - \exp\left(-\frac{t}{\tau_{res\to LE}}\right)\right] \quad \text{if } \tau_{res\to LE} \ll \tau_{rad}^{LE}$$

$$s_{LE}(t) = \frac{n_{res}(t=0)}{\tau_{res\to LE}}\left[\exp\left(-\frac{t}{\tau_{res\to LE}}\right) - \exp\left(-\frac{t}{\tau_{rad}^{LE}}\right)\right] \quad \text{if } \tau_{res\to LE} \gg \tau_{rad}^{LE}$$

In both cases, the PL dynamic is the same which means that a very long decay time can be related to a very long radiative lifetime (case 1) or a very long capture time (case 2). Nevertheless, it has

been shown in previous sections that the LE PL peak involves indirect transitions between X conduction levels and heavy hole levels. Thus we can reasonably believe that it is associated with a long radiative lifetime. Moreover, in the case $\tau_{res\rightarrow LE} \gg \tau_{rad}^{LE}$, the PL rising time should be τ_{rad}^{LE}. But, we will show that the PL rising time is of the order of 20-30 ps, which is too fast to be a radiative lifetime. Thus we can conclude that the measured decay time of 1.2 µs is the radiative lifetime of the LE transition.

Now, we have to clarify the decrease of the PL decay time with increasing power density. In Fig. 4-26, we plot the time integrated PL intensity as a function of excitation density in a logarithm scale (black square points). The variation is found to be sub-linear strengthening the results of Fig. 4-21 obtained for cw PL. This behaviour can be explained either by a non-radiative channel which is activated by the carrier density or by a decrease of the capture efficiency with increasing the carrier density. The maximum PL intensity, which is detected just after the laser pulse, is found to be linear with the excitation density (red circle points in Fig. 4-26). This proves that the capture efficiency by the LE state is not affected by the carrier density in these experiments. Thus, both the sub-linear variation of the time-integrated PL intensity and the acceleration of the PL dynamic are due to non-radiative Auger recombinations.

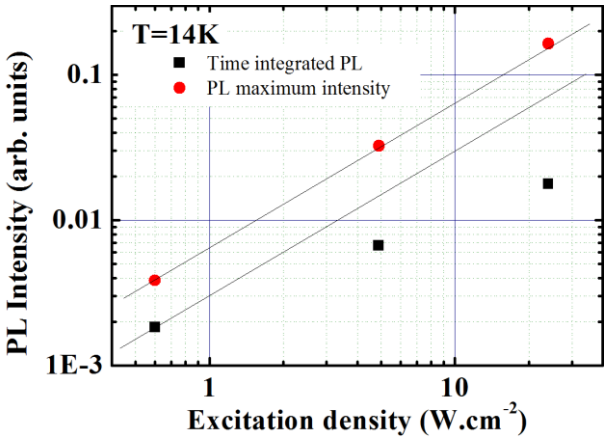

Fig. 4-26: Time integrated PL intensity of sample S3 at E_{LE} as a function of excitation power density (black square points) and PL maximum intensity (just after the laser pulse) (red circle points). The thin black line is a guide to the eye to match with an expected linear variation. The repetition rate is 0.8 MHz.

4.5.5.3 Relaxations toward the LE ground state transition

After discussing the recombination channels for the LE state of QD, we now provide insights for the relaxation mechanisms toward this LE state. For the other QD systems, many

relaxation schemes have been proposed in the literature. In particular, the role of the WL has been the subject of many controversies (for an updated summary see Ref. 54 and references therein). In Fig. 4-14, we may see that the weak signal related to the WL observed in cw PL is maximized at 40 K. The streak image of Fig. 4-27(a), presenting the PL dynamic at this temperature, shows that the WL PL decay (around 2.1 eV) is also very long. Fig. 4-27(b) shows that it is even longer than the QD PL decay. We can thus reasonably believe that the relaxation channel between the WL and the QD is very inefficient at low temperature and that the QD are fed directly by the GaP barrier. It is important to remind that the features around 2.35 eV are due to the shallow traps in the GaP substrate (as discussed in Fig. 4-14) and that no GaP barrier PL has been clearly detected.

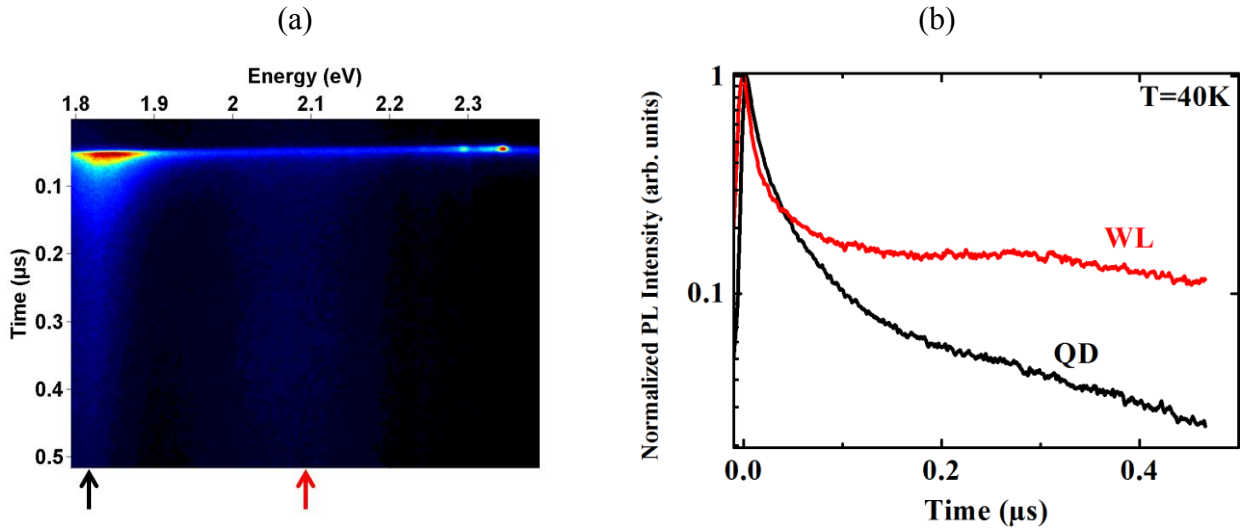

Fig. 4-27: (a) Streak image of sample S2 at 40 K. The repetition rate is 0.8 MHz and the excitation density is 24 W.cm^{-2}. (b) Normalized PL dynamic of both QD and WL.

A convenient technique to study the relaxation mechanisms is to measure the rise times. Unfortunately, the detection temporal resolution is insufficient when using the experimental setup with a repetition rate of 0.8 MHz. A small temporal resolution of 6 ps can be achieved only by using the synchro-scan mode of the streak camera and thus with a repetition rate of 80 MHz. We have already mentioned the issue of using a repetition period much smaller than the decay times; i.e. the carrier density in the sample does not fall to zero before the next laser pulse. Fig. 4-28 shows the PL rising of QD for the two selected energies E_{LE} and E_{HE} at a high excitation density. Fast rise times of the order of 20 ± 10 ps are measured. Similar rise times have been measured for the WL. We do not see a clear dependency on the detection energy, indicating that at this

excitation density the capture of carriers by the different QD levels has similar probabilities. Fig. 4-29 presents the PL rising at E_{LE} for various excitation densities. The rise time is difficult to measure especially when decreasing the excitation density, but we do not see a clear dependency of the rise time with excitation density. Nevertheless, we can assert that the fast measured rise times demonstrate an efficient carrier capture by the QD, which can explain the good luminescence efficiency of InGaAs/GaP QD despite the very long radiative lifetime.

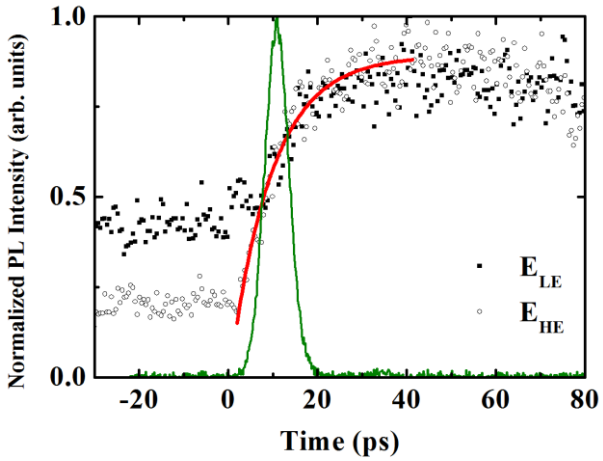

Fig. 4-28: Normalized PL rising of sample S3 at E_{LE} and E_{HE}. The repetition rate is 80 MHz and the excitation density is 2800 W.cm^{-2}. The temperature is 40 K. The red line is a mono exponential fit of the E_{HE} rising PL. The green line is the impulse response showing a temporal resolution of 6 ps.

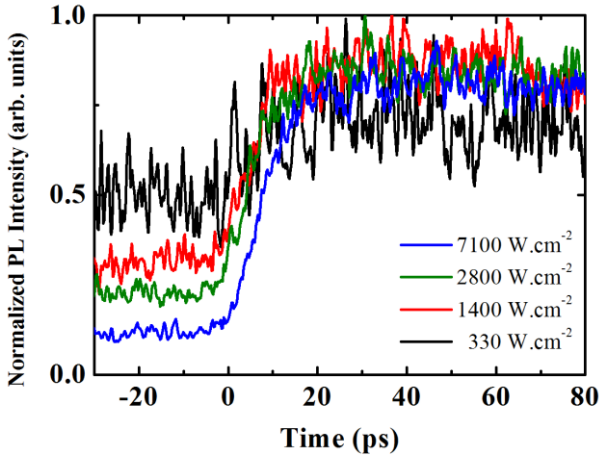

Fig. 4-29: Normalized PL rising of sample S3 at E_{LE} at various excitation densities. The repetition rate is 80 MHz and the temperature is 40 K.

4.6 Refinement of the electronic structure calculation

4.6.1 Motivations

In section 4.4.2, we have presented a first description of the InGaAs/GaP QD. With this model, the ground optical transition level in the low In content range is associated to the first X_{XY} electronic and first heavy hole confined level of QD. Whatever the In content and QD shape, the first direct transition is found to be at a slightly higher energy than this ground state transition and is expected to play a role in the optical properties. Nevertheless, pressure experiments of section 4.5.3 and excitation-power dependent PL measurements of section 4.5.4.1 suggest that both X excited states and X conduction band of GaP barrier may also play a role in the optical properties. Moreover, a radiative lifetime of 1.2 µs for the main optical transition has been measured by TRPL. The theoretical strategy of section 4.4.2 does not provide the calculation of this radiative lifetime because the X electron state and the Γ hole state are calculated with two different methods and for two different nanostructures (a QW for the X electron state and a cone shape QD for the Γ hole level). A full supercell TB simulation of QD is required to get a deeper understanding of the QD optical properties.

4.6.2 Geometry of the simulated QD

One of the advantages of the supercell TB model by comparison to the axial $\mathbf{k}\cdot\mathbf{p}$ model is that it does not require any approximation on the QD shape. We can thus simulate a very realistic geometry. The dimensions of the chosen QD are measured on the plane-view STM image of Fig. 4-30(a) and are summarized on Fig. 4-30(b). The effect of GaP capping is assumed to be a truncation of the height. According to X-STM measurements, the QD is truncated at a height of 3.4 nm. To simplify the issue of indium composition and position, we first simulate an indium-free GaAs/GaP QD. The effect of indium will be discussed separately.

To limit the number of atoms in the 1 million range, the lateral size of the supercell is fixed to 66 lattice constants square (around 36 x 36 nm^2). It is actually not a limiting factor because it is equivalent to a QD areal density of 7.7 x 10^{10} cm^{-2} which is below the measured density (see Fig. 4-1(a)). The height in the [001] direction is 30 lattice constants providing a GaP buffer below and above the QD with thicknesses of twice the QD height.

(a) (b)

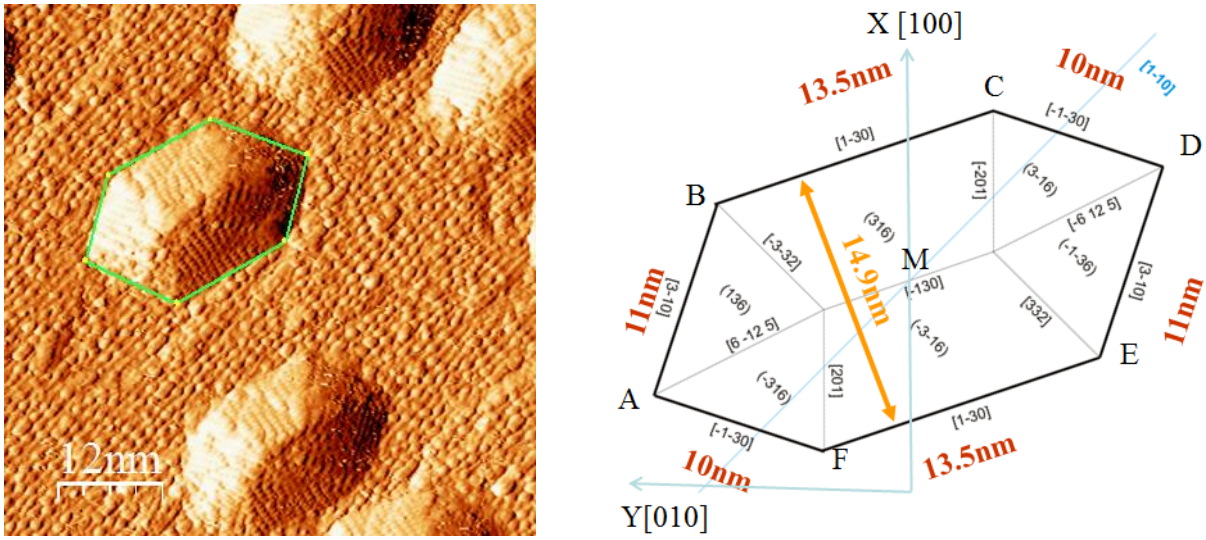

Fig. 4-30: (b) Geometry of the GaAs/GaP QD for the TB simulation as measured on the plane-view STM image of (a). The QD height is truncated at 3.4 nm according to X-STM image of buried QD.

4.6.3 Strain calculation

The atomic positions are relaxed thanks to the VFF method described in section 2.3.2.2. The hydrostatic and biaxial components of the strain along the z [001] direction through the QD center are shown in Fig. 4-31. Fig. 4-32 shows the 2D strain mapping in the WL ((a) and (b)) and for the QD mid-height plan ((c) and (d)).

(a) (b)

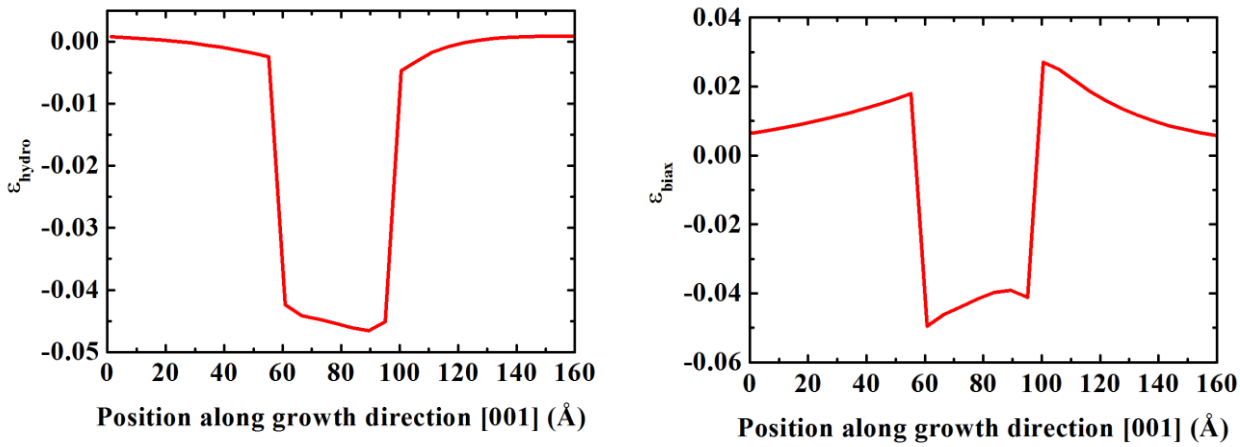

Fig. 4-31: Hydrostatic ($\varepsilon_{hydro}=\varepsilon_{xx}+\varepsilon_{yy}+\varepsilon_{zz}$) and biaxial ($\varepsilon_{biax}=½(\varepsilon_{xx}+\varepsilon_{yy})-\varepsilon_{zz}$) components of the strain along the z direction [001] through the QD center.

The strain field is found to be homogeneous inside the QD. The strain in the GaP matrix tends to zero when going away the QD but the biaxial strain is slightly positive in the vicinity of the QD especially at the apex of the QD.

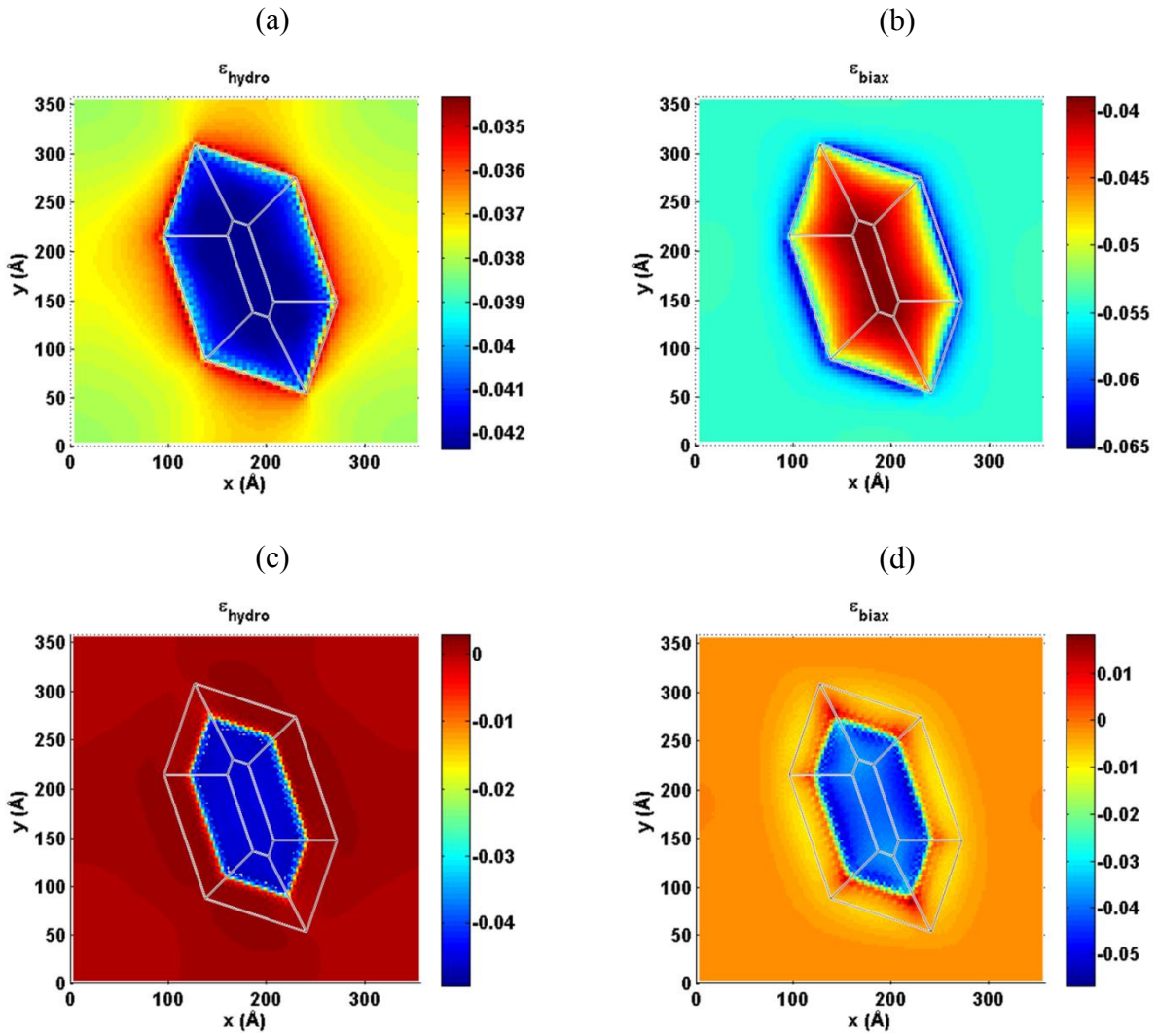

Fig. 4-32: Hydrostatic ($\varepsilon_{hydro}=\varepsilon_{xx}+\varepsilon_{yy}+\varepsilon_{zz}$) and biaxial ($\varepsilon_{biax}=½(\varepsilon_{xx}+\varepsilon_{yy})-\varepsilon_{zz}$) components of the strain for (a), (b) the WL and (c), (d) the QD mid-height plan.

4.6.4 Electronic band structure

4.6.4.1 First hole states

The TB results for the first four confined hole levels are presented in Table 4-3 (each level is doubly degenerated due to spin). The ground hole state is located at 0.458 eV above the

VBM of bulk GaP which is good agreement with the calculation of Fig. 4-7 for QD with geometry B.

Energy (eV)	Square wave function	TB orbitals decomposition
0.458	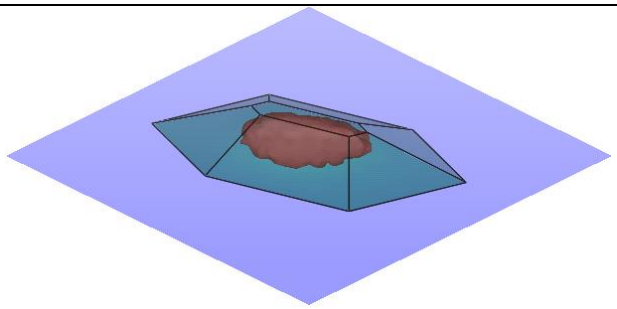	s=0.37% s^*=0.04% **p_x=35.1% p_y=40.3%** p_z=3.7% d_{yz}=8.95% d_{zx}=10.7% d_{xy}=0.8% $d_{x^2-y^2}$=0.004% $d_{3z^2-r^2}$=0.009%
0.441	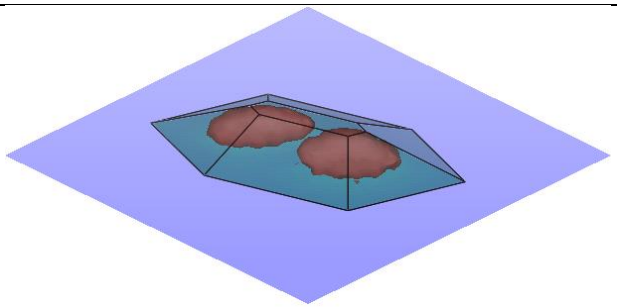	s=0.56% s^*=0.06% **p_x=35.3% p_y=38.5%** p_z=5.5% d_{yz}=8.95% d_{zx}=10.1% d_{xy}=1.2% $d_{x^2-y^2}$=0.009% $d_{3z^2-r^2}$=0.01%
0.430	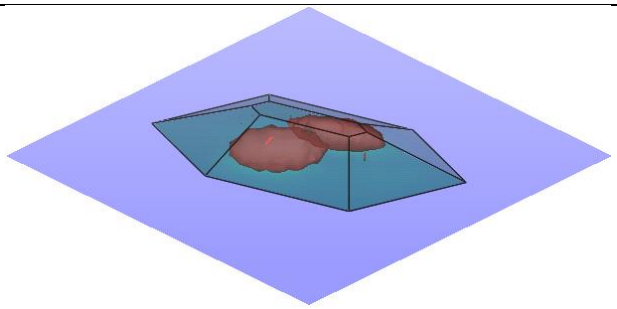	s=0.59% s^*=0.07% **p_x=34.8% p_y=35.8%** p_z=8.7% d_{yz}=8.85% d_{zx}=9.3% d_{xy}=1.9% $d_{x^2-y^2}$=0.01% $d_{3z^2-r^2}$=0.02%
0.426	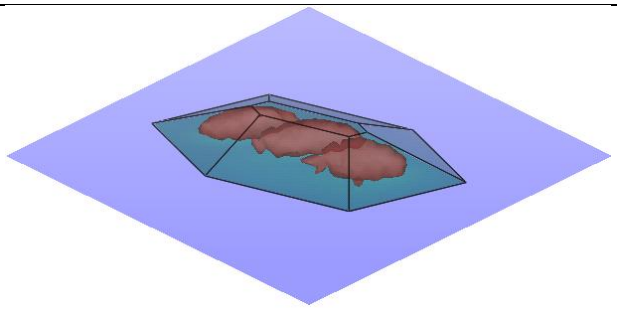	s=0.68% s^*=0.07% **p_x=34.5% p_y=37.5%** p_z=7.3% d_{yz}=8.68% d_{zx}=9.7% d_{xy}=1.6% $d_{x^2-y^2}$=0.02% $d_{3z^2-r^2}$=0.02%

Table 4-3: First four hole states in a GaAs/GaP QD. The reference of energies is the VBM of bulk GaP. The representation of wave functions considers probability volumes including 80% of the presence probability of the hole.

The decomposition of the square wave functions (related to electronic density) on the ten orbitals of the $sp^3d^5s^*$ basis is presented in the last column of the table. The main part of the weight is on

the p_x and p_y orbitals for the four hole states calculated here, which proves that they are HH-like states. The level splitting between the first two levels is only 17 meV and is due to the elongated shape of the QD (with a length of 28 nm between points A and D in Fig. 4-30(b)).

4.6.4.2 First electron states

In the same way, we present the results for the first two electron states (Table 4-4). Surprisingly, we find that the wave function is not confined in the GaAs QD but at the top of the QD in the GaP matrix. The main part of the weight is on the p_z, d_{xy} and d_{3z^2-r} orbitals in which the z axis is a symmetry axis. This is characteristic of X_Z-like states.

Energy (eV)	Square wave function	TB orbitals decomposition
2.248	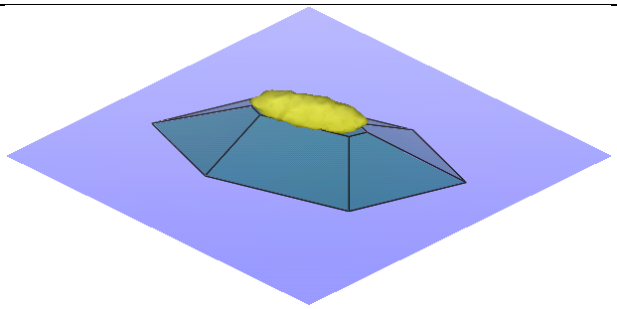	s=7.8% s^*=2.2% p_x=0.14% p_y=0.15% **p_z=43.9%** d_{yz}=6e-3% d_{zx}=1e-2% **d_{xy}=18%** $d_{x^2-y^2}$=3e-4% **$d_{3z^2-r^2}$=28.1%**
2.262	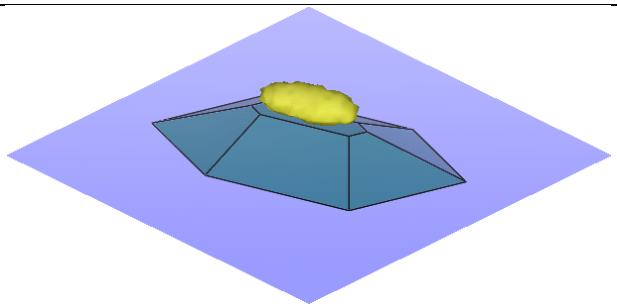	s=8.1% s^*=2.1% p_x=0.13% p_y=0.14% **p_z=43.4%** d_{yz}=5e-3% d_{zx}=9e-3% **d_{xy}=18%** $d_{x^2-y^2}$=2e-4% **$d_{3z^2-r^2}$=27.1%**

Table 4-4: First two electron states in a GaAs/GaP QD. The reference of energies is the VBM of bulk GaP. The representation of wave functions considers probability volumes including 80% of the presence probability of the electron.

To understand the origin of these X_Z states, we have to go back to the strain profile presented in Fig. 4-31. We have noticed that the GaP matrix is deformed at the apex of the QD and that it results in a positive biaxial strain. As seen in chapter 2 (see Fig. 2-5), a biaxial strain splits the X conduction band into X_{XY} and X_Z. In the GaAs QD, the biaxial strain is negative so that the X_{XY} band is shift down and the X_Z band is shift up. But in the GaP matrix just above the QD, the situation is reversed with the X_Z band being the lowest one. In Fig. 4-33, we plot the confinement potentials due to the strain profile calculated in Fig. 4-31. These potentials are

calculated considering the linear deformation potential theory described in chapter 2 and focusing only on the hydrostatic and biaxial parts of the strain. This simple picture highlights the existence of a potential for X_Z electrons in the surrounding of the QD which confines the electrons. The energy of X electrons in bulk unstrained GaP is 2.367 eV in this model, so that the confinement of electrons by the strain field amounts to 119 meV. Moreover, according to this picture, the confinement potential for X_{XY} electrons in the QD may be stronger. The ground electronic state is a GaP X_Z state rather than a GaAs X_{XY} state because the quantum confinement effect is weaker in the tensile strained GaP area. This is actually an effect of both smoother confinement potential profile and stronger X-effective mass in GaP than in GaAs[55].

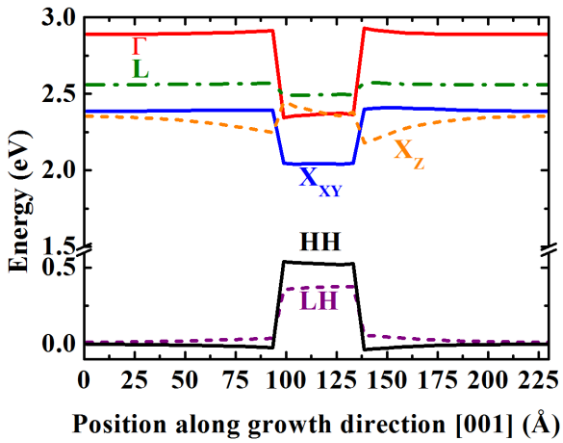

Fig. 4-33: Confinement potentials for the GaAs/GaP QD along the z direction [001] through the QD center calculated with the linear deformation potential theory. Only the hydrostatic and the biaxial parts of the strain are considered.

To explain the wave function shapes shown in Table 4-4, we can notice that, in the [001] direction, the X_Z confinement potential can be approached by a triangular profile. The solutions of the Schrödinger equation for an infinite triangular quantum well are based on the Airy functions[56] (Fig. 4-34). The two first electron states confined in the tensile strained GaP matrix have actually similar wave function shapes in the [001] direction.

Such strain-induced interface localized states have also been predicted in InP/GaP QD[44,57,58] and SiGe/Si QD[59–61]. In both cases, the barrier is a semiconductor with a CBM in the X (or Δ) valleys. We want to mention that the GaAs/GaP QD band alignment is different from a true type-II band alignment such as GaSb/GaAs QD[62]. Indeed, when neglected the electron-hole Coulomb interaction in a GaSb/GaAs QD, the electron wave function is delocalized in the whole

GaAs barrier. The localization of the electron in the vicinity of the QD is only achieved when considering the modification of the confinement potentials resulting from the Coulombic attraction by a hole. In a GaAs/GaP QD, the electron localization at the QD apex is favored by strain. The Coulombic field is also expected to enhance the localization of the electron close to the GaAs/GaP interface but this study is beyond the scope of this thesis.

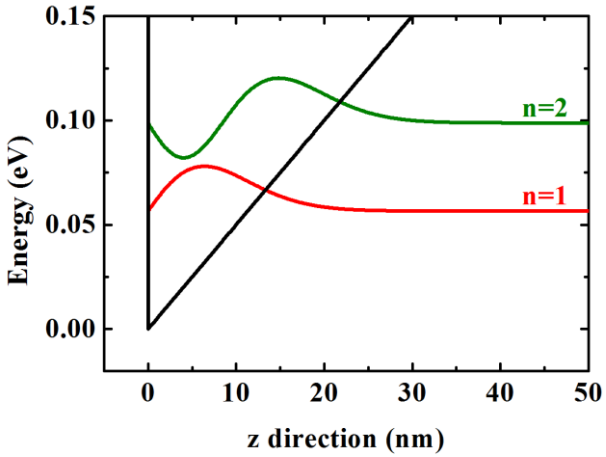

Fig. 4-34: Wave functions of the two first confined states in an infinite triangular quantum well (5 meV.nm^{-1}).

4.6.4.3 Higher electron states

It is interesting to simulate higher electron states to find the first state really localized in the GaAs QD is. Fig. 4-35 presents the next electron excited states which are all located in a 38 meV energy range. These are all X_Z-like states mechanically confined above and even below the GaAs QD. According to Fig. 4-33, a similar X_Z confinement potential is present below the QD. Nevertheless, it is weaker than the confinement potential above the QD and explains why the states confined below the QD are at a higher energy than the states confined above it.

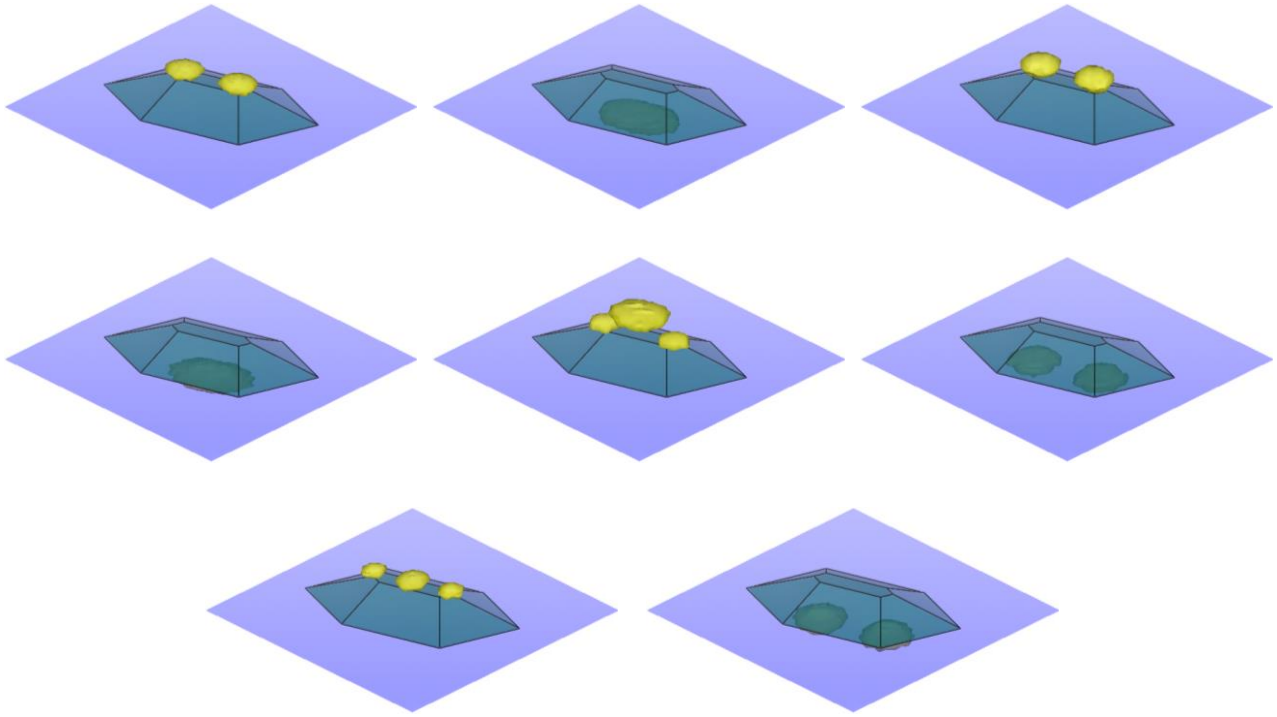

Fig. 4-35: Square wave function of excited states in the range 2.268 – 2.306 eV. The representation of wave functions considers probability volumes including 80% of the presence probability of the electron.

The first electron state confined in the QD is finally found at the energy of 2.31 eV (see Table 4-5) that is 62 meV above the ground state and 57 meV below the X band of unstrained bulk GaP. This is a X_Y-like state as proved by the strong weight on the p_y orbital. Other X_X and X_Y-like states are found at energies below the X band of unstrained bulk GaP barrier. In contrast, no Γ-like confined state is found because it lies well above the X band of unstrained bulk GaP barrier as demonstrated in Fig. 4-7 (for a 0 % In content).

Energy (eV)	Square wave function	TB orbitals decomposition
2.310	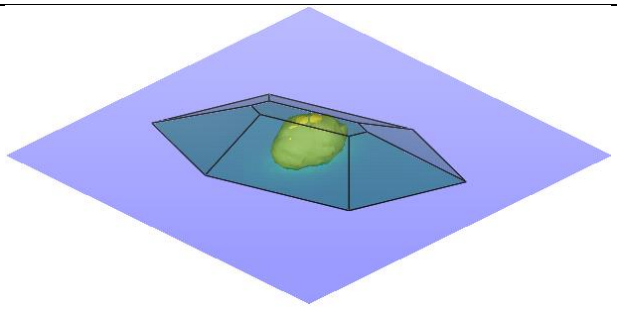	s=4.6% s^*=3.1% p_x=0.21% **p_y=42.5%** p_z=0.18% d_{yz}=0.01% d_{zx}=17.7% d_{xy}=4e-3% $d_{x^2-y^2}$=23.7% $d_{3z^2-r^2}$=8.1%

Table 4-5: First electron state confined in the GaAs QD. The reference of energies is the VBM of bulk GaP. The representation of wave function considers probability volumes including 80% of the presence probability of the electron.

4.6.5 Optical properties calculation

According to the supercell TB simulation of a GaAs/GaP QD, the X_{XY} state of QD is actually not the electronic ground state, as predicted in the first calculation of section 4.4.2. Many electron states mechanically confined at the apex and at the base of the QD are found at lower energies. We now present the role of these electron states in the optical transitions with the first confined hole states.

Fig. 4-36 presents the calculation of the absorption spectrum for a transverse electric (TE) or transverse magnetic (TM) polarizations of the incoming light (without excitonic effects). The first four hole states (each being doubly degenerated due to spin) and the first thirteen electron states (each being doubly degenerated due to spin) are considered for this calculation.

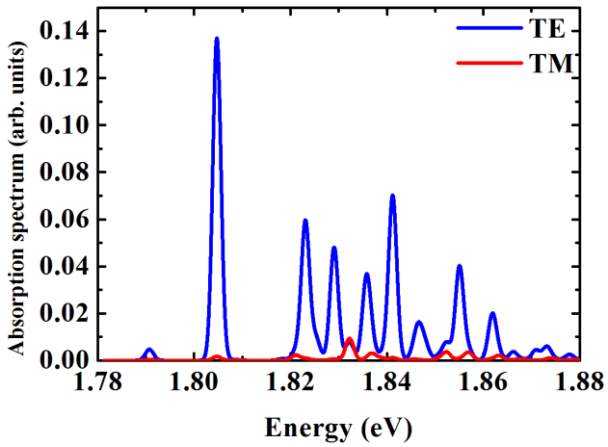

Fig. 4-36: Absorption spectrum of the GaAs/GaP QD calculated with the TB supercell model.

A first conclusion is that the TE polarization is strongly dominant. This is a consequence of optical transitions involving HH states. We also notice the numerous peaks above 1.82 eV which are the transitions involving the many electron states of Fig. 4-35. Interestingly, the second optical transition at 1.804 eV, which involves the first HH state and the second X_Z state, is found to be more efficient than the ground one (at 1.79 eV) between the first HH state and the first X_Z state. This may be explained by a strongest spatial overlap due to a slightly stronger electron wave function penetration in the QD. The calculated corresponding radiative lifetime is 9.6 µs. Despite the favored spatial overlap, the first type-I optical transition (involving the X_Y state of Table 4-5 and the first HH state) is much less efficient. The calculated corresponding radiative lifetime is 2.4 s. To understand such a long time, a **k**-space analysis of the electron states is

required[63]. This is beyond the scope of this thesis but we can expect that mixing with bulk-like Γ bands is much stronger in the X_Z bulk-like states than in the X_Y bulk-like state.

4.6.6 Expected effect of indium

The effect of indium content on the Γ and X_{XY} electron levels has been discussed in Fig. 4-7 using the mixed **k**·**p**/TB model. Similar trends for these states are expected using the full TB model. The Γ-like electron state of InGaAs QD strongly shifts down in energy with increasing In content while the X_{XY} just slightly shifts down. The influence of the strain-induced confinement effect on the X_Z states can be predicted analyzing the strain profile. Fig. 4-37 shows the biaxial strain profile for a cone-shape InGaAs/GaP for various In content. In this section, the strain is calculated with the LCE theory for computing time considerations. Obviously, the tensile strain in the GaP matrix at the apex and at the base of the QD increases with increasing In content in the QD. This is a result of the larger lattice-mismatch between InGaAs and GaP when the In content increases. Thus the strain-induced confinement potential for X_Z electrons at the top of the QD may be stronger when increasing In content.

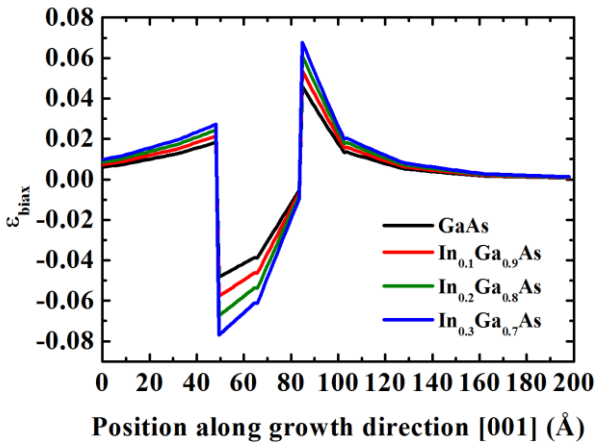

Fig. 4-37: Biaxial ($\varepsilon_{biax}=½(\varepsilon_{xx}+\varepsilon_{yy})-\varepsilon_{zz}$) strain component along the z direction [001] through the QD center. A cone-shape InGaAs/GaP QD is considered in this calculation. The height is 3.5 nm and the diameter is 18 nm. The strain is calculated with the LCE theory described in chapter 2.

The important issue of In spatial localization has to be mentioned now. Indeed, we have not considered the alloy fluctuations inside the QD. Yet, they are expected to have a strong influence on the spatial localization of the hole wave function inside the QD. In the GaAs/GaP QD simulation of Table 4-3, the wave function is centered in the QD. But for an In-contained QD, the In composition is probably not homogeneous. In InAs/GaAs QD, the dots contain

significant concentration of Ga. Fry *et al.* have demonstrated that the hole wave function in an InAs/GaAs QD is localized at the top of the QD due to a higher concentration of In at the top of the QD[64]. In their detailed X-STM study of InGaAs/GaP QD, Prohl *et al.*[27] have indeed shown that the QD exhibit a reversed-cone stoichiometric profile of InGaAs (see Fig. 4-38). Such a composition profile may also lead to a localization of the hole wave function closer to the top of the QD, enhancing the spatial overlap with the electron wave function. This effect may explain the discrepancy of one order of magnitude between the calculated radiative lifetime in a GaAs/GaP QD (9.6 µs) and the measured radiative lifetime in InGaAs/GaP QD (1.2 µs).

Fig. 4-38: InGaAs/GaP composition as determined by Prohl *et al.*[27].

4.6.7 Expected effect of QD shape

In the same way, the effect of QD shape is discussed. Fig. 4-39 shows the biaxial strain profile as a function of the truncated height. The sharper is the QD apex, the stronger is the positive tensile strain in the GaP matrix and thus the stronger is the confinement potential for X_Z electrons.

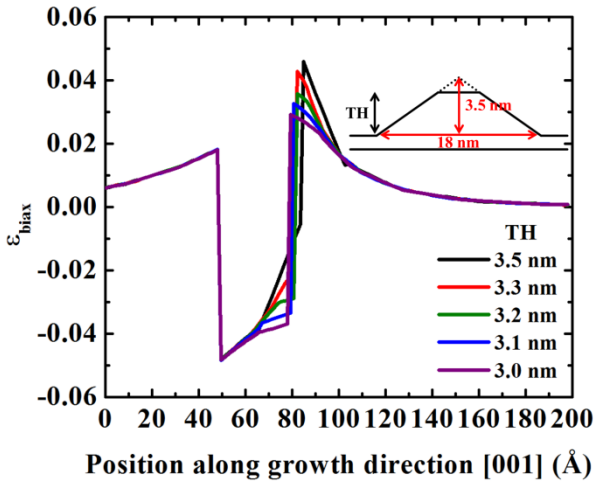

Fig. 4-39: Biaxial ($\varepsilon_{biax}=½(\varepsilon_{xx}+\varepsilon_{yy})-\varepsilon_{zz}$) strain component along the z direction [001] through the QD center for various truncated height (TH). A truncated cone-shape GaAs/GaP QD is considered in this calculation. The height of the cone is 3.5 nm and the diameter is 18 nm. The strain is calculated with the LCE theory described in chapter 2.

4.6.8 Back to experimental observations

In the pressure experiments of section 4.5.3, we have observed a red-shift of the PL peak and an intensity quenching with increasing pressure. We have suggested an interpretation with several optical transitions involving X conduction states. According to the supercell TB simulation, these X states could be attributed to strain-induced confined X_Z-like states of GaP. Their theoretical small red-shift with increasing hydrostatic pressure is in agreement with experimental observations. The indirect band gap of bulk GaP red-shifts at a rate of -13 meV/GPa[49]. But because the lattice-mismatch between the QD material and the GaP matrix decreases with increasing pressure, the X_Z confinement potential also decreases. This explains both the PL intensity quenching with pressure and a red-shift of optical transitions somewhat smaller than -13 meV/GPa.

In the temperature dependent PL experiments of Fig. 4-12, we have measured a small activation energy of 11 meV that could not be interpreted with the simulation results of Fig. 4-7. A possible interpretation is the existence of a defect-related non-radiative channel in the GaP matrix which is activated when excited states with decreasing spatial localization are populated[65].

Finally, the complex blue-shift of the PL peak with increasing excitation power density presented in Fig. 4-20 may result from both filling of X_Z or HH excited states and increased Coulombic potential. Indeed, due to the spatial separation of hole and electron wave function, the Coulombic field may also have a role on the energy of confined states in a similar way to a true type-II band alignment.

4.7 Improvements of optical properties

4.7.1 Tuning the indium content

A first way to improve the properties of InGaAs/GaP QD is to increase the In content. Indeed, we have shown in Fig. 4-7 that it should lower the energy of the first direct and type-I optical transition in order to reach the indirect/direct crossover. Moreover, as discussed in section 4.6.6, it should increase the confinement potential for X_Z electrons which are responsible of LE PL peak in section 4.5.

One of the possible routes to increase In content is to lower the growth temperature and increase the In sticking coefficient[32]. Fig. 4-40 presents the influence of the growth temperature on the room temperature integrated PL intensity. A bell-shaped trend, with an optimized growth temperature at 550 °C, is visible. The decrease of the PL intensity below 550 °C is attributed to the beginning of plastic relaxation due to the too large lattice-mismatch. Unfortunately, the plastic relaxation occurs before reaching the X_Z/Γ crossover and the InGaAs/GaP QD grown at 550 °C still exhibit long radiative lifetimes.

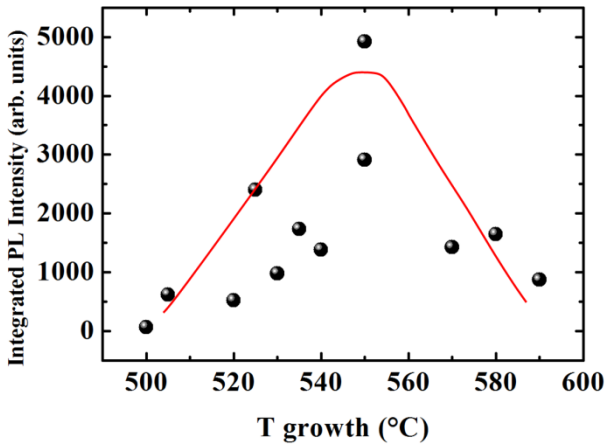

Fig. 4-40: Room temperature integrated PL intensity of InGaAs/GaP QD as a function of the growth temperature. The red line is a guide to the eye.

4.7.2 Tuning the QD shape

Changing the shape of the InGaAs QD is also expected to change their optical properties. Fig. 4-7 has shown that enlarging the QD may reduce the strong quantum confinement effect occurring on the Γ electronic state and thus lower the energy of the direct type-I optical transition. Moreover, when the QD apex is sharper, the X_Z confinement potential is stronger, which may increase the room temperature PL intensity of the involved optical transitions.

We have also studied the influence of the growth interruption time under As just after the InGaAs deposition. A longer time favors a ripening of QD. Table 4-6 presents the AFM measurements of mean height, mean diameter and areal density for two samples with a different ripening time. Increasing the ripening time is found to increase the height of the QD while decreasing its diameter. The PL intensity of corresponding capped samples is found to be higher by a factor of ten when the ripening time is 180 s. This supports the simulated trends.

Ripening time (s)	Height (nm)	Diameter (nm)	Density (cm^{-2})
30	3	28	1.5×10^{11}
180	4	22	1.0×10^{11}

Table 4-6: AFM measurements for two uncapped InGaAs/GaP QD with different ripening time.

4.7.3 Pros and cons of InGaAs/GaP QD

We have presented a detailed study of InGaAs/GaP QD but our initial goal was to evaluate their potentiality for lasing. In this section, we discuss about the advantages and drawbacks of InGaAs/GaP QD in laser applications.

First, the band structure is not ideal for radiative recombination because the QD are not direct and type-I. But despite this band alignment, the PL intensity is found to be relatively strong. Room temperature PL seen with a naked eye is achieved and is thus a sign of the very good structural quality. The very strong confinement of the holes in the QD ensures a limited PL quenching with temperature with a factor 3.8 between 10 K and 230 K. In efficient InAs/InP QD lasers, slightly better performances have been achieved with a factor of 3 between low and room temperature[66]. The very high QD density is also a very good point.

The long radiative lifetime may be an unfavorable point at first glance because it is related to a low probability of transition and thus to a low material gain. But it should be also easier to achieve the population inversion condition. The remaining question is: do we have enough material gain to compensate the low optical losses?

Finally, the interest of QD for lasing applications discussed in section 4.1 is partially lost due to the high number of excited states located at energies very close to the ground one. Nevertheless, it probably provides many relaxation channels which may explain the very efficient capture of carriers and the fast PL rise times. Another possible explanation of the efficient carrier injection into electronic confined states of the QD with strong X component is that the electronic states involved into carrier mobility in the barrier are also X states.

4.7.4 Incorporation of nitrogen in InGaAsN/GaP QD

Incorporation of nitrogen in the QD is expected to bring a solution to the band alignment issue[14]. Moreover, it may shift the emission wavelength to get closer of the transparency window of silicon. We present in this section the very first results of InGaAsN/GaP QD.

Samples have been grown using SSMBE in a similar way to InGaAs/GaP QD. The atomic N plasma cell has been opened during the InGaAs deposition. The growth temperature is fixed to 535 °C to get a reproducible incorporation of N[67]. The InGaAsN deposition has been followed by a 30 s growth interruption under As and N_2. Fig. 4-41 presents a 3 x 3 μm^2 AFM image of an uncapped sample. A similar to InGaAs/GaP QD mean height of (3.5 ± 1.1) nm is found. In contrast the mean diameter is found to be larger (40 ± 14) nm with a broad statistical distribution. The QD density is also found to be reduced to (2.5 x 10^{10} ± 0.2 x 10^{10} cm^{-2}).

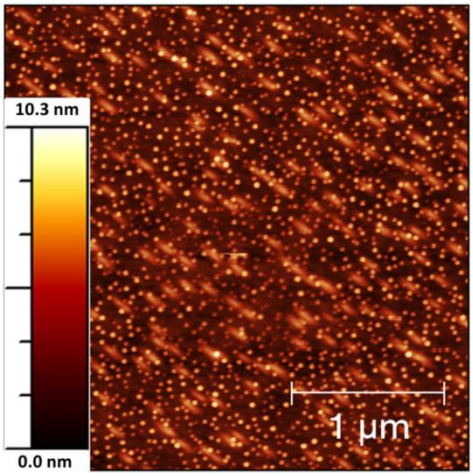

Fig. 4-41: 3 x 3 µm2 AFM image of uncapped InGaAsN QD.

Fig. 4-42 presents a comparison of low temperature PL spectra of InGaAs/GaP QD and InGaAsN/GaP QD. First we notice the strong red-shift of the emission energy from 1.77 eV to 1.43 eV due to the N-related giant band gap bowing. Secondly, the integrated PL intensity is slightly reduced by 17 %, but the maximum PL intensity is reduced by a factor of 3 and the FWHM is increased to 180 meV. This is related to both increased distribution of QD diameter and distribution of N local configurations. Any PL signal is detected above 200 K, which proves that N incorporation induces many non-radiative defects. To get efficient InGaAsN/GaP QD, an optimization of growth conditions will be required in the next future.

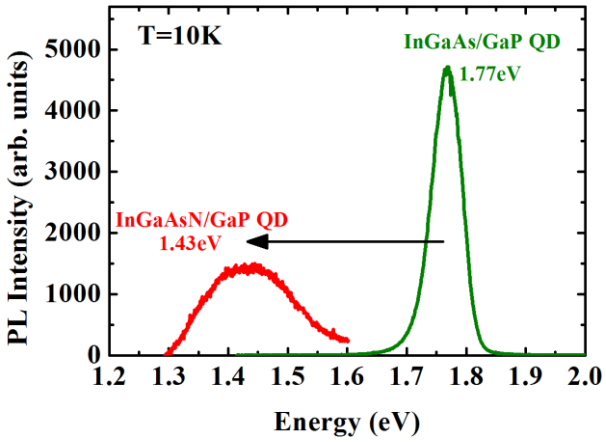

Fig. 4-42: Low temperature PL spectrum of InGaAs/GaP QD (green line) and InGaAsN/GaP QD (red line).

4.8 Conclusions

In conclusion, we have obtained a very high density of InGaAs QD on GaP. The PL has been studied as a function of temperature, pressure and excitation density to clarify the electronic structure. These experiments, backed by supercell TB simulation suggest the following picture: while the hole state has properties common to other nanostructures; i.e. a heavy hole confined in the QD, the ground electron state may come from X_Z states mechanically confined in the GaP matrix at the QD apex. The indirect character in real and reciprocal spaces explains the observed long radiative lifetime in the microsecond range.

In spite of these features, efficient room temperature PL has been achieved, visible to the naked eye. The first trends given on the carrier recombination dynamics suggest that the carrier capture is efficient, with rise times around 20 ps, and proceeds directly from the GaP barrier to the QD. Moreover, a second PL peak is observed at 100 meV above the LE transition. The thermalization of excitons between the LE and the HE levels shows that the HE optical transition is radiatively more efficient than the LE one, and time resolved PL also gives a shorter decay time at the HE energy. A mixing of Γ and X states may favor carrier capture and relaxation in these QD and may explain the relatively strong PL efficiency.

The question of whether InGaAs/GaP QDs can be used as the active region of a laser remains open. Our model suggests that an indirect/direct crossover is possible with increasing In content and/or enlarging the QD. Finally, the optimization of some of the growth conditions has

been found to improve the optical properties. Many optimizations are still possible, especially concerning the incorporation of N in InGaAsN/GaP QD, and will be studied in the next future.

References of Chapter 4

[1] Y. Arakawa and H. Sakaki, Appl. Phys. Lett. **40**, 939 (1982).
[2] M. Asada, Y. Miyamoto, and Y. Suematsu, Ieee J. Quantum Electron. **22**, 1915 (1986).
[3] N.N. Ledentsov, V.M. Ustinov, A.Y. Egorov, A.E. Zhukov, M.V. Maksimov, I.G. Tabatadze, and P.S. Kop'ev, Semiconductors **28**, 832 (1994).
[4] N. Kirstaedter, N.N. Ledentsov, M. Grundmann, D. Bimberg, V.M. Ustinov, S.S. Ruvimov, M.V. Maximov, P.S. Kop'ev, Z.I. Alferov, U. Richter, P. Werner, U. Gosele, and J. Heydenreich, Electron. Lett. **30**, 1416 (1994).
[5] H. Hirayama, K. Matsunaga, M. Asada, and Y. Suematsu, Electron. Lett. **30**, 142 (1994).
[6] N.N. Ledentsov, M. Grundmann, F. Heinrichsdorff, D. Bimberg, V.M. Ustinov, A.E. Zhukov, M.V. Maximov, Z.I. Alferov, and J.A. Lott, Ieee J. Sel. Top. Quantum Electron. **6**, 439 (2000).
[7] S.S. Mikhrin, A.R. Kovsh, I.L. Krestnikov, A.V. Kozhukhov, D.A. Livshits, N.N. Ledentsov, Y.M. Shernyakov, I.I. Novikov, M.V. Maximov, V.M. Ustinov, and Z.I. Alferov, Semicond. Sci. Technol. **20**, 340 (2005).
[8] M. Kuntz, G. Fiol, M. Lammlin, C. Schubert, A.R. Kovsh, A. Jacob, A. Umbach, and D. Bimberg, Electron. Lett. **41**, 244 (2005).
[9] S. Gerhard, V. Baumann, S. Höfling, and A. Forchel, Nanotechnology **20**, 434016 (2009).
[10] F. Hatami, W.T. Masselink, and L. Schrottke, Appl. Phys. Lett. **78**, 2163 (2001).
[11] A.R. Goñi, C. Kristukat, F. Hatami, S. Dreßler, W.T. Masselink, and C. Thomsen, Phys. Rev. B **67**, 075306 (2003).
[12] F. Hatami, V. Lordi, J.S. Harris, H. Kostial, and W.T. Masselink, J. Appl. Phys. **97**, 096106 (2005).
[13] F. Hatami, W.T. Masselink, L. Schrottke, J.W. Tomm, V. Talalaev, C. Kristukat, and A.R. Goñi, Phys. Rev. B **67**, 085306 (2003).
[14] F. Fukami, K. Umeno, Y. Furukawa, N. Urakami, S. Mitsuyoshi, H. Okada, H. Yonezu, and A. Wakahara, Phys. Status Solidi C **8**, 322 (2011).
[15] R. Leon, C. Lobo, T.P. Chin, J.M. Woodall, S. Fafard, S. Ruvimov, Z. Liliental-Weber, and M.A. Stevens Kalceff, Appl. Phys. Lett. **72**, 1356 (1998).
[16] W. Guo, A. Bondi, C. Cornet, H. Folliot, A. Létoublon, S. Boyer-Richard, N. Chevalier, M. Gicquel, B. Alsahwa, A.L. Corre, J. Even, O. Durand, and S. Loualiche, Phys. Status Solidi C **6**, 2207 (2009).
[17] T.S. Shamirzaev, D.S. Abramkin, A.K. Gutakovskii, and M.A. Putyato, Appl. Phys. Lett. **97**, 023108 (2010).
[18] K. Umeno, Y. Furukawa, N. Urakami, R. Noma, S. Mitsuyoshi, A. Wakahara, and H. Yonezu, Phys. E Low-Dimens. Syst. Nanostructures **42**, 2772 (2010).
[19] S. Fuchi, Y. Nonogaki, H. Moriya, A. Koizumi, Y. Fujiwara, and Y. Takeda, Phys. E Low-Dimens. Syst. Nanostructures **21**, 36 (2004).
[20] Y. Song, P.J. Simmonds, and M.L. Lee, Appl. Phys. Lett. **97**, 223110 (2010).
[21] T. Nguyen Thanh, C. Robert, C. Cornet, M. Perrin, J.M. Jancu, N. Bertru, J. Even, N. Chevalier, H. Folliot, O. Durand, and A. Le Corre, Appl. Phys. Lett. **99**, 143123 (2011).
[22] K. Rivoire, S. Buckley, Y. Song, M.L. Lee, and J. Vučković, Phys. Rev. B **85**, 045319 (2012).
[23] Y. Song and M. Larry Lee, Appl. Phys. Lett. **100**, 251904 (2012).
[24] C. Robert, C. Cornet, P. Turban, T. Nguyen Thanh, M.O. Nestoklon, J. Even, J.M. Jancu, M. Perrin, H. Folliot, T. Rohel, S. Tricot, A. Balocchi, D. Lagarde, X. Marie, N. Bertru, O. Durand, and A. Le Corre, Phys. Rev. B **86**, 205316 (2012).

[25] C. Robert, T.N. Thanh, C. Cornet, P. Turban, M. Perrin, A. Balocchi, H. Folliot, N. Bertru, L. Pedesseau, M.O. Nestoklon, J. Even, J.-M. Jancu, S. Tricot, O. Durand, X. Marie, and A. Le Corre, Nanoscale Res. Lett. **7**, 643 (2012).
[26] G. Stracke, A. Glacki, T. Nowozin, L. Bonato, S. Rodt, C. Prohl, A. Lenz, H. Eisele, A. Schliwa, A. Strittmatter, U.W. Pohl, and D. Bimberg, Appl. Phys. Lett. **101**, 223110 (2012).
[27] C. Prohl, A. Lenz, D. Roy, J. Schuppang, G. Stracke, A. Strittmatter, U.W. Pohl, D. Bimberg, H. Eisele, and M. Dähne, Appl. Phys. Lett. **102**, 123102 (2013).
[28] P. Caroff, N. Bertru, A.L. Corre, O. Dehaese, T. Rohel, I. Alghoraibi, H. Folliot, and S. Loualiche, Jpn. J. Appl. Phys. **44**, L1069 (2005).
[29] R. Heitz, I. Mukhametzhanov, A. Madhukar, A. Hoffmann, and D. Bimberg, J. Electron. Mater. **28**, 520 (1999).
[30] A.D. Giddings, J.G. Keizer, M. Hara, G.J. Hamhuis, H. Yuasa, H. Fukuzawa, and P.M. Koenraad, Phys. Rev. B **83**, 205308 (2011).
[31] S.C. Lee, L.R. Dawson, S.R.J. Brueck, and A. Stintz, J. Appl. Phys. **96**, 4856 (2004).
[32] F. Fournier, R.A. Metzger, A. Doolittle, A.S. Brown, C. Carter-Coman, N.M. Jokerst, and R. Bicknell-Tassius, J. Cryst. Growth **175–176, Part 1**, 203 (1997).
[33] F. Turco and J. Massies, Appl. Phys. Lett. **51**, 1989 (1987).
[34] J.-P. Reithmaier, H. Riechert, H. Schlötterer, and G. Weimann, J. Cryst. Growth **111**, 407 (1991).
[35] M. Mashita, Y. Hiyama, K. Arai, B.-H. Koo, and T. Yao, Jpn. J. Appl. Phys. **39**, 4435 (2000).
[36] A.A. Mbaye, F. Turco, and J. Massies, Phys. Rev. B **37**, 10419 (1988).
[37] K. Jacobi, Prog. Surf. Sci. **71**, 185 (2003).
[38] P. Kratzer, Q.K.K. Liu, P. Acosta-Diaz, C. Manzano, G. Costantini, R. Songmuang, A. Rastelli, O.G. Schmidt, and K. Kern, Phys. Rev. B **73**, 205347 (2006).
[39] G. Costantini, A. Rastelli, C. Manzano, P. Acosta-Diaz, R. Songmuang, G. Katsaros, O.G. Schmidt, and K. Kern, Phys. Rev. Lett. **96**, 226106 (2006).
[40] J. Márquez, L. Geelhaar, and K. Jacobi, Appl. Phys. Lett. **78**, 2309 (2001).
[41] H. Lee, R. Lowe-Webb, W. Yang, and P.C. Sercel, Appl. Phys. Lett. **72**, 812 (1998).
[42] Y. Hasegawa, H. Kiyama, Q.K. Xue, and T. Sakurai, Appl. Phys. Lett. **72**, 2265 (1998).
[43] Y.-H. Li, A. Walsh, S. Chen, W.-J. Yin, J.-H. Yang, J. Li, J.L.F. Da Silva, X.G. Gong, and S.-H. Wei, Appl. Phys. Lett. **94**, 212109 (2009).
[44] A.J. Williamson, A. Franceschetti, H. Fu, L.W. Wang, and A. Zunger, J. Electron. Mater. **28**, 414 (1999).
[45] L. Landin, M. Borgström, M. Kleverman, M.-E. Pistol, L. Samuelson, W. Seifert, and X.. Zhang, Thin Solid Films **364**, 161 (2000).
[46] S. Hinooda, S. Loualiche, B. Lambert, N. Bertru, M. Paillard, X. Marie, and T. Amand, Appl. Phys. Lett. **78**, 3052 (2001).
[47] C. Kristukat, A.R. Goñi, K. Pötschke, D. Bimberg, and C. Thomsen, Phys. Status Solidi B **244**, 53 (2007).
[48] A.R. Goni, K. Strössner, K. Syassen, and M. Cardona, Phys. Rev. B **36**, 1581 (1987).
[49] A.R. Goi, K. Syassen, K. Strössner, and M. Cardona, Phys. Rev. B **39**, 3178 (1989).
[50] S.L. Chuang, *Physics of Optoelectronic Devices* (John Wiley & Sons, Incorporated, 1995).
[51] M.K.K. Nakaema, F. Iikawa, M.J.S.P. Brasil, E. Ribeiro, G. Medeiros-Ribeiro, W. Carvalho, M.Z. Maialle, and M.H. Degani, Appl. Phys. Lett. **81**, 2743 (2002).
[52] Y.-A. Liao, W.-T. Hsu, P.-C. Chiu, J.-I. Chyi, and W.-H. Chang, Appl. Phys. Lett. **94**, 053101 (2009).

[53] C. Cornet, C. Labbé, H. Folliot, P. Caroff, C. Levallois, O. Dehaese, J. Even, A. Le Corre, and S. Loualiche, Appl. Phys. Lett. **88**, 171502 (2006).
[54] M. Syperek, M. Baranowski, G. Sęk, J. Misiewicz, A. L f fler, S. H f ling, S. Reitzenstein, M. Kamp, and A. Forchel, Phys. Rev. B **87**, 125305 (2013).
[55] I. Vurgaftman, J.R. Meyer, and L.R. Ram-Mohan, J. Appl. Phys. **89**, 5815 (2001).
[56] G. Bastard, *Wave Mechanics Applied to Semiconductor Heterostructures* (Les Éditions de Physique, 1988).
[57] A.J. Williamson, A. Zunger, and A. Canning, Phys. Rev. B **57**, R4253 (1998).
[58] V. Popescu and A. Zunger, Phys. Rev. B **84**, 125315 (2011).
[59] A.I. Yakimov, N.P. Stepina, A.V. Dvurechenskii, A.I. Nikiforov, and A.V. Nenashev, Phys. Rev. B **63**, 045312 (2001).
[60] M. Brehm, T. Suzuki, T. Fromherz, Z. Zhong, N. Hrauda, F. Hackl, J. Stangl, F. Schäffler, and G. Bauer, New J. Phys. **11**, 063021 (2009).
[61] M. El Kurdi, S. Sauvage, G. Fishman, and P. Boucaud, Phys. Rev. B **73**, 195327 (2006).
[62] K. Gradkowski, N. Pavarelli, T.J. Ochalski, D.P. Williams, J. Tatebayashi, G. Huyet, E.P. O'Reilly, and D.L. Huffaker, Appl. Phys. Lett. **95**, 061102 (2009).
[63] L.-W. Wang, L. Bellaiche, S.-H. Wei, and A. Zunger, Phys. Rev. Lett. **80**, 4725 (1998).
[64] P.W. Fry, I.E. Itskevich, D.J. Mowbray, M.S. Skolnick, J.J. Finley, J.A. Barker, E.P. O'Reilly, L.R. Wilson, I.A. Larkin, P.A. Maksym, M. Hopkinson, M. Al-Khafaji, J.P.R. David, A.G. Cullis, G. Hill, and J.C. Clark, Phys. Rev. Lett. **84**, 733 (2000).
[65] R. Heitz, M. Veit, N.N. Ledentsov, A. Hoffmann, D. Bimberg, V.M. Ustinov, P.S. Kop'ev, and Z.I. Alferov, Phys. Rev. B **56**, 10435 (1997).
[66] C. Paranthoen, C. Platz, G. Moreau, N. Bertru, O. Dehaese, A. Le Corre, P. Miska, J. Even, H. Folliot, C. Labbé, G. Patriarche, J.C. Simon, and S. Loualiche, J. Cryst. Growth **251**, 230 (2003).
[67] J. Kuyyalil, T. Nguyen Thanh, T. Quinci, S. Almosni, A. Létoublon, T. Rohel, N. Bertru, A. Le Corre, O. Durand, and C. Cornet, J. Cryst. Growth **377**, 17 (2013).

Conclusion

Summary

This dissertation is devoted to the theoretical and experimental study of III-V nanostructures on GaP for lasing emission on Si.

The chapter 1 presents the state-of-the-art of lasing emission on Si which remains one of the main challenges for the development of Si photonics. The monolithic integration of III-V semiconductor structures on Si is expected to fulfill the requirements for the development of very large scale integration applications. The pseudomorphic approach which consists in growing lattice-matched GaPN-based heterostructures on Si is one of the key technologies which might lead efficient and robust lasers.

The chapter 2 presents the theoretical challenges that the pseudomorphic approach faces. In particular, the simulation of electronic band structures and optical properties requires to master the modeling of indirect band gap semiconductors, correctly introducing the strain effects and describing the unusual properties of dilute nitride alloys. An extended tight-binding model is presented to address these issues and tested on benchmark structures (superlattices, quantum wells, quantum dots and bulk dilute nitride alloys). The derivation of optical properties, including material gain and refractive index is described.

The chapter 3 is devoted to the study of dilute nitride GaAsPN-based structures. The main optical properties of bulk GaPN are first highlighted. The incorporation of nitrogen strongly shifts the band gap toward lower energies and increases the luminescence efficiency up to a given concentration before the non-radiative defects become dominant. Localized radiative states created by lattice disorder yield a density of states below the band gap. A perfectly lattice-matched quaternary alloy GaAsPN (with low As content) can be grown on GaP or Si substrates. It is proposed as a barrier material in the laser active zone. Compressively strained GaAsPN quantum wells (with high As content) are studied by temperature dependent and time-resolved

photoluminescence. The carrier dynamics is linked to the density of radiative localized states and non-radiative states. Finally, the AlGaP alloy is proposed as cladding layers for a laser on GaP. Significant index contrast is measured between AlGaP and GaP enabling an efficient confinement of the optical mode. Elements for the design of laser structures on GaP and Si are provided.

The chapter 4 presents a detailed study of InGaAs/GaP quantum dots. High density and room temperature photoluminescence are demonstrated. The electronic band structure is studied by both **k·p** tight-binding models. The measured long radiative lifetime and the red shift of the photoluminescence peak with hydrostatic pressure are interpreted as the result of optical transitions involving X conduction states. The appearance of a more efficient optical transition at room temperature is interpreted as a possible evidence of a direct type-I transition as predicted by simulations. The mixing of Γ and X states may favor carrier capture and relaxation in these quantum dots.

Perspectives

During this PhD thesis, encouraging results have been achieved concerning the optical efficiency of GaAsPN quantum wells, with demonstration of room temperature photoluminescence on Si substrate. A strong improvement of the optical properties is expected in the near future benefiting from the recent progress of Foton laboratory in achieving a good GaP/Si interface.

Nevertheless, the development of efficient GaAsPN-based lasers on GaP and Si substrates will require a specific investigation of both growth conditions and post-growth annealing in order to reduce the disorder effects and the density of non-radiative defects in dilute nitride alloys. Increasing the N content without degrading the structural quality will also be necessary to increase the emission wavelength and to get closer to the transparency window of Si. From the theoretical view, the N induced disorder effects may be studied by calculating the density of states in a large supercell.

The development of cladding layers has been initiated by studying the properties of the AlGaP alloy. An electrically pumped laser on GaP substrate will require doping of AlGaP layers. The As and N contents in the GaAsPN barrier material have to be optimized to ensure both

efficient injection of carriers in the active zone and confinement of electrons in the quantum wells. For the laser on Si substrate, the compatibility of incorporation of N with Al based alloys have to be studied.

Finally, the InGaAs/GaP quantum dots system is interesting for both theoretical and experimental studies. From the theoretical view, the effect of In localization inside the quantum dots should be investigated by supercell tight-binding simulations. Moreover, a k-space analysis of the electronic states should be performed to understand the optical efficiencies of the different transitions. The studies on the effects of growth conditions have to be completed. Incorporating more In without degrading the structural quality will be required to have a ground optical transition of direct type. Enhancing the confinement of the electrons in the mechanically deformed barrier should be also considered. Capping with AlP or stacking the quantum dots layers should be studied in this way. Finally, incorporation of N in InGaAsN quantum dots should be studied both theoretically and experimentally.

Appendices

A. Time-resolved photoluminescence experimental setup for measurements of short times (<12 ns)

The experimental setup used to measure the time dependence of photoluminescence is presented in Fig. A. 1. A mode-locked Ti:Sapphire (Spectra Physics, Tsunami) is pumped by a continuous wave frequency doubled Nd-YaG (Coherent, Verdi) to produce picoseconds laser pulses with a repetition rate of 80 MHz. A non-linear frequency doubler crystal is used to lower the excitation wavelength to 405 nm in order to excite the samples at an energy just above the direct band gap of GaP. Experiments are performed from 10 K to 300 K using a helium closed-cycle cryostat. Photoluminescence is detected by a Horiba iHR320 spectrometer followed by a synchroscan streak camera in order to obtain both the spectral and temporal dependence.

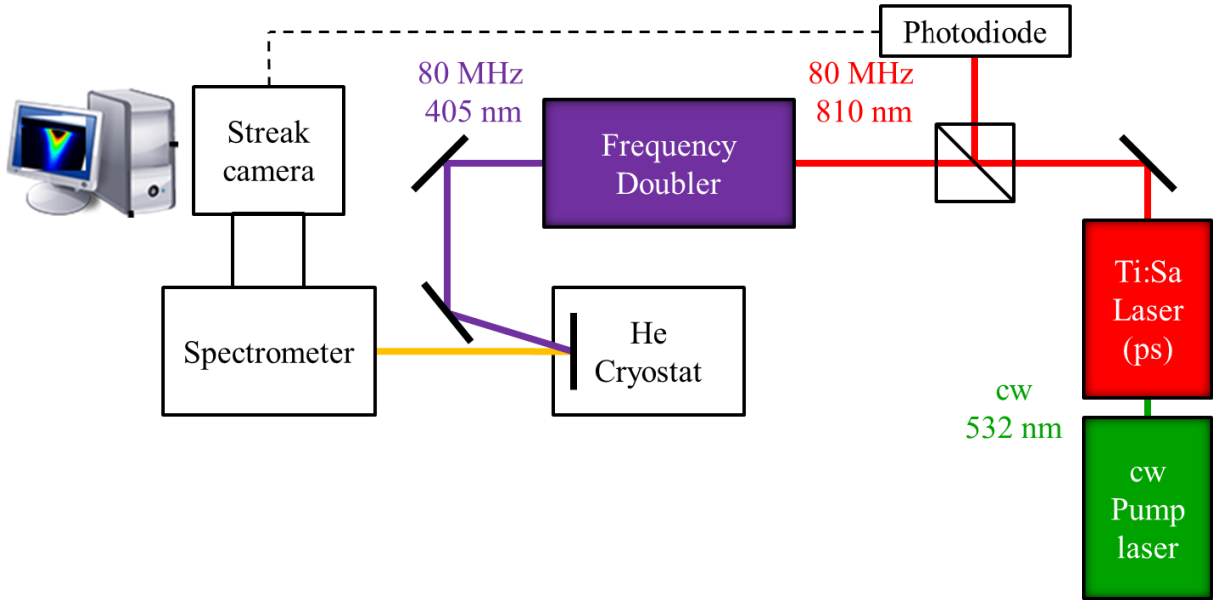

Fig. A. 1: Time resolved photoluminescence experimental setup.

The detection principle of the streak system is sketched in Fig. A. 2. After being wavelength-dispersed by the spectrometer, the photons hit a S20 photocathode and are converted

into electrons. The electrons are horizontally accelerated by electrodes not represented in Fig. A. 2 and are vertically deflected by sweep electrodes. The high voltage signal applied on the sweep electrodes is triggered by the laser pulses through the photodiode shown in Fig. A. 1 so that the deflected angle depends on the time of passage of electrons between the electrodes. The electrons are multiplied by a microchannel plate (MCP) and finally hit a phosphor screen for a conversion back to photons. The vertical position is the time axis whereas the horizontal position is the wavelength axis. The streak image obtained on the phosphor screen is finally converted into a digital signal by a two dimensional CCD array.

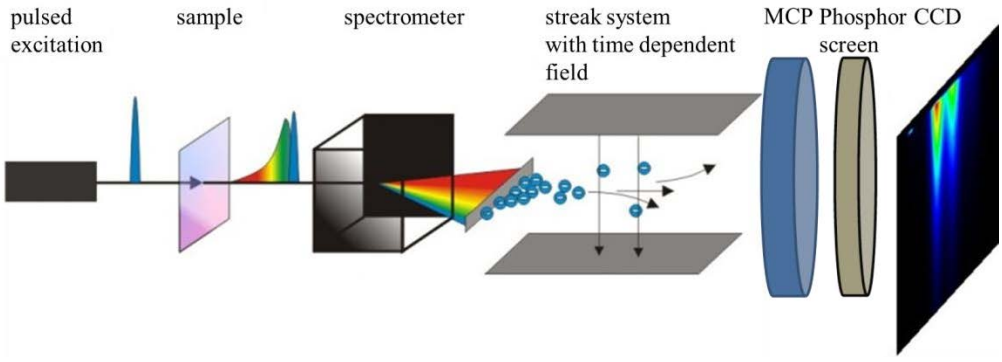

Fig. A. 2: Sketch view of the streak camera.

The spectral resolution used in these experiments is around 2 nm. The temporal resolution depends on the temporal detection window. For the measurements of decay times, the largest temporal detection window of 2200 ps is used (corresponding to a measured temporal resolution of 17 ps) whereas the smallest one of 160 ps is used for the measurements of rise times (corresponding to a measured temporal resolution of 6 ps).

B. Time-resolved photoluminescence experimental setup for measurements of long times (>12 ns)

The experimental setup presented in Appendix A is not suitable for the measurements of decay times which are longer than the repetition period of the Ti:Sa laser pulses (12 ns). The repetition period of pulses exciting the sample is decreased by extracting laser pulses from the 80 MHz fast train with a smaller repetition rate of 4 MHz or 0.8 MHz (depending on the experiments). This function is carried out by a pulse picker which is placed after the Ti:Sa laser (see Fig. B. 1).

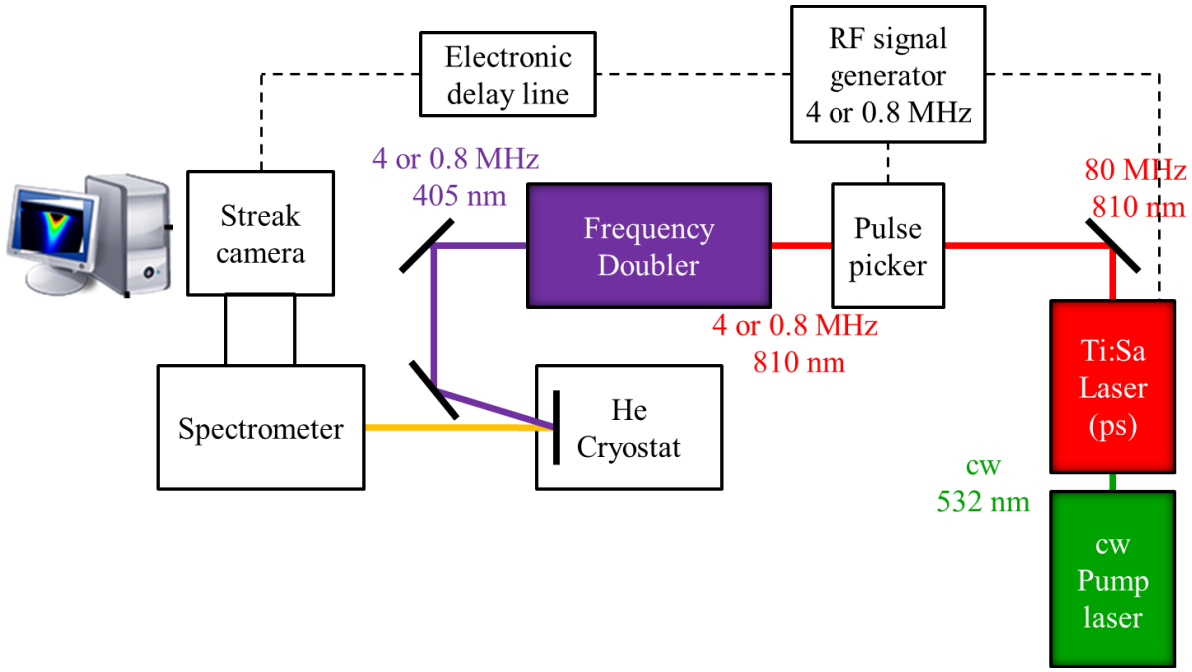

Fig. B. 1:Time resolved photoluminescence experimental setup with the pulse picker.

The principle of the pulse picker is to apply a short RF pulse to an acousto-optic modulator. The RF pulses have a repetition rate of 4 MHz or 0.8 kHz and periodically create an acoustic wave in a piece of transparent glass. This acoustic wave is seen as a diffraction grating by the incident laser beam. The first order diffracted beam which is slightly deflected by the grating and can pass through the output aperture whereas the other diffraction orders are blocked. Consequently, the repetition rate of the laser pulse train at the output of the pulse picker has the same repetition rate than the RF signal. The RF signal is synchronized with the Ti:Sa pulses. The high voltage signal applied on the sweep electrodes of the streak camera is triggered by the RF

signal. An electronic delay line is used to adjust the delay time between the RF pulse and the triggering of the streak camera.

This experimental setup enables to increase the repetition period of pulses exciting the sample but it also decreases the average excitation power and the temporal resolution. A best temporal resolution of about 250 ps is obtained with the smallest temporal detection window of 5 ns. Thus, the fast rise times cannot be measured with this experimental setup.

C. Photocurrent experimental setup

The principle of photocurrent measurements is sketched in Fig. C. 1. Quantum wells are placed in the space charge region of a polarized p-i-n junction. Photons created by a large spectral source are absorbed by the structure and create electron-hole pairs which are extracted from the confinement potential by an applied external electric field. For a given wavelength, a current is detected which intensity is proportional to the number of incident photons, to the absorption of the spectrum and to a term related to carrier extraction efficiency. At low excitation density and for an efficient extraction, the photocurrent intensity is expected to be roughly proportional to the absorption spectrum.

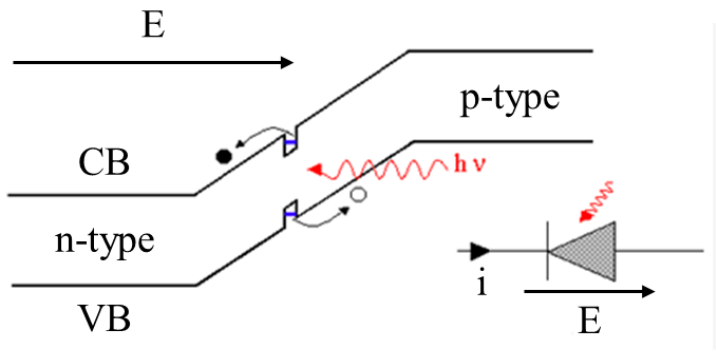

Fig. C. 1: Principle of photocurrent measurements.

The experimental setup is sketched in Fig. C. 2. The LED is illuminated with a 250 W tungsten-halogen lamp via a Horiba-Jobin-Yvon H25 monochromator equipped with a 1200 g.mm^{-1} grating and an optical fiber. A low-pass filter at 0.55 µm is used. The photocurrent signal is measured using standard lock-in technique. The incident optical power depends on the wavelength, with a mean value of 70 µW.cm^{-2}. The spectral resolution is roughly estimated at 0.5 meV.

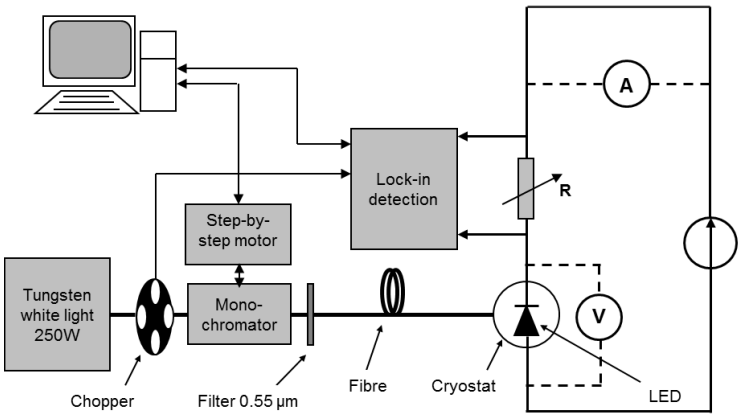

Fig. C. 2: Experimental setup for the photocurrent measurements.

D. Pressure dependent photoluminescence experimental setup

Photoluminescence measurements under high hydrostatic pressure have been performed at room temperature employing a gasketed diamond anvil cell (DAC)[1]. The sample is placed inside a 200-300 μm hole drilled into a metal gasket which is enclosed by the flat parallel faces of two diamonds anvils (see Fig. D. 1(a)). The sample is subjected to pressure when the two diamonds are pushed together decreasing the chamber volume, while slightly deforming the gasket (see Fig. D. 1(b)). A 4:1 methanol/ethanol mixture has been used as pressure transmitting medium for best hydrostatic conditions up to 10 GPa. Helium has also been used in one case for comparison.

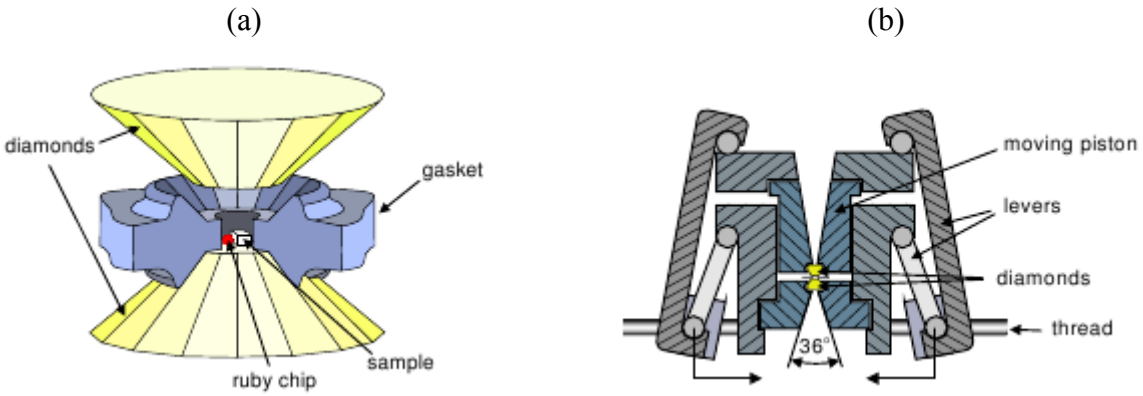

Fig. D. 1: Sketch of the diamond anvil cell. (a) Illustration of the two diamonds and the gasket. (b) Lever mechanism to move the upper piston. The end points of the levers are driven by two threads. From Ref. 1.

The small volume of the chamber requires the sample dimensions not to exceed 100x100x50 μm^3. Consequently, the sample has been thinned by mechanical polishing from the substrate side to about 30 μm. It has been checked that photoluminescence signal does not suffer from the polishing procedure.

The pressure in the anvil cell is determined in situ via the pressure dependent shift fluorescence of a Cr^{3+} doped Al_2O_3 ruby which is placed in the chamber (see Fig. D. 1(a))[2]. The sample has been excited using a 405 nm line of a continuous wave laser diode. The photoluminescence spectra have been collected using a LabRam HR800 spectrometer equipped with a charge-coupled device detector.

References

[1] J.S. Reparaz, Optical Properties of Low-Dimensional Semiconductor Nanostructures Under High Pressure, Universidad Autonoma de Barcelona, 2008.
[2] H.K. Mao, J. Xu, and P.M. Bell, J. Geophys. Res. Solid Earth **91**, 4673 (1986).

Publications

- Evaluation of InGaPN and GaAsPN materials lattice-matched to Si for multi-junction solar cells.
  S. Almosni, C. Robert, T. Nguyen Thanh, C. Cornet, A. Létoublon, T. Quinci, C. Levallois, M. Perrin, J. Kuyyalil, L. Pedesseau, A. Balocchi, P. Barate, J. Even, J.M. Jancu, N. Bertru, X. Marie, O. Durand and A. Le Corre. ***Journal of Applied Physics 113 123509 (2013).***

- Structural and optical properties of AlGaP confinement layers and InGaAs quantum dots light emitters onto GaP substrate: towards photonics on silicon applications.
  C. Robert, T. Nguyen Thanh, M. Perrin, C. Cornet, A. Létoublon, J.M. Jancu, J. Even, N. Bertru, P. Turban, A. Balocchi, X. Marie, O. Durand, A. Le Corre. ***Thin solid Films 541 87(2013).***

- Synchrotron X-ray diffraction analysis for quantitative defect evaluation in GaP/Si nanolayers.
  T. Nguyen Thanh, C. Robert, A. Létoublon, C. Cornet, T. Quinci, E. Giudicelli, S. Almosni, N. Boudet, A. Ponchet, J. Kuyyalil, M. Danila, O. Durand, N. Bertru and A. Le Corre. ***Thin solid Films 541 36 (2013).***

- Quantitative study of microtwins in GaP/Si thin film and GaAsPN quantum wells grown on silicon substrate.
  T. Nguyen Thanh, C. Robert, E. Giudicelli, A. Létoublon, C. Cornet, A. Ponchet, T. Rohel, A. Balocchi, J.S. Micha, M. Perrin, S. Loualiche, X. Marie, N. Bertru, O. Durand and A. Le Corre. ***Journal of Crystal Growth 378 25 (2013).***

- Structural and optical properties of (In,Ga)As/GaP quantum dots and (GaAsPN/GaPN) diluted_nitride nanolayers coherently grown onto GaP and Si substrates for photonics and photovoltaics applications.
  O. Durand, C. Robert, T. Nguyen Thanh, S. Almosni, T. Quinci, J. Kuyyalil, C. Cornet, A. Létoublon, C. Levallois, J.M. Jancu, J. Even, L. Pédesseau, M. Perrin, N. Bertru, A. Sakri, N. Boudet, A. Ponchet, P. Rale, L. Lombez, J.F. Guillemoles, X. Marie, A. Balocchi, P. Turban, S. Tricot, M. Modreanu, S. Loualiche and A. Le Corre. *Photonics west 2013 San Francisco (2012-01-21) IEEE,* ***Proceedings of the SPIE, Vol. 8631, 863126.***

- Electronic, optical and structural properties of (In,Ga)As/GaP quantum dots.
  C. Robert, C. Cornet, P. Turban, T. Nguyen Thanh, M.O. Nestoklon, J. Even, J.M. Jancu, M. Perrin, H. Folliot, T. Rohel, S. Tricot, A. Balocchi, D. Lagarde, X. Marie, N. Bertru, O. Durand and A. Le Corre. ***Physical Review B* 86 *205316 (2012).***

- Atomistic calculations of Ga(NAsP)/GaP(N) quantum wells on silicon substrate: Band structure and optical gain.
  C. Robert, M. Perrin, C. Cornet, J. Even and J.M. Jancu. ***Applied Physics Letters* 100 *111901 (2012).***

- Structural and optical analyses of GaP/Si and (GaAsPN/GaPN)/GaP/Si nanolayers for integrated photonics on silicon.
  T. Nguyen Thanh, C. Robert, W. Guo, A. Létoublon, C. Cornet, G. Elias, A. Ponchet, T. Rohel, N. Bertru, A. Balocchi, O. Durand, J.S. Micha, M. Perrin, S. Loualiche, X. Marie and A. Le Corre. ***Journal of Applied Physics 112 053521 (2012).***

- Theoretical and experimental study of (In,Ga)As/GaP quantum dots.
  C. Robert , T. Nguyen Thanh, C. Cornet, P. Turban, M. Perrin, A. Balocchi, N. Bertru, J. Even, J.M. Jancu, S. Tricot, O. Durand, X. Marie and A. Le Corre. ***Nanoscale Research Letters* 7 *643 (2012).***

- Atomistic simulations of the optical absorption of type-II CdSe/ZnTe superlattices.
  S. Boyer-Richard, C. Robert, L. Gérard, J. - P. Richters, R. André, J. Bleuse, H. Mariette, J. Even, J. M. Jancu. ***Nanoscale Research Letters* 7 *543 (2012).***

- Coherent integration of photonics on silicon through the growth of nanostructures on GaP/Si.
  T. Nguyen Thanh, C. Robert, C. Cornet, W. Guo, A. Létoublon, M. Perrin, N. Bertru, J. Even, N. Chevalier, H. Folliot, S. Loualiche, A. Ponchet, G. Elias, J.-S. Micha, O. Durand and A. Le Corre. *Photonics west 2012 San Francisco (2012-01-21) IEEE,* ***Proceedings of the SPIE, Vol. 8268, 82681H.***

- Room temperature photoluminescence of high density (In,Ga)As/GaP quantum dots.
  T. Nguyen Thanh, C. Robert, C. Cornet, M. Perrin, J. M. Jancu, N. Bertru, J. Even, N. Chevalier, H. Folliot, O. Durand, and A. Le Corre. ***Applied Physics Letters 99 143123 (2011).***

- Room temperature operation of GaAsP(N)/GaP(N) quantum well based light-emitting diodes: effect of the incorporation of nitrogen.
  C. Robert, A. Bondi, T. Nguyen Thanh, J. Even, C. Cornet, O. Durand, J.P. Burin, J.M. Jancu, W. Guo, A. Létoublon, H. Folliot, S. Boyer, M. Perrin, N. Chevalier, O. Dehaese, K. Tavernier, S. Loualiche and A. Le Corre. ***Applied Physics Letters 98 251110 (2011).***

- Carrier injection in GaAsPN/GaPN quantum wells on silicon.
  C. Cornet, C. Robert, T. Nguyen Thanh, W. Guo, A. Bondi, G. Elias, A. Létoublon, S. Richard, J.-P. Burin, M. Perrin, J. M. Jancu, O. Durand, J. Even, S. Loualiche, H. Folliot, N. Bertru, A. Ponchet and A. Le Corre. ***Indium Phosphide and Related Materials Proceedings IEEE (2011).***

- Structural characterization of GaP/Si nanolayers.
  W. Guo, T. Nguyen Thanh, G. Elias, A. Létoublon, C. Cornet, A. Ponchet, A. Bondi, T. Rohel, N. Bertru, C. Robert, O. Durand, J.S. Micha and A. Le Corre. ***Indium Phosphide and Related Materials Proceedings IEEE (2011).***

Update: 31/08/2013

Résumé

Cadre de l'étude

La photonique sur silicium constitue actuellement un domaine de recherche particulièrement actif. Il est en effet désormais bien établi qu'une rupture technologique majeure concernant la circulation de l'information numérique passera par l'abandon des interconnexions métalliques à chaque échelle de dimensions[1]. De par leur temps de réponse associée et leur dissipation thermique, elles constituent aujourd'hui le frein principal à l'augmentation des débits d'informations. Les interconnexions optiques, déjà utilisées pour les communications à longue distance, sont ainsi proposées pour répondre aux enjeux des communications courtes distances : entre ordinateurs, entre cartes, entre puces voire même intra-puces.

Pour des raisons de coûts et de maturité technologique, le secteur de la microélectronique repose depuis maintenant 50 ans sur la maîtrise du silicium, il convient donc de développer les composants photoniques sur substrat silicium. La plupart des composants optiques ont ainsi été développés ces dernières années: photodétecteurs[2], modulateurs[3], multiplexeurs[4]. Cependant, le point bloquant reste indubitablement le développement d'un émetteur laser sur silicium.

En effet, de par ses propriétés intrinsèques (bande interdite indirecte), ce matériau est très peu propice à l'émission de lumière. Diverses solutions ont été proposées pour augmenter l'émission de photons provenant du silicium. On peut, par exemple, exploiter les effets de confinement quantique dans les nanocristaux de silicium[5] ou utiliser des transitions atomiques dans des nanocristaux de silicium dopés Er[6]. Un laser pompé optiquement a même été démontré en utilisant l'effet Raman[7]. Mais l'approche la plus mature technologiquement consiste à reporter des matériaux III-V à bande interdite directe sur substrat de silicium pour constituer la zone active du laser[8]. Cette approche, généralement basée sur la technique du collage moléculaire, est notamment envisagée à très court terme par Intel pour répondre aux enjeux de l'intégration de la

photonique dans les centres de traitement de données. Cependant, son utilisation pour les applications nécessitant une très forte densité d'intégration et une production de masse reste encore hypothétique.

L'approche monolithique, consistant à faire croitre une structure laser directement sur Si, est ainsi considérée comme le « Graal » de la photonique sur Si. La croissance sur Si des autres matériaux semiconducteurs de la colonne IV tel que le Ge est intensivement étudiée par de nombreux groupes de recherche pour remplir la fonction d'émetteur de lumière[9]. Malheureusement, le caractère légèrement indirect de la bande interdite du Ge, et les difficultés inhérentes à l'hétéroépitaxie d'un matériau ayant un paramètre de maille différent de celui du Si, n'ont pas permis d'obtenir des performances significatives.

Une autre approche monolithique consiste à faire croître métamorphiquement sur Si des matériaux III-V, classiquement utilisés dans les lasers à semiconducteurs, tels que l'InP le GaAs ou le GaSb[10–12]. Le problème de la bande interdite indirecte est alors résolu, mais le problème du désaccord de maille entre la structure épitaxiée et le substrat de Si demeure et entraîne généralement une densité importante de dislocations, incompatible avec une durée de vie importante des composants.

L'approche pseudomorphique, étudiée dans cette thèse, consiste à intégrer monolithiquement une structure laser III-V en accord de maille sur Si. Dans cette approche, le GaP joue un rôle majeur car il est le composé III-V binaire ayant le plus faible désaccord de maille avec le Si (0.37 %) (cf. Figure 1). Un parfait accord de maille peut même être obtenu en incorporant environ 2 % d'azote formant ainsi un alliage nitrure dilué GaPN. Malheureusement, le GaP possède également une bande interdite indirecte ce qui l'empêche d'être un émetteur de lumière efficace. La croissance cohérente sur GaP de nanostructures à base de semiconducteurs à bande interdite directe tel que le GaAs semble être indiquée pour obtenir une zone active compatible avec l'émission laser. L'incorporation d'azote est également connue pour exalter les propriétés d'émission de lumière dans GaP. Ces deux points sont étudiés dans cette thèse.

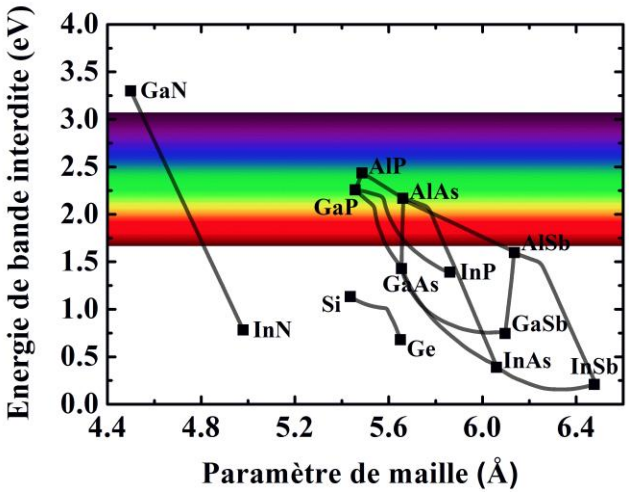

Figure 1: Energie de bande interdite des principaux semiconducteurs en fonction de leur paramètre de maille.

Défis théoriques

Afin d'orienter les choix de design d'une structure laser, les propriétés électroniques et optiques des structures semiconductrices doivent être simulées. La méthode **k·p** huit-bandes est couramment utilisée pour la simulation de composants optoélectroniques basés sur des nanostructures de GaAs, InP ou GaSb[13]. La raison principale de ce succès est la simplicité et l'efficacité de cette méthode pour décrire la structure de bande de nanostructures aussi complexes que des boites quantiques. Cependant, la structure de bandes décrite par cette méthode n'est valable qu'au voisinage d'un point **k**. Dans le cas des nanostructures à bande interdite directe, cette méthode est donc tout à fait applicable. Néanmoins, dans le cas des nanostructures sur GaP, elle devient obsolète. En effet, GaP étant un semiconducteur à bande interdite indirecte, il ne peut pas être correctement décrit. De plus, même pour le cas de nanostructures à base de GaAs (matériau massif pourtant à bande interdite directe lorsqu'il est non-contraint) sur GaP, l'effet des contraintes mécaniques sur les bandes d'énergie requiert une simulation de la structure électronique sur toute la première zone de Brillouin. Le premier défi que cette thèse doit relever est donc théorique.

La méthode des liaisons fortes est présentée à cette fin. Cette méthode atomistique permet aujourd'hui de simuler des systèmes contenant plusieurs millions d'atomes[14], ce qui en

fait un outil de choix pour la simulation de boites quantiques enterrées. De plus, lorsqu'elle utilise une base étendue d'orbitales atomiques $sp^3d^5s^*$, elle permet de décrire correctement la structure de bandes d'énergies sur toute la première zone de Brillouin[15]. Les alliages de semiconducteurs III-V peuvent également être simulés en considérant des supercellules regroupant un grand nombre d'atomes répartis aléatoirement dans le réseau cristallin. Néanmoins, cette simulation coûteuse en ressources computationnelles s'avère être inutile pour la plupart des alliages qui peuvent être plus simplement décrits par un système à deux atomes (un cation et un anion moyens) dont les paramètres liaisons fortes sont interpolés entre ceux des différents semiconducteurs binaires composant l'alliage.

La simulation des alliages de nitrures dilués nécessite plus de prudence. En effet, l'atome d'azote diffère significativement des autres atomes de la colonne V (tels que l'arsenic et le phosphore) de par son plus faible rayon covalent et sa plus grande électronégativité. Ces deux caractéristiques sont à l'origine des propriétés inhabituelles observées dans les alliages de nitrures dilués, telle que la forte réduction de l'énergie de bande interdite avec l'incorporation d'azote. Une manière simple de décrire les effets de l'azote sur la structure de bandes est de considérer un modèle d'anti-croisement de bandes entre un niveau d'énergie localisé lié à l'azote et la bande de conduction du matériau hôte[16]. Cette idée peut être transposée dans le modèle des liaisons fortes en ajoutant une orbitale supplémentaire liée à l'azote dans la base de décomposition de le Hamiltonien[17]. Cette méthode présente le gros avantage de modéliser un alliage nitrure dilué avec seulement deux atomes et des paramètres identiques à ceux du matériau hôte complétés par deux paramètres reliés à l'énergie du niveau d'azote et à son couplage avec la bande de conduction du matériau hôte.

Etude des structures à base de nitrures dilués

Les structures à base de puits quantiques GaAsPN sont à l'heure d'aujourd'hui les seules ayant permis d'obtenir un effet laser sur substrats de GaP et Si dans l'approche pseudomorphique[18,19]. Une étude expérimentale, basée sur des mesures de photoluminescence en température et de photoluminescence résolue en temps, appuyée par les résultats de simulations par la méthode des liaisons fortes permettent de mettre en évidence plusieurs points cruciaux pour l'amélioration des propriétés optiques.

Les effets du désordre engendré par l'incorporation d'azote sont directement observés sur les spectres de photoluminescence. Une grande largeur à mi-hauteur ainsi qu'une queue sur le flanc basse énergie sont ainsi observées pour les matériaux massifs GaPN et GaAsPN ainsi que pour les puits quantiques de GaAsPN (cf. Figure 2(a)).

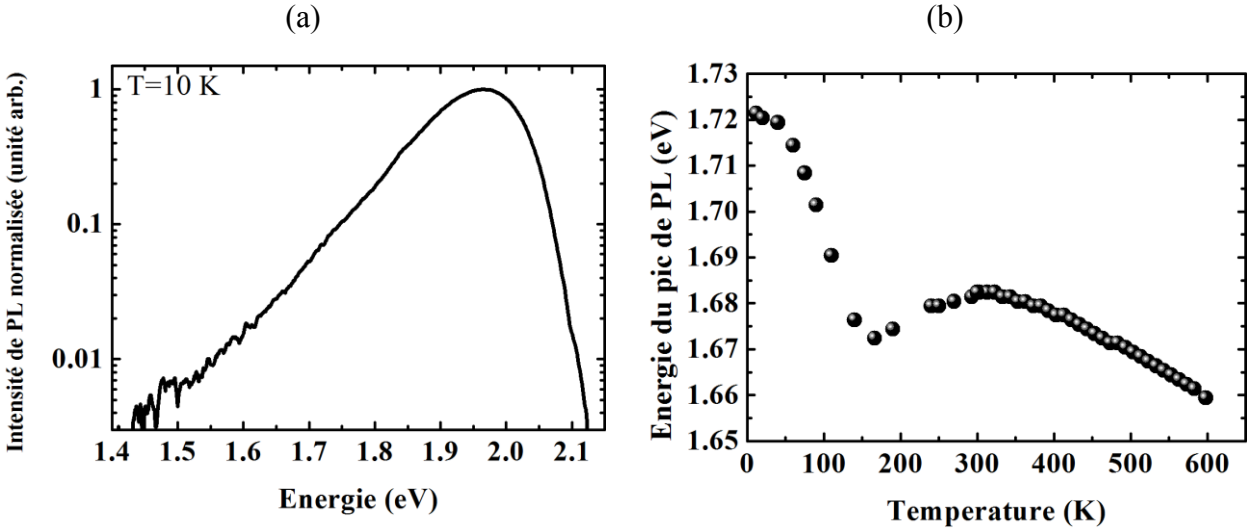

Figure 2: (a) Spectre de photoluminescence d'une couche de $GaP_{0.972}N_{0.012}$ pris à 10 K. (b) Energie du pic de photoluminescence de puits quantiques GaAsPN/GaPN en fonction de la température.

La dépendance en température de l'énergie du pic de photoluminescence suit un comportement en forme de S caractéristique des systèmes où cohabitent états localisés et états délocalisés (cf. Figure 2(b)). Enfin, la dynamique d'injection et de relaxation des porteurs observée par photoluminescence résolue en temps montrent que les états non radiatifs et les états radiatifs localisés dans la bande interdite jouent un rôle important.

La simulation des propriétés optiques des puits quantiques GaAsPN/GaP montre qu'une augmentation de la composition d'azote doit permettre d'augmenter le gain matériau et de réduire le seuil de transparence. Un compromis avec l'augmentation de la densité de défauts est donc à trouver.

Les premiers résultats de croissance de puits quantiques GaAsPN/GaPN sur substrat de Si montrent des résultats très encourageants avec l'obtention de photoluminescence à température ambiante (cf. encart de la Figure 3).

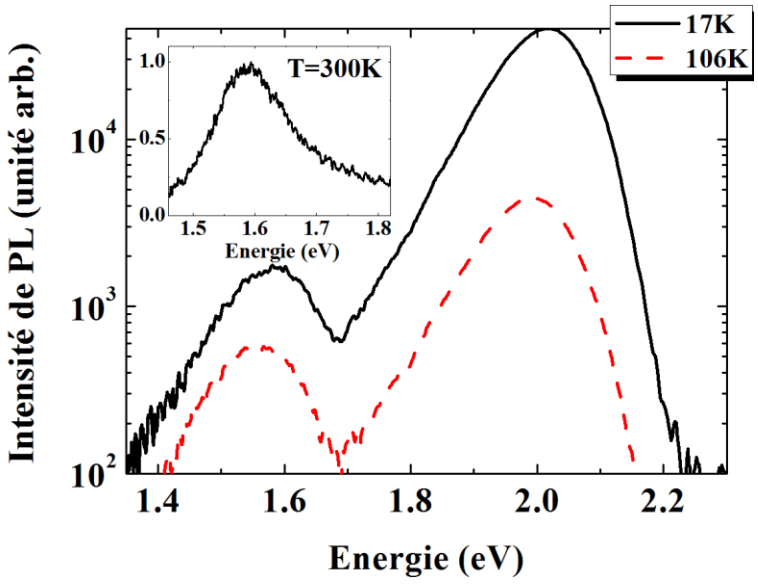

Figure 3: Spectres de photoluminescence de puits quantiques GaAsPN/GaPN sur Si. A 17 K et 106 K les pics des puits quantiques GaAsPN (1.56 eV) et de la barrière GaPN (2.02 eV) sont visibles. A température ambiante (encart), seule la photoluminescence des puits est détectée.

Une structure laser efficace requiert également de guider le mode optique dans la zone de gain. L'alliage AlGaP est étudié comme candidat potentiel pour les couches de confinement optique. Les mesures d'indice de réfraction déduites des expériences d'ellipsométrie spectroscopique montrent un bon contraste avec le GaP. Un facteur de confinement de 50 % est calculé en choisissant l'$Al_{0.5}Ga_{50.5}P$ pour entourer une zone active d'épaisseur 300 µm composée de nanostructures dans GaP émettant à 850 nm. Néanmoins, l'alignement des bandes entre AlGaP et GaP est de type II. Ainsi, une barrière de potentiel est prédite pour l'injection des électrons dans la zone active. Nous proposons d'utiliser l'alliage GaAsPN comme matériau barrière dans la zone active afin de résoudre ce problème. Cette alliage peut être crû en parfait accord de maille sur substrats de GaP et Si en considérant une teneur de quelques pourcents en arsenic et en azote.

Etude des boites quantiques InGaAs/GaP

Cette thèse présente finalement une étude des boites quantiques InGaAs/GaP afin d'évaluer le potentiel de ces nanostructures pour composer la zone active des lasers sur GaP et sur Si.

Une forte densité de boites quantiques (10^{11} cm^{-2}) est obtenue (cf. Figure 4). Cette densité est compatible avec les applications laser.

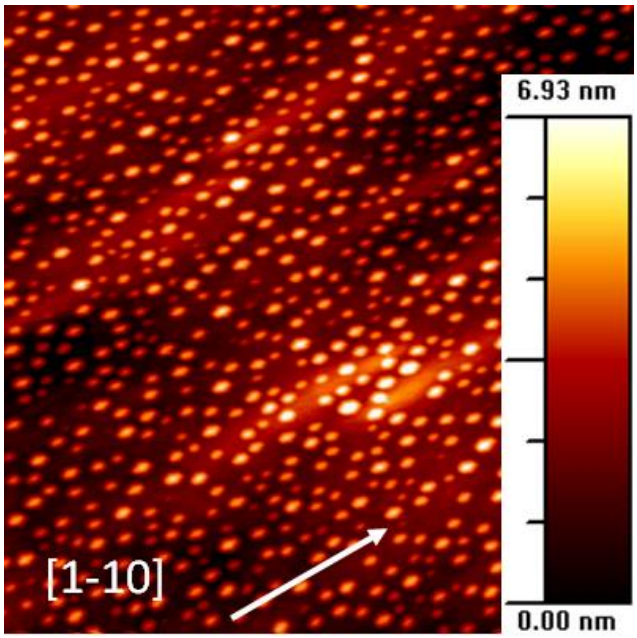

Figure 4: Image STM 800 x 800 nm^2 de boites quantiques InGaAs/GaP.

La photoluminescence à température ambiante est aussi observée (cf. Figure 5). En augmentant la température, une deuxième transition optique plus efficace apparait à plus haute énergie. Des simulations couplant méthode $\mathbf{k}\cdot\mathbf{p}$ et méthode des liaisons fortes suggèrent que cette deuxième transition est directe dans les deux espaces alors que la première implique des états de conduction de type X.

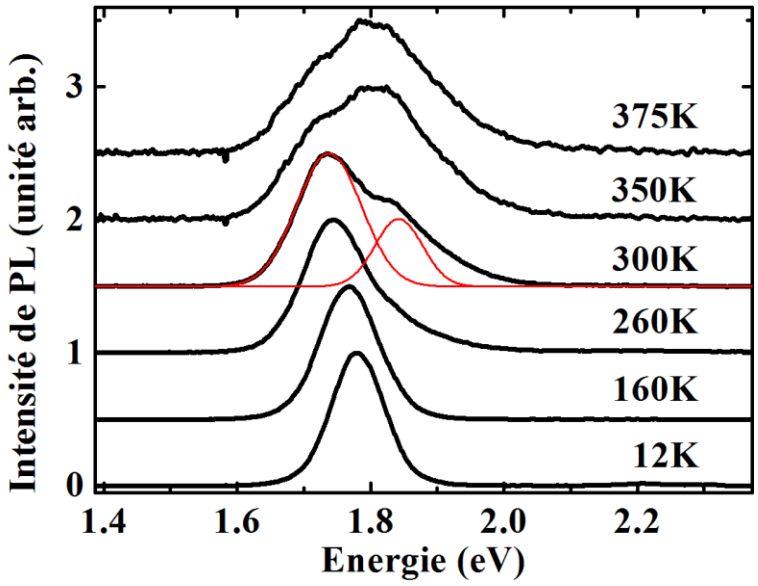

Figure 5: Photoluminescence de boites quantiques InGaAs/GaP en fonction de la température.

Le caractère X de la transition fondamentale est confirmé par la réduction de l'énergie d'émission lorsqu'une pression hydrostatique est appliquée et par la mesure d'un temps de vie radiatif long (1.2 µs). Le bon rendement de luminescence observé à température ambiante est expliqué par une très bonne capture des porteurs par les boites quantiques (avec un temps de montée de l'ordre de 20 ps) ainsi que par la contribution apportée par les états de conduction Γ à la relaxation des porteurs.

Une boite quantique de GaAs/GaP est également simulée par la méthode des liaisons fortes dans une supercellule contenant un million d'atomes. Un résultat peu commun est obtenu. La boite quantique de GaAs confine efficacement les trous (cf. Figure 6(a)), mais les premiers états d'électrons sont confinés au sommet de la boite quantique (cf. Figure 6(b)). Ce comportement est expliqué par la présence d'une déformation biaxiale au sommet de la boite qui confine les électrons dans un potentiel de type X_Z.

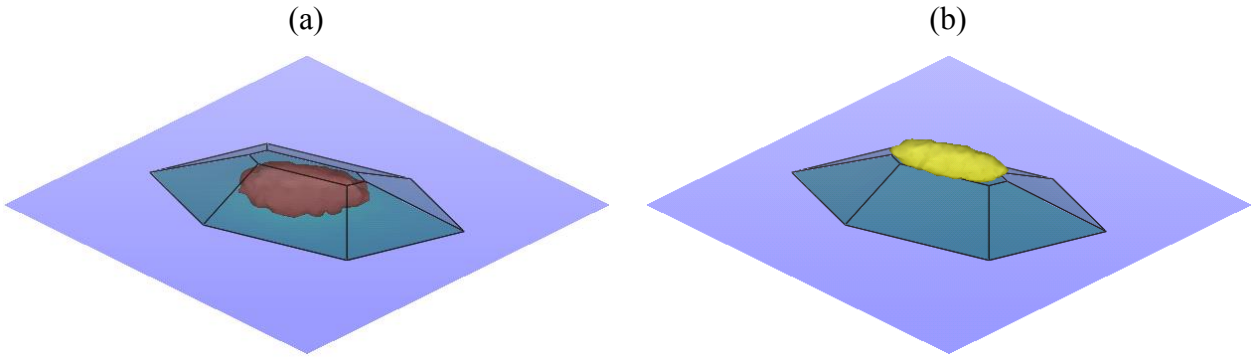

Figure 6: Isosurface de probabilité de densité électronique montrant la localisation de la fonction d'onde du premier niveau de trou dans la boite (a) et du premier niveau électronique au sommet de la boite (b).

Finalement nous démontrons que l'incorporation d'azote dans les boites InGaAsN permet de se rapprocher de la zone de transparence du silicium avec l'obtention de photoluminescence à 1.43 eV (870 nm).

Références bibliographiques

[1] D. Miller, Proc. Ieee **97**, 1166 (2009).
[2] L. Vivien, M. Rouvière, J.-M. Fédéli, D. Marris-Morini, J.F. Damlencourt, J. Mangeney, P. Crozat, L. El Melhaoui, E. Cassan, X. Le Roux, D. Pascal, and S. Laval, Opt. Express **15**, 9843 (2007).
[3] G.T. Reed, G. Mashanovich, F.Y. Gardes, and D.J. Thomson, Nat. Photonics **4**, 518 (2010).
[4] W. Bogaerts, S.K. Selvaraja, P. Dumon, J. Brouckaert, K. De Vos, D. Van Thourhout, and R. Baets, Sel. Top. Quantum Electron. Ieee J. **16**, 33 (2010).
[5] L. Pavesi, L. Dal Negro, C. Mazzoleni, G. Franzo, and F. Priolo, Nature **408**, 440 (2000).
[6] G. Franz , F . Priolo, S. Coffa, A. Polman, and A. Carnera, Appl. Phys. Lett. **64**, 2235 (1994).
[7] H. Rong, R. Jones, A. Liu, O. Cohen, D. Hak, A. Fang, and M. Paniccia, Nature **433**, 725 (2005).
[8] D. Liang and J.E. Bowers, Nat. Photonics **4**, 511 (2010).
[9] R.E. Camacho-Aguilera, Y. Cai, N. Patel, J.T. Bessette, M. Romagnoli, L.C. Kimerling, and J. Michel, Opt. Express **20**, 11316 (2012).
[10] M. Razeghi, M. Defour, R. Blondeau, F. Omnes, P. Maurel, O. Acher, F. Brillouet, J.C. C-Fan, and J. Salerno, Appl. Phys. Lett. **53**, 2389 (1988).
[11] A. Lee, Q. Jiang, M. Tang, A. Seeds, and H. Liu, Opt. Express **20**, 22181 (2012).
[12] L. Cerutti, J.B. Rodriguez, and E. Tournie, Photonics Technol. Lett. Ieee **22**, 553 (2010).
[13] O. Stier, M. Grundmann, and D. Bimberg, Phys. Rev. B **59**, 5688 (1999).
[14] G. Klimeck, S.S. Ahmed, H. Bae, N. Kharche, S. Clark, B. Haley, S. Lee, M. Naumov, H. Ryu, F. Saied, M. Prada, M. Korkusinski, T.B. Boykin, and R. Rahman, Electron Devices Ieee Trans. **54**, 2079 (2007).
[15] J.-M. Jancu, R. Scholz, F. Beltram, and F. Bassani, Phys. Rev. B **57**, 6493 (1998).
[16] W. Shan, W. Walukiewicz, J.W. Ager, E.E. Haller, J.F. Geisz, D.J. Friedman, J.M. Olson, and S.R. Kurtz, Phys. Rev. Lett. **82**, 1221 (1999).
[17] N. Shtinkov, P. Desjardins, and R.A. Masut, Phys. Rev. B **67**, 081202 (2003).
[18] N. Hossain, S.J. Sweeney, S. Rogowsky, R. Ostendorf, J. Wagner, S. Liebich, M. Zimprich, K. Volz, B. Kunert, and W. Stolz, Electron. Lett. **47**, 931 (2011).
[19] S. Liebich, M. Zimprich, A. Beyer, C. Lange, D.J. Franzbach, S. Chatterjee, N. Hossain, S.J. Sweeney, K. Volz, B. Kunert, and W. Stolz, Appl. Phys. Lett. **99**, 071109 (2011).

INSA de RENNES
Service des Formations

AVIS DU JURY SUR LA REPRODUCTION DE LA THESE SOUTENUE

Titre de la thèse:
Etude de nanostructures III-V sur GaP pour l'émission laser sur Si

Nom Prénom de l'auteur : ROBERT CEDRIC

Membres du jury :
- Monsieur VOISIN Paul
- Monsieur ROUILLARD Yves
- Monsieur POHL Udo
- Monsieur GONI Alejandro
- Monsieur DUPERTUIS Marc-André
- Monsieur EVEN Jacky
- Monsieur DURAND Olivier
- Monsieur CORNET Charles

Président du jury : DURAND Olivier

Date de la soutenance : 27 Août 2013

Reproduction de la these soutenue

☒ Thèse pouvant être reproduite en l'état
☐ Thèse pouvant être reproduite après corrections suggérées

Fait à Rennes, le 27 Août 2013

Signature du président de jury

Le Directeur,

M'hamed DRISSI